MECHANOCHEMISTRY OF FLUORIDOARGENTATES(II)

Matic Belak Vivod

Doctoral Dissertation
Jožef Stefan International Postgraduate School
Ljubljana, Slovenia

Supervisor: Asst. Prof. Dr. Mirela Dragomir, Jožef Stefan Institute, Ljubljana, Slovenia

Evaluation Board:
Prof. Dr. Tadej Rojac, Chair, Jožef Stefan Institute, Ljubljana, Slovenia
Assist. Prof. Dr. Marta Počkaj, Member, Faculty of Chemistry and Chemical Technology, University of Ljubljana
Prof. Dr. Dominik Kurzydłowski, Member, Faculty of Mathematics and Natural Sciences, Cardinal Stefan Wyszynski University, Warsaw, Poland

MEDNARODNA PODIPLOMSKA ŠOLA JOŽEFA STEFANA
JOŽEF STEFAN INTERNATIONAL POSTGRADUATE SCHOOL



Matic Belak Vivod

MECHANOCHEMISTRY OF FLUORIDOARGENTATES(II)

Doctoral Dissertation

MEHANOKEMIJA FLUORIDOARGENTATOV(II)

Doktorska disertacija

Supervisor: Asst. Prof. Dr. Mirela Dragomir

Ljubljana, Slovenia, December 2025

To my family and loved ones.

Acknowledgments

First and foremost, I would like to express my deepest gratitude to my PhD supervisor, Dr. Mirela Dragomir, for her unwavering support, guidance, and encouragement throughout the course of this research. Her scientific insight and mentorship have been invaluable at every stage of this work.

I gratefully acknowledge the financial support provided by the Slovenian Research Agency (ARRS) and the K5 department at the Jožef Stefan Institute, whose resources and infrastructure enabled the realisation of this thesis.

Special thanks are due to Dr. Matic Lozinšek and the ECCL research team, not only for their scientific advice and assistance, but also for the collegial spirit and enjoyable moments shared during conferences and collaborative meetings.

I would like to thank Dr. Zvonko Jagličić for carrying out the magnetic measurements, Dr. Graham King for assistance with synchrotron powder diffraction experiments, Dr. Lukáš Palatinus for conducting the three-dimensional electron diffraction analyses, and Dr. Thomas Hansen for performing the neutron powder diffraction measurements. I also wish to thank the undergraduate student Sara Sovdat for her contribution to the experimental work involving $NaAgF_3$.

Finally, I extend my sincere thanks to all colleagues and staff at the K5 department for their help, support, and for creating a friendly and stimulating working environment.

Abstract

Silver, a coinage metal alongside copper and gold, uniquely serves as the only "normal transition metal" in the triad. Whilst copper exhibits a reddish hue and gold displays a yellow lustre, silver possesses a bright white metallic sheen and surpasses all metals in electrical conductivity, thermal conductivity and reflectivity. Beyond its common +1 oxidation state, silver can adopt the much rarer +2 state. The Ag^{2+} cation, with a $4d^9$ electron configuration and an unpaired $4d$ electron, exhibits intriguing chemical and physical properties. It is confined almost exclusively to fluorine environment and together they form the family of compounds called fluoridoargentates(II). The extreme moisture sensitivity of Ag^{2+} demands rigorous handling techniques, resulting in only approximately a hundred of Ag^{2+} compounds compared to the thousands of known Ag^{+} compounds.

Fluoridoargentates(II) display fascinating magnetic properties and have been proposed as analogues to cuprates, with predictions of unconventional superconductivity. However, detailed studies has been hampered by difficulties in their preparation. Currently, these compounds are synthesised via two methods: (i) conventional solid-state synthesis at temperatures >360 °C, which causes decomposition of the main AgF_2 precursors and contamination with secondary phases, and (ii) solution-based methods using hazardous anhydrous hydrogen fluoride that also require specialized equipment and offers access only to a limited subset of compounds. These limitations underscore the need for a room-temperature synthetic approach capable of producing phase-pure samples.

To overcome these obstacles and expand Ag^{2+} chemistry, this thesis introduces mechanochemistry as a viable synthetic route for fluoridoargentates(II). Mechanochemistry operates at room temperature without requiring solvents, affording precise control over milling parameters and enabling access to metastable phases. Whilst mechanochemistry of oxides is well-established, mechanochemistry of fluorides remains nascent, with mechanochemistry of fluoridoargentates(II) entirely unexplored at the outset of this work.

This thesis first benchmarked the mechanochemical synthesis using the $M$$AgF_4$ series (M = Ba, Sr, Hg, Ca, Cd) of compounds, and resolved their structures and magnetic properties via synchrotron and neutron powder diffraction. The optimized conditions were then applied to the alkali metal fluoridoargentates(II) in the $M$$AgF_3$ and $M_2$$AgF_4$ series (M = Na, K, Rb, Cs), enabling ccomprehensive structural and magnetic characterization. Mechanochemistry subsequently enabled discovery of novel phases, including $NaAgF_3$, Ag_2F_3, Ag_3F_4, Ag_3YF_8, and Ag_3BiF_8, with structures determined using three-dimensional electron diffraction complemented by synchrotron and neutron powder diffraction. Magnetic studies revealed antiferromagnetic and ferromagnetic behaviours, with some compounds exhibiting synthesis-dependent properties.

Overall, this thesis demonstrates that mechanochemistry is a powerful method for discovering new fluoridoargentate(II) phases and advancing the understanding of their structural and magnetic properties. It establishes a foundation for future research on the Ag^{2+} cation, potentially uncovering unconventional superconductivity in this system.

Povzetek

Srebro, ena od žlahtnih kovin ob bakru in zlatu, je v tej trojici edini »normalni« prehodni element. Medtem ko ima baker rdečkasto obarvanost, zlato rumen sijaj, se srebro ponaša s svetlo-belim kovinskim leskom in prekaša vse druge kovine v električni in toplotni prevodnosti ter v reflektivnosti. Poleg običajnega oksidacijskega stanja +1 se lahko srebro nahaja tudi v precej redkejšem stanju +2. Kation Ag^{2+}, z elektronsko konfiguracijo $4d^9$ in enim nesparjenim $4d$-elektronom, ima zanimive kemijske in fizikalne lastnosti. Pojavlja se skoraj izključno v prisotnosti fluora in skupaj tvorita družino spojin, imenovanih fluoridoargentati(II). Ekstremna občutljivost Ag^{2+} na vlago zahteva zahtevne tehnike za delo s temi spojinami, zato je znanih le približno 100 spojin Ag^{2+}, v primerjavi s tisočimi znanih spojin Ag^{+}.

Fluoridoargentati(II) imajo fascinantne magnetne lastnosti in so bili predlagani kot analogi kupratom, pri čemer je bilo govora celo o nekonvencionalni superprevodnosti. Podrobna karakterizacija pa je bila doslej otežena zaradi težav pri pripravi. Trenutno se te spojine sintetizirajo z dvema pristopoma: z običajno sintezo v trdnem stanju pri temperaturah nad 350 °C, kar vodi do razpada glavnega reagenta AgF_2 in kontaminacije s sekundarnimi fazami, ter z mokro kemijo, kjer se pa uporablja nevaren brezvodni vodikov fluorid, kar pa zahteva specializirano opremo in omogoča dostop le do omejenega nabora spojin. Te omejitve poudarjajo potrebo po sintetičnem pristopu pri sobni temperaturi, ki bi omogočil pripravo vzorcev brez nečistoč.

S tem namenom se v disertaciji uporabi mehanokemija kot izvedljiva pot sinteze fluoridoargentatov(II). Mehanokemija deluje pri sobni temperaturi brez uporabe topil, omogoča natančno kontrolo parametrov mletja in odpira dostop do metastabilnih faz. Medtem ko je mehanokemija oksidov dobro razvita, je mehanokemija fluoridov še v povojih, mehanokemija fluoridoargentatov(II) pa je bila pred začetkom tega dela popolnoma neraziskana.

V prvem delu disertacije je bil mehanokemijski postopek testiran na seriji $M\mathrm{AgF_4}$ (M = Ba, Sr, Hg, Ca, Cd), pri čemer so bile s sinhrotronsko in nevtronsko praškovno difrakcijo določene strukture in magnetne lastnosti. Optimizirani pogoji so nato bili uporabiljeni za sintezo fazno čistih alkalnih fluoridoargentatov v serijah $M\mathrm{AgF_3}$ and $M_2\mathrm{AgF_4}$ (M = Na, K, Rb, Cs), kar je omogočilo temeljito karakterizacijo. Mehanokemija je nadalje omogočila odkritje novih faz, vključno z $NaAgF_3$, Ag_2F_3, Ag_3F_4, Ag_3YF_8, in Ag_3BiF_8; njihove strukture so bile določene z tridimenzionalno elektronsko difrakcijo in dopolnjene s sinhrotronsko in nevtronsko praškovno difrakcijo. Magnetne študije so razkrile antiferomagnetizem in feromagnetizem, pri nekaterih spojinah pa so se pojavile magnetne lastnosti, ki so se razlikovale v odvisnosti od načina sinteze.

Ta disertacija dokazuje, da je mehanokemija učinkovit pristop za odkrivanje novih faz fluoridoargentatov(II) in za poglabljanje razumevanja njihovih strukturnih in magnetnih lastnosti. Delo postavlja temelje za nadaljnje raziskave kationa Ag^{2+}, ki bi lahko v prihodnje privedle tudi do odkritja nekonvencionalne superprevodnosti v tej družini spojin.

Contents

List of Figures **xv**

List of Tables **xxiii**

Abbreviations **xxvii**

Symbols **xxix**

1 Introduction **1**
1.1 Definition of the Problem ... 1
1.2 Magnetism ... 2
1.3 Fluoridoargentates(II) ... 7
1.4 Mechanochemistry ... 11
1.5 Aims and Hypothesis ... 14

2 Materials and Methods **17**
2.1 Materials ... 17
2.2 Methods ... 17
2.2.1 Synthesis ... 18
2.2.1.1 Mechanochemical synthesis ... 18
2.2.1.2 Solid-state synthesis ... 18
2.2.2 Characterisation ... 19
2.2.2.1 Powder X-ray diffraction (PXRD) ... 19
2.2.2.2 Single-crystal X-ray diffraction (SCXRD) ... 19
2.2.2.3 Raman spectroscopy ... 20
2.2.2.4 Three-dimensional electron diffraction (3D ED) ... 20
2.2.2.5 Magnetic measurements ... 20
2.2.2.6 Synchrotron powder X-ray diffraction ... 20
2.2.2.7 Neutron powder diffraction (NPD) ... 20

3 Results and Discussion **21**
3.1 The MAgF$_4$ series (M = Ba, Sr, Hg, Ca and Cd): Synthesis, Structure, and Magnetism ... 21
3.2 Mechanochemical Synthesis of Alkali Metal Fluoridoargentates(II) ... 38
3.2.1 MAgF$_3$ Series (M = Na, K, Rb and Cs) ... 38
3.2.1.1 CsAgF$_3$ and RbAgF$_3$ ... 41
3.2.1.2 KAgF$_3$ ... 48
3.2.1.3 NaAgF$_3$ ... 62
3.2.2 M_2AgF$_4$ series (M = Na, K, Rb and Cs) ... 70
3.2.2.1 Na$_2$AgF$_4$ ... 71
3.2.2.2 β-K$_2$AgF$_4$ ... 74
3.2.2.3 Rb$_2$AgF$_4$ and Cs$_2$AgF$_4$ ... 80

3.3 Synthesis, Structural and Magnetic Characterisation of the First Mixed-valent Binary Silver(I,II) Compounds 85
3.3.1 $Ag^{I}_{2}Ag^{II}F_{4}$ 85
3.3.2 $Ag^{I}Ag^{II}F_{3}$ 96
3.4 Exploring the Ternary Systems Ag–Y–F and Ag–Bi–F: Synthesis of $Ag^{I}Ag^{II}_{2}YF_{8}$ and $Ag^{I}Ag^{II}_{2}BiF_{8}$ 110
3.4.1 $Ag^{I}Ag^{II}_{2}YF_{8}$ 110
3.4.2 $Ag^{I}Ag^{II}_{2}BiF_{8}$ 117

4 Conclusions **127**

Appendix A Laboratory PXRD Data Collected on the Starting Material **129**

References **133**

Bibliography **143**

Biography **147**

List of Figures

Figure 1: (a) Ferromagnetic and (b) antiferromagnetic superexchange interaction between two magnetic metal cations bridged by a non-magnetic ligand anion. 4

Figure 2: (a) Schematic representation of exchange interactions in magnetic spin chains where black circles symbolise magnetic centres in the crystal lattice and (b) infinite $[AgF]^+$ chains propagating along *c*-crystallographic direction in $CsAgF_3$ (Cs atoms are omitted for clarity). Blue bonds correspond to the direction of intrachain coupling (J_{1D}) and red bonds to the direction of interchain coupling (J'). 6

Figure 3: (a) Schematic representation of exchange interactions in spin layers where black circles symbolise magnetic centres in the crystal lattice and (b) infinite $[AgF_2]$ layers in Cs_2AgF_4, which propagate along the *ab* plane. 7

Figure 4: Extended unit cell of silver difluoride viewed along *b*-crystallographic direction....8

Figure 5: Crystal structure of $Ag(SbF_6)_2$ with magnetically isolated $[AgF_6]^{4-}$ octahedra shown in blue....9

Figure 6: Packing in $[AgF][BF_4]$ where compressed $[AgF_6]^{4-}$ octahedra are stacked along *c* crystallographic direction, forming $[AgF]^+$ infinite chains. 10

Figure 7: Layered crystal structure of α-K_2AgF_4 where compressed $[AgF_6]^{4-}$ octahedra are forming puckered $[AgF_2]$ sheets in the *ac* plane. 10

Figure 8: Stages during the high-energy milling. 13

Figure 9: Energy landscape of a chemical reaction illustrating mechanochemical access to metastable phases. Blue lines denote energy levels of reactants, metastable product and the thermodynamically stable product. The red curve represents conventional solid-state synthesis, which proceeds directly to the stable product. In contrast, the green curve depicts the mechanochemical route, where mechanical energy surmounts kinetic barriers, stabilizing a metastable phase before relaxation to the stable state. The red dotted curve represents additional annealing of the metastable product. Adapted from [56]. 14

Figure 10: (a) Retsch shaker mill MM 400 and (b) 10 ml milling jars and milling balls with different diameters, used for the ball-milling reactions. 18

Figure 11: Setup for the solid-state reaction employed in the work presented in this thesis....19

Figure 12: Rietveld refinements of the room-temperature laboratory PXRD data measured on $MAgF_4$ samples prepared with the solid-state method for (a) $BaAgF_4$, (b) $SrAgF_4$, (c) $HgAgF_4$, (d) $CaAgF_4$ and (e) $CdAgF_4$. 23

Figure 13: (a) Expanded unit cell of $BaAgF_4$ viewed along the *b*-axis, (b) coordination of the Ag^{2+} cation. Ellipsoids are drawn with 50 % probability. (c) Single crystal of $BaAgF_4$ mounted on the goniometer. 25

Figure 14: Time-dependant PXRD data collected on the ball-milled (a) AgF_2 and (b) SrF_2. The milling conditions used for the synthesis are detailed in Table 6. 27

Figure 15: PXRD data of milled $SrAgF_4$ showing the effects of (a) milling frequency, (b) milling ball diameter, and (c) milling cycle duration on the synthesis, and (d) time-dependent data under optimized milling conditions. 28

Figure 16: Laboratory PXRD patterns of $SrAgF_4$ samples prepared by ball milling under various milling conditions. Sample S0 corresponds to the PXRD pattern of $SrAgF_4$ synthesized by the solid-state method. The most intense AgF peak is indicated by an orange dotted line. 29

Figure 17: Rietveld refinements of high-resolution synchrotron PXRD data of: (a) solid-state synthesised $SrAgF_4$ and (b) mechanochemically synthesised $SrAgF_4$. 30

Figure 18: Comparison of the PXRD data obtained on the ball-milled (BM), ball-milled and annealed (BMA), and solid-state (SS) synthesised samples of the MAgF$_4$ series, M = Ba, Sr, Hg, Ca and Cd. 31

Figure 19: Crystal structure of $BaAgF_4$ viewed along the c-axis, highlighting a single layer of $[AgF_4]^{2-}$ anions. Ag–F distances are shown, with solid lines representing shorter, primary Ag–F bonds and dashed lines indicating longer, secondary Ag–F contacts. 32

Figure 20: Magnetic susceptibility (ZFC) versus temperature measured under a 1 kOe field for ball-milled (BM), ball-milled and annealed (BMA), and solid-state synthesized (SS) samples of (a) $BaAgF_4$ and (b) $SrAgF_4$. Left insets show $\mathrm{d}(\chi \cdot T)/\mathrm{d}T$ versus temperature for the SS samples. Right insets present Curie-Weiss fits to the inverse magnetic susceptibility of the SS samples. 33

Figure 21: ZFC magnetic susceptibility measured as a function of temperature in the magnetic field of 1 kOe for ball-milled (BM), ball-milled and additionally annealed (BMA) and solid-state synthesised (SS) samples of: (a) $CaAgF_4$ and (b) $CdAgF_4$. The left insets represent $\mathrm{d}(\chi \cdot T)/\mathrm{d}T$ as a function of temperature for the solid-state samples while the Curie-Weiss fits to the inverse of the magnetic susceptibility of the solid-state samples are shown in the right insets. 34

Figure 22: The T_N plotted as a function of ionic radius of the M^{2+} cation, with a linear fit given by the following equation: $y = -18(1) \cdot x + 30(2)$; $R^2 = 0.991$. 35

Figure 23: (a) The NPD data measured at 9 and 1.83 K and the difference plot. Magnetic peaks are marked with green arrows. (b) Rietveld fit to the NPD data measured at 1.83 K on the solid-state synthesised $SrAgF_4$, refined using a combined structural and magnetic model; wt.% ($SrAgF_4$) = 91.4(1); wt.% (AgF) = 8.6(1). (c) Magnified region in the 10–70 2θ range showing the magnetic peaks accounted in the Rietveld refinement, which are marked with green arrows; the unidentified peaks are marked with black star symbols. (d) Magnetic structure of $SrAgF_4$. Strontium and fluorine atoms are omitted for clarity. 36

Figure 24: (a) Crystal structure of $CsAgF_3$. Bond lengths of the $[AgF_6]^{4-}$ octahedra are marked with letters s (small), m (medium) and l (large). (b) Crystal structure of $KAgF_3$. 39

Figure 25: Rietveld refinement of the laboratory PXRD data of ball-milled (a) $RbAgF_3$ and (b) $CsAgF_3$ measured at room temperature. Comparison of the laboratory PXRD data of BM, BMA and SS samples of (c) $RbAgF_3$ and (d) $CsAgF_3$. Green star symbols indicate peaks of unidentified impurities. 41

Figure 26: Room-temperature Raman spectra measured on $RbAgF_3$ samples, which were synthesised by three different methods: ball-milling (BM), ball-milling and annealing (BMA) and solid-state synthesis (SS).....42

Figure 27: Room-temperature Raman spectra measured on $CsAgF_3$ samples, which were synthesised by three different methods: ball-milling (BM), ball-milling and annealing (BMA) and solid-state synthesis (SS).....44

Figure 28: ZFC magnetic susceptibility, $\chi(T)$, measured in an applied field of 1 kOe for $RbAgF_3$ (a) and $CsAgF_3$ (b). Temperature dependence of the effective magnetic moment, $\mu_{eff}(T)$, derived from the data in (a, b) for $RbAgF_3$ (c) and $CsAgF_3$ (d). Field-dependent magnetization, $M(H)$, at 2 K for $RbAgF_3$ (e) and $CsAgF_3$ (f).....46

Figure 29: (a) Rietveld refinement of the 2K NPD data obtained on the ball-milled $CsAgF_3$ sample. Black star symbols represent unidentified peaks. (b) NPD data obtained on the ball-milled $CsAgF_3$ sample measured at 2 and 70 K with the difference plot.....47

Figure 30: (a) Laboratory PXRD data of BM, BMA-200, BMA-300 and SS $KAgF_3$ samples measured at 100 K and at 293 K. (b) Room temperature Raman spectra of BM, BMA-200, BMA-300 and SS $KAgF_3$ samples.....49

Figure 31: (a) Rietveld refinement analysis of the room-temperature synchrotron data of the BM $KAgF_3$ sample using the *Pnma* space group. Inset shows the (111), (211) and (112) reflections of the *Pnma* space group, which are absent in the *Pcma* structural model. Wt.% ($KAgF_3$) = 90.8(4)°% and wt.% (AgF) = 9.2(1) %. (b) Rietveld refinement analysis of the room-temperature synchrotron PXRD data measured on the BM $KAgF_3$ using *Pcma* space group. Inset shows weak reflections which were not accounted in the refinement and belong to the *Pnma* space group. Wt.% ($KAgF_3$) = 91.2(2) % and wt.% (AgF) = 8.8(1) %.....51

Figure 32: Temperature-dependent synchrotron PXRD data of the BM sample measured from 225 K to 500 K. The grey pattern at 380 K marks the temperature at which the (111) reflection of the *Pnma* polymorph and group of reflections in the green bracket at around 12.5° 2θ, which are also associated with the *Pnma* polymorph, disappear. The violet pattern at 460 °C corresponds to the temperature at which the sample decomposition begins.....52

Figure 33: (a) Unit-cell parameters *a*, *b* and *c* for $KAgF_3$. (b) Unit-cell volumes of $KAgF_3$ and AgF. (c) Wight residual factors (R_{wp}) plotted as a function of temperature. All were obtained with the Rietveld refinement of the synchrotron PXRD data collected between 100–450 K on the BM sample.....53

Figure 34: TEM images of $KAgF_3$ crystallites on which the 3D electron diffraction data was collected. Image (a) corresponds to the sample prepared with ball-milling, image (b) to the sample prepared with ball-milling and additional annealing step and image (c) to the sample prepared with the solid-state method.....55

Figure 35: (a) Unit cell of the *Pnma* $KAgF_3$ obtained with 3D electron diffraction at 273 K. The red bond of $[AgF_6]^{4-}$ octahedra is the longest, while those in blue are the shortest. (b) Packing of $[AgF_6]^{4-}$ octahedra along *a* crystallographic direction. (c) Packing of $[AgF_6]^{4-}$ octahedra along *c* crystallographic direction. In all three figures, ellipsoids are presented with 50 % probability.....55

Figure 36: Temperature-dependent magnetic susceptibility measured at 1 kOe for (a) BM, (b) BMA-200, (c) BMA-300, and (d) SS samples of $KAgF_3$. Insets show the first derivative of the ZFC curves, highlighting the transition temperatures.....58

Figure 37: Effective magnetic moment measured as a function of temperature for the $KAgF_3$ samples synthesised in this study.....59

Figure 38: (a) Magnetic susceptibility measured as a function of temperature for BM, BMA-200, BMA-300 and SS samples. For comparison, the susceptibility reported in the literature [87] is also shown. (b) Magnetisation measured as a function of magnetic field at the temperature of 2 K for BM, BMA-200, BMA-300 and SS samples. 60

Figure 39: (a) Rietveld refinement of the NPD data collected at 70 K using the *Pnma* space group. Wt.% (KAgF3) = 92.3(1) %; wt.% (AgF) = 7.7(1) %. (b) Comparison of the 2 K, 40 K and 70 K NPD data. The inset shows weak peak at about 16.6° 2θ. 61

Figure 40: Comparison of the laboratory PXRD data measured at room temperature with Ag Kα wavelength of ball-milled and two annealed samples of $NaAgF_3$. The $NaAgF_3$ phase will be discussed later in this chapter. 63

Figure 41: TEM images of four different $NaAgF_3$ crystallites observed in the BMA-300 sample on which the 3D electron diffraction data was collected. Red circles mark irradiated area..... 64

Figure 42: (a) Crystal structure of $NaAgF_3$ obtained with the 3D ED experiment. Ellipsoids are drawn with 50 % probability and Ag–F–Ag angle α = 120.3(3)°. (b) Packing along *a* and (c) packing along *b* crystallographic direction. 65

Figure 43: Three-phase Rietveld refinement of the laboratory PXRD data of the BMA-300 sample. Black star marks an unidentified peak. 68

Figure 44: (a) Magnetic susceptibility curves (ZFC and FC) measured as a function of temperature in the field of 1 kOe. Inset shows the maximum of the first derivative of ZFC magnetic susceptibility, which corresponds to the transition temperature of $NaAgF_3$. (b) Curie-Weiss fit in the linear region between 100 and 300 K to the inverse of the ZFC magnetic susceptibility measured as a function of temperature in the field of 1 kOe. (c) Magnetisation of $NaAgF_3$ sample as a function of magnetic field measured at 2 K. A hysteresis shown in the inset indicates a ferromagnetic ground state. (d) Plot of the effective magnetic moment, μ_{eff}, as a function of temperature for FC and ZFC curves at 1 kOe... 69

Figure 45: (a) Comparison of the laboratory PXRD data collected on BM and BMA-300 Na_2AgF_4 samples. (b) Unit cell of Na_2AgF_4. (c) Three-phase Rietveld refinement of the BMA-300 laboratory PXRD data. (d) Comparison of Raman spectra of BM and BMA-300 Na_2AgF_4 samples..... 72

Figure 46: (a) Magnetic susceptibility measured as a function of temperature for BM Na_2AgF_4 sample. Inset shows two Bonner-Fisher fits in the 2–25 K region. (b) Curie-Weiss fit of the inverse of the ZFC magnetic susceptibility in the 10-200 K region of the BM Na_2AgF_4 sample. (c) Magnetic susceptibility measured as a function of temperature for BM-300 Na_2AgF_4 sample. Inset shows Bonner-Fisher fit in the 2–25 K region. (d) Curie-Weiss fit of the inverse of the ZFC magnetic susceptibility in the 10–200 K region of the BM Na_2AgF_4 sample..... 73

Figure 47: Crystal structure of (a) α-K_2AgF_4 and (b) β-K_2AgF_4..... 75

Figure 48: (a) Four-phase Rietveld refinement of the laboratory PXRD data collected on the BM K_2AgF_4 sample. (b) Laboratory PXRD data of time-dependent milling of K_2AgF_4..... 76

Figure 49: (a) Laboratory PXRD data for BM and BMA-300 β-K_2AgF_4 samples. Violet lines mark the Bragg reflections of β-K_2AgF_4, while pink full circles indicate an unidentified impurity. (b) Raman spectra of BM and BMA-300 β-K_2AgF_4 samples. 77

Figure 50: Three-phase Rietveld refinement of the laboratory PXRD data collected on the BMA-300 β-K_2AgF_4 sample. Pink full circles represent an unidentified impurity. 77

Figure 51: Magnetic susceptibility shown as a function of temperature for (a) BM and (b) BMA-300 samples. The insets in a and b show $-d\chi/dT$ vs. T plots. Curie-Weiss fits of an inverse of ZFC magnetic susceptibility for (c) BM and (d) BMA-300 samples. Effective magnetic moments plotted as a function of temperature for (e) BM and (f) BMA-300 samples. Magnetisation plotted as a function of magnetic field for (g) BM and (h) BMA-300 samples.....79

Figure 52: (a) Crystal structure of Cs_2AgF_4 crystallising in $I4/mmm$ space group and (b) coordination of Ag^{2+} cation forming an equatorially compressed [AgF_6] octahedra. (c) Crystal structure of Cs_2AgF_4 crystallising in *Bbcm* space group and (d) coordination of Ag^{2+} cation forming an axially elongated [AgF_6] octahedra.....81

Figure 53: Rietveld refinement of the laboratory PXRD data obtained on the ball-milled (a) Rb_2AgF_4 and (b) Cs_2AgF_4. (c) Comparison of Raman spectra of Rb_2AgF_4 and Cs_2AgF_4 samples.....82

Figure 54: Magnetic susceptibility measured as a function of temperature with the Curie-Weiss fits presented in the insets for (a) Rb_2AgF_4 and (b) Cs_2AgF_4. Magnetization curves measured as a function of magnetic field at 2 K for (c) Rb_2AgF_4 and (d) Cs_2AgF_4.....83

Figure 55: Room-temperature Raman spectrum of AgF_2 particle measured using 785 nm excitation laser with 1 mW power (red line) and Raman spectrum obtained after the same AgF_2 particle was illuminated with green laser with 532 nm wavelength and 12.5 mW power for 20 seconds (black line).....86

Figure 56: (a) Laboratory PXRD patterns of ball-milled (BM) and solid-state (SS) synthesised 2:1 phase samples (AgF_2:AgF molar ratio = 2:1). (b) Raman spectra of the 2:1 phase and β-K_2AgF_4, both synthesised by ball-milling. 88

Figure 57: (a) Indexing ($P2_1/c$ space group) of the synchrotron PXRD data measured with $\lambda = 0.3497$ Å. (b) Three-phase Rietveld refinement of the synchrotron PXRD data collected on the $Ag^{I}_2Ag^{II}F_4$ sample prepared with by the solid-state method. 89

Figure 58: (a) Rietveld refinement of the laboratory PXRD data of solid-state sample of $Ag^{I}_2Ag^{II}F_4$.. (b) Rietveld refinement of the laboratory PXRD data of mechanochemically synthesised sample of $Ag^{I}_2Ag^{II}F_4$ 91

Figure 59: (a) The expended unit-cell of $Ag^{I}_2Ag^{II}F_4$. (b) Coordination surroundings with atom distances for silver(II) cation (Ag1). (c) The double-fluorine bridged chain, which propagates along the *a*-crystallographic direction. (d) Coordination surroundings with atom distances for silver(I) cation (Ag2). 92

Figure 60: (a) Temperature-dependent magnetic susceptibility of mechanochemically synthesised $Ag^{I}_2Ag^{II}F_4$ sample measured in a magnetic field of 1 kOe. The inset shows the Curie-Weiss fit to the inverse of magnetic susceptibility in the 15–300 K range. (b) Magnetization of $Ag^{I}_2Ag^{II}F_4$ as a function of magnetic field measured at 2 K and 5 K, respectively. The inset shows a hysteresis indicating a ferromagnetic ground state. 94

Figure 61: (a) Two-phase Rietveld refinement of the NPD data collected at 5 K. Wt.% ($Ag^{I}_2Ag^{II}F_4$) = 88.9(1)%; wt.% (AgF) = 11.1(1) %. (b) Comparison of the NPD data measured at 5 and 1.7 K shows a weak feature around 15° 2θ – green arrow in the inset..... ..95

Figure 62: Bonner–Fisher fit to the ZFC magnetic susceptibility of the $Ag^{I}_{2}Ag^{II}F_4$ sample prepared by ball milling, measured in the 2–25 K temperature range. 96

Figure 63: Indexing of the high-resolution synchrotron data of the 1:1 sample measured with $\lambda = 0.3497$ Å..... 97

Figure 64: (a) Three-phase Rietveld refinement of a synchrotron data collected on the $Ag^{I}Ag^{II}F_3$ sample prepared by solid-state method. (b) Rietveld refinement of the laboratory PXRD data collected on a fresh mechanochemically synthesised $Ag^{I}Ag^{II}F_3$ sample measured at 100 K immediately after the synthesis. 99

Figure 65: Raman spectra of freshly ball-milled $Ag^{I}Ag^{II}F_3$ and $Ag^{I}_{2}Ag^{II}F_4$ samples, measured with a 785 nm laser at 1 mW. For comparison, the spectrum of $KAgF_3$ prepared by the solid-state method is also shown. 102

Figure 66: (a) Unit cell of $Ag^{I}Ag^{II}F_3$ with $[AgF_6]^{4-}$ octahedra color-coded by bond length: red = longest, blue = medium, green = shortest. (b) Packing of $[AgF_6]^{4-}$ octahedra along the *c*-crystallographic axis. (c) Packing of $[AgF_6]^{4-}$ octahedra along the *a*-crystallographic axis..... 103

Figure 67: (a) Weight fractions of phases in the samples obtained by Rietveld refinement of laboratory PXRD data during the milling experiment. (b) Time-dependent phase composition of mechanochemically synthesized $Ag^{I}Ag^{II}F_3$ over 30 days, obtained by Rietveld refinement..... 106

Figure 68: Temperature-dependent susceptibility, χ, of $Ag^{I}Ag^{II}F_3$, measured in a magnetic field of 1 kOe. The left inset shows magnified 2–25 K region and the right inset shows the first derivative of the magnetic susceptibility as a function of temperature, where the transition temperature of 7.3(7) K was determined. 107

Figure 69: (a) Plot of the effective magnetic moment, μ_{eff}, as a function of temperature for field cooled and ZFC curves at 1 kOe and for the ZFC curve measured at 10 kOe. (b) Magnetization of $Ag^{I}Ag^{II}F_3$ as a function of magnetic field, measured at 2 K. 108

Figure 70: (a) Expanded unit cell of $Ag^{I}Ag^{II}_{2}YF_8$, where four short Ag–F contacts around Ag^{2+} cations are presented as square plaquettes; coordination surroundings with atom distances in Å for both non-equivalent divalent silver cations in the crystal structure – (b) Ag3 and (c) Ag4. (d) Single-layer of edge-sharing $[AgF_8]^{6-}$ units viewed along *b*-crystallographic direction. (e) Packing of $Ag^{I}Ag^{II}_{2}YF_8$ viewed along *a*-crystallographic direction..... .. 112

Figure 71: (a) Rietveld refinement of the synchrotron PXRD data collected on the green part of the solid-state synthesised $Ag^{I}Ag^{II}_{2}YF_8$ sample. (b) Laboratory PXRD data collected on the yellow part of the solid-state synthesised sample. 114

Figure 72: Comparison of (a) PXRD patterns and (b) Raman spectra of the starting materials (YF_3 and AgF_2), along with the BM and BMA-350 samples. Black squares in the PXRD pattern of the BM sample indicate reflections from YF_3. (c) Rietveld refinement of laboratory PXRD data collected for the BMA-350 sample. (d) Raman spectra of the BMA-350 sample with indicated peak positions. 115

Figure 73: (a) Magnetic susceptibility of BMA-350 sample measured as a function of temperature in the field of 1 kOe. An inset shows Fisher's heat capacity, where the transition temperature of 11.6(1) K was determined. (b) Curie-Weiss fit to the inverse of ZFC magnetic susceptibility measured as a function of temperature. 116

Figure 74: (a) Rietveld refinement of the NPD data collected on the BMA-350 sample at 15 K. Green star marks one unidentified peak. (b) The NPD data measured at 2 and 15 K and the difference plot. The inset shows region where magnetic peaks are observed (marked with dark green squares)..... 116

Figure 75: Rietveld refinement of the laboratory PXRD data collected on (a) BM sample and (b) BMA-350 sample. 117

Figure 76: Comparison of the laboratory PXRD data collected on the SS (red pattern) and BMA (black pattern) samples using Ag Kα radiation (λ = 0.5609 Å). Green broken lines represent peaks of the new Ag–Bi–F phase. 118

Figure 77: (a) Unit-cell of $Ag^{I}Ag^{II}_{2}BiF_{8}$. Shorter Ag–F contacts are represented with full orange bonds while longer Ag–F contacts are represented with broken orange bonds. Ellipsoids are drawn with 50 % probability. (b) Coordination surroundings of Ag2 (Ag^{2+}) cation with bond distances in Å. Crystal packing shown along (b) *b*-crystallographic direction and (c) *c*-crystallographic direction. 119

Figure 78: (a) Laboratory PXRD data of AgF_2, BiF_3, BM, and BMA-350 samples. Bragg reflections of $Ag^{I}Ag^{II}_{2}BiF_{8}$ are indicated with pink lines. (b) One-phase Rietveld refinement of the PXRD data for the BMA-350 sample. (c) Raman spectra of the BMA-350 sample with indicated peak positions. 121

Figure 79: (a) Temperature-dependent susceptibility χ measured in a magnetic field of 1 kOe for BMA-350 and S2 samples. An inset shows Fisher's heat capacity as a function of temperature for the BMA-350 sample, where the transition temperature of 13.7(1) K is determined. The question mark points on an onset of ferromagnetic transition of unidentified impurity. (b) Curie-Weiss fit to the inverse of magnetic susceptibility for the BMA-350 sample and (c) S2 sample. 122

Figure 80: Rietveld refinement of the laboratory PXRD data collected on the Bi-NPD sample at the room temperature (synthesis conditions in Table 39). 123

Figure 81: (a) Rietveld refinement of the 16.8 K NPD data collected on the Bi-NPD sample. (b) The NPD data measured at 1.8 (black) and 16.8 K (red) and the difference plot (blue). Magnetic peaks are marked with black star symbol. 124

Figure 82: (a) Temperature dependent NPD data measured in the 1.8–16.8 K range with an approximate 1 K step magnified on the most intense magnetic peak at 21.8° 2θ. (b) Peak intensity of the lower-angle magnetic peak, 21.8°, versus temperature indicating T_N ~ 18 K. The solid line is a power-law fit with an equation: $I = I0 \cdot (1 - xTN)2\beta$..... 124

Figure 83: (a) Rietveld refinement of the room-temperature laboratory PXRD data (Ag Kα) collected on the AgF_2 provided by Sigma Aldrich. (b) Comparison of the PXRD patterns between AgF_2 purchased from Sigma Aldrich, Fluorochem and Thermo Scientific. (c) Laboratory PXRD data collected on the $KAgF_3$ samples, prepared by two different AgF_2 sources..... 130

Figure 84: Rietveld refinement of the room-temperature laboratory PXRD data (Ag Kα) collected on (a) AgF and (b) BaF_2. 130

Figure 85: Rietveld refinement of the room-temperature laboratory PXRD data (Ag Kα) collected on (a) BiF_3, (b) CaF_2, (c) CdF_2, (d) CsF, (e) HgF_2, (f) KF, (g) LaF_3 and (h) NaF..... 131

Figure 86: Rietveld refinement of the room-temperature laboratory PXRD data (Ag Kα) collected on RbF, SrF_2 and YF_3. 132

List of Tables

Table 1: List of reagents used for the synthesis of compounds in the thesis with specified provider and purity. 17

Table 2: Solid-state synthesis conditions for the preparation of the MAgF$_4$ compounds..22

Table 3: Selected structural parameters obtained with the Rietveld refinement analysis of the laboratory PXRD data of MAgF$_4$ samples synthesised with the solid-state method in this study compared to the lattice parameters reported by Odenthal and Hoppe [36]. 24

Table 4: Crystal data and structure refinement for BaAgF$_4$. 26

Table 5: Atomic positions and atomic displacement parameters for atoms in BaAgF$_4$. ...26

Table 6: Milling conditions for separate milling of the starting reagents (AgF$_2$ and SrF$_2$)27

Table 7: Milling conditions for the synthesis of SrAgF$_4$ samples in Figure 16, using different combination of milling parameters. 29

Table 8: Synthesis conditions for the mechanochemical synthesis of the MAgF$_4$ series....30

Table 9: Crystallographic parameters of the magnetic SrAgF$_4$ phase obtained by the Rietveld refinement of NPD data. Note that Ag^{2+} cation was replaced with Cu^{2+} cation as an approximation for the Rietveld refinement. 37

Table 10: Synthesis conditions for the preparation of RbAgF$_3$ and CsAgF$_3$ samples with three different methods. 41

Table 11: Comparison of Raman peak positions for solid-state synthesised RbAgF$_3$ obtained in this study with those reported by Koteras *et al.* [4]. 43

Table 12: Comparison of Raman peak positions for solid-state synthesised CsAgF$_3$ obtained in this study with those reported by Koteras *et al.* [4]. 45

Table 13: Synthesis conditions for the preparation of KAgF$_3$ samples with four different synthesis procedures. 48

Table 14: Comparison of peak positions in the Raman spectrum of solid-state synthesised KAgF$_3$ prepared in this study versus from the study of Koteras *et al.* [91]. 50

Table 15: Weighted profile R-factor, R_{wp}, (%) obtained with the Rietveld refinement of the laboratory PXRD data of KAgF$_3$ samples prepared with different methods. The data was measured at the 293 K and at 100 K and refined with each of the space groups. 54

Table 16: Crystallographic information on the SS KAgF$_3$ sample obtained at 100 K. 56

Table 17: Comparison of the unit-cell parameters obtained by 3D ED of the SS synthesised KAgF$_3$ with the *Pnma* space group at different temperatures, as determined by 3D ED.57

Table 18: Synthesis conditions for the NaAgF$_3$ samples. 62

Table 19: Crystallographic information and refinement details on the $NaAgF_3$ sample obtained by the 3D ED experiment. 66

Table 20: Atomic parameters and thermal displacement parameters for atoms in $NaAgF_3$ obtained with the refinement of the 3D ED data..... 67

Table 21: Interatomic distances and bond valence sum analysis [96] for silver atoms in $NaAgF_3$. The following bond valence parameters were employed: $b = 0.37$ Å; $R_0 = 1.79$ Å (Ag^{II}—F) [97]..... 67

Table 22: Conditions for the synthesis of Na_2AgF_4 samples. 71

Table 23: Conditions used in this study for the synthesis of β-K_2AgF_4 samples. 75

Table 24: Synthesis conditions for Rb_2AgF_4 and Cs_2AgF_4..... 81

Table 25: Conditions for the synthesis of the 2:1 phase using the solid-state synthesis and ball-milling 87

Table 26: Crystallographic parameters of $Ag^{I}_2Ag^{II}F_4$ phase obtained with the Rietveld refinement of synchrotron data. 90

Table 27: Interatomic distances and BVS analysis [96] for both silver atoms in $Ag^{I}_2Ag^{II}F_4$. The following bond valence parameters were employed: $b = 0.37$ Å; $R_0 = 1.80$ Å (Ag^{I}—F) and 1.79 Å (Ag^{II}—F) [123, 97]. 93

Table 28: Synthesis conditions of the solid-state synthesis and ball-milling of 1:1 phase. 97

Table 29: Crystallographic parameters of $Ag^{I}Ag^{II}F_3$ obtained with the Rietveld refinement of synchrotron data 100

Table 30: Influence of the ionic radius of the M^+ cation on the crystal symmetry of $MAgF_3$ phases. Goldschmidt tolerance factors (t) were calculated with formula: $\mathsf{t = rM + +rF - (rAg2 + +rF-) \times 2}$, where $\mathsf{rM+}$ is the size of M^+ cation. For the calculations, the values for Ag^{2+} cation and F^- anion of $\mathsf{rAg2+=}$ 0.94 Å (CN = 6) and $\mathsf{rF-=}$ 1.33 Å (CN = 6) were used..... 101

Table 31: Interatomic distances and bond valence sum analysis [96] for two silver(I) atoms in $Ag^{I}Ag^{II}F_3$. The following bond valence parameters were employed: $b = 0.37$ Å and $R_0 = 1.80$ Å (Ag^{I}—F) [123, 97]. 104

Table 32: Interatomic distances and bond valence sum analysis [96] for four silver(II) atoms in $Ag^{I}Ag^{II}F_3$. The following bond valence parameters were employed: $b = 0.37$ Å and $R_0 = 1.79$ Å (Ag^{II}—F) [123, 97]. 105

Table 33: Conditions for the synthesis of $Ag^{I}Ag^{II}_2YF_8$ with three different methods. 111

Table 34: Atomic parameters for $Ag^{I}Ag^{II}_2YF_8$ determined via 3D ED. 112

Table 35: Interatomic distances and bond valence sum for all atoms in $Ag^{I}Ag^{II}_2YF_8$. ... 113

Table 36: Positions of atoms and atomic displacement parameters in the crystal structure of $Ag^{I}Ag^{II}_2BiF_8$ determined via 3D ED. 120

Table 37: Interatomic M–F (M = Ag^+, Ag^{2+}, Bi^{3+}) distances and BVS analysis for $Ag^{I}Ag^{II}_2BiF_8$..... 120

Table 38: Synthesis conditions used for the $Ag^{I}Ag^{II}_2BiF_8$ phase..... 120

Table 39: The synthesis conditions for the preparation of the $Ag^{I}Ag^{II}_2BiF_8$ sample for the NPD data collection with the sample code Bi-NPD..... 123

Table 40: Overview of compounds investigated in the thesis. 127

Abbreviations

1D	. . . One-dimensional
2D	. . . Two-dimensional
3D ED	. . . Three-dimensional electron diffraction
aHF	. . . Anhydrous hydrogen fluoride
BRR	. . . Ball-to-reagents-ratio
CN	. . . Coordination number
DFT	. . . Density functional theory
FC	. . . Field cooled
ILL	. . . Institute Laue Langevin
NPD	. . . Neutron powder diffraction
PXRD	. . . Powder X-ray diffraction
SCXRD	. . . Single-crystal X-ray diffraction
TEM	. . . Transition electron microscopy
ZFC	. . . Zero field cooled

Symbols

α, β, γ ... Greek letters used to denote polymorphs or unit-cell angles
a, b, c ... Unit-cell parameters
B ... Magnetic flux density
C ... Curie constant
d ... Interatomic distance
e ... Elementary charge
E ... Energy
g ... G-factor
g_{L} ... Electron orbital g-factor
g_{S} ... Electron spin g-factor
H_{ab} ... Heisenberg Hamiltonian
J ... Superexchange constant
J_{1D} ... Superexchange constant in one dimension
J_{2D} ... Superexchange constant in two dimensions
J_{ab} ... Superexchange constant between two coupled magnetic cations a and b
J' ... Superexchange constant between the chains or between the layers
k ... Magnetic propagation vector
k_{B} ... Boltzmann constant
L ... Orbital angular momentum
l ... Azimuthal quantum number
m_{e} ... Electron mass
N_{A} ... Avogadro number
r ... Distance
R_{wp} ... Weight residual factor
S ... Spin angular momentum
s ... Spin quantum number
T ... Temperature
t ... Time
T_{C} ... Curie temperature
T_{N} ... Néel temperature
$\hbar$ ... Planck constant
θ ... Theta angle in powder X-ray diffraction

θ_{CW} ... Curie-Weiss temperature
λ ... Wavelength
μ_0 ... Permeability in vacuum
μ_1, μ_2 ... Magnetic dipoles
μ_B ... Bohr magneton
μ_{eff} ... Effective magnetic moment
μ_L ... Orbital magnetic dipole moment
μ_S ... Spin magnetic dipole moment
π ... Pi constant
ρ ... Molar ratio of isolated magnetic moments
χ_m ... Molar magnetic susceptibility

Chapter 1

Introduction

The introduction provides a brief overview of the literature on the topics relevant to this thesis. The first chapter begins with the definition of the problem and the motivation for this research. In the following sections, the basic concepts of magnetism are introduced, followed by description of fluoridoargentates(II) with particular attention devoted to their structural and magnetic properties. State-of-the-art in methods for the preparation of fluoridoargentates(II) are also discussed and mechanochemistry is proposed as an alternative method. This chapter concludes with a description of the aims of the dissertation.

1.1 Definition of the Problem

Fluoridoargentates(II) are a family of compounds based on divalent silver and fluorine. At the beginning of the twenty-first century, they were recognised as analogues to cuprate superconductors, which was also the main motivation of the research [1]. Theoretical studies suggested that the presence of Ag^{2+} in a fluorine framework could lead to similar electronic structures as those observed in copper-based superconductors. However, the extreme reactivity and moisture sensitivity of fluoridoargentates(II) [2] not only restricts the available synthetic methods but also significantly hampers progress in this field.

Currently, fluoridoargentates(II) can be prepared either by high-temperature solid-state synthesis or in solution, where the solvent of choice is the highly hazardous anhydrous hydrogen fluoride (aHF). The main disadvantage of solid-state synthesis, which is currently the most widely used technique for the preparation of fluoridoargentates(II), is the decomposition of the main precursor, AgF_2, at relatively low temperatures (360 °C) [3]. This often results in the presence of magnetic impurities in the sample, which complicates the magnetic characterisation significantly [4]. These issues highlight the need for an alternative synthetic route. Mechanochemistry, which can be performed under inert conditions and at room temperature, offers a promising alternative synthetic route that may minimise the decomposition of AgF_2 and enable the synthesis of pure materials. Although this approach has yet to be applied to fluoridoargentates(II), its proven efficacy in other fluoride-based systems [5, 6, 7] suggests it could overcome the limitations associated with the high-temperature solid-state method.

This work aims to demonstrate that mechanochemistry, sometimes combined with soft annealing, provides an elegant route to synthesize fluoridoargentates(II), ultimately contributing to the expansion of the known spectrum of Ag^{2+}-based compounds.

1.2 Magnetism

The exploration of magnetism spans an impressive history that extends back approximately 3000 years. The fascination with this phenomenon can be traced to the Ancient Greek, who astutely observed that lodestones, magnetized fragments of the mineral magnetite (Fe_3O_4), possessed the remarkable ability to attract iron. By the 11th century, the Chinese had harnessed the power of these lodestones, employing them as compasses for navigation and transforming the way humanity traversed the world's seas. However, it was not until 1819 that a pivotal breakthrough unfolded, marking the inception of a profound understanding of the intricate relationship between electricity and magnetism. Hans Christian Ørsted, a professor at the University of Copenhagen, serendipitously revealed this connection when he observed the movement of a compass needle in proximity to an electric current-carrying wire. Ørsted's ground-breaking work laid the foundation for the subsequent advancements in magnetism, unlocking doors to countless technological innovations and discoveries that continue to shape our modern world.

The macroscopic magnetic properties of a material arise from the magnetic moments associated with electrons. The magnitude of these magnetic moments is equivalent to the Bohr magneton (μ_B), which is defined as [8]:

$$\mu_B = \frac{e\hbar}{2m_e} \tag{1.1}$$

where e is the elementary charge and m_e is the electron rest mass. The value of μ_B equals $9.274 \cdot 10^{-24}$ J·T^{-1}. Two different types of angular momentum are characteristic for an electron. The first one is the orbital angular momentum L and is associated with orbital motion of an electron around the nucleus. It is proportional to:

$$L = \hbar\sqrt{l(l+1)} \tag{1.2}$$

where l is the azimuthal quantum number. Electron also exhibits spin angular momentum S, which is defined as:

$$S = \hbar\sqrt{s(s+1)} \tag{1.3}$$

where s represents spin quantum number, which for an electron takes the value of $s = 1/2$. Given that the electron is a charged particle, its rotation produces a magnetic dipole moment, which is further divided into orbital and spin magnetic dipole moment. An orbital magnetic dipole moment, μ_L, is defined as:

$$\mu_L = -g_L\mu_B\frac{L}{\hbar} \tag{1.4}$$

where g_L is the electron orbital g-factor. On the other hand, spin magnetic dipole moment, μ_S, is defined as:

$$\mu_S = -g_S\mu_B\frac{S}{\hbar} \tag{1.5}$$

where g_S is the electron spin g-factor. The way magnetic atoms are connected in the crystal structure plays a key role in determining the type of magnetism, as this connectivity affects how their dipole moments interact. However, when all electrons in a particle (atom, molecule, or material) are paired, the material exhibits *diamagnetic* properties, which means that the magnetic moments align antiparallel to the applied magnetic field.

Diamagnetism is a quantum mechanical phenomenon observed in all materials. However, it is an extremely weak form of magnetism and is usually negligible if other forms of magnetism are present, except in the case of superconductors, which act like a perfect diamagnets, since they expel the magnetic field completely.

On the other hand, in some materials, atoms have unpaired electrons that create permanent magnetic moments. Without an external magnetic field, these moments point in random directions. When a magnetic field is applied, the moments align with the field, causing the material to become magnetised. This phenomenon is called *paramagnetism*. This temperature-dependent form of magnetism, which is among the simplest, is observed for example in gaseous oxygen and follows an inverse relationship with temperature known as Curie's law. However, some materials exhibit deviations from Curie's law due to strong spin correlations between magnetic moments. To account for these interactions, the Curie-Weiss law was introduced:

$$\chi_m = \frac{C}{T - \theta_{CW}} \tag{1.6}$$

where χ_m is magnetic susceptibility, C is a material specific Curie constant, T is temperature and θ_{CW} is the Curie-Weiss temperature.

In the case of paramagnetism, there is no interaction between the neighbouring spins. However, spins can also "feel" each other through magnetic dipolar interaction or magnetic superexchange and consequently long-range magnetic ordering takes place. The magnetic dipolar interaction between two magnetic dipoles μ_1 and μ_2, which are separated by a distance r, have an energy equal to:

$$E = \frac{\mu_0}{4\pi r^3}[\mu_1 \cdot \mu_2 - \frac{3}{r^2}(\mu_1 \cdot r)(\mu_2 \cdot r)] \tag{1.7}$$

where μ_0 is permeability of vacuum. The strength of magnetic dipolar interaction for two magnetic moments each of $\mu \approx \mu_B$ separated by a distance $r \approx 1$ Å can be estimated to be 10^{-23} J, which is approximately 1 K. Given the fact that much higher ordering temperatures are observed in different materials, the magnetic dipolar interaction is too weak to account for the magnetic ordering in the vast majority of magnetic materials.

On the other hand, the superexchange interaction is considerably stronger and plays a crucial role in the long-range ordering observed in magnetic materials. It was first proposed by Kramers [9] and later refined by Anderson [10]. This interaction is defined as an indirect exchange interaction between non-neighbouring magnetic ions, covalently bonded with a non-magnetic ion positioned between the magnetic ions. Strong magnetic superexchange is considered crucial for the superconducting cuprates [11], where extremely high critical temperatures at ambient conditions can be achieved due to strong magnetic coupling [12]. Similar to the cuprates, iron pnictides are also strongly coupled and have also been shown to exhibit high-temperature superconductivity upon charge doping [13].

In Figure 1, two different outcomes for superexchange are considered.

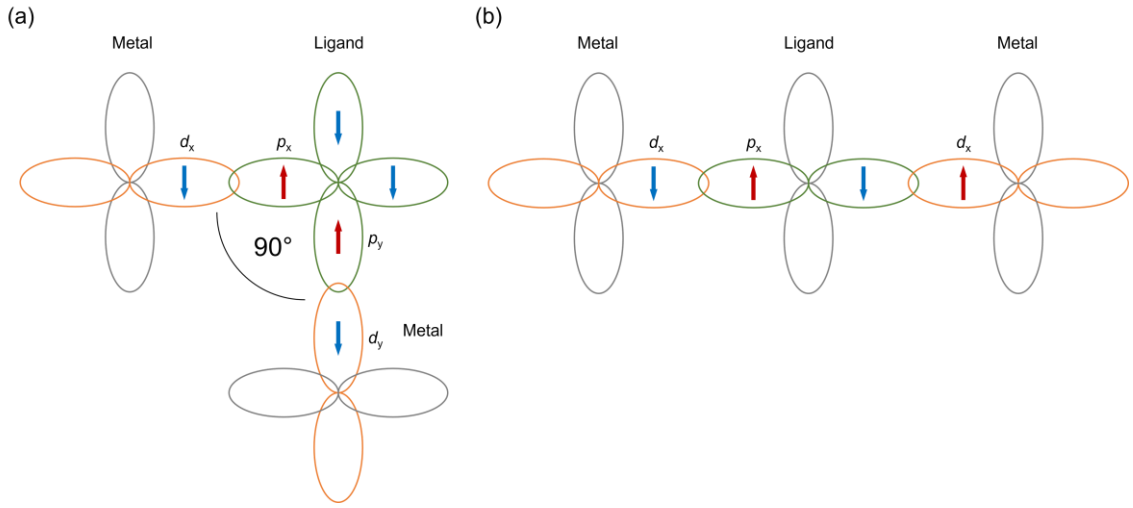


Figure 1: (a) Ferromagnetic and (b) antiferromagnetic superexchange interaction between two magnetic metal cations bridged by a non-magnetic ligand anion.

If the angle between two bridged magnetic cations is closer to 90°, ferromagnetic interaction takes place (Figure 1a). Here spins orient in a parallel orientation which results in a macroscopic magnetisation of the ferromagnetic material. Ferromagnetic material exhibits spontaneous magnetisation below the ordering temperature, also known as the Curie temperature (T_C). Above the T_C, thermal energy disrupts the ordered alignment and the material becomes paramagnetic. In the second case, the angle between two bridged magnetic cations can be closer to 180° (Figure 1b). Here antiferromagnetic superexchange interaction takes place since the electron spins align antiparallel. Similar to ferromagnetic materials, antiferromagnets exhibit an ordering temperature, also known as the Néel temperature (T_N), below which the material orders antiferromagnetically. However, in contrast to ferromagnets, antiferromagnetic materials do not exhibit spontaneous magnetisation.

Assuming the simplest approach, the magnetic coupling of two neighbouring spins can be described using Heisenberg Hamiltonian:

$$H_{ab} = -J_{ab} S_a S_b \tag{1.8}$$

where J_{ab} is the exchange constant or the magnetic coupling constant while S_a and S_b represent spins a and b, respectively. The exchange constant is measured in energy units (usually in electron-volts, eV). It does not only quantify the magnitude of the magnetic interaction, but also the type of interaction through the sign. If the material is ferromagnetic, the exchange constant is positive, while for antiferromagnets it is negative.

Non-collinear spin arrangements emerge whenever simple collinear ordering cannot simultaneously satisfy the symmetry or energetic requirements of the magnetic lattice. A classic example is the Dzyaloshinskii–Moriya interaction in non-centrosymmetric crystals, which introduces an antisymmetric exchange term that tilts adjacent spins away from exact parallel or antiparallel alignment, which results in canted antiferromagnetism or spiral modulations. An antiferromagnet that exhibits spin canting would give weakly ferromagnetic response. An example of such compound is $Ag(WOF_5)_2$ [14]. Likewise, geometric frustration on triangular, Kagome or pyrochlore networks forces spins into 120° or umbrella-type configurations because not all antiferromagnetic bonds can be satisfied simultaneously. Even in non-frustrated lattices, competition between ferromagnetic nearest-neighbour and antiferromagnetic next-neighbour couplings can stabilise long-period

helical order. Strong single-ion anisotropy at low-symmetry sites may further misalign the local easy-axis directions, while magneto-elastic coupling can subtly distort ligand environments and induce local canting to lower the total energy. In certain multiferroics, such as rare-earth manganates [15], the very adoption of a non-collinear spiral breaks inversion symmetry and generates ferroelectric polarization via the inverse Dzyaloshinskii–Moriya mechanism. In all these instances, the simple Heisenberg Hamiltonian must be augmented with symmetry-allowed anisotropic and higher-order terms, originating from spin–orbit coupling, lattice geometry or spin–lattice feedback, to capture the rich diversity of non-collinear ground states observed in low-dimensional and frustrated magnets.

Low-dimensional magnetism describes systems in which magnetic exchange is strongly anisotropic and effectively confined to one or two crystallographic directions. In practice, this anisotropy is imposed by specific bridging ligands, most often via superexchange pathways that link magnetic centres into chains, layers or other reduced-dimensional motifs. When the inter-chain or inter-layer coupling remains sufficiently weak, true long-range 3D order is suppressed, giving rise to characteristic phenomena such as spin-chain antiferromagnetism or spin-ladder behaviour. However, if the residual interactions between these low-dimensional units are non-negligible, long-range magnetic order at finite temperatures can occur. The simplest realisation of this concept is the magnetic dimer, in which two $S = 1/2$ centres are coupled by a single ligand bridge to form an antiferromagnetic singlet ground state separated by an energy gap from the ferromagnetic triplet excited state.

The simplest magnetic lattice in one dimension is a linear chain of $S = 1/2$ moments. Both the antiferromagnetic Heisenberg chain and the ferromagnetic Ising chain lack long-range order at any finite temperature, as first demonstrated for the Heisenberg model via the Bethe ansatz solution and later generalised by the Mermin–Wagner theorem to continuous symmetries in one and two dimensions. Bonner and Fisher's numerical study of the $S = 1/2$ Heisenberg chain confirmed that the uniform susceptibility remains finite and exhibits only a broad maximum around $T \sim 0.64$ J/k$_B$, without divergent behaviour down to the lowest temperatures [16, 17]. Likewise, the 1D Ising model shows no spontaneous magnetisation at $T > 0$, and its zero-field susceptibility is analytic for all $T > 0$ [18]. In real materials, however, residual interchain couplings, no matter how weak, eventually drive a crossover to 3D behaviour and induce true long-range order below a T_N or T_C determined by the strength of those couplings. Consequently, $S = 1/2$ chain compounds display a high-temperature regime governed by 1D physics, followed by a low-temperature ordered phase once interchain exchange (or anisotropy) becomes significant. Similar to the magnetic dimer systems, the interchain exchange coupling constant J' must be much weaker than the intrachain exchange coupling constant J_{1D} (Figure 2a).

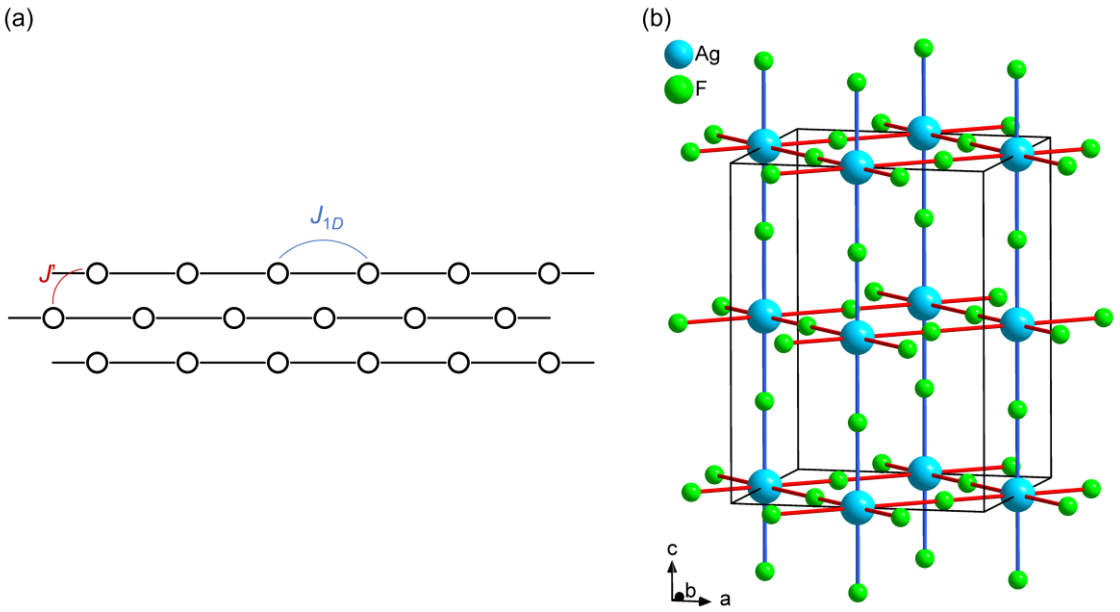


Figure 2: (a) Schematic representation of exchange interactions in magnetic spin chains where black circles symbolise magnetic centres in the crystal lattice and (b) infinite $[AgF]^+$ chains propagating along c-crystallographic direction in $CsAgF_3$ (Cs atoms are omitted for clarity). Blue bonds correspond to the direction of intrachain coupling (J_{1D}) and red bonds to the direction of interchain coupling (J').

The J'/J_{1D} ratio is a good indication of how close a particular material is to being a fully isolated spin chain compound, or in other words a measure of magnetic anisotropy. Macroscopically, the anisotropy affects the value of the T_N according to the equation:

$$\frac{J'}{J_{1D}} = \frac{k_B T_N}{3c \cdot J_{1D} \sqrt{ln\frac{\lambda J_{1D}}{k_B T_N} + \frac{1}{2} ln\frac{\lambda J_{1D}}{k_B T_N}}} \tag{1.9}$$

where λ and c are numerically derived constants [19]. This equation is an elegant way to correlate the experimentally observed properties to the magnetic anisotropy directly. Moreover, it is relatively easy to calculate the value of J' and predict T_N. A good example of extremely strong antiferromagnetic superexchange in one direction is $CsAgF_3$ [20], where large negative superexchange constant ($J_{1D} = -160.9$ meV) along c axis was calculated with DFT (Figure 2b). Here $S = 1/2$ Ag^{2+} cations are bridged with fluorine anions and the Ag–F–Ag angle equals 180 °, resulting in strong antiferromagnetic superexchange coupling.

Addition of another dimension brings us to the spin layers. In these materials, the layers are strongly coupled in one specific plane (J_{2D}), while the magnetic coupling between the layers (J') is much weaker (Figure 3a). In layered materials, both ferromagnetic and antiferromagnetic ordering is possible. Most research is being focused on compounds that exhibit $S = 1/2$ layers.

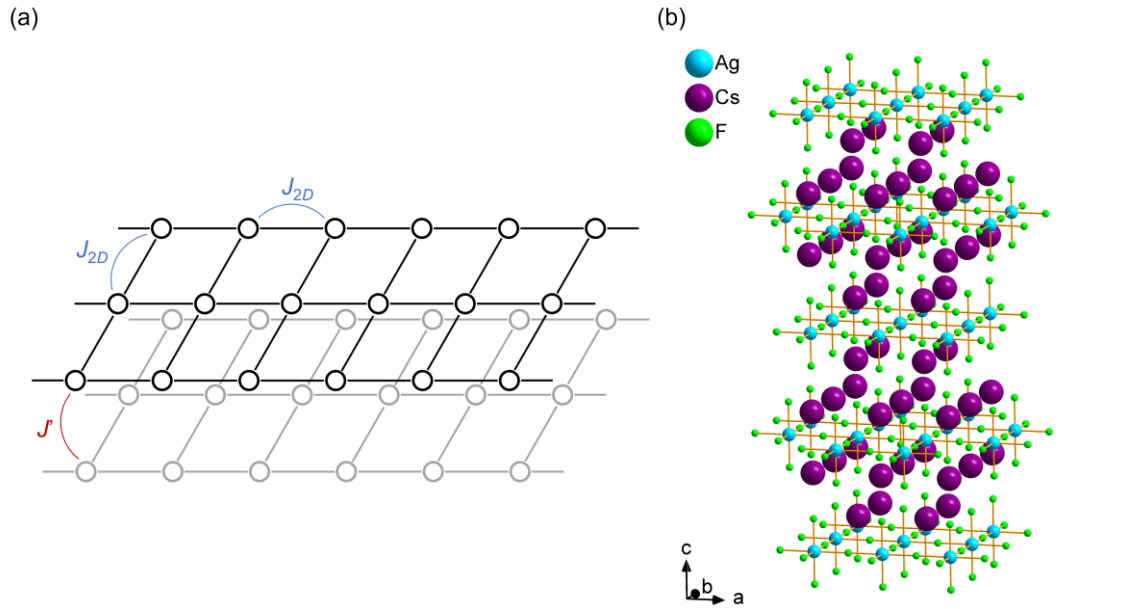


Figure 3: (a) Schematic representation of exchange interactions in spin layers where black circles symbolise magnetic centres in the crystal lattice and (b) infinite $[AgF_2]$ layers in Cs_2AgF_4, which propagate along the *ab* plane.

Just like in the magnetic spin chains, magnetic anisotropy in two dimensions can be measured through the relation:

$$\frac{J'}{J_{2D}} = e^{(b-\frac{4\pi\rho_s}{k_B T_N})} \tag{1.10}$$

where b and ρ_S are numerically derived constants [19]. Strong anisotropy is observed in superconducting cuprates, where the square $[CuO_2]$ layers are coupled antiferromagnetically [11]. While Cs_2AgF_4 with analogous $[AgF_2]$ layers (Figure 3b) exhibits many similarities to the superconducting cuprates, it was observed that it orders ferromagnetically with T_C of 14.9 K [21, 22].

1.3 Fluoridoargentates(II)

Silver, located one period below copper in the periodic table, has attracted interest as a potential candidate for developing a new family of unconventional superconductors [1]. However, in contrast to the well-known cuprates, divalent silver rarely forms stable oxides [23]. There are only a few exceptions, such as silver(II) sulphate [24], as Ag^{2+} typically undergoes disproportionation into Ag^{+} and Ag^{3+} species. A common example is AgO; however, its actual composition is $Ag^{I}Ag^{III}O_2$ [25]. Despite this instability as oxides, the highly oxidizing Ag^{2+} cation readily forms covalent bonds with fluorine, giving rise to a diverse family of compounds known as fluoridoargentates(II).

Although silver belongs to the same group as copper and gold, these elements exhibit significant differences in their chemical and physical properties. For example, silver metal exhibits silverish lust, which is typical for transition metals. In contrast, copper is red-brown and gold is a yellow metal. These elements also exhibit different chemical properties, such as oxidation states. The most common oxidation state for copper is +2, while for silver is +1 and for gold +3. In order to access the second oxidation state of silver, one

needs to open the closed *d*-shell of the Ag^{+} cation. This results in the formation of extremely reactive Ag^{2+} cations, which tries to fill its $4d$ orbital. As a consequence, compounds containing divalent silver are one of the strongest oxidisers. This is supported by the unusually large second ionisation potential of silver (21.45 eV [23]), which is larger compared to xenon and almost as large as for bromine (21.80 eV). In another words, there are only few ligands that can stabilise silver in +2 oxidation state, with fluorine, the most electronegative element, is the most common ligand. In contrast, silver(II) is incompatible with the most inorganic ligands, such as chlorides, bromides, iodides, sulphides, and the vast majority of organic ligands, such as carbonates, cyanides, alcoholates, carboxylates, imides, amides and phosphates [26, 27]. Moreover, the strong oxidising nature of the Ag^{2+} cation manifests in large positive standard redox potential for the redox pair Ag^{2+}/Ag^{+}, which is +1.98 V versus normal hydrogen electrode [28].

The Ag^{2+} cation has a d^9 electron configuration. Consequently, compounds that contain Ag^{2+} cation in octahedral ligand environment are susceptible to the Jahn-Teller distortion, which can lead to an elongation or compression of the $[AgF_6]^{4-}$ octahedra [3]. The difference between the equatorial and apical Ag–F bond lengths of the octahedra are larger than 5 % for the compressed octahedron and reach even 10 % for an elongated octahedron [3]. This indicates on large flexibility and plasticity of the first coordination sphere of the Ag^{2+} cations. These distortions have a large influence on the magnetism in fluoridoargentates(II).

Silver difluoride, AgF_2, is the most basic compound of Ag^{2+} and fluorine. AgF_2 was first prepared by Moissan in 1891 during the testing of reactivity of fluorine [29]. AgF_2 can be synthesized by fluorination of Ag^{+} compounds at temperatures around 200–250 °C. Alternatively, it can also be obtained at room temperature with minor impurities by reacting elemental fluorine with $AgNO_3$ in aHF [3]. As-obtained AgF_2 powder is brown in colour and spontaneously releases fluorine at temperatures above 360°C [3], forming fluorine-deficient, nonstoichiometric AgF_{2-x}, which appears as dark yellow grains [26]. The crystal structure of AgF_2 is shown in Figure 4. The compound crystallises in the orthorhombic crystal system with the *Pbca* space group [30]. Here Ag^{2+} is coordinated with six F^{-} anions, forming an elongated $[AgF_6]^{4-}$ octahedra with four shorter (2.068 Å) and two longer (2.584 Å) Ag–F contacts. These corner-sharing octahedra are forming slightly puckered $AgF_{4/2}$ sheets, which directly affect the magnetic properties of this compound.

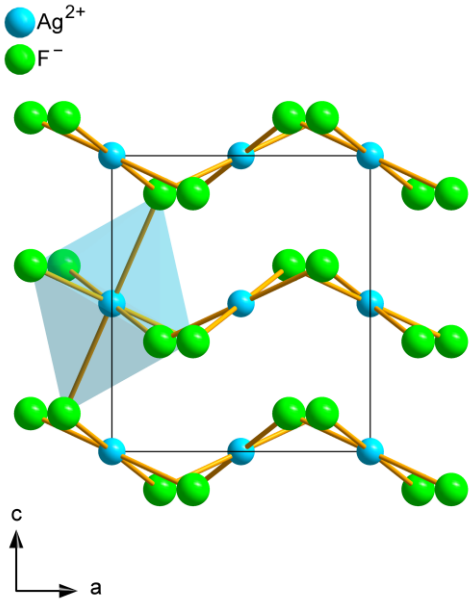


Figure 4: Extended unit cell of silver difluoride viewed along *b*-crystallographic direction.

Fluoridoargentates(II) can be divided into three main groups based on the connectivity between the magnetic Ag^{2+} cations. The first group includes structures in which the Ag^{2+} cations are magnetically isolated. In these compounds, the Ag^{2+} cations are not connected via nonmagnetic fluoride anions, which prevents magnetic superexchange interactions from occurring. As a result, each Ag^{2+} cation behaves as an isolated magnetic centre, and such compounds are paramagnets. One example is $Ag[SbF_6]_2$ [31] - its crystal structure is shown in Figure 5.

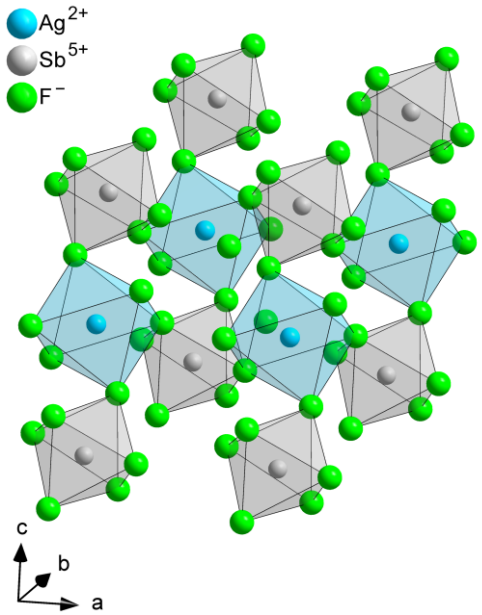


Figure 5: Crystal structure of $Ag(SbF_6)_2$ with magnetically isolated $[AgF_6]^{4-}$ octahedra shown in blue.

The second group are structures containing infinite $[AgF]^+$ chains and thus have a pronounced 1D character. Here, Ag^{2+} cations are bridged with fluorine anions, which enables magnetic superexchange and long-range magnetic order. However, the magnetic ordering is highly dependent of the Ag–F–Ag angle. A 90° angle favors ferromagnetic coupling. On the other hand, if the angle value is closer to 180°, antiferromagnetic coupling prevails. An example of compound with infinite $[AgF]^+$ chains is $[AgF][BF_4]$ [32] with its crystal structure shown in Figure 6. This compound exhibits one of the strongest calculated (DFT) antiferromagnetic superexchange interactions in one dimension ($J \approx -300$ meV [20]) along the $[AgF]^+$ chains, which is even stronger compared to the Sr_2CuO_3 ($J \approx -240$ meV [33]), a 1D cuprate which becomes superconducting upon doping [34].

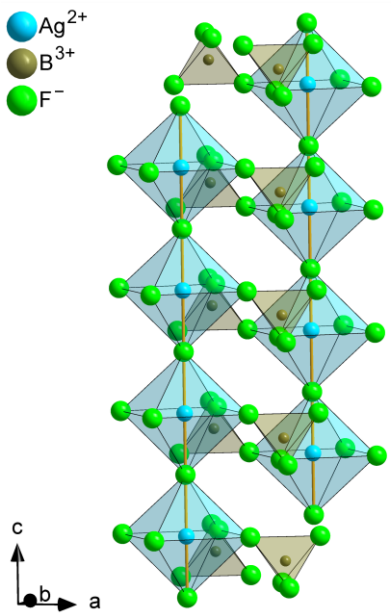


Figure 6: Packing in [AgF][BF_4] where compressed $[AgF_6]^{4-}$ octahedra are stacked along *c* crystallographic direction, forming $[AgF]^+$ infinite chains.

The third group are compounds with $[AgF_2]$ sheets. These compounds have a layered crystal structure therefore they exhibit 2D magnetic properties. In contrast to fluoridoargentates(II) with $[AgF]^+$ chains, where superexchange interaction can only occur in one dimension, here the magnetic behaviour is much more complex. An example of a layered compound with $[AgF_2]$ sheets is α-K_2AgF_4 [35] and its crystal structure is shown in Figure 7. This layered perovskite exhibits ferrodistortive ordering of compressed $[AgF_6]^{4-}$ octahedra. Since the $[AgF_2]$ sheets are not flat but rather slightly puckered, this compound is characterised as a ferromagnet with Currie temperature of 13.4 K [36].

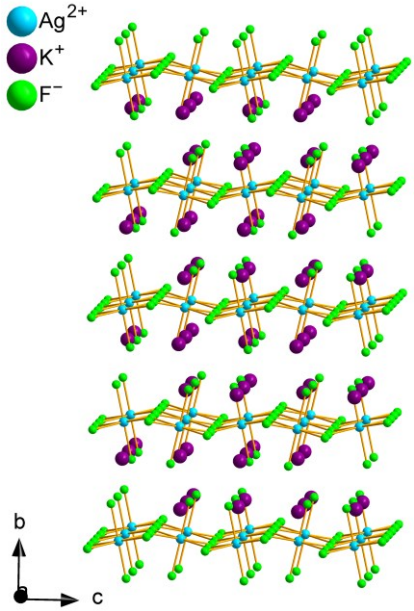


Figure 7: Layered crystal structure of α-K_2AgF_4 where compressed $[AgF_6]^{4-}$ octahedra are forming puckered $[AgF_2]$ sheets in the *ac* plane.

The $4d^9$ electronic configuration of Ag^{2+} mirrors the $3d^9$ configuration of Cu^{2+}, the $S = 1/2$ magnetic centre of cuprate superconductors. This orbital analogy has driven the search for fluoridoargentate(II) compounds that might emulate the electronic and magnetic behaviour of La_2CuO_4, the canonical Mott insulator whose doping results in high-temperature superconductivity. By targeting silver analogues of this layered oxide, researchers aim to translate the well-established superexchange-mediated magnetism and charge-transfer physics of cuprates into a fluoride framework—potentially opening a new frontier in unconventional superconductivity. It is believed that the parent compound of fluoridoargentates(II) should exhibit three key structural features, which would lead to antiferromagnetic ordering at appreciable temperature (100–300 K), similarly to La_2CuO_4: Flat $[AgF_2]$ sheets, elongated $[AgF_6]^{4-}$ octahedra and 4-fold axes of $[AgF_6]^{4-}$ octahedra should be aligned parallel [37]. Theoretical studies already confirmed these assumptions since critical temperatures up to −195 K were predicted in a hypothetical epitaxially engineered silver fluoride cuprate analogue with flat $[AgF_2]$ sheets [38].

Due to the extreme moisture sensitivity of the main precursor, AgF_2, and fluoridoargentates(II) in general, the synthesis techniques for the preparation of this compounds are severely limited. Currently, two synthesis methods are most commonly used for the synthesis of fluoridoargentates(II). The first one is conventional high-temperature solid-state synthesis conducted in inert or fluorine atmosphere [3]. Here, the most common precursors for the synthesis are AgF_2 in combination with other metal fluorides. Some Ag^+ compounds could also be used as a precursor, but in that case fluorine atmosphere is needed in combination with dynamic vacuum [39]. The main problem that occurs during the synthesis with the solid-state method is partial decomposition of AgF_2 into AgF at relatively low temperatures (above 350°C) [3], which alters the starting ratio of reagents and consequently different secondary phases form [4]. This makes the structural and magnetic characterisation of the targeted phase extremely challenging. In order to partially avoid this issue, excess of AgF_2 is usually added (10–20 mol%). The second method is synthesis in solution. Due to the moisture sensitivity of fluoridoargentates(II), the solvent of choice is aHF. However, the limiting factor here is the poor solubility of AgF_2 in aHF (approximately 0.05 g of AgF_2 per 100 g of aHF [40]).

The challenges encountered with conventional synthetic approaches—particularly the thermal decomposition of the precursor and the poor solubility of AgF_2 in aHF—underscore the importance of developing alternative methods for preparing fluoridoargentates(II). A room—or low-temperature route conducted under inert conditions could thus represent a superior strategy for accessing this intriguing family of compounds.

1.4 Mechanochemistry

The mechanochemical reaction is defined by IUPAC as a “chemical reaction that is induced by mechanical energy” [41]. The origins of mechanochemistry can be traced back to ancient times—specifically around 315 B.C.—when cinnabar (HgS) was ground in a copper mortar using a copper pestle with added vinegar, leading to the formation of mercury, as evidenced by the appearance of a liquid metal [42]. Between antiquity and the 18th century, several mechanochemical processes were documented, primarily in the context of metallurgy and mining [43, 44]. The field experienced a major surge in the second half of the 20th century, particularly with the development of oxide materials [45]. More recently, mechanochemistry has expanded into a broad range of disciplines, including polymers [46] and pharmaceuticals [47].

Mechanochemistry has emerged as a broadly applicable method for solvent-free synthesis [48]. This approach not only offers a cleaner, faster, and simpler alternative to

conventional methods but also enables the targeted synthesis of compounds that were previously challenging to achieve [49, 50]. While the mechanochemical reactions can be carried out even with pestle and mortar, they are usually conducted in high-energy mills. The most commonly used are planetary and shaker or vibrational mills. In a planetary mill, the milling jar containing milling material and milling balls rotates around a central axis of the planetary mill while it additionally spins around its own axis. Extremely strong centrifugal forces are created by such planetary motion. On the other hand, a shaker mill creates vibrations of the milling jar of certain frequency, with influence on the energetics of the milling. While shaker mills are typically used for smaller sample quantities, larger batches can be prepared using planetary mills [51].

A term frequently used in mechanochemistry is *mechanochemical activation*. The main difference between the mechanochemical reaction and mechanochemical activation is that during the mechanochemical activation the milled powder remains chemically unchanged, which means that the chemical composition and crystal structure remain the same during the course of high-energy milling [51].

During the milling process, the balls repeatedly strike not only the powder and the jar walls, but also each other when multiple balls are present, which reduces the individual impact energy and causes a significant overall temperature increase of the powder and jar over time. Two temperature effects can be considered: the local temperature pulses and the overall temperature increase in the milling jar [52]. The local temperature pulses could surpass the temperatures of 1000 °C [51], however they occur in the order of nanoseconds to microseconds and contribute to the overall temperature in the milling jar. Temperatures of 200 °C are usually achieved inside of the milling jars during the milling in planetary mills and slightly lower temperatures are reached with shaker mills [53]. In some cases, these temperatures might promote decomposition of sensitive reagents. To avoid this, one can use the cryomill, where the milling jars are continuously cooled with liquid nitrogen during the milling or to simply immerse the milling jars into liquid nitrogen between the milling cycles [54]. To the contrary, when the energy input is not sufficient to drive the desired reaction, the milling jars can be heated during the milling process [55, 56].

Generally, three distinct stages of the milling process can be identified [57, 58], as illustrated in Figure 8. The first is the *Rittinger stage*, during which particle size is reduced while interparticle interactions are negligible. This is followed by the *aggregation stage*, where the increase in surface area no longer scales proportionally with the energy input due to the onset of particle–particle interactions. As a result, small aggregates form, held together by weak van der Waals forces. In the final *agglomeration stage*, chemical reactions occur, leading to the formation of strong chemical bonds between particles.

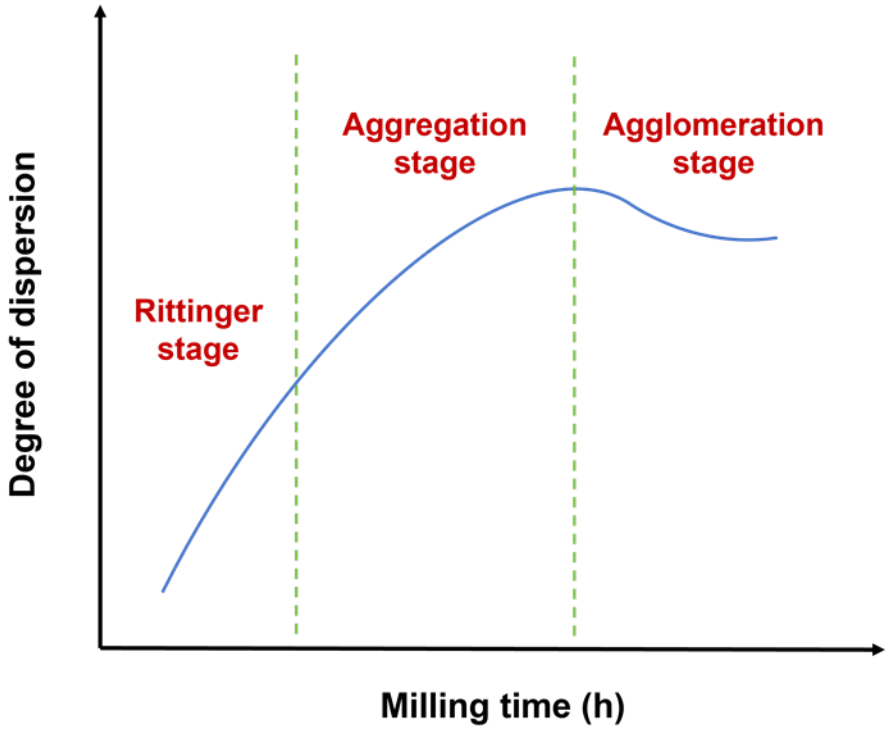


Figure 8: Stages during the high-energy milling. Adapted from [51].

Mechanochemistry can also provide an alternative synthetic pathway for accessing metastable phases that are often inaccessible via conventional thermal methods. Unlike traditional solid-state reactions, which typically proceed under conditions that favour the formation of the thermodynamically most stable phase, mechanochemical synthesis operates under far-from-equilibrium conditions, where the mechanical energy input modifies the reaction pathway pathway and enables the formation of kinetically stabilised products. As illustrated in the energy diagram in Figure 9, mechanochemical activation provides an energy pathway that circumvents high-energy barriers associated with conventional synthesis, enabling the direct formation of metastable phases. These phases reside in local energy minima that are higher in energy compared to the most thermodynamically stable product but can exhibit unique structural, electronic, or magnetic properties. The mechanical energy imparted during ball-milling disrupts existing chemical bonds, creates lattice defects, and enhances diffusion, promoting the stabilization of intermediate or metastable states that would otherwise convert into the product with the lowest Gibbs free energy. This approach overcomes the thermodynamic limitations inherent in conventional methods and facilitates the synthesis of non-equilibrium phases with potentially novel properties.

Although the mechanochemistry of fluorides is relatively underexplored, several studies have reported the successful synthesis of metastable phases via ball milling, highlighting its potential to stabilize non-equilibrium structures in these materials. Examples include $BaSnF_4$ for which conventional solid-state synthesis at elevated temperatures yields the thermodynamically stable tetragonal phase [59]. By contrast, ball milling produces a metastable cubic polymorph that remains stable at room temperature and subsequently transforms into the tetragonal phase upon annealing.

Similarly, the synthesis of BaF_2–CaF_2 solid solutions further exemplifies the advantages of mechanochemical methods [60]. In this case, the substantial difference in ionic radii between Ba^{2+} (1.42 Å) and Ca^{2+} (1.12 Å) typically precludes the formation of a solid

solution using conventional high-temperature techniques, as the resulting lattice strain favors phase separation. High-energy ball milling, however, promotes an effective atomic mixing and induces local lattice distortions, enabling the formation of a homogeneous $Ba_{1-x}Ca_xF_2$ solid solution.

Both examples demonstrate the significant potential of mechanochemistry for the deliberate design of materials with tailored properties. By harnessing the mechanical energy during milling, it is possible to stabilise metastable phases that might otherwise remain inaccessible, thereby expanding the compositional and structural landscape.

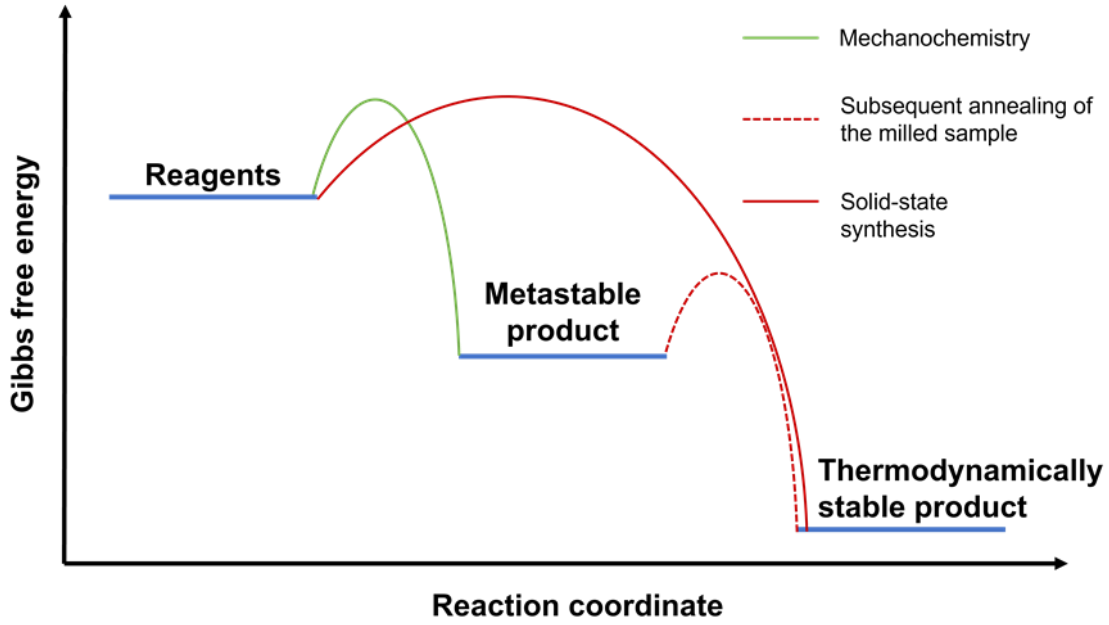


Figure 9: Energy landscape of a chemical reaction illustrating mechanochemical access to metastable phases. Blue lines denote energy levels of reactants, metastable product and the thermodynamically stable product. The red curve represents conventional solid-state synthesis, which proceeds directly to the stable product. In contrast, the green curve depicts the mechanochemical route, where mechanical energy surmounts kinetic barriers, stabilizing a metastable phase before relaxation to the stable state. The red dotted curve represents additional annealing of the metastable product. Adapted from [61].

1.5 Aims and Hypothesis

The main purpose of this dissertation is to investigate the potential of the Ag^{2+} cation ($S = 1/2$ species) in the field of solid-state chemistry. This will be attempted by implementing new synthetic approaches that have not been utilised for Ag^{2+} chemistry so far. An additional aim is to enrich the current spectrum of Ag^{2+} compounds by exploring new compositional spaces inspired by the analogies to superconducting cuprate systems and guided by theoretical calculations. Alongside novel systems, known phases will be subjected to detailed investigation to address gaps in their characterisation within the existing literature. The investigated systems include $MAgF_4$ series (M = Ba, Sr, Hg, Ca and Cd), alkali-metal fluoridoargentates(II) with the formula $MAgF_3$ and M_2AgF_4 (M = Na, K, Rb and Cs), binary mixed-valence Ag^+/Ag^{2+} fluoridoargentates $Ag^IAg^{II}F_3$ and $Ag^I_2Ag^{II}F_4$, and mixed-valence Ag^+/Ag^{2+} fluoridoargentates $Ag^IAg^{II}_2MF_8$ (M = Y and Bi). The new phases will be characterised structurally and magnetically using a combination of state-of-the-art

techniques available in our laboratory and at the large-scale facilities. This work pursues several aims:

- Test if the ball-milling can be applied to the field of fluoridoargentates(II): This will be achieved by performing ball-milling reaction of AgF_2 with other metal fluorides and the successfulness of the method will be evaluated.
- Benchmark the ball-milling method: Already known compounds will be prepared by ball-milling and solid-state synthesis. Successfulness of the ball-milling will be assessed by comparing the ball-milled laboratory PXRD and Raman spectroscopy data with the literature and the solid-state results.
- Optimisation of the milling parameters: Milling parameters, such as milling frequency, total milling time, milling cycle time, and ball-to-reagents-ratio (BRR), will be carefully tuned with an aim to achieve the best possible results in terms of efficiency, yield, quality of the final product, and polymorph control.
- Reinvestigation of structural and magnetic properties of selected fluoridoargentates(II): In the literature it is often reported that samples are contaminated with magnetic impurities, which hinders their magnetic characterisation. It will be aimed to prepare samples with higher purity, which would enable their magnetic characterisation.
- Explore new compositional spaces: This will be achieved by preparing currently unexplored chemical compositions by solid-state synthesis and by ball-milling, sometimes combined with soft annealing.
- Structural characterisation of the new compounds: This will be achieved with techniques available in our laboratory (SCXRD, PXRD, Raman spectroscopy). If data with higher resolution is required for powder samples to determine the crystal structure, high-resolution synchrotron PXRD data will be obtained at large-scale facilities.
- Magnetic characterisation of fluoridoargentates(II): Preliminary magnetic characterisation will be performed by magnetic susceptibility measurements. Phase pure samples with interesting magnetic properties will be additionally analysed by neutron powder diffraction.

Different hypotheses will also be tested:

- Ball-milling is likely to be a successful method for the preparation of fluoridoargentates(II). Ball-milling offers inert synthesis conditions at the room-temperature, which is desired for the synthesis of fluoridoargentates(II).
- The samples produced by ball milling should have less impurities compared to the samples prepared with the solid-state method. This result is expected because ball-milling is a room-temperature synthetic procedure, therefore AgF_2 thermal decomposition should be minimised.
- The ball-milled sample will exhibit structural differences and altered magnetic properties compared to the same sample produced by the solid-state method. This outcome is anticipated due to the formation of nanocrystalline powder, the introduction of strain during the ball-milling process and the presence of defects, all of which are likely to contribute to the observed structural differences and magnetic response.
- The ball-milling method might lead to the formation of metastable phases. This hypothesis is probable since many examples in the literature report on the formation of metastable phases by the ball milling method.
- New fluoridoargentates(II) phases will be prepared. This is to be expected, as many different compositional spaces will be explored using conventional synthesis approaches and mechanochemistry.

Chapter 2

Materials and Methods

2.1 Materials

For the synthesis of fluoridoargentates(II) the reagents listed in the Table 1 were used.

Table 1: List of reagents used for the synthesis of compounds in the thesis, with specified provider and purity.

Chemical formula	**Provider**	**Purity** [%]
AgF_2	Fluorochem*	99
AgF_2	Sigma Aldrich	98
AgF_2	Thermo Scientific	98
AgF	Fluorochem	99
BaF_2	Alfa Aesar	99.99
BiF_3	Fluorochem	99
CaF_2	Sigma Aldrich	99.99
CdF_2	Alfa Aesar	99.99
CsF	Fluorochem	99
HgF_2	Sigma Aldrich	97
KF	Fluorochem	99
LaF_3	Fluorochem	99
NaF	Alfa Aesar	99.99
RbF	Fluorochem	99
SrF_2	Fluorochem	99
YF_3	Fluorochem	99

*Some batches of this provider included an unknown impurity. The laboratory PXRD data and comparison between pure and contaminated AgF_2 is shown in the appendix.

2.2 Methods

Due to the extreme moisture sensitivity of fluoridoargentates(II) all chemicals were handled in the glovebox (MBRAUN, Germany) in argon atmosphere, with oxygen and water levels below 0.1 ppm. All the equipment used for the synthesis and characterisation of the

synthesized samples (milling jars, milling balls, solid-state reactor, quartz capillaries, etc.) was dried over night at 160 °C prior to use.

2.2.1 Synthesis

2.2.1.1 Mechanochemical synthesis

For a typical mechanochemical reaction, the starting materials were weighted and hand-homogenised inside a glove box. The homogenized powder was enclosed into the air-tight milling jar, equipped with Teflon O-ring (as shown in the Figure 10b), and transferred outside of the glovebox and milled in a shaker mill. Most of the experiments were conducted with tungsten carbide ball and milling jar. However, for the milling experiments, where the milling jars had to be immersed in the liquid nitrogen between the milling cycles to stabilise the targeted phase, stainless steel milling equipment was used as tungsten carbide would crack if used at such low temperatures. A typical milling equipment used for the milling reactions in this thesis is shown in the Figure 10. The milling parameters, which were carefully selected and tested, were: (i) the milling frequency, (ii) total milling time, (iii) milling cycle time, (iv) cooling time of the jars between the milling cycles, (v) mass of the sample, (vi) milling-ball diameter and (vii) ball-to-reagents-ratio (BRR).

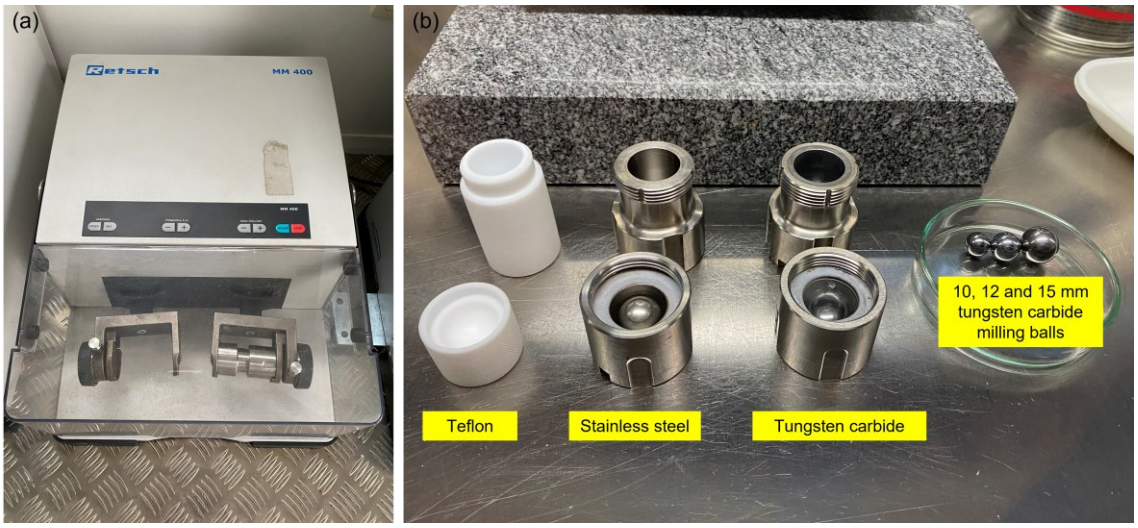


Figure 10: (a) Retsch shaker mill MM 400 and (b) 10 ml milling jars and milling balls with different diameters, used for the ball-milling reactions.

2.2.1.2 Solid-state synthesis

The solid-state synthesis setup consisted of a nickel reactor, a heating mantle, a temperature controller with temperature sensor, and a water chiller. The starting materials were weighted in the glovebox, hand-homogenised in an agate mortar and then placed in a platinum crucible, which was enclosed in a nickel reactor. Afterwards, the reactor was transferred out of the glovebox and mounted like similar to the setup shown in Figure 11.

The following synthesis parameters were considered: (i) heating rate, (ii) dwell time, (iii) dwell temperature, and (iv) cooling rate. In a typical synthesis, the heating rate and cooling rate of 100 °C per hour were used. In contrast, slower cooling rates (2–5 °C per hour) were used for the solid-state single-crystal growth attempts. The temperatures employed for the syntheses performed in this thesis ranged from 300 °C up to 500 °C. The same setup was also used for the annealing experiments.

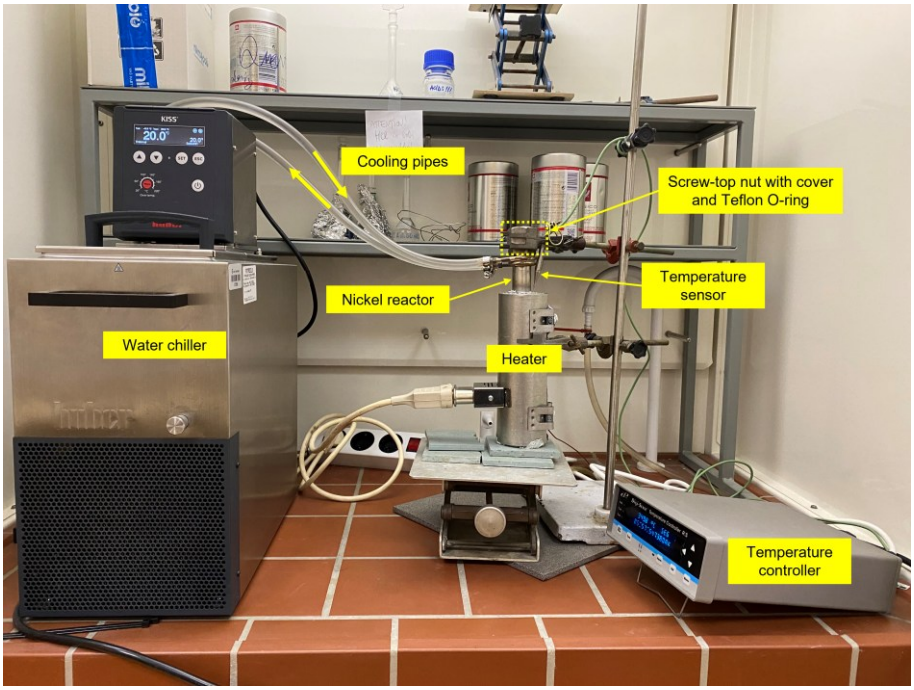


Figure 11: Setup for the solid-state reaction employed in the work presented in this thesis.

2.2.2 Characterisation

2.2.2.1 Powder X-ray diffraction (PXRD)

Powder X-ray diffraction patterns were measured with a Rigaku OD XtaLAB Synergy-S, Dualflex diffractometer equipped with Eiger2 R CdTe 1M hybrid pixel array detector using Ag Kα radiation (λ = 0.56087 Å) at 65 kV, 0.67 mA. The data were collected in transmission mode with a detector distance of 90 mm. The powder patterns were extracted by CrysAlisPro software [62]. The phase identification was performed using X-Pert High Score Plus [63] and PDF-4+ database while qualitative phase analyses were performed with Rietveld refinement in GSAS II [64] or Topas Academic [65].

2.2.2.2 Single-crystal X-ray diffraction (SCXRD)

For the single-crystal X-ray diffraction (SCXRD) the obtained crystals ($BaAgF_4$) were transferred into a quartz capillary under inert atmosphere in the glovebox, and flame sealed. The capillary was then broken under a cold nitrogen stream (−60 °C). The crystals were selected under a Motic SMZ-171 microscope and attached to a MiTeGen MicroLoop with Fomblin oil. Holder with the attached crystal were picked up with cryotongs, which were previously cooled to −196 °C, and quickly transferred into the cold nitrogen stream (−123 °C) of the diffractometer and mounted to the goniometer head [66]. The data were collected on XtaLAB synergy S, Dualflex diffractometer equipped with Eiger2 1M hybrid pixel array detector using Ag Kα radiation (65 kV, 0.67 mA) at −123 °C. The absorption correction was applied using spherical harmonics. The structures were solved using Olex2 and refined with ShelXL [67] and Olex2 [68]. The figures were prepared using DIAMOND software [69].

2.2.2.3 Raman spectroscopy

Raman spectra were measured at room-temperature in quartz capillaries on two different Raman instruments. The first one was a Bruker Senterra II confocal Raman. The spectra were measured in the range from 50 to 1410 cm^{-1} with a resolution of 1.5 cm^{-1}. Two excitation wavelengths (532 and 785 nm) were used, and their laser powers were adjusted using optical filters to prevent sample decomposition.

The second Raman instrument was a Horiba Jobin-Yvon LabRAM HR Raman spectrometer equipped with a holographic notch filter and a CCD detector using the He-Ne diode laser excitation (532.1 nm, 25000 mW). The capillaries filled with powder samples were placed on an Olympus BX 40 microscope equipped with a 50× objective.

2.2.2.4 Three-dimensional electron diffraction (3D ED)

A sample grid (Cu square grid G300 from SPI supplies) was loaded on a cryogenic TEM sample holder, and the holder was furthercooled with liquid N_2 in a nitrogen-filled glovebox. Once the holder was cooled below 160 °C, a small amount of a sample was dispensed onto the grid. The excess sample was removed by gentle tapping of the holder. The holder was then covered with a sleeve to prevent exposure to the atmosphere, removed from the glovebox, and then very quickly transferred into FEI Tecnai G2 20 transmission electron microscope for data collection. The microscope was operated at 200 kV with a LaB_6 cathode, equipped with a Medipix 3 hybrid pixel detector ASI Cheetah (512x512 pixels, 24bit dynamic range). Data sets were collected at 100 K temperature using a continuous rotation electron diffraction (cRED) method at ± 60° tilt angles with a step size of 0.30°.

Indexing, lattice parameter determination, and intensity integration were performed using PETS2 [70]. The processed data were then imported into Jana2020 [71] software, and the crystal structures were determined using Superflip [72].

2.2.2.5 Magnetic measurements

Between 10 and 30 mg of sample was filled into a quartz capillary (1 mm, Hilgenberg) and flame sealed. The magnetic susceptibility measurements were performed with a Quantum Design MPMS-XL-5 SQUID magnetometer in a temperature range from 2–300 K in a magnetic field of 1 kOe (or 10 kOe in some cases). The isothermal magnetisation was measured from −50 to +50 kOe at 2 K in all cases and additionally at higher temperatures if needed. The data were corrected for the experimentally determined contribution of quartz capillaries and the diamagnetic response of the compound due to closed atomic shells as obtained from Pascal's tables [73].

2.2.2.6 Synchrotron powder X-ray diffraction

Samples were sealed in 0.3 mm quartz capillaries and measured at the Canadian Light Source (CLS) at the Brockhouse High Energy Wiggler Beamline using λ = 0.3497 Å radiation and a Varex area detector.

2.2.2.7 Neutron powder diffraction (NPD)

From 300 to 1000 mg of sample was loaded into vanadium cans inside the glovebox and the sample was measured at the Institute Laue-Langevin (ILL) at the high intensity two-axis neutron powder diffractometer D20 with a λ = 2.41 Å wavelength and a large PSD covering 160° in 2θ.

Chapter 3

Results and Discussion

3.1 The MAgF$_4$ series (M = Ba, Sr, Hg, Ca and Cd): Synthesis, Structure, and Magnetism

Compounds with the formula ABF$_4$, where A^{2+} (CN = 8) is an alkaline earth metal cation and B^{2+} (CN = 6) is a transition metal cation, represent a remarkable class of materials known for their diverse and intriguing physical properties. These materials exhibit ferroelectric behaviour at room temperature for certain B^{2+} cations such as Co^{2+} [74], Ni^{2+} [75] and Zn^{2+} [76] and antiferromagnetic ordering with T_N in the range of 20–80 K for B^{2+} cations such as Mn^{2+} [77], Fe^{2+} [78], Co^{2+} [74] and Ni^{2+} [75]. In contrast, compounds with the Ag^{2+} cation on the B-site have been less studied, leaving gaps in our understanding of their properties.

Compounds in the MAgF$_4$ series, where M = Ba, Sr, Hg, Ca and Cd, were first synthesised by Odenthal and Hoppe in 1971 [39] by a high-temperature fluorination of a mixture of starting reagents ($BaCO_3$, $Sr(NO_3)_2$, $CaCO_3$, $HgCl_2$, $CdCO_3$ with Ag_2SO_4) at 500 °C, except for the case of HgAgF$_4$, where lower temperature of 300 °C was used due to the sublimation of HgF_2. The PXRD patterns were indexed with a tetragonal unit cell and it was proposed that the series is isostructural to K[BrF$_4$] [79]. Analogous to bromine in K[BrF$_4$], it was established that the Ag^{2+} cation is coordinated with four fluorine atoms and forms square planar $[AgF_4]^{2-}$ anions, which are also magnetically isolated. From this it was deduced that there is no long-range magnetic order, and consequently these compounds were considered to be temperature-independent paramagnets [39, 80].

Several objectives were pursued in this thesis through a re-examination of the MAgF$_4$ series:

(i) The primary aim was to introduce and benchmark mechanochemistry in the field of fluoridoargentates(II) by synthesising MAgF$_4$ compounds using high-energy ball milling. In parallel, the results were compared with those obtained via conventional solid-state synthesis.

(ii) Although the unit cells of these compounds had been previously indexed, their crystal structures had not yet been solved. Therefore, another key objective was to grow single crystals suitable for single-crystal X-ray diffraction (SCXRD) to enable accurate structure determination.

(iii) Furthermore, earlier magnetic susceptibility measurements showed deviations from Curie–Weiss behaviour between 3 and 10 K, indicating that the low-temperature magnetic properties of these materials remain insufficiently characterised. The limited data available in this temperature range highlight

the need for extended low-temperature measurements to enable a more comprehensive magnetic analysis [80].

To avoid the risks associated with handling fluorine at high temperatures, especially enhanced corrosion and increased reactivity, the MAgF$_4$ series was synthesised here in an argon atmosphere. This approach required to replace reagents used in the literature, such as carbonates and nitrates, with metal fluoride precursors. Despite this change, the same annealing temperature and dwell time were used in this synthesis procedure (Table 2).

Table 2: Solid-state synthesis conditions for the preparation of the MAgF$_4$ compounds.

Targeted phase	**Ratio of reagents (MF$_2$: AgF$_2$)**	***T* (°C)**	***t* (h)**
BaAgF$_4$	1:1.2	500	24
SrAgF$_4$	1:1.2	500	24
HgAgF$_4$	1:1.2	300[a]	24
CaAgF$_4$	1:1.2	500	24
CdAgF$_4$	1:1.2	500	24

[a] HgF$_2$ sublimes at temperatures above 300 °C

Since AgF$_2$ tends to spontaneously release fluorine at elevated temperatures (above 360 °C), leading to the formation of AgF, a 20 mol% excess of AgF$_2$ was added to maintain the 1:1 stoichiometric ratio of the reagents. Preliminary data also indicated that if the synthesis of BaAgF$_4$ was carried out from 1:1 ratio of reagents, a secondary phase, Ba$_2$AgF$_6$ forms. The addition of excess AgF$_2$ not only preserved the stoichiometry, which resulted in a successful synthesis of the targeted phase, but also prevented the formation of the secondary Ba$_2$AgF$_6$ phase. The MAgF$_4$ series was successfully synthesised using the solid-state method, as confirmed by the Rietveld refinement of the laboratory PXRD data shown in Figure 12. Since the crystal structures for these compounds have not yet been determined, the crystal structure of K[BrF$_4$] was used as the starting model for the Rietveld refinement analysis.

All samples were purple in colour, in good agreement with previous literature observations, with the exception of the HgAgF$_4$ sample (grey), most likely due to the high content of secondary phases.

The qualitative phase analysis of the laboratory PXRD data collected on the solid-state samples also revealed different phase compositions within the MAgF$_4$ series. Both BaAgF$_4$ and SrAgF$_4$ had AgF as the only impurity, which originated from the decomposition of AgF$_2$. While AgF was also expected to be the main impurity throughout the series, this was not the case as rapid reaction between AgF and unreacted AgF$_2$ resulted in the formation of mixed-valence silver fluorides, identified as Ag$_3$F$_4$ and Ag$_2$F$_3$, which are discussed in detail later in the thesis. However, it remains unclear what was the driving force for the formation of mixed-valence silver fluorides in three out of the five samples.

The structural parameters obtained from the Rietveld refinement analysis in this study are compared with those reported by Odenthal and Hoppe [39] in Table 3. The results show a good agreement between the two data sets. As shown in the table, both the a- and c-unit cell parameters decrease with decreasing size of the M^{2+} cation. As both the Ag^{2+} and M^{2+} cations occupy specific positions, only the positions of the fluorine atoms were refined in the analysis. (Table 3).

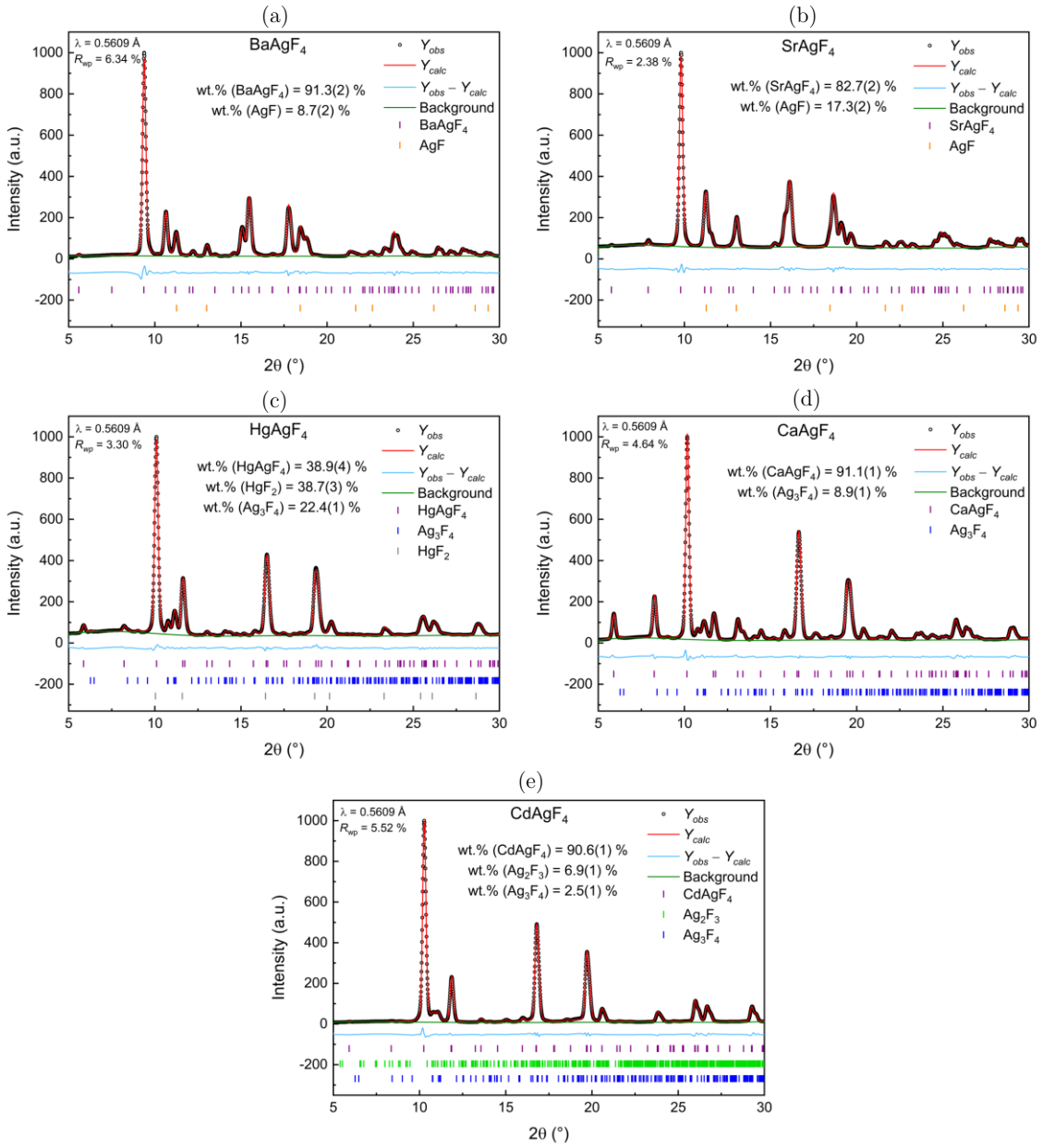


Figure 12: Rietveld refinements of the room-temperature laboratory PXRD data measured on MAgF$_4$ samples prepared with the solid-state method for (a) BaAgF$_4$, (b) SrAgF$_4$, (c) HgAgF$_4$, (d) CaAgF$_4$ and (e) CdAgF$_4$.

Table 3: Selected structural parameters obtained with the Rietveld refinement analysis of the laboratory PXRD data of $M\mathrm{AgF_4}$ samples synthesised with the solid-state method in this study compared to the lattice parameters reported by Odenthal and Hoppe [39].

Compound	**Lattice parameter *a* (Å)**	**Lattice parameter *c* (Å)**	**Coordinates for the fluorine atom (*x*, *y*, *z*)**	**Lattice parameters (Å) reported in ref.** [39]
$\mathrm{BaAgF_4}$	6.0433(2)	11.4787(5)	0.3232(6) 0.1768(6) 0.6244(8)	$a = 6.03$ $c = 11.46$
$\mathrm{SrAgF_4}$	5.7447(1)	11.1279(3)	0.3121(3) 0.1879(3) 0.6320(4)	$a = 5.73$ $c = 11.12$
$\mathrm{HgAgF_4}$	5.5248(4)	10.938(1)	0.30516(3) 0.1948(4) 0.6257(3)	$a = 5.52$ $c = 10.92$
$\mathrm{CaAgF_4}$	5.4993(2)	10.8759(5)	0.3061(2) 0.1939(2) 0.6332(1)	$a = 5.49$ $c = 10.86$
$\mathrm{CdAgF_4}$	5.4277(3)	10.830(1)	0.3036(4) 0.1964(4) 0.6327(4)	$a = 5.42$ $c = 10.80$

The literature reported unit cell parameters for the compounds in the $M\mathrm{AgF_4}$ series were obtained from the indexation of the PXRD data, but their crystal structures have not yet been solved at the onset of this work. This provided the motivation for the present study—to obtain detailed structural information for these compounds. Accurate crystal structure determination is essential for understanding material properties, and single crystals are particularly valuable for this purpose, as they allow structure solution using SCXRD. However, methods for growing single crystals of fluoridoargentates(II) are limited. Reported approaches include solution-based synthesis in aHF, such as metathesis or electrochemical methods, as well as high-temperature solid-state reactions but this can lead to the thermal decomposition of the compound. In this study, attempts to grow crystals from solution were unsuccessful, due to the low solubility of $\mathrm{AgF_2}$ in aHF. As a result, efforts were redirected toward thermal solid-state methods.

Despite numerous efforts to optimise the synthesis conditions by varying the temperature, dwell time and cooling rate, it was possible to obtain sufficiently large crystallites for SCXRD experiment for $\mathrm{BaAgF_4}$ only. The crystallite on which the data were collected was deep purple in colour and about 100 x 60 x 50 μm in size. This compound crystallises in the tetragonal crystal system in space group $I4/mcm$.

As can be seen in Figure 13, the coordination of the $\mathrm{Ag^{2+}}$ cation consists of four fluorine atoms that form square planar $[\mathrm{AgF_4}]^{2-}$ anions with four equivalent Ag−F distances of 2.0692(6) Å. In addition, the $\mathrm{Ag^{2+}}$ cation has four longer Ag−F contacts (3.1112(5) Å). Layers of magnetically isolated square planar $[\mathrm{AgF_4}]^{2-}$ anions in the ab crystal plane, orientated perpendicular to each other, are separated by layers of barium cations. Each barium cation is coordinated with eight fluorine atoms in the shape of a square antiprism

with eight equivalent Ba−F distances of 2.6539(4) Å. The crystal data and structure refinement parameters are listed in Table 4, while atomic parameters and thermal displacement parameters are listed in Table 5.

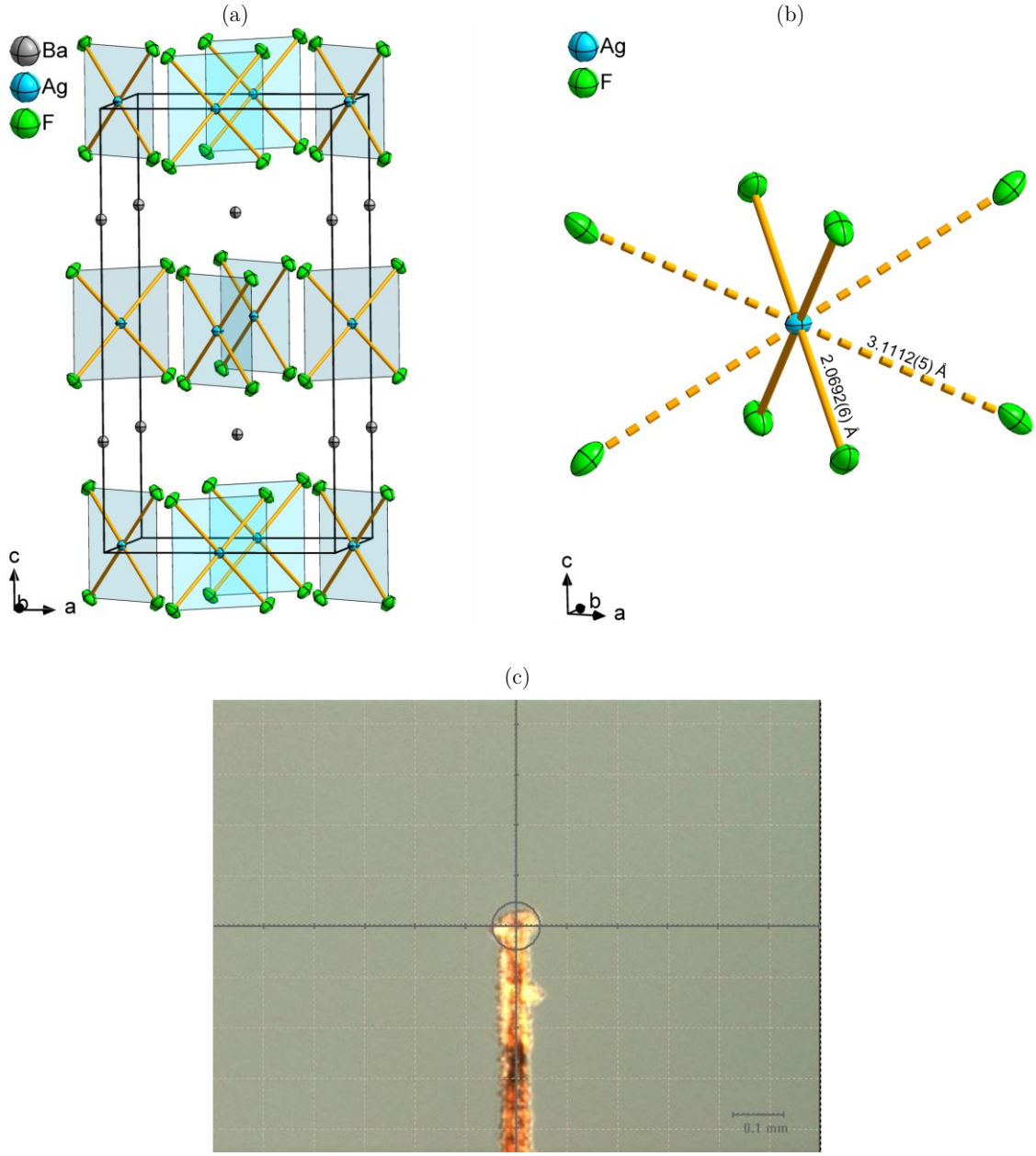


Figure 13: (a) Expanded unit cell of $BaAgF_4$ viewed along the *b*-axis, (b) coordination of the Ag^{2+} cation. Ellipsoids are drawn with 50 % probability. (c) Single crystal of $BaAgF_4$ mounted on the goniometer.

Table 4: Crystal data and structure refinement for $BaAgF_4$.

$BaAgF_4$	
Space group	$I4/mcm$
FW (g mol^{-1})	321.21
T (K)	150
a (Å)	6.0364(1)
c (Å)	11.4745(3)
V (Å^3)	418.109(18)
Z	4
ρ_{calc} (g cm^{-3})	5.103
λ (Å)	0.5609
μ (mm^{-1})	7.308
GOF indicator	1.094
R_1 [a]	0.0234
wR_2 ($I > 2.00\sigma(I)$) [b]	0.0617
Min., max. $\Delta\rho$ (eÅ^{-3})	−2.735, 1.406

[a] $R_1\ [F^2 > 2\sigma(F^2)] = \Sigma||F_o| - |F_c||/\Sigma|F_o|$; [b] wR_2 (all) $= [\Sigma(w(F_o^2 - F_c^2)^2)/\Sigma(w(F_o^2)^2)]^{½}$.

Table 5: Atomic positions and atomic displacement parameters for atoms in $BaAgF_4$.

Atom	***x***	***y***	***z***	U_{eq}
Ba	0.5	0.5	0.75	0.00810(6)
Ag	0.5	0	0.5	0.00887(6)
F	0.32407(8)	0.17593(8)	0.62405(6)	0.01616(15)

The preliminary laboratory PXRD data showed that the diffractograms of the mechanochemically synthesised vs the solid-state synthesised sample exhibited the highest degree of similarity for the $SrAgF_4$ case. Therefore, $SrAgF_4$ was selected for further optimisation of the milling parameters.

The starting reagents for the $SrAgF_4$ synthesis, AgF_2 and SrF_2, were first ball-milled separately to understand the effect of ball-milling on each of the precursors. In both cases, ball-milling resulted in a reduction in particle size and an increase in microstrain, as indicated by broadening of the diffraction peaks (Figure 14). In addition, a higher background, especially at low angles, indicates a partial amorphization of the starting material. The laboratory PXRD data for ball-milled SrF_2 revealed weak diffraction peaks associated with tungsten carbide, likely originating from wear of the milling equipment. This contamination could be effectively mitigated by using new milling jars and balls. In the case of AgF_2, overlapping diffraction peaks precluded a definitive determination of tungsten carbide contamination.

During the milling, local temperature pulses can reach extremely high temperatures [53], which could lead to the decomposition of AgF_2. Although its extreme reactivity initially raised concerns, the compound proved to be relatively stable under the applied milling conditions. Interestingly, no diffraction peaks corresponding to AgF were observed. Instead, new peaks emerged that are likely associated with a mixed-valence Ag^{2+}/Ag^{+} phase as it will be discussed later, suggesting that any AgF generated from partial decomposition rapidly reacted with residual AgF_2 to form this secondary phase.

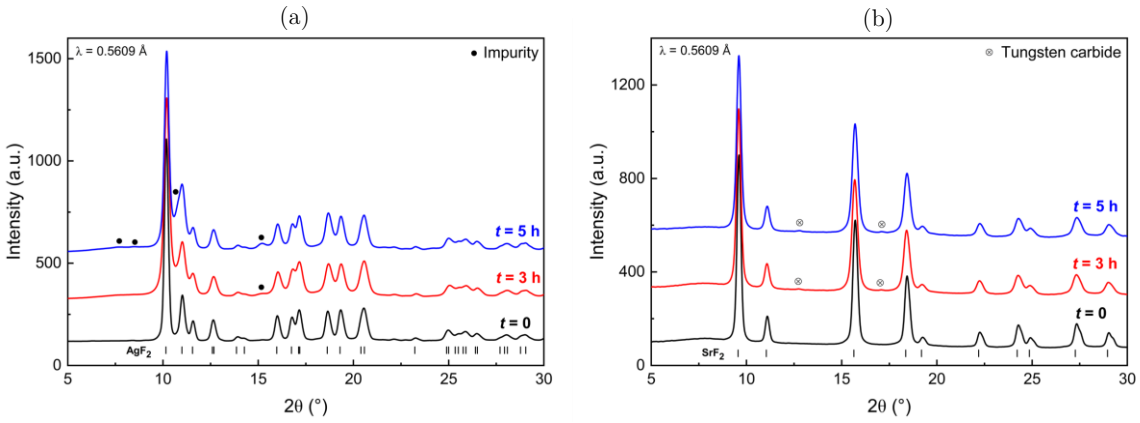


Figure 14: Time-dependent PXRD data collected on the ball-milled (a) AgF_2 and (b) SrF_2. The milling conditions used for the synthesis are detailed in Table 6.

Table 6: Milling conditions for separate milling of the starting reagents (AgF_2 and SrF_2).

Milling ball diameter (mm)	**Milling cycle (min)**	**Frequency (Hz)**	**BRR (ball-to-reagents-ratio)**
10	15	30	50

Another aim of this study was to identify milling conditions under which the decomposition of AgF_2 could be avoided or at least minimised. To optimise the synthesis of $SrAgF_4$ and reduce the thermal decomposition of AgF_2, various milling parameters were systematically investigated, including milling frequency, ball diameter, and milling cycle duration.

Firstly, the laboratory PXRD data in Figure 15a indicate that changing the milling frequency from 30 to 20 Hz led to a reduction in AgF_2 decomposition, resulting in a decrease in AgF content below the detection limit of the diffractometer. However, this reduction in thermal decomposition was accompanied by a decrease in reaction kinetics, which led to a significantly slower the conversion of the reagents into reaction products.

Secondly, the influence of the milling ball diameter on the synthesis process was investigated. Three different milling ball sizes were used: 15, 12 and 10 mm diameter. The mass of the milling ball with a diameter of 15 mm is approximately 26 g, the one with a diameter of 12 mm weighs around 13 g and the smallest one with a diameter of 10 mm weights around 8 g. It is important to mention that the mass of the balls also affects the impact energies. Although the temperature in the milling jar could not be monitored during milling, it can be assumed that the overall temperature in the milling jar and the local temperature pulses reached higher temperatures in the experiment with larger milling balls. This hypothesis is supported by the PXRD results shown in the Figure 15b where no AgF peaks were observed when using the smallest milling ball ($d = 10$ mm). However, the total time of milling to complete the reaction increased from 1.5 h for the 15 mm milling ball to 3 h for the 12 mm milling ball and up to 5 h for the 10 mm milling ball.

Finally, the influence of the length of the milling cycle was evaluated by comparing three different milling cycle durations: 30, 15 and 5 minutes. Between the milling cycles, the jars were let to cool to the room temperature. A similar conclusion could be drawn here as in the previous examples: longer milling cycle leads to a higher overall temperature in the milling jar and consequently a greater amount of AgF is observed in the PXRD data shown in the Figure 15c.

The effect of each individual milling parameter was investigated using a synthesis of $SrAgF_4$ starting from a 1:1 molar ratio of the reagents. The reaction was carried out with a 10 mm milling ball at a frequency of 30 Hz, and each milling cycle lasted 15 minutes. As shown in Figure 15d, PXRD data reveal that, after 5 hours of milling, the diffraction peaks corresponding to the starting materials disappeared. The only crystalline impurity detected was tungsten carbide, originating from the milling equipment. However, the presence of unreacted reagents or AgF in the amorphous phase cannot be completely ruled out.

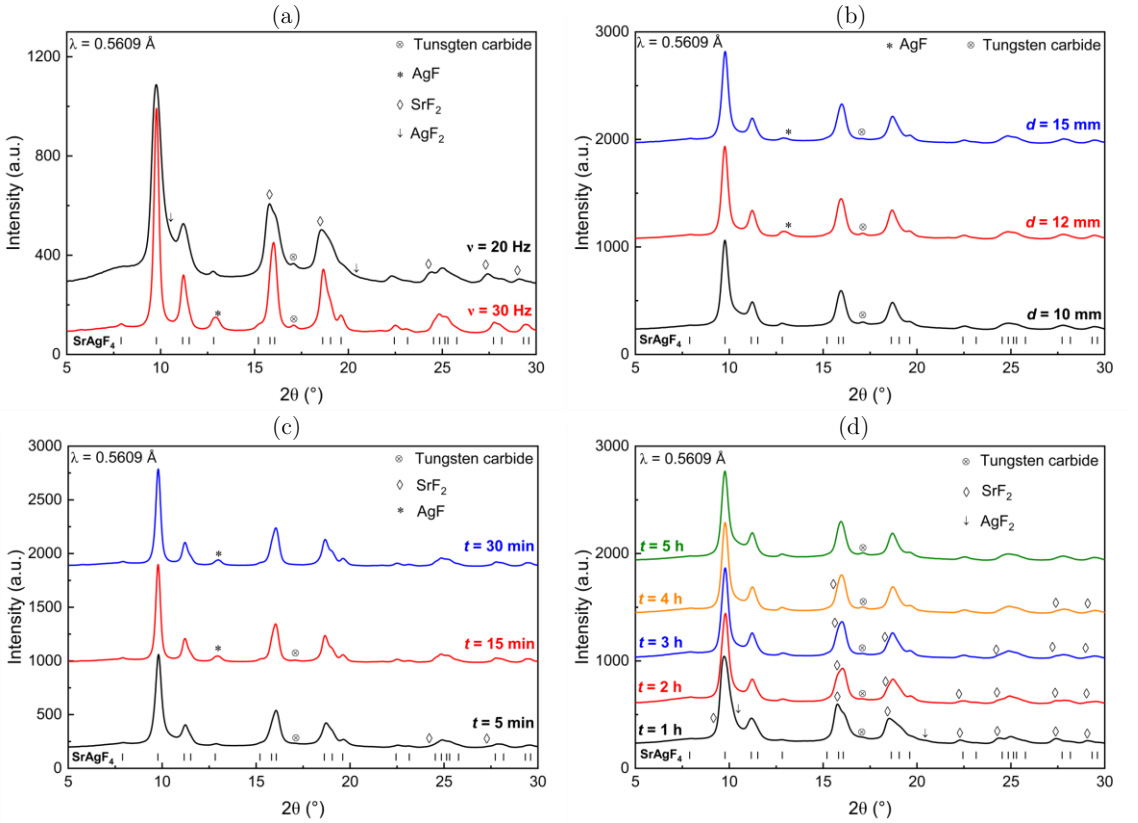


Figure 15: PXRD data of milled $SrAgF_4$ showing the effects of (a) milling frequency, (b) milling ball diameter, and (c) milling cycle duration on the synthesis, and (d) time-dependent data under optimized milling conditions.

It was discovered that the synthesis of $SrAgF_4$ requires 5 hours of ball milling followed by an additional 5 hours of cooling. To reduce the total processing time, higher-energy milling conditions were tested, but this resulted in increased AgF content in the final product. Four different $SrAgF_4$ syntheses with different combination of milling parameters were attempted through the ball milling, all successful with $SrAgF_4$ as the main phase, as confirmed by PXRD results (Figure 16, the milling conditions are listed in Table 7). Milling with smaller balls or shorter cycles reduced the amount of AgF but the process required longer milling times, which also led to more WC impurities. Based on these findings, the optimized milling conditions used for sample S1 were selected, which yielded the target phase after 90 minutes of milling. This sample is suitable for magnetic studies since all impurities are diamagnetic.

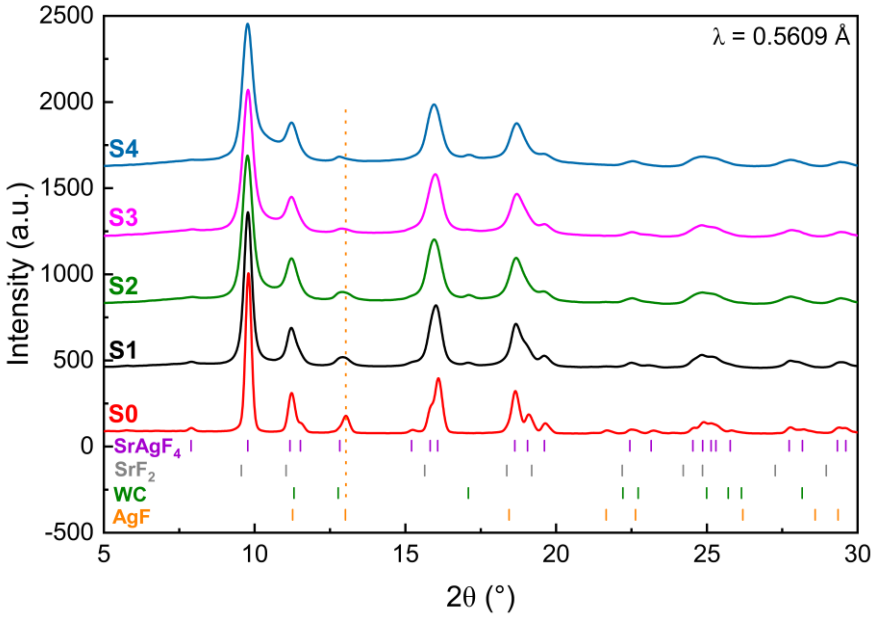


Figure 16: Laboratory PXRD patterns of $SrAgF_4$ samples prepared by ball milling under various milling conditions. Sample S0 corresponds to the PXRD pattern of $SrAgF_4$ synthesized by the solid-state method. The most intense AgF peak is indicated by an orange dotted line.

Table 7: Milling conditions for the synthesis of $SrAgF_4$ samples in Figure 16, using different combination of milling parameters.

Sample code	**Milling frequency (Hz)**	**Total milling time (h)**	**Milling cycle (min)**	**Ball diameter (mm)**
S1	30	1.5	15	15
S2	30	3	15	12
S3	30	2	5	15
S4	30	5	15	10

The optimised milling conditions (S1 in Table 7) were applied to the synthesis of $SrAgF_4$, and the phase composition of both ball-milled and solid-state synthesized samples was subsequently investigated using high-resolution synchrotron PXRD. Rietveld refinement of the data showed that both samples contained over 70 wt.% $SrAgF_4$ (Figure 17). The analysis also revealed that the crystallites in the solid-state sample were approximately one micrometer in size, while ball-milling produced nanosized crystallites around 20 nm. Despite similar sample purities, the ball milling synthesis required only 3 hours of milling, compared to 24 hours for the solid-state method. This substantial reduction in synthesis time highlights the efficiency of mechanochemistry in achieving comparable purity much faster than conventional solid-state synthesis.

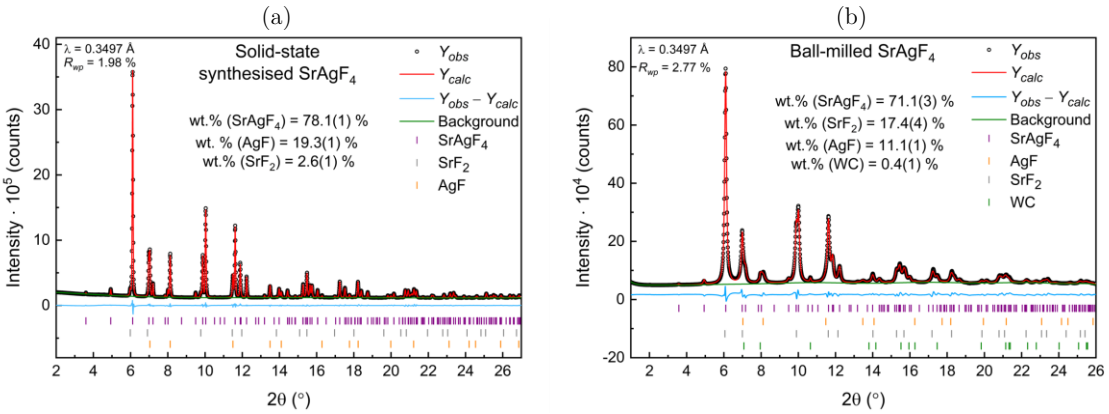


Figure 17: Rietveld refinements of high-resolution synchrotron PXRD data of: (a) solid-state synthesised $SrAgF_4$ and (b) mechanochemically synthesised $SrAgF_4$.

Once the optimal milling conditions for the synthesis of $SrAgF_4$ phase had been determined, the rest of the series was synthesised by ball-milling using the established milling conditions (Table 8). To improve crystallinity, the ball-milled samples were additionally annealed at 300 °C (except $HgAgF_4$ at 200 °C) for 24 hours. The PXRD data obtained on the solid-state samples was used to asses if the targeted MAgF$_4$ phase was successfully formed.

Table 8: Synthesis conditions for the mechanochemical synthesis of the MAgF$_4$ series.

Targeted phase	**Molar ratio of reagents (MF_2 : AgF_2)**	**BRR**	**Milling-ball diameter (mm)**	**Total milling time (h)**	**Milling frequency (Hz)**	**Milling cycle (min)**
$BaAgF_4$	1:1.1	50	15	3	30 Hz	15
$SrAgF_4$	1:1.1	50	15	3	30 Hz	15
$HgAgF_4$	1:1.1	43	15	3	30 Hz	15
$CaAgF_4$	1:1.1	50	15	3	30 Hz	15
$CdAgF_4$	1:1.1	56	15	3	30 Hz	15

Additional peaks are observed in the PXRD data obtained on the ball-milled $BaAgF_4$, which could not be assigned to any known phase in the PDF-4+ or ICSD database (Figure 18a). However, if the ball-milled sample is additionally annealed at 300 °C, those unidentified peaks disappear and the $BaAgF_4$ phase crystallises, which may indicate that the unidentified phase is metastable. In contrast, as it was stated earlier in this chapter, the ball-milled $SrAgF_4$ sample showed similar phase composition as the solid-state sample with an additional tungsten carbide impurity (Figure 18b). Interestingly, the PXRD data obtained on the ball-milled $HgAgF_4$ sample exhibited peaks that could be assigned to HgF_2 and another unknown phase (Figure 18c).

Annealing at 200 °C did not lead to the formation of $HgAgF_4$ (or to a very small amount), since the phase composition of annealed sample is mainly comprised of HgF_2, mixed-valence binary Ag^+/Ag^{2+} fluorides–as will be described later–and an additional unidentified phase. Ball-milling of the CaF_2 and AgF_2 mixture led to the formation of solid solution of $Ca_{1-x}Ag_xF_2$ ($x = 0.5$) with fluorite structure (Figure 18d). After annealing, the solid solution transformed into tetragonal $CaAgF_4$. Similar phenomenon was observed in the $BaSnF_4$ [59]. Lastly, the PXRD analysis of $CdAgF_4$ sample revealed that the

mechanochemically synthesised sample included an additional unidentified phase (Figure 18e). However, analysis of the PXRD data obtained on the annealed sample indicated that the sample consisted of approximately 30 wt.% of $CdAgF_4$ phase while Ag_3F_4 and CdF_2 represented the majority of the annealed sample.

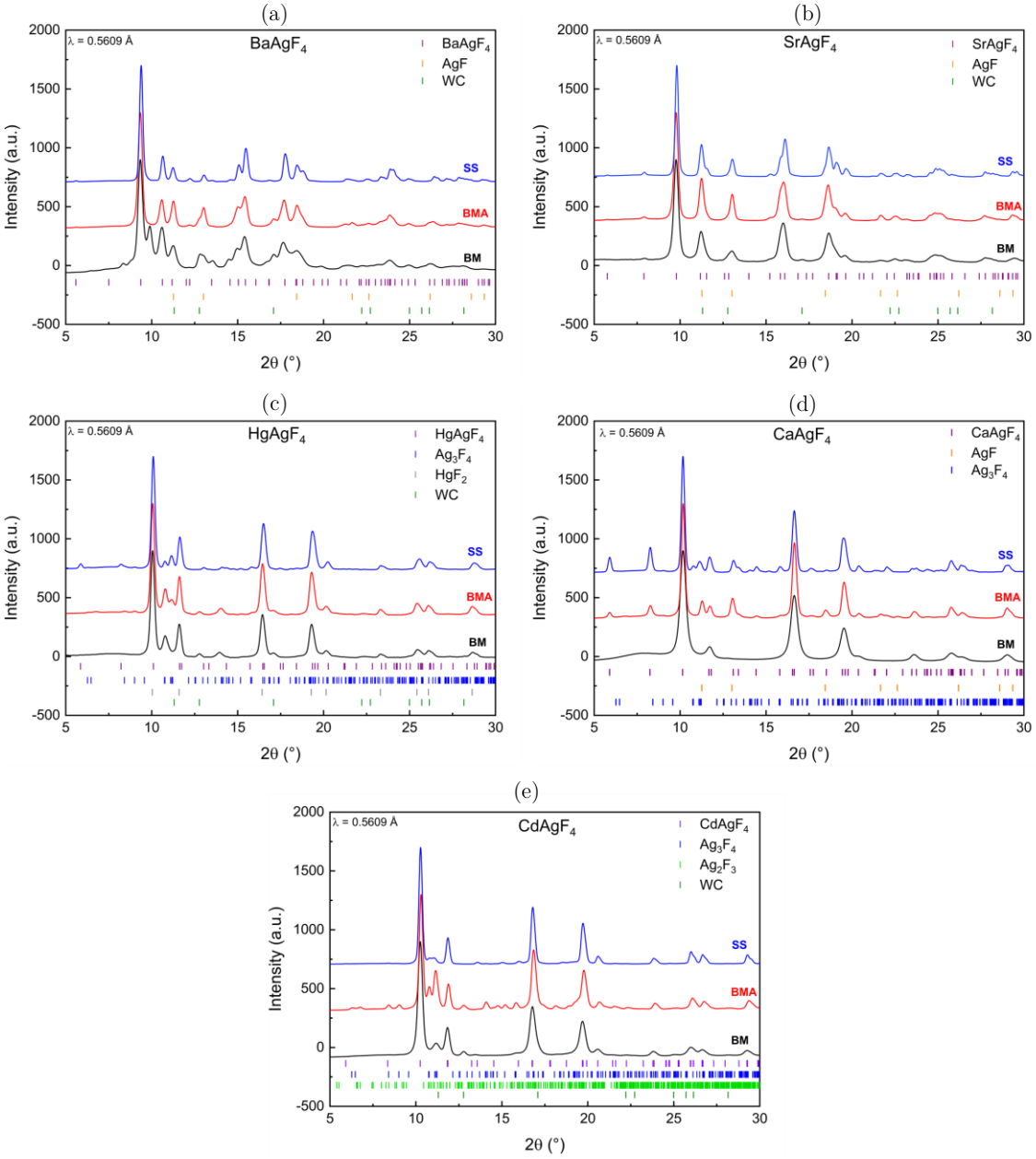


Figure 18: Comparison of the PXRD data obtained on the ball-milled (BM), ball-milled and annealed (BMA), and solid-state (SS) synthesised samples of the $MAgF_4$ series, M = Ba, Sr, Hg, Ca and Cd.

These results suggest that ball milling may enable access to metastable phases that are difficult or impossible to obtain through conventional methods like high-temperature solid-state synthesis. Furthermore, annealing the ball-milled sample allows the system to reach its energy minimum, causing the most thermodynamically stable phases to crystallise. In addition to changing the phase composition, annealing reduces strain and increases crystallite size, which leads to sharper diffraction peaks. The decreased background in the

PXRD patterns of annealed samples, compared to ball-milled ones, likely results from a reduced amount of amorphous material.

The literature suggests that the whole MAgF$_4$ series is isostructural to KBrF$_4$, which was also confirmed in this work by the determination of the crystal structure of BaAgF$_4$. Here, the main structural motif are magnetically isolated $[AgF_4]^{2-}$ square planar anions, which could result in a paramagnetic behaviour. The magnetic measurements carried out in 1974 by Odenthal and Hoppe confirmed the paramagnetic behaviour, however a start of a deviation from the Curie-Weiss law was observed for the cases of BaAgF$_4$ ($\theta_{CW} = -4$ K), SrAgF$_4$ ($\theta_{CW} = -6$ K) and HgAgF$_4$ ($\theta_{CW} = -6$ K) [80].

A closer examination of the crystal structure of the barium analogue solved in this study, provided additional insights into the structural features of the series. If one views the crystal structure perpendicular to the ab plane, the Ag^{2+} cations that form the $[AgF_4]^{2-}$ square planar anions are located at three positions on the c-axis: 0, $c/2$ and c. Between the layers of these anions, which propagate in the ab plane, are layers of Ba^{2+} cations, which make magnetic superexchange between Ag^{2+} cations along c-crystallographic direction rather complicated. In contrast, the anions could form weak superexchange interactions in the ab plane as they are oriented perpendicular to each other (Figure 19). In this case, the environment of the Ag^{2+} cation would consist of eight F^- atoms and not four, as it was proposed in the study by Odenthal and Hoppe [39], with a [4+4] coordination comprising of four longer and four shorter Ag–F contacts. With such interpretation of the crystal structure, there is a possibility for a superexchange interaction in the ab plane, as F^- atoms become bridging ligands between the Ag^{2+} cations. This could lead to a 2D-like character of the investigated compound and offers a possible explanation for the observed deviations from the Curie-Weiss law at low temperatures.

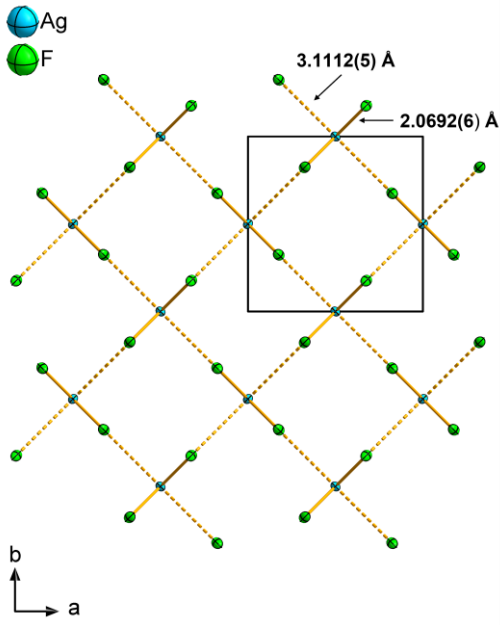


Figure 19: Crystal structure of BaAgF$_4$ viewed along the c-axis, highlighting a single layer of $[AgF_4]^{2-}$ anions. Ag–F distances are shown, with solid lines representing shorter, primary Ag–F bonds and dashed lines indicating longer, secondary Ag–F contacts.

Magnetic susceptibility measurements conducted in this study on MAgF$_4$ samples synthesised via the solid-state method reveal clear evidence of an antiferromagnetic transition, as indicated by distinct features in the temperature-dependent susceptibility

plots (Figure 20 and Figure 21). The transition temperatures were accurately determined from the maxima of the $\mathrm{d}(\chi \cdot T)/\mathrm{d}T$ curves or the "Fisher heat capacity" [81], revealing a systematic relationship between the M^{2+} cation size and the antiferromagnetic ordering temperature: larger M^{2+} cations correspond to lower transition temperatures. Curie constants obtained with the Curie-Weiss fit were consistent for $S = 1/2$ for Ag^{2+} and showed increasingly negative θ_{CW} with decreasing M^{2+} cation size, indicating stronger antiferromagnetic interactions. The θ_{CW} values ranged from −5.2(8) K for $BaAgF_4$, which is the compound with the largest M^{2+} cation, to −21.7(8) K for $CdAgF_4$, which is the compound with the smallest M^{2+} cation.

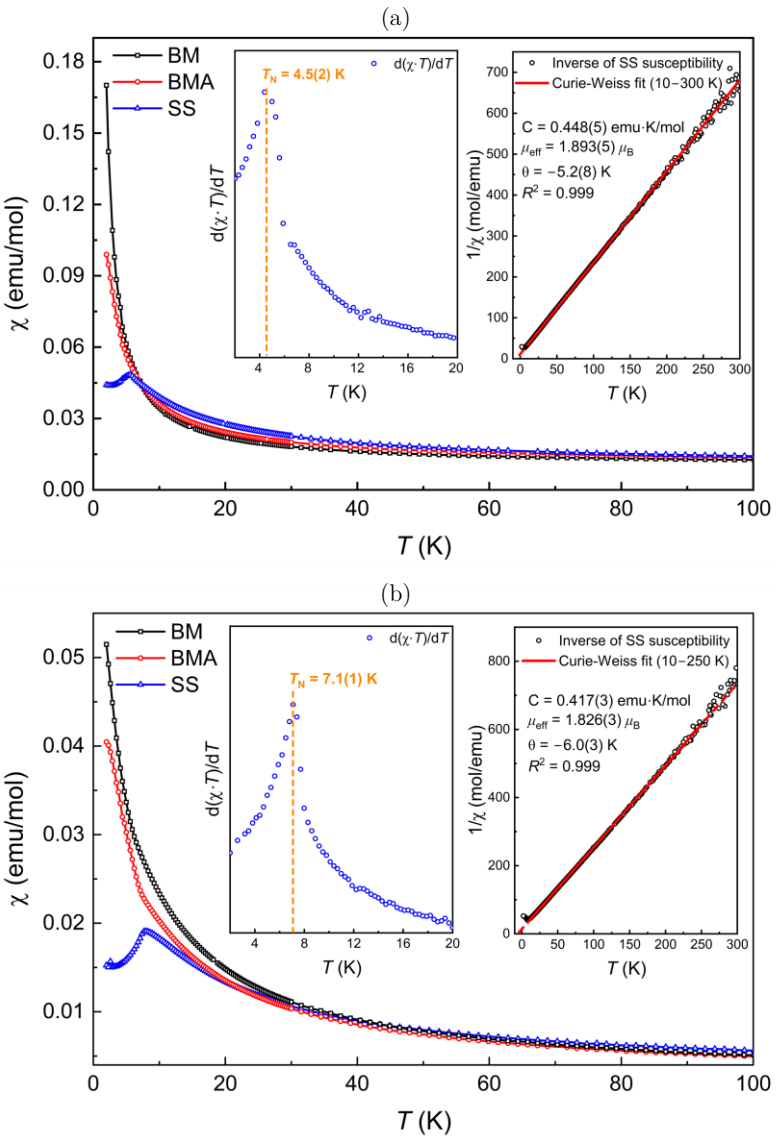


Figure 20: Magnetic susceptibility (ZFC) versus temperature measured under a 1 kOe field for ball-milled (BM), ball-milled and annealed (BMA), and solid-state synthesized (SS) samples of (a) $BaAgF_4$ and (b) $SrAgF_4$. Left insets show $\mathrm{d}(\chi \cdot T)/\mathrm{d}T$ versus temperature for the SS samples. Right insets present Curie-Weiss fits to the inverse magnetic susceptibility of the SS samples.

Further structural analysis based on Rietveld refinement of the laboratory PXRD data revealed that the four longer Ag–F contacts in the [4+4]-coordinated silver cations show a

significant decrease as the size of the M^{2+} cation decreases: from 3.1112(1) Å in $BaAgF_4$ to 2.738(3) Å in $CdAgF_4$. This contraction of the longer Ag–F bond lengths suggests an increased orbital overlap, which results in stronger superexchange interactions. The structural trend of decreasing Ag–F bond lengths with smaller M^{2+} cations provide a convincing explanation for the observed variation in magnetic behaviour in the $MAgF_4$ series and highlights the crucial interplay between crystal structure and magnetic properties. While longer Ag–F bond lengths show a clear relationship with the transition temperature, no similar pattern was observed for the shorter Ag–F bonds in the [4+4]-coordinated Ag^{2+} cation.

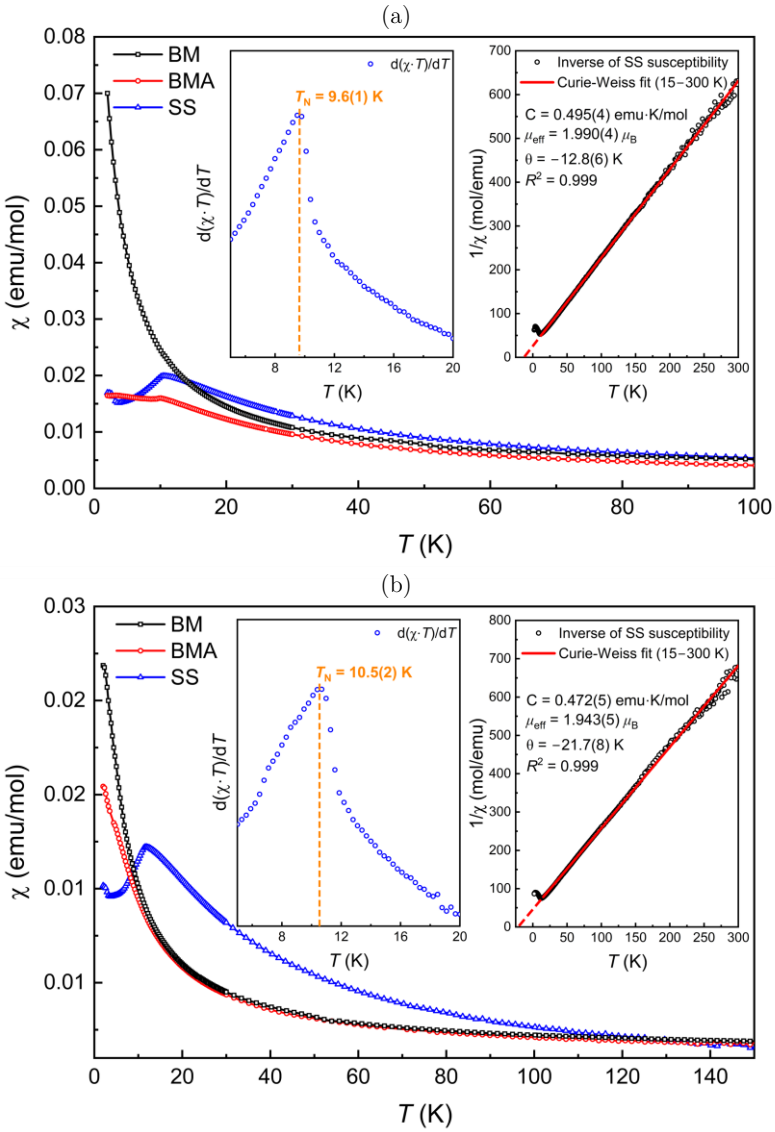


Figure 21: ZFC magnetic susceptibility measured as a function of temperature in the magnetic field of 1 kOe for ball-milled (BM), ball-milled and additionally annealed (BMA) and solid-state synthesised (SS) samples of: (a) $CaAgF_4$ and (b) $CdAgF_4$. The left insets represent $\mathrm{d}(\chi \cdot T)/\mathrm{d}T$ as a function of temperature for the solid-state samples while the Curie-Weiss fits to the inverse of the magnetic susceptibility of the solid-state samples are shown in the right insets.

The magnetic susceptibility data showed clear differences in magnetic behavior between ball-milled and solid-state synthesised samples in the MAgF$_4$ series. In particular, the antiferromagnetic transition is only seen in solid-state samples, while mechanochemically synthesised ones mostly behave as paramagnets. These differences could arise from variations in phase purity, but this explanation does not apply to SrAgF$_4$. PXRD analysis (Figure 17) confirmed that both synthesis methods produce phase-pure SrAgF$_4$, so their magnetic properties should be similar—yet they were not.

It was hypothesised that in the case of SrAgF$_4$, the different magnetic behaviour was most likely observed due to the introduction of defects caused by ball-milling, which was also reported in the field of oxides and alloys [82, 83]. Ball-milling produces nano-sized crystallites and leads to a high density of structural defects, such as point defects and dislocations, which could disrupt the long-range magnetic order, leading to the observed paramagnetic behaviour. In contrast, solid-state synthesis leads to larger, well-formed crystallites with fewer defects, which facilitates the establishment of long-range magnetic order and leads to the antiferromagnetic transition at 7.1 K. Hence, the choice of synthesis method critically influences the magnetic behaviour of SrAgF$_4$ by affecting its microstructure or/and the amount and type of defects.

Building on these results, the magnetic properties of HgAgF$_4$ were also investigated by correlating the cation size with the antiferromagnetic transition temperatures. A linear correlation was observed in the plot of T_N as a function of ionic radius of the M^{2+} cation (Figure 22). Based on the ionic radius of the Hg^{2+} cation, it was estimated that the transition temperature for HgAgF$_4$ would be about 9.5 K.

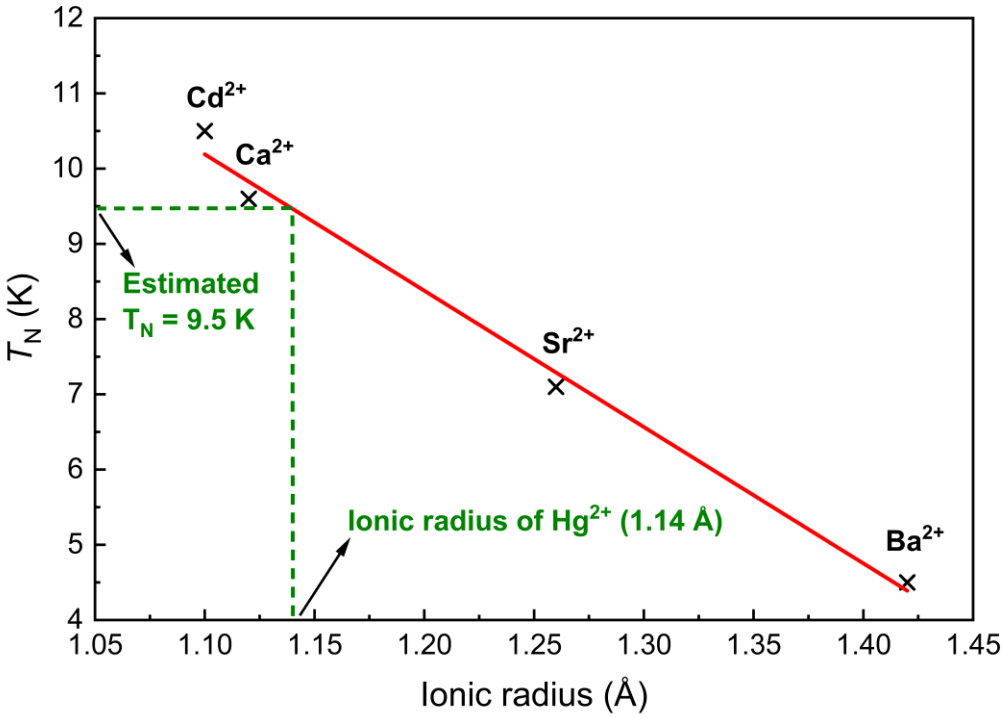


Figure 22: The T_N plotted as a function of ionic radius of the M^{2+} cation, with a linear fit given by the following equation: $y = -18(1) \cdot x + 30(2)$; $R^2 = 0.991$.

As antiferromagnetism was observed in all measured MAgF$_4$ samples prepared by the conventional solid-state method, the magnetic structure was studied by NPD. Owing to the isostructural nature of the series, it was sufficient to solve the magnetic structure of

just one member. The NPD data were collected on the solid-state synthesised $SrAgF_4$ sample below (1.83 K) and above (9 K) the transition temperature of 7.1(1) K. The difference plot in Figure 23a shows the occurrence of five magnetic peaks, which were used for the determination of the magnetic propagation vector $k = (1, 0, 0)$ with the FullProf software [84]. To identify the possible maximum magnetic space groups for the parent space group $I4/mcm$ and the propagation vector $k = (1, 0, 0)$, Bilbao Crystallographic Server [85, 86, 87] was used, which provided four possible candidates: P_I4_2/mbc, P_I4/mcc, C_Amca, and P_Ibcn. Several refinements were performed considering each magnetic space group candidate and it was concluded that the magnetic peaks could only be fitted with the P_Ibcn space group. Since the magnetic form factors for the Ag^{2+} cation have not yet been determined, the magnetic form factors of Cu^{2+} were used instead in the refinement of the NPD data measured at 1.83 K and the results are presented in Figure 23b.

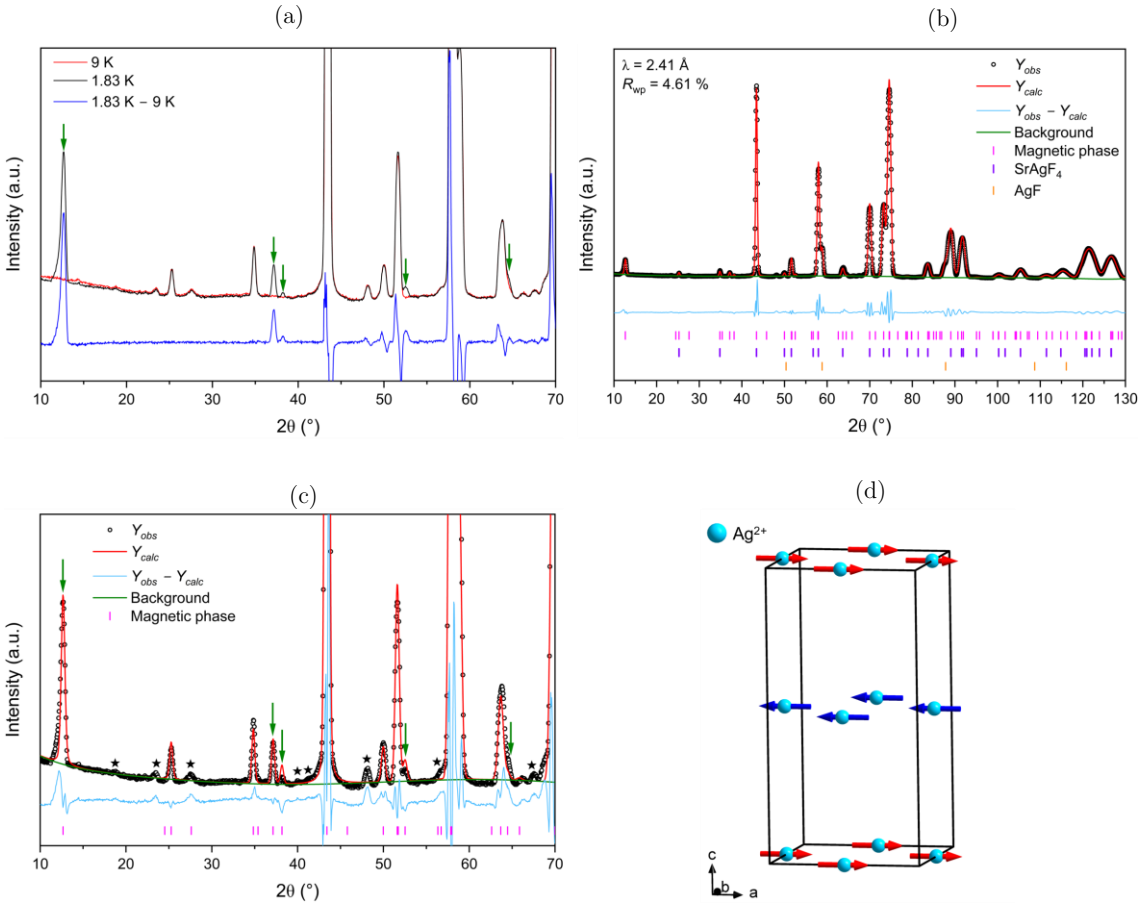


Figure 23: (a) The NPD data measured at 9 and 1.83 K and the difference plot. Magnetic peaks are marked with green arrows. (b) Rietveld fit to the NPD data measured at 1.83 K on the solid-state synthesised $SrAgF_4$, refined using a combined structural and magnetic model; wt.% ($SrAgF_4$) = 91.4(1); wt.% (AgF) = 8.6(1). (c) Magnified region in the 10–70 2θ range showing the magnetic peaks accounted in the Rietveld refinement, which are marked with green arrows; the unidentified peaks are marked with black star symbols. (d) Magnetic structure of $SrAgF_4$. Strontium and fluorine atoms are omitted for clarity.

A closer look in the region where the magnetic peaks appear (Figure 23c) reveals that all of the magnetic peaks were accounted in the refinement. However, small deviation of the model function to the experimental data of the magnetic peaks was observed, which could be due to the fact that the refinement was performed using the form factors of Cu^{2+}

cations. Rietveld refinement was also attempted using magnetic form factors of Pd^{+}, however the final refinement result did not differ significantly compared to the refinement performed using the Cu^{2+} magnetic form factors. Some unidentified peaks were also observed, which are marked with black star symbol in Figure 23c. Since these peaks were present above and below the transition temperature, they are not magnetic and could be attributed to an impurity in the sample. The presence of impurities is not surprising since this sample was prepared by the thermal solid-state method, which often leads to the formation of secondary phases. Figure 23d illustrates the magnetic structure of $SrAgF_4$, with the crystallographic data provided in Table 9. In this structure, the spins on the magnetic Ag^{2+} cations align ferromagnetically within the *ab* plane, as they point along *a*-crystallographic axis. Conversely, along the *c*-crystallographic direction, the spins are coupled antiferromagnetically. This arrangement corresponds to an *A*-type antiferromagnetic ordering [8].

Table 9: Crystallographic parameters of the magnetic $SrAgF_4$ phase obtained by the Rietveld refinement of NPD data. Note that Ag^{2+} cation was replaced with Cu^{2+} cation as an approximation for the Rietveld refinement.

Space group	***P*$_1$*bcn* (no. 60.432)**
a, *b*, *c* [Å]	5.7273(3), 5.7273(3), 11.1160(5)
Cu^{2+} (*x*, *y*, *z*)	0, 0.5, 0
M (*mx*, *my*, *mz*)	0.91(1), 0, 0
U_{iso}	0.030(1)

In conclusion, this chapter investigates the use of mechanochemistry as an alternative synthesis method for fluoridoargentates(II). A series of $MAgF_4$ compounds (*M* = Ba, Sr, Hg, Ca, Cd) was prepared, and the crystal structure of $BaAgF_4$ was determined using SCXRD. $SrAgF_4$ was selected as a model system for optimising ball-milling parameters, which were then applied to the synthesis of the full $MAgF_4$ series. The mechanochemical approach provided new insights into the magnetic behaviour of these compounds. Comparative magnetic measurements of ball-milled, annealed, and samples prepared by a conventional solid-state method, revealed a strong influence of the synthesis route on magnetic properties. NPD further confirmed *A*-type antiferromagnetic ordering in $SrAgF_4$. Following these results, the conditions used in this chapter were employed as starting points for the mechanochemical synthesis of the rest of fluoridoargentates(II) described in this thesis. These results demonstrate the versatility of mechanochemistry and its usefulness in studying the structural and magnetic characteristics of fluoridoargentates(II).

3.2 Mechanochemical Synthesis of Alkali Metal Fluoridoargentates(II)

Alkali metal fluoridoargentates(II) represent a fascinating class of materials in which the distinctive connectivity of silver and fluorine atoms establishes strong superexchange pathways and gives rise to diverse magnetic phenomena. Within the MAgF$_3$ series (M = K, Rb and Cs), the compounds crystallise in a perovskite-like structure, where Ag^{2+} centres are octahedrally coordinated by F^- anions. These corner-sharing $[AgF_6]^{4-}$ octahedra assemble into a 3D framework that supports extended Ag–F–Ag superexchange interactions. By contrast, members of the M_2AgF$_4$ series (M = K, Rb and Cs) adopt a layered structural motif, structurally related to double perovskites, in which the alternation of silver and fluorine layers leads to quasi-2D magnetic properties. The magnetic behaviour of these materials is therefore strongly dictated by dimensionality, with the 2D connectivity of M_2AgF$_4$ contrasting sharply with the 3D networks of MAgF$_3$. Beyond their structural diversity, the Ag^{2+} cations themselves are of particular interest as they possess an electronic configuration closely analogous to that of Cu^{2+} in cuprate superconductors. Although superconductivity has not been observed in these fluorides, their structural and electronic characteristics provide valuable opportunities to probe parallels with other low-dimensional correlated systems. Consequently, the study of MAgF$_3$ and M_2AgF$_4$ compounds is of broad significance, offering insights into the relationship between crystal structure, dimensionality, and magnetism, while hinting at potential connections to phenomena such as superconductivity.

The magnetic characterisation of the MAgF$_3$ series (M = K, Rb, Cs) presents significant challenges, primarily due to the presence of magnetic secondary phases, such as ferromagnetic M_2AgF$_4$ phases, which form during the solid-state synthesis. These secondary phases complicate the interpretation of magnetic properties of the target compounds. Consequently, the primary objective of this study was to synthesise high-purity MAgF$_3$ samples devoid of undesired secondary phases, facilitating a more reliable magnetic characterisation of these materials. To this end, ball-milling was selected as a core synthetic strategy. This technique, conducted at room-temperature conditions, reduces the risk of thermal decomposition of AgF$_2$, a common issue in high-temperature synthesis, while also minimising the formation of undesired secondary phases. In parallel, the effectiveness of ball-milling was evaluated against other synthetic approaches, including traditional solid-state methods and ball-milling with an additional annealing step. Different synthetic approaches were systematically compared by evaluating the phase composition and magnetic properties of the resulting MAgF$_3$ samples. This comparative analysis allowed an exploration the synthesis-structure-property relationships in greater depth, addressing long-standing gaps in the understanding of the magnetic behaviour in the MAgF$_3$ series. Furthermore, the first reported synthesis and characterisation of NAgF$_3$ was attempted, a previously unstudied compound within the silver fluoride family. Additionally, the role of ball-milling in the synthesis of M_2AgF$_4$ phases was examined, further elucidating how this method influences phase purity and magnetic properties. Together, these efforts contribute valuable insights into the synthesis and characterisation of silver fluorides, enhancing our understanding of their complex magnetic and structural properties.

3.2.1 MAgF$_3$ Series (M = Na, K, Rb and Cs)

Compounds in the MAgF$_3$ series garnered a lot of interest since they exhibit unusually strong antiferromagnetic superexchange interaction in 1D [20], a characteristic similar to Sr_2CuO_3 [33], a compound without [CuO_2] layers, which becomes superconducting upon

doping [34]. The MAgF$_3$ series, encompassing KAgF$_3$, RbAgF$_3$, and CsAgF$_3$, constitutes a unique class of fluoridoargentates(II). These compounds were first synthesised by Odenthal and Hoppe in the 1970s [88]. The structural type that is adopted by compounds in the MAgF$_3$ series is the distorted perovskite structure and the size of the alkali metal cation influences the level of the distortion with the larger cation results in smaller distortion [4, 3]. According to previous reports [4, 88], both CsAgF$_3$ and RbAgF$_3$ crystallise in the tetragonal crystal system with the $I4/mcm$ space group. In this crystal structure, the Ag^{2+} cation is coordinated with six fluorine anions with two short, two medium and two long Ag–F contacts (Figure 24a). Since the bond lengths of short and medium Ag–F bonds are comparable, the coordination of the Ag^{2+} cation is forming an elongated $[AgF_6]^{4-}$ octahedra. These octahedra are forming infinite $[AgF]^+$ chains along the c-axis, along which strong antiferromagnetic superexchange interaction takes place. The superexchange coupling constant J_{1D} was theoretically determined for CsAgF$_3$ ($J_{1D} \approx -160$ meV) and RbAgF$_3$ ($J_{1D} \approx -144$ meV) since the experimental determination is hindered due to the magnetic impurities present in the samples [4, 20]. In comparison, the J_{1D} value for Sr_2CuO_3 reaches approximately −240 meV [33].

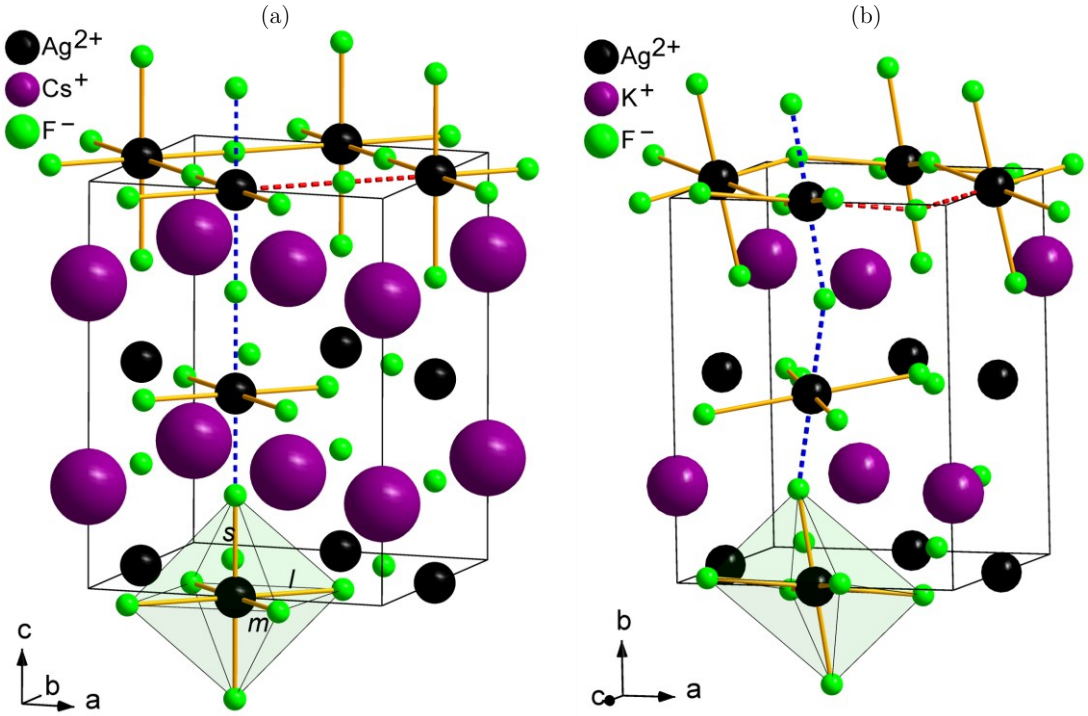


Figure 24: (a) Crystal structure of CsAgF$_3$. Bond lengths of the $[AgF_6]^{4-}$ octahedra are marked with letters s (small), m (medium) and l (large). The intrachain superexchange pathway along the c crystallographic direction is presented with blue broken bonds while the interchain superexchange pathway is presented with red broken bonds. (b) Crystal structure of KAgF$_3$. The intrachain superexchange pathway along b crystallographic direction is presented with blue broken bonds while the interchain superexchange pathway is presented with red broken bonds.

Potassium trifluoridoargentate(II), KAgF$_3$, has a rich history of investigation dating back to its first synthesis in the 1970s by Odenthal and Hoppe. In their early studies, the crystal structure of KAgF$_3$ was determined from the laboratory PXRD data and assigned the *Pbnm* space group [88]. However, due to the low quality of the data at that time, they were unable to determine whether the fluorine atoms deviated from specific positions within

the crystal structure, possibly leading to the puckering of the $[AgF_2]$ layers. In 2009, a study by Mazej *et al.* [35] provided new information about the crystal structure of $KAgF_3$. From the PXRD data, they concluded that $KAgF_3$ crystallises in the orthorhombic space group *Pnma*, which confirms the slight puckering of the $[AgF_2]$ sheets. It could be observed from the crystal structure, shown in the Figure 24b, that the Ag^{2+} cation is found in an elongated [2+2+2] octahedral environment of fluorine atoms characterised by two longer (2.4152 Å) and four shorter (2.1171 Å and 2.0991 Å) Ag–F distances. The $[AgF_6]^{4-}$ octahedra propagate along the *b* axis and form infinite $[AgF]^+$ chains. Due to the tilting of these octahedra, the $[AgF]^+$ chains are not linear, resulting in an Ag–F–Ag angle of 157°. This structural feature has a profound influence on the magnetic properties of $KAgF_3$, as it weakens the antiferromagnetic superexchange interaction within the chain along *b* crystallographic direction. Besides the strongly pronounced antiferromagnetic exchange within the $[AgF]^+$ chains, $KAgF_3$ also exhibits ferromagnetic coupling through superexchange interactions between the chains [20]. This magnetic behaviour contributes to the complex magnetic properties of $KAgF_3$ [80, 89, 90, 91]. In addition, Kurzydłowski *et al.* reported in 2013 that $KAgF_3$ undergoes a structural phase transition from the low-temperature *Pnma* phase to a disordered high-temperature *Pcma* phase at about 230 K [90]. This transition is characterised by an almost halved *b* unit cell parameter. Interestingly, the Ag–F bond lengths within the $[AgF_6]^{4-}$ octahedra are very similar in both polymorphs and the Jahn-Teller distortion is observed throughout, suggesting that the magnetism of both phases is likely to be essentially the same. Although the data obtained were at the detection limit of the instruments used, a recent study [91], which used a combination of powder neutron diffraction and muon spectroscopy as well as theoretical DFT calculations on $KAgF_3$, claims that the ground magnetic state of this compound is an ordered *A*-type antiferromagnet with a $T_{N1} \approx 29$ K. This is close to the temperature of 35 K at which an anomaly was previously found in the susceptibility data reported by Kurzydłowski *et al.* [90]. However, another anomaly was found at $T_{N2} \approx 66$ K, raising the question of whether there is a magnetically ordered intermediate phase between T_{N1} and T_{N2} or does the signal belong to an impurity. The NPD experiments reported by Wilkinson *et al.* [91] did not provide clear evidence for a magnetic phase in this temperature range, and this issue is still under debate. Literature reports on the magnetic properties are also inconsistent. Some studies report only one FM-like transition at 68 K [89] or 80 K [80], while other reports indicate at least two such transitions between 80–5 K [35, 90, 91, 92].

The last member of the series, $NaAgF_3$, has not been successfully synthesised and structurally characterised yet. However, based on the fact that with decreasing the size of the alkali metal cation the symmetry of the perovskite crystal structure lowers, it was proposed that it is either monoclinic or triclinic and is structurally related to $NaCuF_3$ [93].

3.2.1.1 $CsAgF_3$ and $RbAgF_3$

Both targeted phases were prepared with three methods and the synthesis conditions are reported in Table 10. In all cases, light-brown polycrystalline samples were obtained.

Table 10: Synthesis conditions for the preparation of $RbAgF_3$ and $CsAgF_3$ samples with three different methods.

Synthesis method	Synthesis conditions
Ball-milling (BM)	$MF : AgF_2 = 1{:}1.1$, $t = 3$ h, milling cycle = 15 min, ν = 30 Hz, BRR ≈ 40
Ball-milling with additional annealing step (BMA)	$T = 300$ °C, $t = 24$ h
Solid-state synthesis (SS)	$T = 300$ °C, $t = 24$ h, two cycles

Both phases were successfully prepared by ball-milling, as indicated by the Rietveld refinement of the laboratory PXRD data in Figure 25a and Figure 25b. In both cases, the only crystalline impurity present in the milled samples was diamagnetic AgF. Annealing of the ball-milled sample improves the crystallinity, as evident from the Figure 25c and Figure 25d. However, additional peaks appeared that could not be assigned to any known phases in the database (green stars in the Figure 25c and Figure 25d).

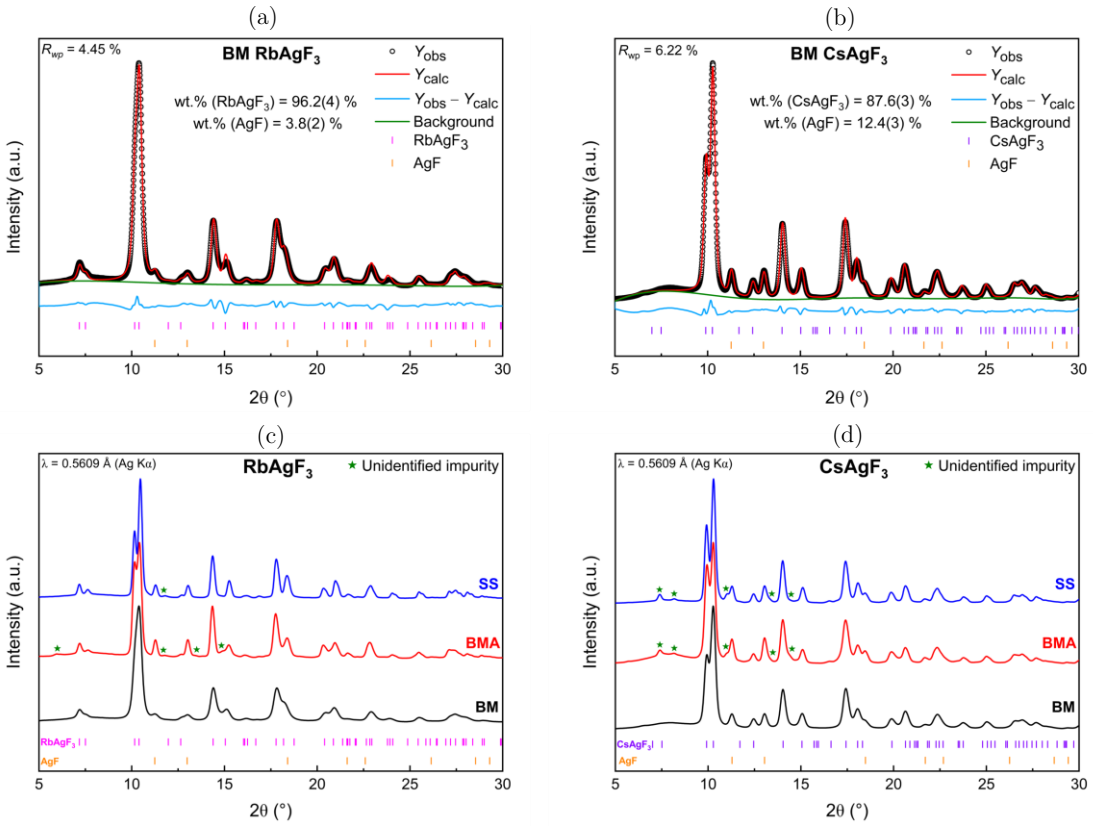


Figure 25: Rietveld refinement of the laboratory PXRD data of ball-milled (a) $RbAgF_3$ and (b) $CsAgF_3$ measured at room temperature. Comparison of the laboratory PXRD data of BM, BMA and SS samples of (c) $RbAgF_3$ and (d) $CsAgF_3$. Green star symbols indicate peaks of unidentified impurities.

Interestingly, the solid-state synthesised $RbAgF_3$ sample included less impurities compared to the ball-milled and additionally annealed sample. In contrast, the solid-state sample of $CsAgF_3$ had included similar amount of the same unidentified impurity as the ball-milled and additionally annealed sample. The laboratory PXRD data therefore indicates that ball-milling does not only result in the targeted phase in much shorter time, but also results in purer sample with the sole secondary phase being diamagnetic AgF. These samples are therefore suitable for further magnetic characterisation.

Raman spectroscopy offered an additional insight into the qualitative and quantitative phase analysis. Since the Raman spectra in the literature were measured on the solid-state synthesised samples, the data obtained on the samples prepared with the same synthesis method were compared. Raman spectra of SS $RbAgF_3$ samples are shown in Figure 26 and the position of the peaks are compared with the literature in Table 11. The Raman spectrum of the solid-state synthesised $RbAgF_3$ resembles the one reported by Koteras *et al.* [4] with few distinct differences observed. The majority of the peaks were shifted for approximately 10 cm^{-1} towards higher wavelengths, which could be attributed to an instrumental calibration. The most notable difference compared to the literature is the difference in the intensities of the two most intense peaks. While in the study by Koteras the most intense peak appeared at 477 cm^{-1}, this data indicates that the most intense peak is located at 387 cm^{-1}. Furthermore, the data in the literature also reports the peak at 423 cm^{-1}, which was assigned to an impurity. In this study, this peak was not observed, suggesting that sample with higher purity was prepared. Lastly, the peak at 503 cm^{-1} (507 cm^{-1} in the literature) was more profound in this data.

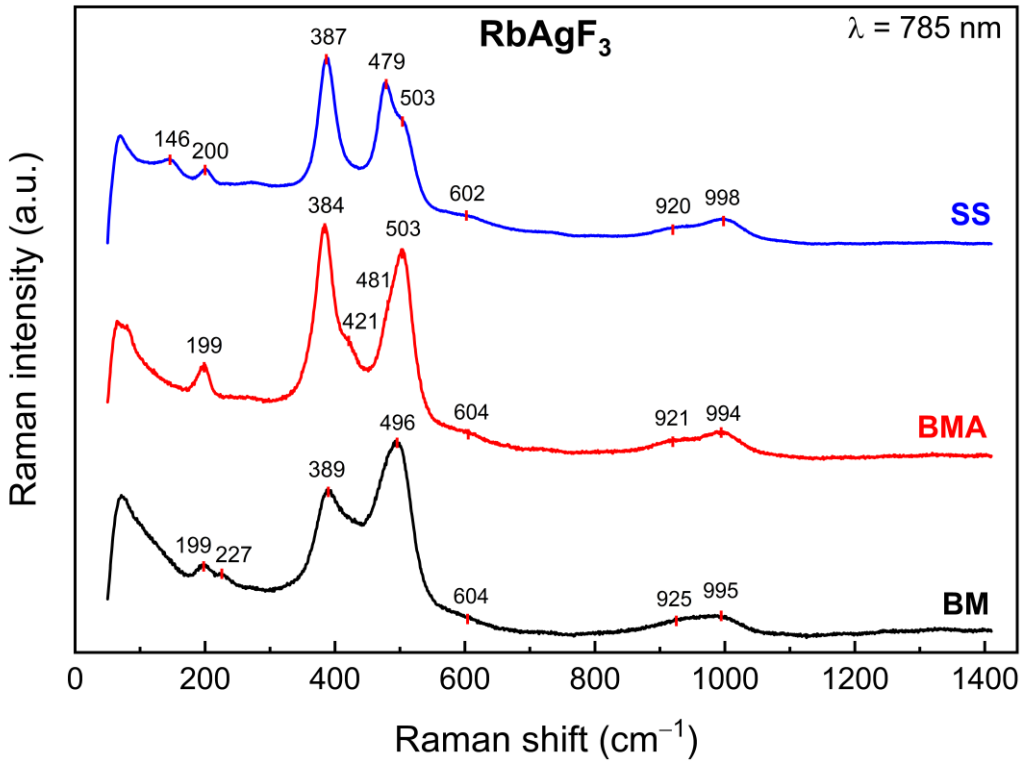


Figure 26: Room-temperature Raman spectra measured on $RbAgF_3$ samples, which were synthesised by three different methods: ball-milling (BM), ball-milling and annealing (BMA) and solid-state synthesis (SS).

The Raman spectrum of ball-milled $RbAgF_3$ closely resembles that of the solid-state synthesised sample, but the two most intense peaks at 389 and 496 cm^{-1} are shifted in intensity. The broad band near 496 cm^{-1} may in fact consist of two overlapping peaks, similar to those in the solid-state sample (479 and 503 cm^{-1}). The 389 cm^{-1} peak likely shows a right-hand shoulder near 420 cm^{-1}, which could correspond to an impurity previously reported for solid-state synthesised $RbAgF_3$.

Upon annealing the ball-milled sample, the Raman peaks become sharper, indicating increased crystallinity. The 227 cm^{-1} peak—present only in the ball-milled material—disappears, while the relative intensities of the 481 and 503 cm^{-1} peaks differ from those of the solid-state sample. Furthermore, the 146 cm^{-1} peak is absent, suggesting slight differences in phase composition between the two samples.

Table 11: Comparison of Raman peak positions for solid-state synthesised $RbAgF_3$ obtained in this study with those reported by Koteras *et al.* [4].

Peak position (cm^{-1})		**Difference (cm^{-1})**	**Symmetry**	**Assignment**
Our data	***Koteras et al.*** [4]			
146	/	/	?	Not assigned
200	189	13	E_g	$[AgF_6]$ octahedron bending
387	378	11	A_{1g}	$[AgF_2]$ plane stretching
/	423	/	/	Impurity
479	477	2	B_{2g}	$[AgF_6]$ octahedron stretching
503	507	4	?	Impurity or a combination of modes
602	602	0	/	Impurity
920	910	10	/	Impurity or a combination of modes
998	986	12	/	Impurity or a combination of modes

The Raman spectrum of solid-state synthesised $CsAgF_3$ (Figure 27) closely matches the spectrum reported by Koteras *et al.* [4] with peak shifts not exceeding 6 cm^{-1} (Table 12). The literature also reports a peak at 398 cm^{-1}, which may be present in this study's spectrum, as the corresponding peak is slightly asymmetric and appears to have a right shoulder near 400 cm^{-1}. The Raman spectrum of ball-milled $CsAgF_3$ displays an additional vibrational mode centered around 235 cm^{-1}, which is also observed in the ball-milled $RbAgF_3$ sample. This mode diminishes considerably upon annealing, suggesting that it may be associated with structural disorder or defects induced by the mechanochemical treatment. Furthermore, annealing leads to the emergence of a new peak near 425 cm^{-1}, likely indicative of secondary phases or impurity formation during thermal treatment. The appearance and evolution of these features highlight subtle changes in local bonding environments and phase purity between the as-milled and annealed samples.

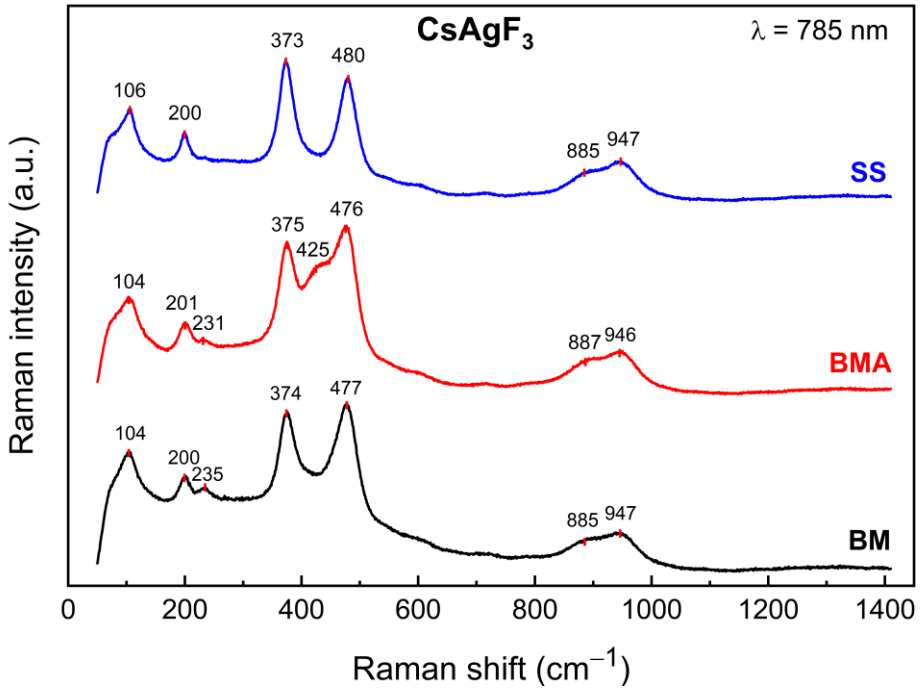


Figure 27: Room-temperature Raman spectra measured on $CsAgF_3$ samples, which were synthesised by three different methods: ball-milling (BM), ball-milling and annealing (BMA) and solid-state synthesis (SS).

Comprehensive Raman and PXRD analyses unequivocally establish that mechanochemical synthesis markedly surpasses the conventional solid-state approach in the preparation of $RbAgF_3$ and $CsAgF_3$, particularly in terms of phase purity and synthesis efficiency. The ball-milling process affords nearly phase-pure products, with only trace quantities of diamagnetic AgF detected as a minor impurity, achieving complete synthesis within a notably brief timeframe of six hours. In contrast, the solid-state synthesis demands prolonged heating exceeding two days and results in comparatively lower sample purity. The significant reduction in synthesis duration not only enhances the practical feasibility of these silver fluoride compounds but also mitigates thermal decomposition of AgF_2, a common issue arising from extended high-temperature treatment inherent to the solid-state method. These compelling advantages underscore mechanochemistry as a superior, scalable, and more reliable synthetic strategy, thereby facilitating advanced studies of the structural and magnetic properties of these materials. Subsequently, this investigation proceeded to a detailed comparative analysis of the magnetic properties of samples synthesized via these distinct methodologies, with the objective of elucidating the impact of synthetic route on the intrinsic magnetic behaviour of $RbAgF_3$ and $CsAgF_3$.

Table 12: Comparison of Raman peak positions for solid-state synthesised $CsAgF_3$ obtained in this study with those reported by Koteras *et al.* [4].

Peak position (cm^{-1})		**Difference (cm^{-1})**	**Symmetry**	**Assignment**
Our data	***Koteras et al.*** [4]			
106	/	/	?	Not assigned
200	202	2	E_g	$[AgF_6]$ octahedron bending
373	372	1	A_{1g}	$[AgF_2]$ plane stretching
/	398	/	/	Overtone 202 (E_g x E_g)
480	477	2	B_{2g}	$[AgF_6]$ octahedron stretching
/	711	/	/	Impurity or a combination of modes
885	879	6	/	Impurity or a combination of modes
947	942	5	/	Impurity or a combination of modes

Magnetic susceptibility measurements on $RbAgF_3$ (Figure 28a) reveal that the ball-milled sample exhibits no magnetic ordering within the measured temperature range. In contrast, the ball-milled sample subjected to additional annealing displays more complex magnetic behaviour. A weak increase in susceptibility is observed near 100 K, indicating the possible presence of a ferromagnetic impurity. A more pronounced magnetic transition occurs below 25 K. Analysis of the derivative plot ($-\mathrm{d}\chi/\mathrm{d}\,T$ vs. T) identifies two transition temperatures at approximately 21 K and 16 K. The lower transition at 16 K is likely attributable to ferromagnetic Rb_2AgF_4 [22, 36], which is present in amounts below the detection limit of laboratory PXRD and Raman techniques. The transition at 21 K, however, does not correspond to any known phases in the Rb-Ag-F system. Notably, the solid-state synthesised sample exhibits the same two transitions.

Magnetic susceptibility data for $CsAgF_3$ (Figure 28b) show similar trends to the rubidium analogue. The ball-milled sample alone does not display any abrupt susceptibility changes, whereas the annealed ball-milled sample shows a small increase near 80 K, suggesting a ferromagnetic impurity. This feature is absent in the solid-state synthesised sample. Upon further cooling, both the annealed and solid-state samples exhibit an additional ferromagnetic transition around 16 K, potentially due to trace amounts of Cs_2AgF_4 with $T_C = 15.7$ K [21]

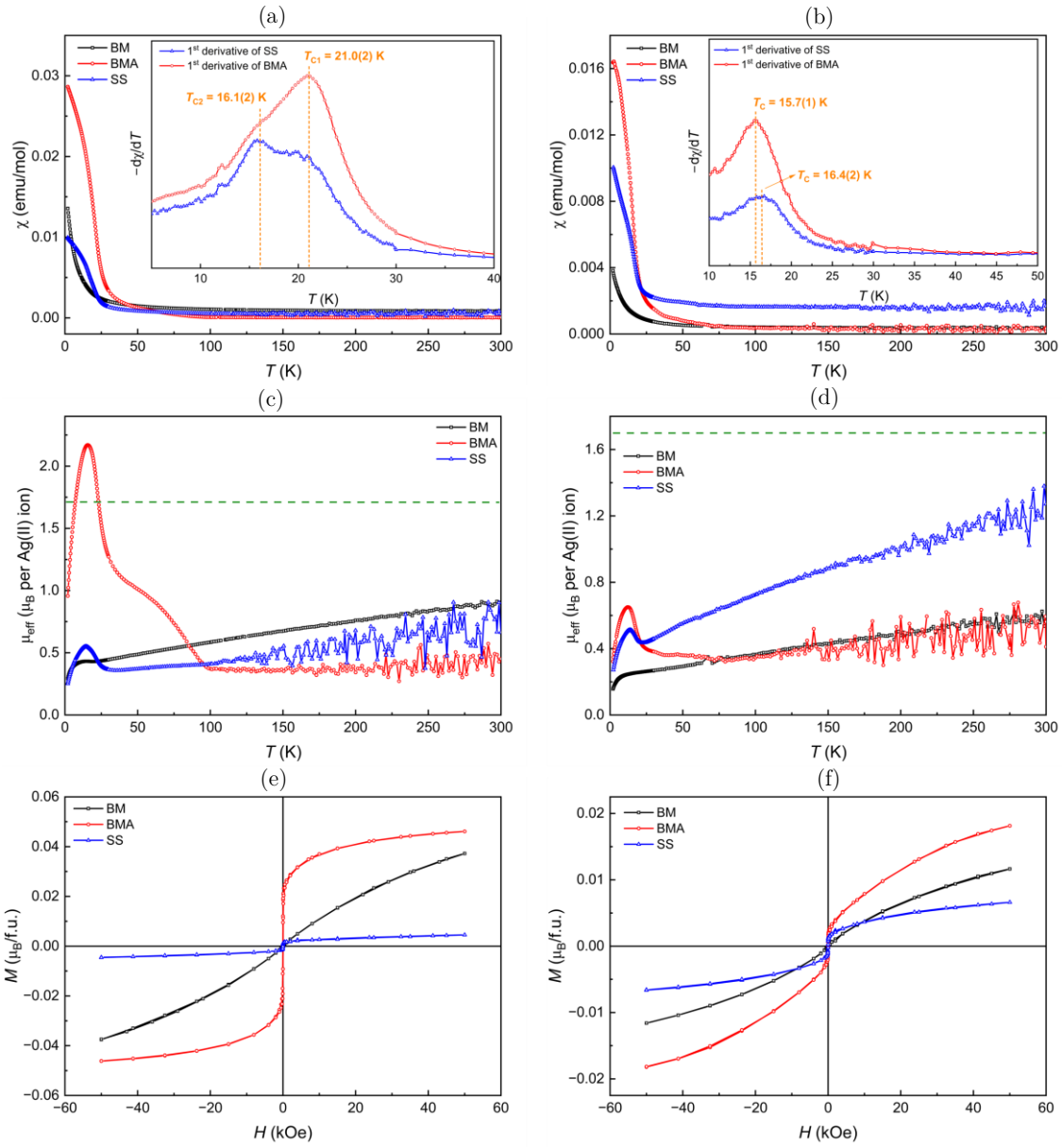


Figure 28: ZFC magnetic susceptibility, $\chi(T)$, measured in an applied field of 1 kOe for $RbAgF_3$ (a) and $CsAgF_3$ (b). Insets: temperature derivatives, $-\mathrm{d}\chi/\mathrm{d}T$, plotted versus T. Temperature dependence of the effective magnetic moment, $\mu_{\mathrm{eff}}(T)$, derived from the data in (a, b) for $RbAgF_3$ (c) and $CsAgF_3$ (d). Field-dependent magnetization, $M(H)$, at 2 K for $RbAgF_3$ (e) and $CsAgF_3$ (f).

In all samples, the effective magnetic moment at room temperature is significantly below the theoretical value expected for an $S = 1/2$ Ag^{2+} cation and decreases with decreasing temperature, indicative of prevailing antiferromagnetic interactions within the measured range (Figure 28c and Figure 28d). Magnetisation curves for the ball-milled samples show paramagnetic behaviour (Figure 28e and Figure 28f), whereas the annealed and solid-state samples contain ferromagnetic impurities, evidenced by magnetisation saturation at higher magnetic fields and the presence of ferromagnetic hysteresis. Across all samples, the saturation magnetisation remains below the theoretical value of 1 μ_B/f.u. expected for an $S = 1/2$ Ag^{2+} cation, reinforcing the dominance of antiferromagnetic interactions.

These magnetic measurements corroborate the PXRD and Raman analyses, confirming the presence of ferromagnetic impurities in annealed and solid-state synthesised samples. This indicates that ball-milling effectively suppresses the formation of magnetic secondary phases that typically form during high-temperature treatment. Given the extremely large and negative predicted superexchange constant J_{1D} for $CsAgF_3$ (−160 meV [20]) the predominantly antiferromagnetic interactions observed in the magnetic susceptibility data from 300 K down to 2 K, the BM sample was selected for NPD analysis for determination of magnetic structure. The NPD patterns were collected at 2 K and 70 K. The Rietveld refinement of the 2 K data (Figure 29a) reveals peaks (marked with dark stars) not accounted for in the model, suggesting possible magnetic ordering at 2 K. However, these peaks are also present at 70 K (Figure 29b). Since their intensity remains unchanged between 2 K and 70 K, they are more likely associated with an impurity phase or indicate that $CsAgF_3$ undergoes a structural phase transition between 70 K and room temperature. This hypothesis could be readily tested in future work by performing temperature-dependent PXRD measurements on this compound.

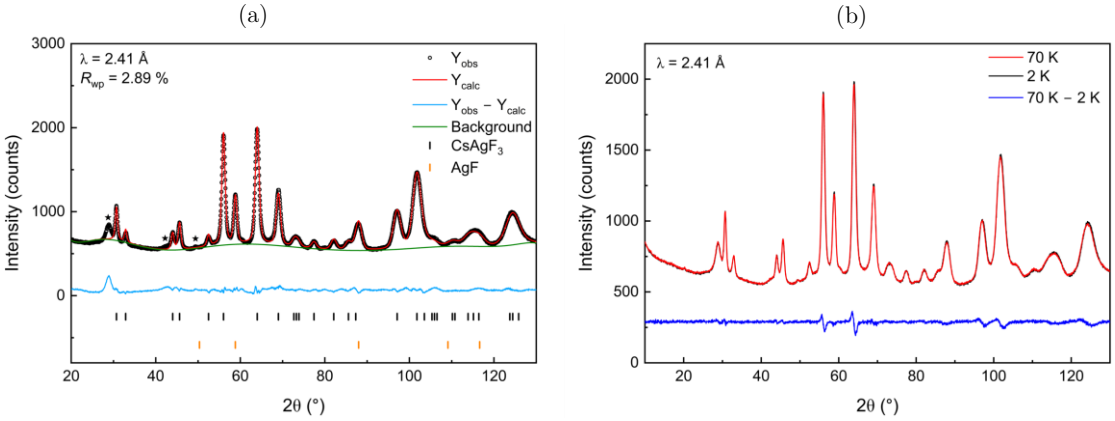


Figure 29: (a) Rietveld refinement of the 2K NPD data obtained on the ball-milled $CsAgF_3$ sample. Black star symbols represent unidentified peaks. (b) NPD data obtained on the ball-milled $CsAgF_3$ sample measured at 2 and 70 K with the difference plot.

In conclusion, the synthesis and characterisation of $RbAgF_3$ and $CsAgF_3$ reveal that ball-milling offer significant advantages over conventional solid-state synthesis as both compounds were successfully prepared through ball-milling, producing light-brown polycrystalline samples with diamagnetic AgF as the only secondary phase. PXRD and Raman analyses demonstrate that the ball-milled samples are not only synthesised more rapidly. i.e., within six hours compared to over two days for solid-state synthesis, but also achieve a higher degree of phase purity. When BM samples are soft annealed to improve crystallinity, additional unidentified peaks appear, suggesting the formation of minor impurities that could arise from thermal decomposition or phase transitions during heating. Magnetic susceptibility measurements provide further insights into the phase purity and magnetism of these samples. The BM samples for both $RbAgF_3$ and $CsAgF_3$ showed no signs of magnetic ordering, suggesting the absence of magnetic impurities, whereas the BMA and SS samples exhibited weak ferromagnetic transitions, most likely due to small amounts of ferromagnetic secondary phases like Rb_2AgF_4 and Cs_2AgF_4. The room-temperature effective magnetic moments are below the theoretical value for $S = 1/2$ Ag^{2+} ions and decrease with temperature, indicating predominantly antiferromagnetic interactions within the samples, which agrees well with the literature. The presence of hysteresis for BMA and SS samples in the magnetisation measurements confirm that the BMA and SS samples exhibit ferromagnetic impurities. Given the higher purity and shorter

synthesis times achieved by ball-milling, this method stands out as an efficient approach for preparing $RbAgF_3$ and $CsAgF_3$.

3.2.1.2 $KAgF_3$

Brown polycrystalline powders of $KAgF_3$ were synthesised with four different synthesis procedures, which are listed in Table 13.

Table 13: Synthesis conditions for the preparation of $KAgF_3$ samples with four different synthesis procedures.

Synthesis method	Synthesis conditions
Ball-milling (BM)	KF : AgF_2 = 1:1.1, t = 3 h, milling cycle = 15 min, ν = 30 Hz, BRR ≈ 40
Ball-milling with additional annealing step (BMA-200 and BMA-300)	T = 200 °C, t = 24 h (BMA-200) T = 300 °C, t = 5 days (BMA-300)
Solid-state synthesis (SS)	T = 300 °C, t = 10 days

The laboratory PXRD data measured at 100 K and 293 K provide valuable insights into the synthesis and structural properties of the $KAgF_3$ samples. In all cases, the successful synthesis of the $KAgF_3$ phase is confirmed as all Bragg reflections associated with the *Pnma* $KAgF_3$ phase are present in all samples (Figure 30a). Although the powder patterns of all samples appear largely similar, small differences are observed. In particular, the BM sample exhibits the broadest diffraction peaks, indicating a small crystallite size and the strain induced during the milling process. Remarkably, there are no significant differences between the diffractograms of the BM and BMA-200 samples measured at 100 K and 293 K, indicating that there is no phase transition from the low-temperature *Pnma* to the high-temperature *Pcma* polymorph as described in the literature [90]. In contrast, the BMA-300 and SS samples show clear differences between the low temperature and high temperature PXRD data. These differences are most likely related to small structural variations manifested as changes in the unit cell parameters and not to the *Pnma–Pcma* phase transition, as peaks corresponding to the *Pnma* polymorph are observed at both temperatures. Qualitative phase analysis of the PXRD data revealed that AgF is the main impurity in all samples. However, in the BMA-300 and the SS sample, additional unidentified peaks are observed that could not be assigned to any known compound in the PDF database. Interestingly, the BM and BMA-200 samples show less AgF impurity compared to the BMA-300 and SS samples, indicating that ball-milling leads to purer samples than the solid-state synthesis method.

Given that the Raman spectrum of $KAgF_3$ is well-explained in the literature, Raman spectroscopy was employed in this study as a complementary method to PXRD for structural characterisation. Firstly, the Raman spectrum of the SS sample was compared with the results of Koteras *et al.* [94] who had also used the solid-state synthesis method. The spectra show a high degree of similarity, indicating a successful synthesis of this phase in both studies. However, a detailed comparison of the peak positions suggests that most of the peaks in our SS sample are slightly shifted to higher frequencies compared to those reported by Koteras *et al.* (Table 14). This shift could be due to calibration errors in their study or slight variations in chemical composition or crystal structure.

Examination of the Raman spectra for all four samples (Figure 30b), although the overall spectral features are similar, the milling process induces subtle changes in specific Raman-active modes—a phenomenon also reported in the literature for ball-milled ZnO [95]. In the BM sample, the B_{2g} mode at 112 cm^{-1}, which is associated with vibrations within the potassium sublattice [94], shows reduced intensity and increased peak broadening. Conversely, the B_{1g} mode at 139 cm^{-1}, which is associated with vibrations of the $[AgF_2]$ layers, and a weak peak at 191 cm^{-1}, which was observed in the SS sample, are absent in the spectrum of the BM sample. Moreover, the B_{2g} mode at 208 cm^{-1} in the BM sample, which represents the in-plane bending of the $[AgF_2]$ layers, shifts to 216 cm^{-1} in the SS sample, accompanied by increased spectral broadening and peak asymmetry.

The most remarkable differences occur in the 450–500 cm^{-1} region. In the BM sample, the most intense peak at 497 cm^{-1}, which has not been assigned in the literature, shows a left shoulder around 467 cm^{-1}, which corresponds to the B_{2g} symmetry stretching of the $[AgF_6]^{4-}$ octahedra. After annealing at 200 °C, this shoulder becomes more pronounced (BMA-200), and further annealing at 300 °C results in the peak at 466 cm^{-1} exceeding the intensity of the peak at 495 cm^{-1} (BMA-300). In the SS sample, the peak at 466 cm^{-1} is the most intense, while the peak at 495 cm^{-1} decreases further. These observations indicate that ball milling causes structural changes and defects. Annealing gradually reduces these defects and increases crystallinity, positioning the ball-milled and annealed samples as intermediate phases between the ball-milled and solid-state synthesised samples.

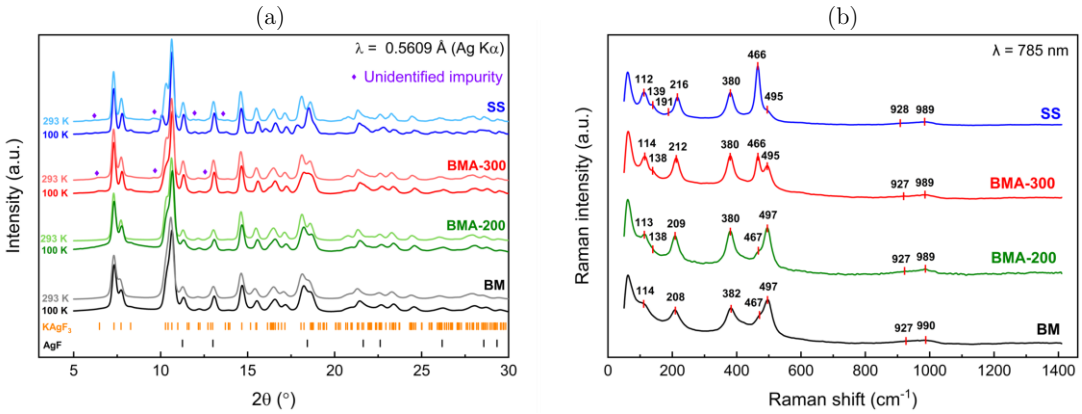


Figure 30: (a) Laboratory PXRD data of BM, BMA-200, BMA-300 and SS $KAgF_3$ samples measured at 100 K and at 293 K. (b) Room temperature Raman spectra of BM, BMA-200, BMA-300 and SS $KAgF_3$ samples.

Table 14: Comparison of peak positions in the Raman spectrum of solid-state synthesised $KAgF_3$ prepared in this study versus from the study of Koteras *et al.* [94].

Peak position (cm^{-1})		**Difference (cm^{-1})**	**Symmetry**	**Assignment**
Our data	***Koteras et al.*** [94]			
112	101	11	B_{2g}	Lattice (in plane K)
139	126	13	B_{1g}	$[AgF_2]$ plane buckling
191	/	/	/	/
216	196	20	B_{2g}	$[AgF_2]$ in plane bending
380	359	21	A_g	$[AgF_2]$ in plane stretching
466	444	22	B_{2g}	$[AgF_6]$ octahedra stretching
495	/	/	/	/
928	899	29		Impurity?
989	949	40		Impurity?

Previous studies have reported that $KAgF_3$ undergoes a phase transition from the low-temperature *Pnma* polymorph to the high-temperature *Pcma* polymorph at about 230 K [90]. However, our room-temperature PXRD data include peaks characteristic for the *Pnma* space group. To investigate this discrepancy, high-resolution synchrotron PXRD data were obtained for the ball-milled sample. The room temperature synchrotron PXRD data of the ball-milled sample was used for the Rietveld refinement analysis, considering both *Pnma* and *Pcma* space groups (Figure 31).

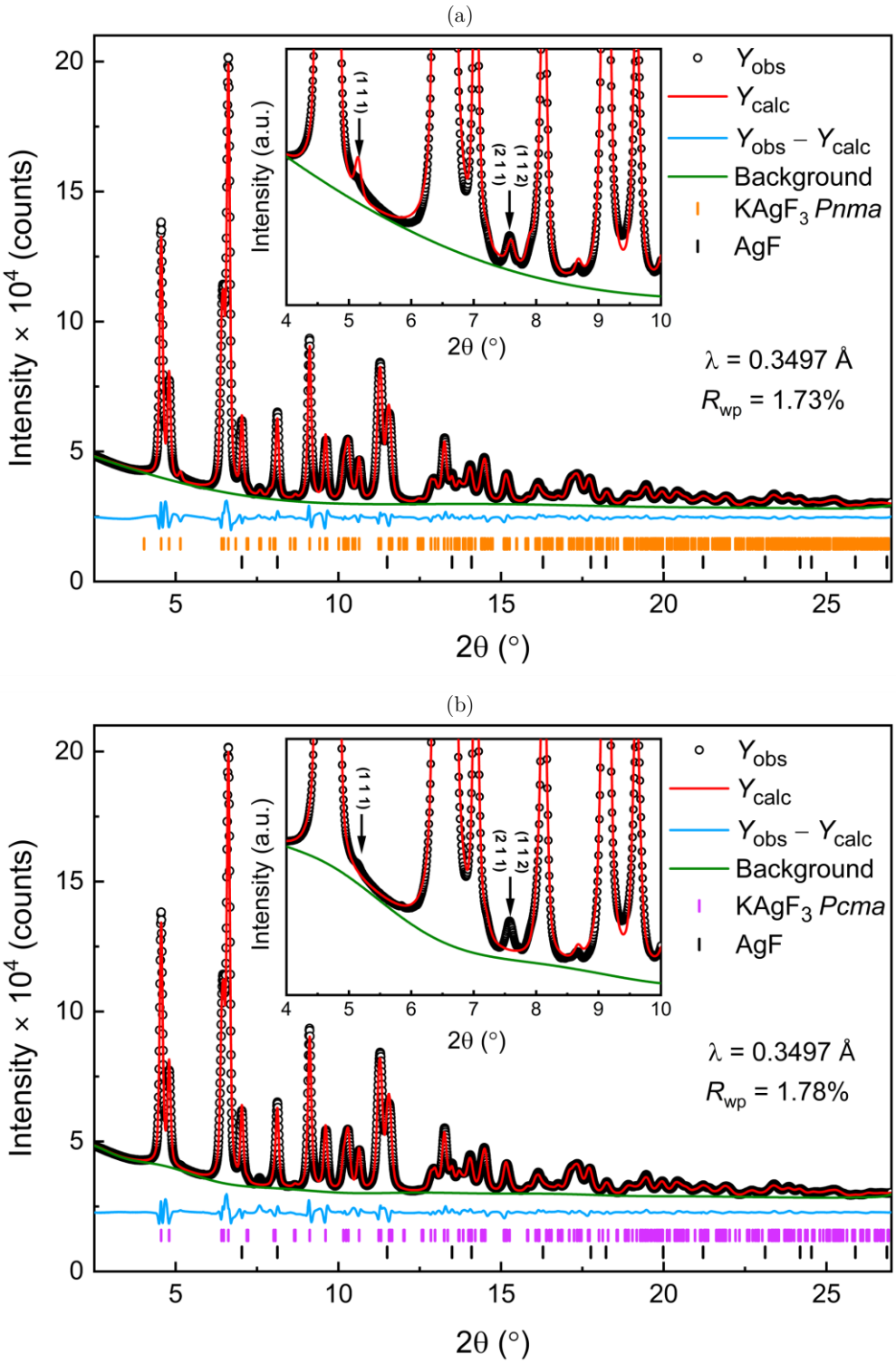


Figure 31: (a) Rietveld refinement analysis of the room-temperature synchrotron data of the BM $KAgF_3$ sample using the *Pnma* space group. Inset shows the (111), (211) and (112) reflections of the *Pnma* space group, which are absent in the *Pcma* structural model. Wt.% ($KAgF_3$) = 90.8(4)°% and wt.% (AgF) = 9.2(1) %. (b) Rietveld refinement analysis of the room-temperature synchrotron PXRD data measured on the BM $KAgF_3$ using *Pcma* space group. Inset shows weak reflections which were not accounted in the refinement and belong to the *Pnma* space group. Wt.% ($KAgF_3$) = 91.2(2) % and wt.% (AgF) = 8.8(1) %.

The Rietveld refinement yielded nearly identical weighted profile *R*-factors: R_{wp} = 1.73% for *Pnma* and R_{wp} = 1.78% for *Pcma*. As can be seen in Figure 31a and Figure 31b, the Rietveld refinement fits show weak peaks at the lower two theta angles corresponding to the (111), (211) and (112) reflections of the *Pnma* polymorph. These peaks were not accounted for in the structural model of the *Pcma* space group. These results indicate that $KAgF_3$ crystallises in the *Pnma* space group at room temperature, in contrast to previous studies that detected the *Pcma* space group above 230 K [90].

The presence of the (111) reflection of the *Pnma* polymorph at room temperature in the synchrotron PXRD data of ball-milled $KAgF_3$ prompted a comprehensive temperature-dependent PXRD study. The main goal was to elucidate the changes in the diffraction pattern with increasing temperature, with particular attention to the disappearance of the (111) reflection associated with the *Pnma* space group. By tracking the evolution of reflections as a function of temperature, the critical transition point could be accurately determined, allowing deeper insights into this structural transformation.

High-resolution synchrotron PXRD data were collected from 225 K to 500 K in 5 K steps, revealing intriguing observations (Figure 32). The (111) reflection associated with the *Pnma* space group gradually weakened and disappeared completely at 380 K. Simultaneously, a subtle feature at around 12.5° 2θ, resulting from the superposition of five reflections with a combined relative intensity of 0.7%, also disappeared at this temperature. In the two-theta region, where additional reflections corresponding to the *Pcma* polymorph should occur, only two peaks were observed with an overall relative intensity of 0.1 %. Decomposition of the sample started at 460 °C due to capillary cracking during the measurement, resulting in a visible colour change of the powder from brown to black.

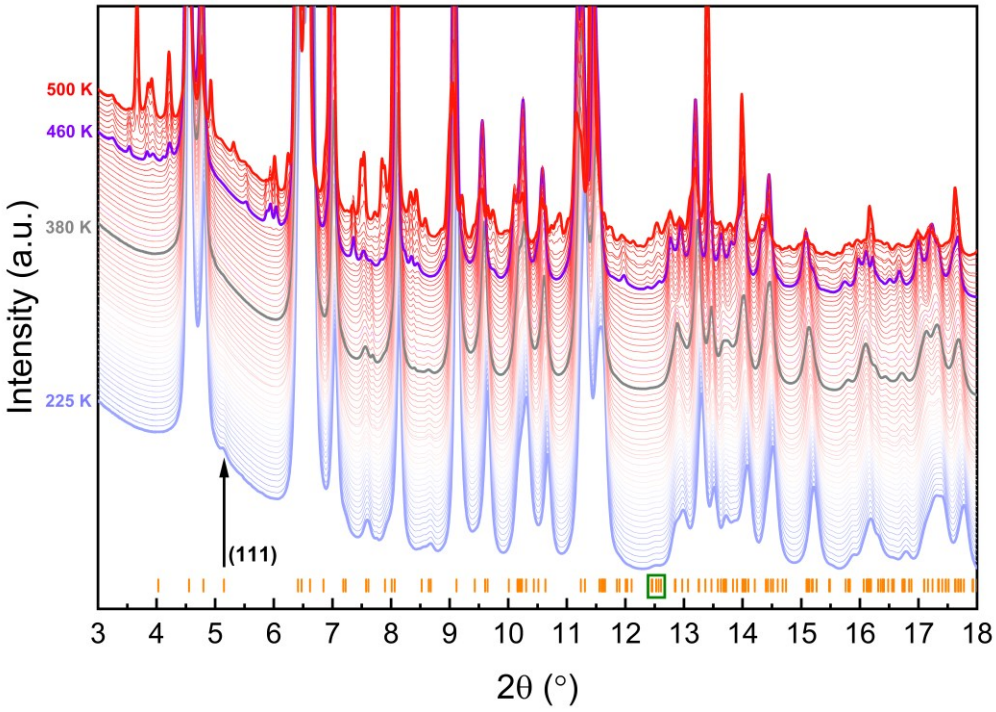


Figure 32: Temperature-dependent synchrotron PXRD data of the BM sample measured from 225 K to 500 K. The grey pattern at 380 K marks the temperature at which the (111) reflection of the *Pnma* polymorph and group of reflections in the green bracket at around 12.5° 2θ, which are also associated with the *Pnma* polymorph, disappear. The violet pattern at 460 °C corresponds to the temperature at which the sample decomposition begins.

These results indicate that the phase transition is gradual, suggesting that it may be a second-order type. The phase transition was found to occur between 380 and 420 K, which is significantly higher than the temperature reported in the literature (230 K [90]). The temperature dependence of the unit-cell parameters obtained from Rietveld refinement of high-resolution synchrotron PXRD data revealed intriguing findings. The *a* and *c* unit-cell parameters increased with temperature (Figure 33a) and showed a similar behaviour up to 380 K (grey line). Between 380 K and 420 K (green line), the *a* unit cell parameter started to decrease, while the *c* parameter increased abruptly. In contrast, the *b* unit cell parameter of the unit cell increased gradually over the entire measurement range. No abrupt changes in the volume of the unit cell were observed in the temperature range of 380–420 K (Figure 33b). Moreover, the R_{wp} values increased significantly above 380 K (Figure 33c), suggesting that *Pnma* may not be the correct space group for Rietveld refinement above this temperature. A discontinuous jump in all lattice parameters was also observed between 320 and 325 K. This feature is present in the unit cell volume of the AgF impurity, suggesting that it could be attributed to an error during measurement.

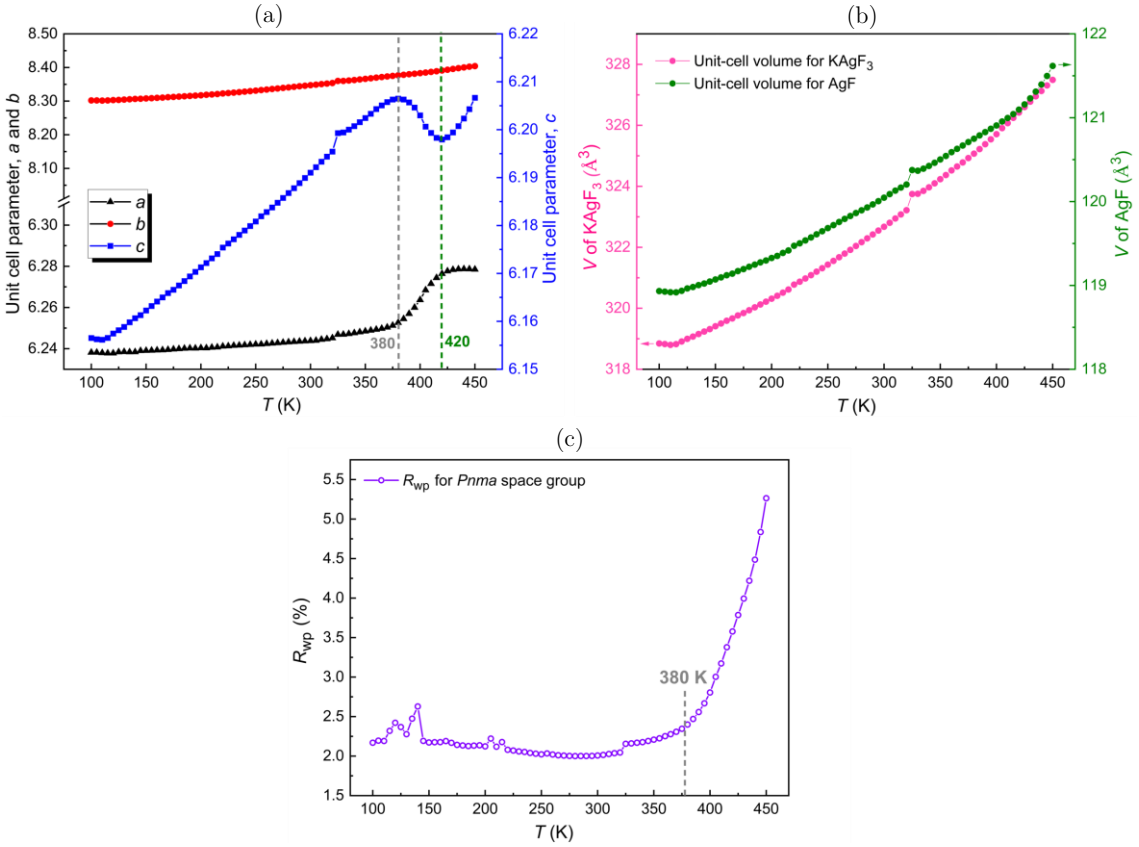


Figure 33: (a) Unit-cell parameters *a*, *b* and *c* for $KAgF_3$. (b) Unit-cell volumes of $KAgF_3$ and AgF. (c) Wight residual factors (R_{wp}) plotted as a function of temperature. All were obtained with the Rietveld refinement of the synchrotron PXRD data collected between 100–450 K on the BM sample.

The results obtained in this work differ from those in the literature [90], where the *a* unit-cell parameter decreases while the *b* and *c* parameters increase with temperature from 80 K to 225 K. From 225 to 235 K, the *a* and *b* parameters decrease (with the *b* parameter being halved), while the *c* parameter increases abruptly. An opposite trend occurs between 235 and 320 K, where the *a* and *b* parameters increase while the *c* parameter decreases slightly.

Rietveld refinement of laboratory PXRD data for $KAgF_3$ samples prepared by four different synthetic methods further confirms that the phase transition occurs above room temperature, which contradicts the literature reports [90]. At 100 K, all samples show R_{wp} factors that are approximately 0.7% lower when refined with the *Pnma* structural model (Table 15). The measurements at room temperature also favoured the *Pnma* space group, although the difference in R_{wp} factors was smaller. For the BMA-300 and BMA-200 samples, the difference in R_{wp} factors was similar to that at 100 K. In contrast, for the BM and SS samples, the R_{wp} factors for both polymorphs were almost identical. Despite only marginal differences in the weighted profile R_{wp} factors obtained from Rietveld refinements using different structural models, the refinement employing the *Pnma* space group consistently yielded slightly lower R_{wp} values. This systematic improvement in fit quality supports the assignment of the *Pnma* polymorph for $KAgF_3$ at 293 and at 100 K.

Table 15: Weighted profile *R*-factor, R_{wp}, (%) obtained with the Rietveld refinement of the laboratory PXRD data of $KAgF_3$ samples prepared with different methods. The data was measured at the 293 K and at 100 K and refined with each of the space groups.

***T* (K)**	**Space group**	**Sample code and obtained R_{wp} (%)**			
		BM	**BMA-200**	**BMA-300**	**SS**
100	*Pnma*	5.27	3.64	6.31	8.07
	Pcma	6.02	4.31	7.01	8.70
293	*Pnma*	5.23	4.44	4.88	4.92
	Pcma	5.34	5.19	5.42	5.16

For the selected $KAgF_3$ samples prepared in this study, a comprehensive 3D ED analysis was performed and their crystal structures were determined. This analysis was performed at two temperatures: 100 K, which is below the phase transition temperature from *Pnma* to *Pcma* reported in the literature, and at 273 K – above the reported transition temperature of 230 K [90]. The results show that there are macroscopic differences between the analysed samples. The BM sample (Figure 34a) showed typical characteristics of mechanochemically synthesised powders, such as an agglomerated nature, a small crystallite size and the presence of an amorphous phase. At 273 K, the data quality was not sufficient for a conclusive analysis due to the low completeness and low resolution. Therefore, the crystal structure could only be solved at 100 K. In contrast, the BMA sample (Figure 34b) and the sample prepared using the SS method (Figure 34c) exhibited higher crystallinity, which enabled successful structure determination at 100 K and at room temperature. Regardless of the synthesis method and the measurement temperature, the space group determined for all samples was *Pnma*.

The crystal structure of $KAgF_3$ determined by 3D ED from the sample prepared by the SS method is shown in Figure 35, while the crystallographic information is given in Table 16.

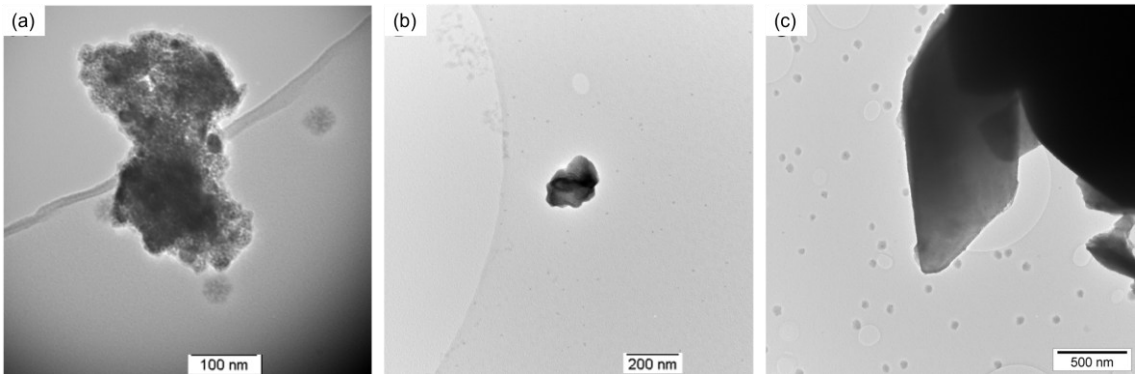


Figure 34: TEM images of $KAgF_3$ crystallites on which the 3D electron diffraction data was collected. Image (a) corresponds to the sample prepared with ball-milling, image (b) to the sample prepared with ball-milling and additional annealing step and image (c) to the sample prepared with the solid-state method.

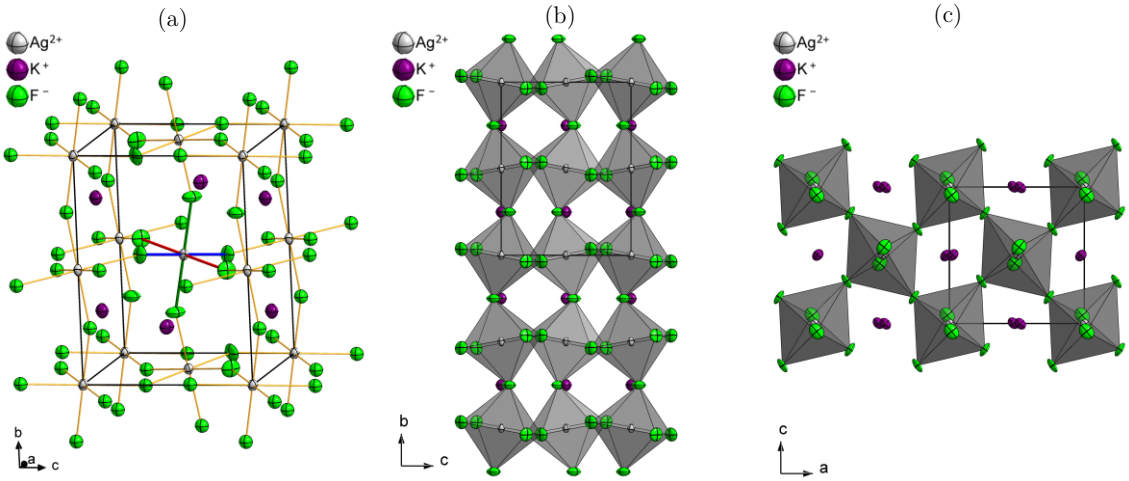


Figure 35: (a) Unit cell of the *Pnma* $KAgF_3$ obtained with 3D electron diffraction at 273 K. The red bond of $[AgF_6]^{4-}$ octahedra is the longest, while those in blue are the shortest. (b) Packing of $[AgF_6]^{4-}$ octahedra along *a* crystallographic direction. (c) Packing of $[AgF_6]^{4-}$ octahedra along *c* crystallographic direction. In all three figures, ellipsoids are presented with 50 % probability.

Table 16: Crystallographic information on the SS $KAgF_3$ sample obtained at 100 K.

SS $KAgF_3$ at 100 K	
Tilt angles α_{min}, α_{max}, $\Delta\alpha$ (deg.)	−59.34, 59.44, 0.30
Exposure time (ms)	504
Beam diameter (nm)	405
Camera length (mm)	1000
Crystal information	
Empirical formula	$KAgF_3$
Formula unit, Z	4
Space group	*Pnma*
a, b, c (Å)	6.3893(9), 8.2740(10), 6.0717(8)
$\alpha = \beta = \gamma$ (deg.)	90
V (Å^3)	320.98
Apparent mosaicity (deg.)	0.1224
Completeness (%)	88.9
Kinematical refinement All atoms treated isotropically	
Max. resolution, d^*_{max} (Å^{-1})	1.4
N_{obs}, N_{all}	388, 454
Parameters	12
R_{obs}, wR(obs)	20.57, 27.37
R(all), wR(all)	21.75, 28.27
Dynamical refinement All atoms treated anisotropically	
Max. resolution, d^*_{max} (Å^{-1})	1.4
N_{obs}, N_{all}	2090, 2367
Parameters	94
R_{obs}, wR(obs)	15.74, 17.90
R(all), wR(all)	16.24, 17.93

The coordination of the silver atom consists of six fluorine atoms with two short 2.044(6) Å, two medium 2.113(2) Å and two longer 2.444(5) Å Ag−F contacts forming an elongated $[AgF_6]^{4-}$ octahedron with a [2+2+2] coordination. These octahedra are forming infinite $[AgF]^+$ chains along *b*-crystallographic direction, leading to the 1D magnetic character of this compound. In contrast to the silver cation, the potassium cation is coordinated with eight fluorine anions and forms a distorted square antiprism. The K−F bond lengths range from 2.689(7) Å to 3.001(7) Å.

The $KAgF_3$ produced by the SS method was also measured above room temperature, as it was found that some reflections weaken with increasing temperature. In addition, the $KAgF_3$ sample prepared by the SS method provided high completeness (> 90 %) and high-resolution data (d^* > 2.0 Å^{-1}), which were higher than the samples prepared by other methods. The unit-cell parameters obtained on the same crystallite at different temperatures are compared in Table 17. The *a* unit cell parameter decreases, while the *b* and *c* parameters increase with temperature. A similar trend of change in lattice parameters as a function of temperature has been observed in the literature [90]. Moreover, the difference of the *a* and *c* parameters at 100 K and 273 K is about 0.2 Å, which is

significantly more than that of the $KAgF_3$ sample prepared by ball milling plus annealing, where the difference is within 0.05 Å.

Table 17: Comparison of the unit-cell parameters obtained by 3D ED of the SS synthesised $KAgF_3$ with the *Pnma* space group at different temperatures, as determined by 3D ED.

T (K)	a (Å)	b (Å)	c (Å)	V (Å^3)
100	6.3893(9)	8.2740(10)	6.0717(8)	320.98(8)
273	6.1891(5)	8.3154(7)	6.2547(6)	322.27(8)
306	6.1999(9)	8.3217(11)	6.2633(9)	323.15(8)
324	6.1913(7)	8.3237(10)	6.2711(8)	323.18(8)
80*	6.3815(9)	8.254(1)	6.0581(8)	319.1(1)

*Unit-cell parameters reported in the literature [90].

The magnetic properties of $KAgF_3$ are determined by the 1D character of the compound, with the $[AgF]^+$ chains propagating along the b crystallographic direction [20, 90, 96]. Due to the tilting of the $[AgF_6]^{4-}$ octahedra, the Ag–F–Ag angle is not 180° but 159.1(4)°, which weakens the strength of the antiferromagnetic superexchange interaction within the chain. The $[AgF]^+$ chains are also weakly ferromagnetically coupled by superexchange between the chains.

The magnetic susceptibility data obtained from the BM sample showed differences compared to the data obtained from the SS sample. For the BM sample a single magnetic transition was observed at 14.5(1) K, which is reflected in the first derivative of the magnetic susceptibility (Figure 36a). Interestingly, annealing the BM sample at 200 °C for 24 hours shifts the magnetic transition to about 42 K (Figure 36b), while the BMA-300 sample annealed at 300 °C for 5 days exhibited two magnetic transitions, occurring at 31.5(3) K and 60.8(2) K (Figure 36c). These mirror the temperatures observed in the SS sample (Figure 36d), where two strong transitions occurred at 64.4(1) K and at 32.6(3) K, both of which have been previously described in the literature [90]. However, the second magnetic transition was much weaker in the BMA-300 sample than in the sample prepared by the SS method. Furthermore, in contrast to the literature reports, magnetic susceptibility data in this study did not show a nearly constant decrease in magnetic susceptibility at higher temperatures in the 300–250 K range or a slight decrease in magnetic susceptibility in the 235–225 K temperature range, where the phase transition should occur according to literature reports [90].

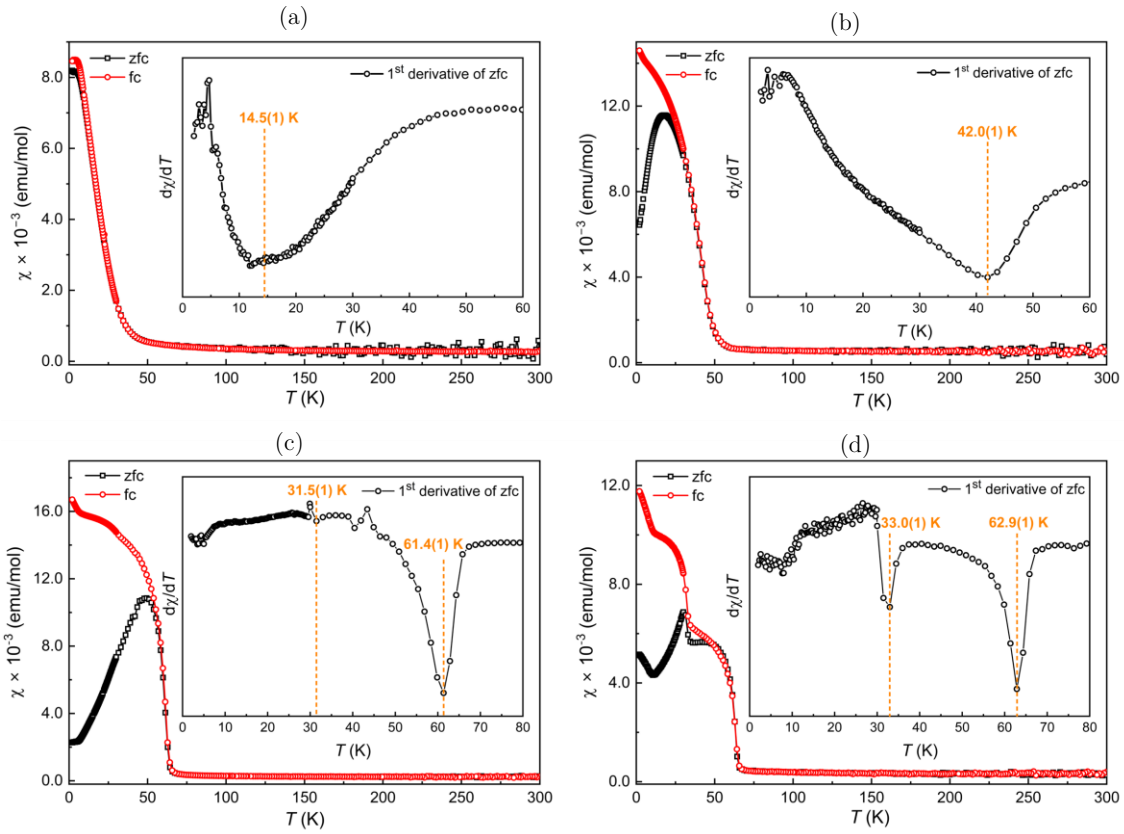


Figure 36: Temperature-dependent magnetic susceptibility measured at 1 kOe for (a) BM, (b) BMA-200, (c) BMA-300, and (d) SS samples of $KAgF_3$. Insets show the first derivative of the ZFC curves, highlighting the transition temperatures.

Our magnetic susceptibility data show that ball milling significantly affects the magnetism of $KAgF_3$. Compared to the SS sample, the transition temperature of the BM sample shifts to a lower temperature. This shift may result from non-stoichiometry or a slight variation in the crystal structure. In addition, the magnetic susceptibility curves show a very broad maximum, which is typical for partially frustrated magnetic interactions [97] or spin-glass materials [98]. Subsequent annealing of the BM sample leads to a change in the structural and microstructural properties. Annealing alleviates some of the defects and strain induced by ball milling, resulting in more crystalline structure. In $KAgF_3$, annealing restores or stabilises the original crystal structure and consequently the magnetic properties, as both transition temperatures are observed again. The prevailing antiferromagnetic interactions in $KAgF_3$ are also in good agreement with the measurements of effective magnetic moment (μ_{eff}) as a function of temperature, which is decreasing with decreasing temperature in all $KAgF_3$ samples (Figure 37).

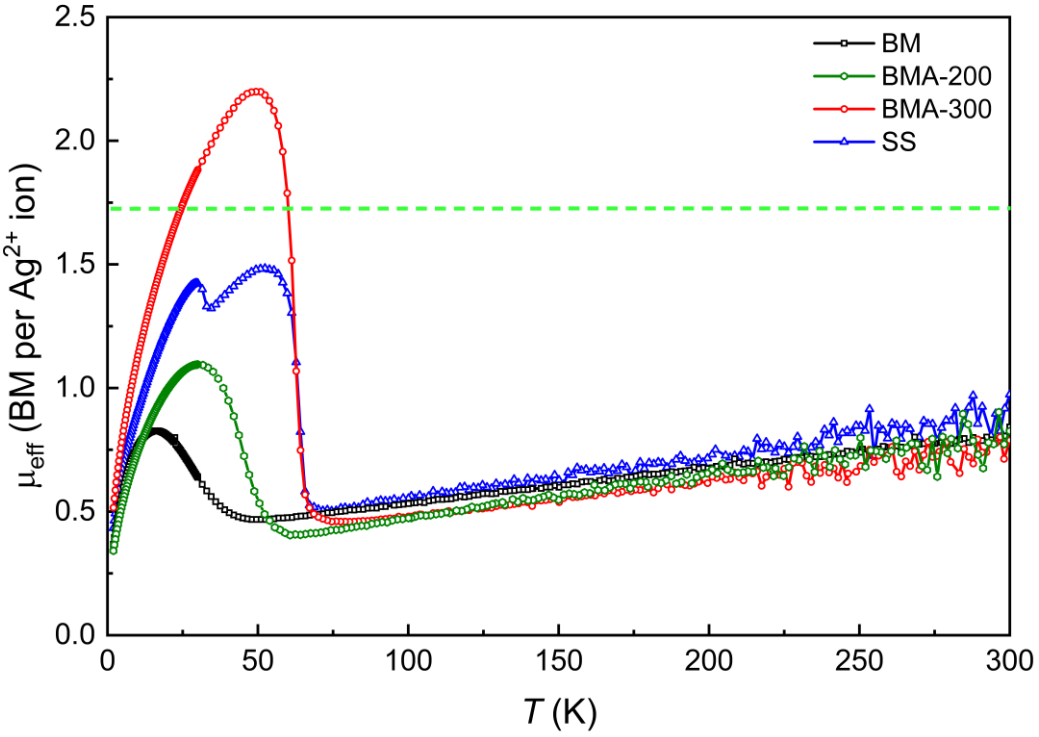


Figure 37: Effective magnetic moment measured as a function of temperature for the $KAgF_3$ samples synthesised in this study.

This behaviour indicates that antiferromagnetic interactions are predominant above the transition temperature.

The magnetic susceptibility data the $KAgF_3$ samples measured as a function of temperature under a magnetic field of 1 kOe is shown in Figure 38a. For comparison with previous work, the solid-state synthesised sample was also measured at 10 kOe, which corresponds to the conditions described in the literature. The magnetic susceptibility of our solid-state synthesised sample exhibits similar properties to those previously reported [90]. This indicates that the $KAgF_3$ phase prepared by our solid-state method is structurally and magnetically consistent with the sample obtained by the two-step synthesis approach documented in previous studies.

Interestingly, the magnetisation measurements indicate that hysteresis is present in all four samples (Figure 38b), which is the least pronounced for the BM sample. In contrast, the hysteresis is stronger for BMA-200, BMA-300 and SS samples, suggesting the presence of ferromagnetic impurities, which in in good agreement with the laboratory PXRD data, which suggested the presence of secondary phases in the BMA-300 and SS samples. In all cases, the measured magnetisation remains well below the expected saturation value of approximately 1 μ_B/f.u. for $S = 1/2$ Ag^{2+} cation, consistent with predominantly antiferromagnetic interactions. The magnetisation of the SS sample does attain saturation at high magnetic fields at about 0.005 μ_B/f.u., while the BM, BMA-200 and BMA-300 magnetisations do not get saturated even at the field of 50 kOe, suggesting that the largest amount of ferromagnetic impurities are present in the SS sample.

Since the structure of solid-state synthesised $KAgF_3$ has already been characterised using NPD in the previous literature reports [91], NPD measurements were performed on the ball-milled sample of $KAgF_3$. The NPD data were collected at three key temperatures:

2 K, 40 K, and 70 K, corresponding to temperatures above, below, and between the reported magnetic transitions.

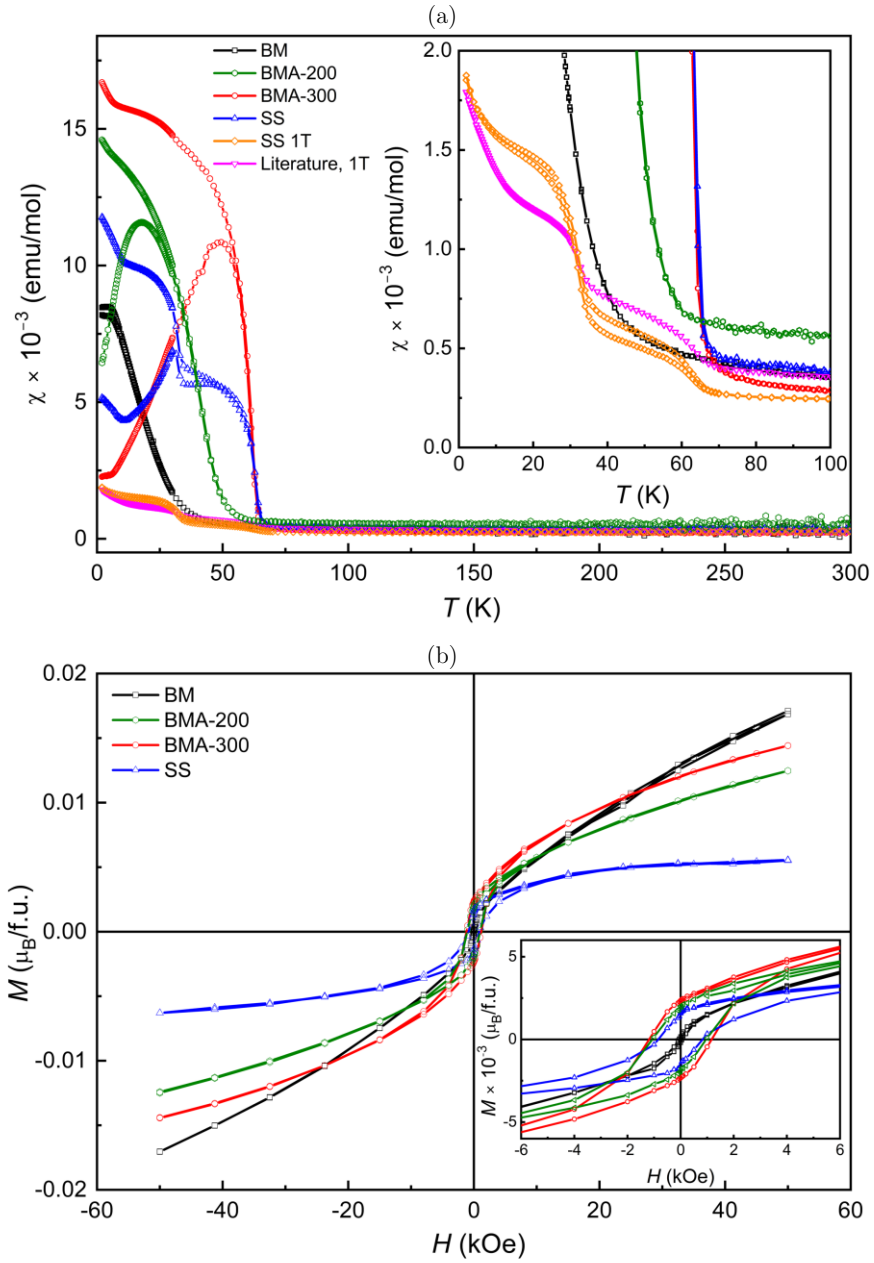


Figure 38: (a) Magnetic susceptibility measured as a function of temperature for BM, BMA-200, BMA-300 and SS samples. For comparison, the susceptibility reported in the literature [90] is also shown. (b) Magnetisation measured as a function of magnetic field at the temperature of 2 K for BM, BMA-200, BMA-300 and SS samples.

The NPD data collected at 70 K were used in the Rietveld refinement to assess the structural model. The refinement produced a good fit, and key reflections specific to the *Pnma* space group, such as the (1 1 1) peak near 36° 2θ, were clearly present. This provides further confirmation that the structure adopts the *Pnma* rather than *Pcma* space group (Figure 39a). In the 2-70 K difference plot shown in the Figure 39b, a weak feature was observed at approximately 16.6° 2θ, closely resembling a similar feature reported in the

literature for the solid-state synthesised $KAgF_3$ at 16.9° 2θ [91]. In prior studies [91], this feature was attributed to an *A*-type magnetic ordering, where ferromagnetic layers in the *a* and *c* directions are antiferromagnetically coupled along the *b*-axis. The similarity of these observations suggests that despite the different synthesis routes, the magnetic structure of $KAgF_3$ remains largely consistent across both ball-milled and solid-state preparations.

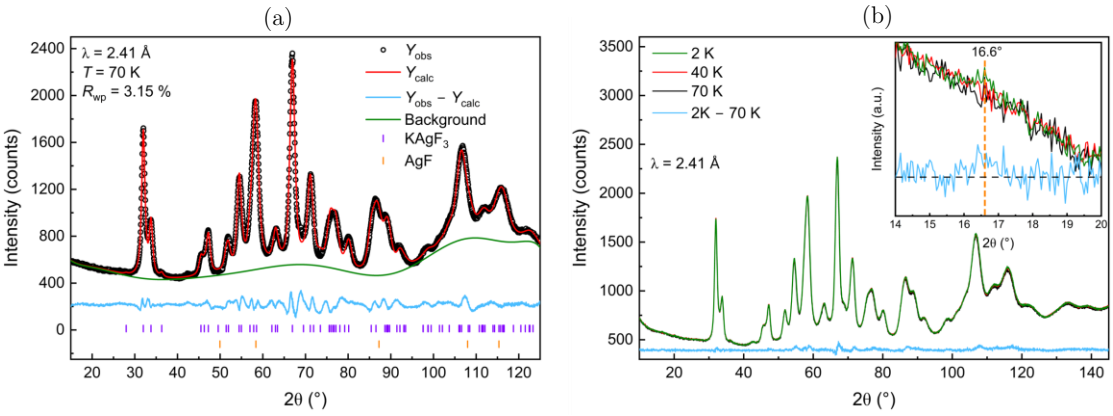


Figure 39: (a) Rietveld refinement of the NPD data collected at 70 K using the *Pnma* space group. Wt.% ($KAgF_3$) = 92.3(1) %; wt.% (AgF) = 7.7(1) %. (b) Comparison of the 2 K, 40 K and 70 K NPD data. The inset shows weak peak at about 16.6° 2θ.

In summary, the structural analysis of $KAgF_3$ using PXRD and Raman spectroscopy reveals a successful synthesis of the *Pnma* phase across all samples, although synthesis methods significantly influence crystallinity and impurity levels. Ball-milling results in smaller crystallite sizes and induced strain, as evidenced by broadened diffraction peaks and altered Raman modes, which gradually diminish with annealing, leading to samples that bridge characteristics between ball-milled and solid-state synthesised samples. Notably, AgF secondary phases are present in all samples, though less so in the BM and BMA-200 samples, indicating that ball-milling process results in a purer product compared to the thermal solid-state method.

The temperature-dependent synchrotron PXRD study challenges previous reports of a phase transition from *Pnma* to *Pcma* around 230 K. Instead, PXRD results show that $KAgF_3$ retains the *Pnma* space group at room temperature, with gradual–rather than abrupt–changes in the diffraction pattern, suggesting a higher and more gradual phase transition near 380–420 K. Synchrotron data reveal nuanced temperature-dependent shifts in unit-cell parameters, with the absence of abrupt volume changes, reinforcing the possibility of a second-order phase transition. 3D ED analysis across different synthesis methods and temperatures consistently identifies the *Pnma* space group, irrespective of the synthetic route or temperature. However, the synthesis method influences the crystallite quality, with the solid-state method yielding highly crystalline samples suitable for room-temperature analysis, while the BM sample exhibits low crystallinity and an amorphous phase. The unit-cell parameters show expected temperature-dependent changes, in line with the literature. Magnetic measurements reflect distinct effects of synthesis on the magnetic properties of $KAgF_3$, emphasising the role of structural defects and microstructural variations. The BM sample exhibits a single magnetic transition at a lower temperature (14.5 K), which shifts higher (42 K) with annealing at 200 °C, while the SS sample and BMA sample at 300 °C both show two magnetic transitions associated with strong antiferromagnetic interactions. Our magnetic measurements also revealed that all

$KAgF_3$ samples exhibit hysteresis in their magnetisation curves, which could be intrinsic property of $KAgF_3$ or signalling the presence of ferromagnetic impurities. Magnetisation of the SS sample reaches saturation at high magnetic fields, which indicates that this sample exhibits the largest amount of ferromagnetic impurities. Lastly, the NPD study was performed on the BM sample. While the magnetic structure could not be solved due to the low intensity of the magnetic peaks, the *Pnma* space group was confirmed at low temperatures and part of the magnetic response is matching previous findings on the sample prepared with the solid-state method.

3.2.1.3 $NaAgF_3$

The $NAgF_3$ phase was targeted with ball-milling of a stoichiometric mixture of commercially available AgF_2 and NaF precursors, as well as subsequent annealing of the ball-milled sample. The successful synthesis conditions are listed in Table 18.

PXRD analysis of the ball-milled sample revealed that all starting reagents reacted, as no peaks associated with NaF or AgF_2 were present in the diffractogram (Figure 40). Nevertheless, the resulting pattern could not be matched to any known phases from the PDF-4+ database, suggesting the formation of a novel phase.

Table 18: Synthesis conditions for the $NaAgF_3$ samples.

Synthesis method	**Synthesis conditions**
Ball-milling (BM)	NaF : AgF_2 = 1:1.1, t = 3 h, milling cycle = 15 min, ν = 30 Hz, BRR ≈ 40
Ball-milling with additional annealing step (BMA-200)	T = 200 °C, t = 24 h
Ball-milling with additional annealing step (BMA-300)	T = 300 °C, t = 24 h

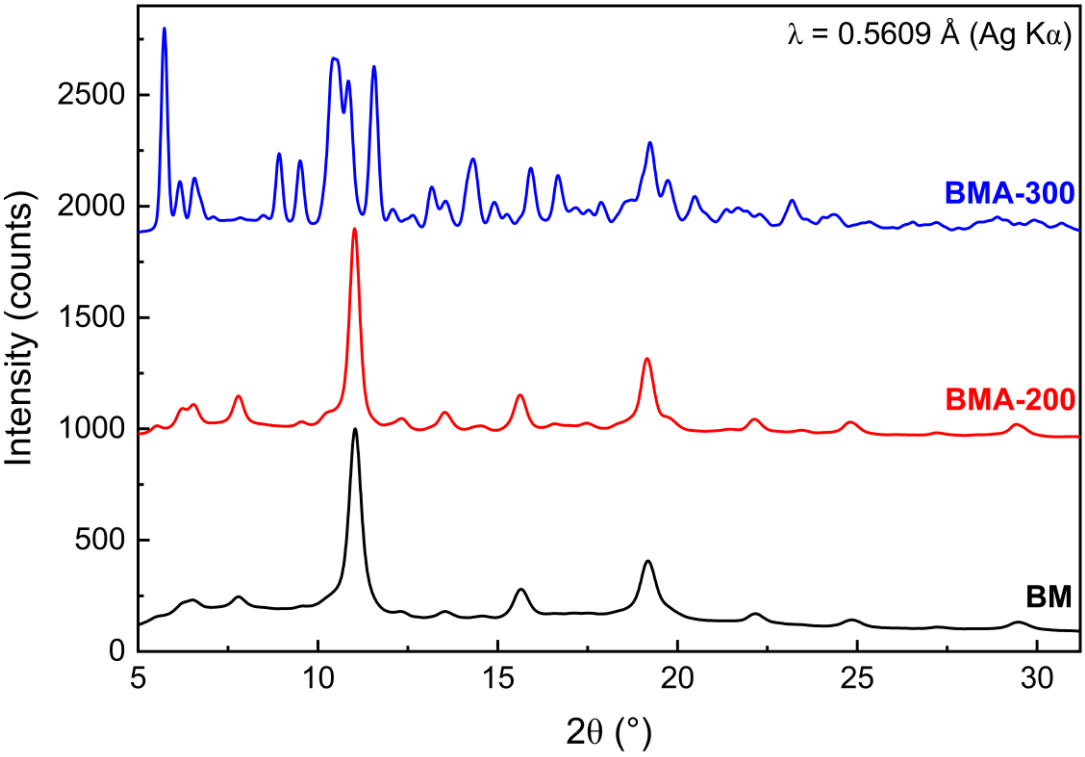


Figure 40: Comparison of the laboratory PXRD data measured at room temperature with Ag Kα wavelength of ball-milled and two annealed samples of $NaAgF_3$. The $NaAgF_3$ phase will be discussed later in this chapter.

It was observed that annealing the sample at 200 °C enhanced its crystallinity, evidenced by sharper diffraction peaks. However, the above-mentioned temperature did not lead to any phase transformation. On the other hand, annealing at 300 °C led to a more complex PXRD pattern, implying the emergence of new phase(s).

All three samples were analysed by 3D ED with the primary goal of determining the crystal structures of the present phase(s). However, the crystallinity of the BM sample was insufficient for structure determination. Although the BMA-200 sample showed improved crystallinity, it was still inadequate for reliable structure resolution. In contrast to the BM and BMA-200 samples, the BMA-300 sample exhibited significantly higher crystallinity, enabling the identification and structural determination of three distinct phases. Two of those phases were already known compounds (Na_2AgF_4 and Na_3WF_8), while the last one was the targeted $NaAgF_3$ phase. The presence of Na_3WF_8 is likely due to contamination from the tungsten carbide milling equipment, which introduced tungsten during the ball-milling process. This tungsten was subsequently incorporated into the sample, resulting in the formation of Na_3WF_8.

Since the investigated compound, $NaAgF_3$, crystallises in triclinic crystal system, datasets collected on four different crystallites were necessary in order to determine the crystal structure with high completeness. The TEM images in Figure 41 show the morphology of the $NaAgF_3$ sample after ball-milling and subsequent annealing (BMA-300). The particles exhibit irregular shapes and a broad size distribution, ranging from nanometres to micrometres. At lower magnification (Figure 41a, scale bar 1000 nm), larger agglomerates are visible, indicating that the mechanical forces during ball-milling promoted particle clustering. In contrast, the higher magnification images (Figure 41b–d, scale bar

200 nm) reveal more detailed views of smaller particles, many of which display angular shapes typical of crystalline structures. The variation in contrast within the images suggests differences in particle thickness or electron density, which may correspond to varying degrees of crystallinity or structural defects. These characteristics are consistent with the formation of $NaAgF_3$ crystallites. The effect of annealing likely enhanced crystallinity, while the particle agglomeration reflects the impact of the mechanical processing.

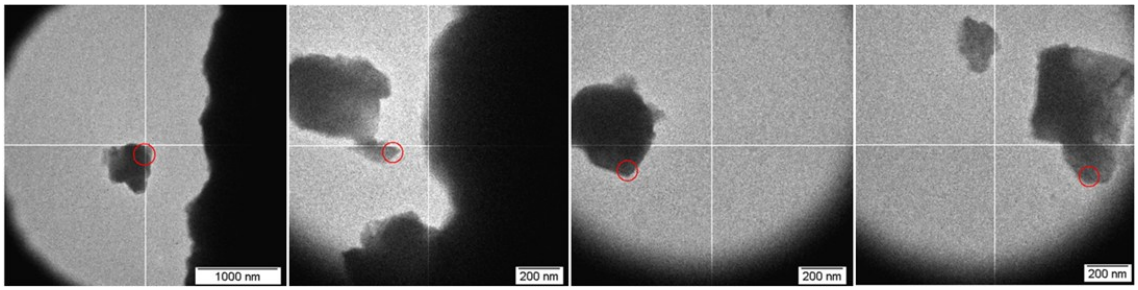


Figure 41: TEM images of four different $NaAgF_3$ crystallites observed in the BMA-300 sample on which the 3D electron diffraction data was collected. Red circles mark irradiated area.

The $NaAgF_3$ phase crystallises in the $P\bar{1}$ space group and its crystal structure is shown in Figure 42a. It can also be viewed as a distorted variant of the $CaIrO_3$ polytype. There are two unique divalent silver atoms in the crystal structure (Table 17) and they are both coordinated with six fluorine atoms with two short, two medium and two long Ag–F contacts, forming an elongated [2+2+2] octahedron. The Ag–F contacts for the Ag1 atom equal 2.014(7), 2.149(7) and 2.494(7) Å, while for the Ag2 atom Ag–F contacts equal 2.061(7), 2.097(7) and 2.861(6) Å. These $[AgF_6]^{4-}$ octahedra are stacking along c crystallographic direction (Figure 33b), forming infinite $[AgF]^{+}$ chains, similar to other members of the $M AgF_3$ series. Because the Ag–F–Ag angle (120.3(3)°) is closer to 90° rather than 180°, the superexchange interaction along the chains should be ferromagnetic. However, unlike in the $M AgF_3$ perovskites (M = K, Rb and Cs), where corner-sharing $[AgF_6]^{4-}$ octahedra propagate in all three directions, here the $[AgF_6]^{4-}$ octahedra share edges along the a-crystallographic direction and form a double fluorine bridges (Figure 33c). Therefore, the crystal structure of $NaAgF_3$ can be viewed as layers of the $[AgF_6]^{4-}$ octahedra, which are propagating in the ac plane and are separated with layers of sodium cations. This layered structure gives this compound a 2D character. Each Na^{+} cation is coordinated with seven fluorine atoms with Na–F bonds ranging from 2.258(9) to 2.599(8) Å. Crystallographic information and refinement details are listed in Table 19, positions of unique atoms in the crystal structure and refined atomic displacement parameters are listed in Table 20. Additionally, the BVS analysis in Table 21 confirms the +2 oxidation state of both silver cations.

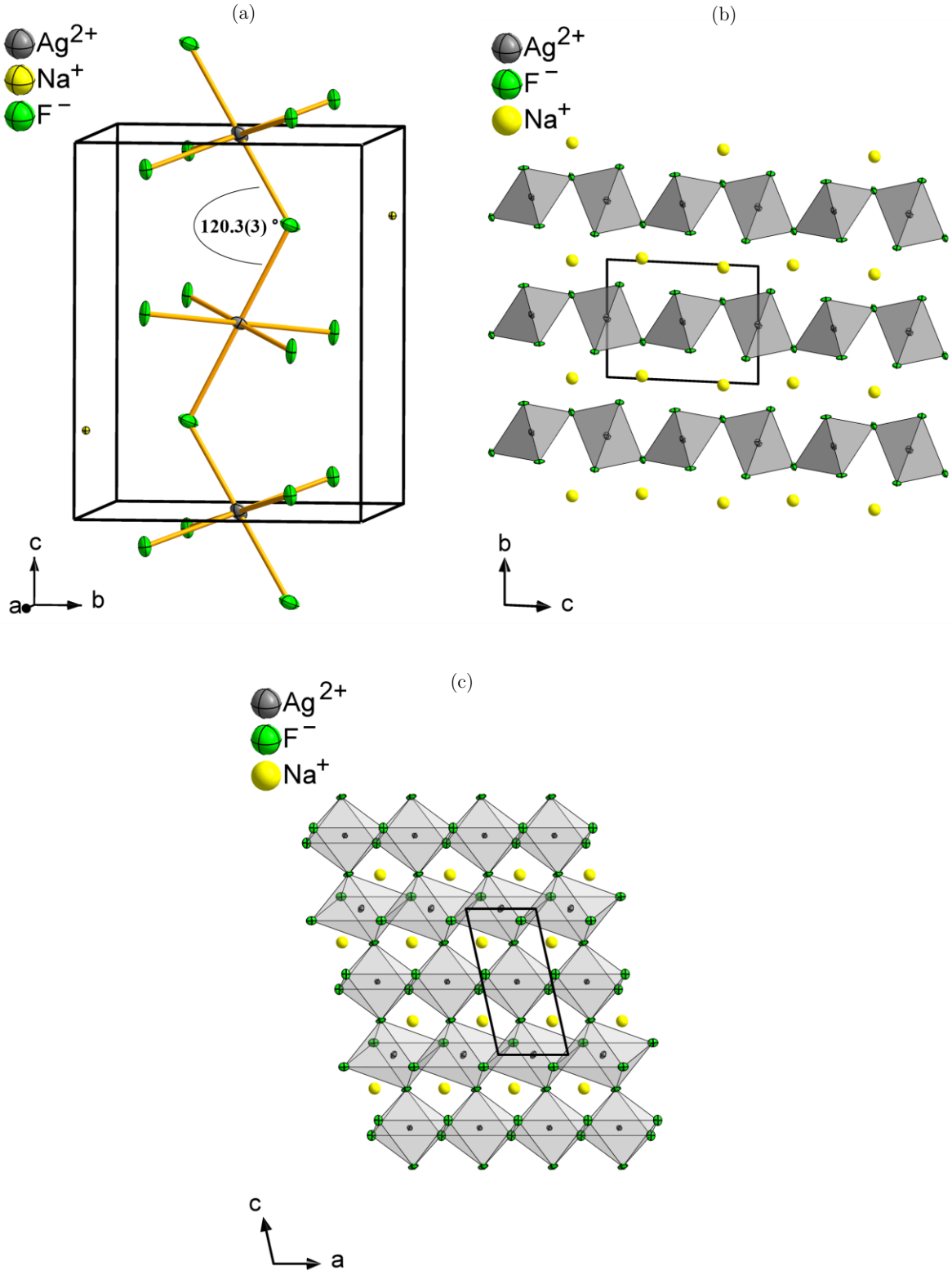


Figure 42: (a) Crystal structure of $NaAgF_3$ obtained with the 3D ED experiment. Ellipsoids are drawn with 50 % probability and Ag–F–Ag angle α = 120.3(3)°. (b) Packing along *a*- and (c) packing along *b*-crystallographic direction.

Table 19: Crystallographic information and refinement details on the $NaAgF_3$ sample obtained by the 3D ED experiment.

$NaAgF_3$		
Tilt information	Crystal label	α_{min}, α_{max}, $\Delta\alpha$ (deg.)
	A	-49.97, 59.85, 0.30
	B	-49.77, 49.40, 0.30
	C	-49.98, 50.02, 0.30
	D	-49.91, 49.63, 0.30
Exposure time (ms)	405, 405, 405, 405	
Beam diameter (nm)	200, 75, 75, 75	
Camera length (mm)	1000	
Crystal information		
Empirical formula	$NaAgF_3$	
Formula unit, Z	2	
Space group	$P\bar{1}$	
a, b, c (Å)	3.455(2), 5.622(2), 7.365(2)	
α, β, γ (deg.)	91.27(3), 102.33(3), 95.90(3)	
V (Å^3)	138.88(10)	
Apparent mosaicities (deg.)	0.0736, 0.1273, 0.1663, 0.1020	
Completeness (%)	98	
Kinematical refinement All atoms treated isotropically		
$\sin(\theta_{max})/\lambda$ (Å^{-1})	1.00	
N_{obs}, N_{all}	2096, 2286	
Parameters	19	
R_{obs}, wR(obs)	28.18, 34.45	
R(all), wR(all)	29.35, 35.06	
Dynamical refinement All atoms treated anisotropically		
$\sin(\theta_{max})/\lambda$ (Å^{-1})	0.70	
N_{obs}, N_{all}	1571, 1728	
Parameters	155	
R_{obs}, wR(obs)	11.98, 14.16	
R(all), wR(all)	12.33, 14.19	

Table 20: Atomic parameters and thermal displacement parameters for atoms in $NaAgF_3$ obtained with the refinement of the 3D ED data.

Atom	***x***	***y***	***z***	U_{eq}
Ag1	0.5	0.5	0.5	0.0081(7)
Ag2	−0.5	0.5	1	0.0114(7)
Na1	0.1200(11)	−0.0232(9)	0.7693(6)	0.0021(8)
F1	0.0734(16)	0.2554(13)	0.5518(10)	0.0152(17)
F2	−0.2511(17)	0.2093(13)	0.9176(9)	0.0157(18)
F3	0.5733(17)	−0.3124(13)	0.7646(9)	0.0153(18)

Table 21: Interatomic distances and bond valence sum analysis [99] for silver atoms in $NaAgF_3$. The following bond valence parameters were employed: $b = 0.37$ Å; $R_0 = 1.79$ Å (Ag^{II}—F) [100].

Interatomic distances [Å]	
Ag1 – F1 (2x)	2.014(7)
Ag1 – F3 (2x)	2.149(7)
Ag1 – F1 (2x)	2.494(7)
Ag2 – F2 (2x)	2.061(7)
Ag2 – F3 (2x)	2.096(7)
Ag2 – F2 (2x)	2.861(6)
Bond valence sum	
Ag1	2.15
Ag2	1.95

Qualitative phase analysis of the laboratory PXRD data revealed that in addition to $NaAgF_3$, the sample also contained Na_2AgF_4 and Na_3WF_8. All three phases were used for the Rietveld refinement of the laboratory PXRD data (Figure 43), which indicate that the majority of the sample (70.2(2) wt.%) consists of the targeted $NaAgF_3$ phase. In addition, the analysis also suggests the presence of Na_2AgF_4 as the main secondary phase (22.6(3) wt.%), which comprises the majority of the remaining sample. Lastly, Na_3WF_8 was detected in smaller quantities, accounting for less than 10 wt.% of the overall composition. All three phases were also observed with 3D ED.

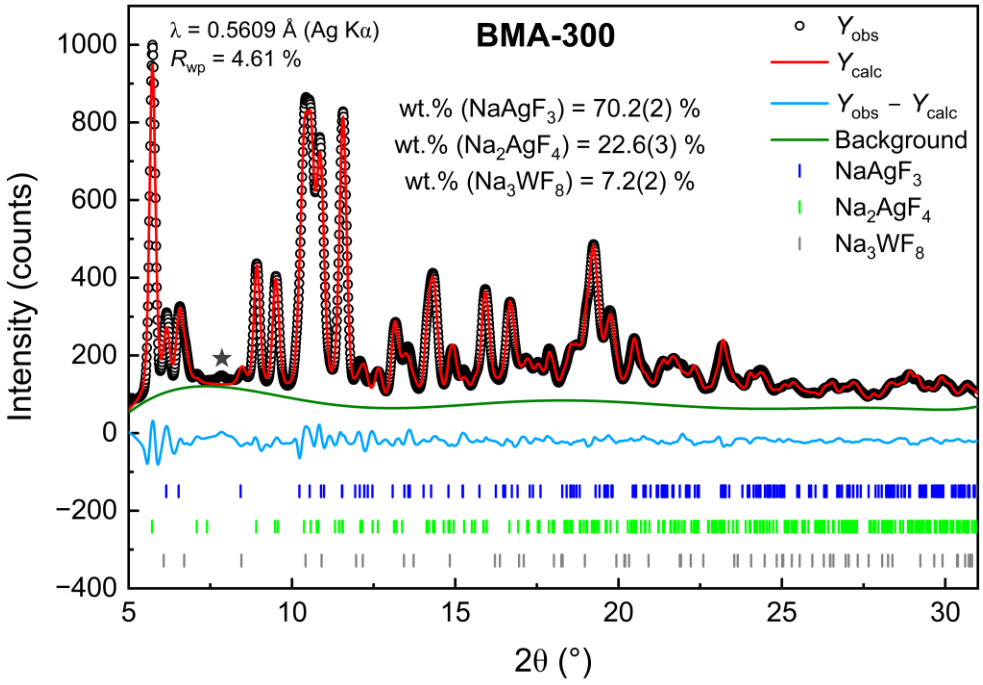


Figure 43: Three-phase Rietveld refinement of the laboratory PXRD data of the BMA-300 sample. Black star marks an unidentified peak.

Given that the Rietveld refinement confirms that the majority of the BMA-300 sample comprises the targeted $NaAgF_3$ phase (70 wt.%), magnetic susceptibility measurements were conducted to further investigate its magnetic properties. It is important to consider that, while the Na_3WF_8 is diamagnetic and does not contribute to the magnetic behaviour of the sample, the Na_2AgF_4 phase exhibits 1D antiferromagnetic properties with a T_N of 4.6 K [101]. This antiferromagnetic behaviour must be carefully accounted for when interpreting the magnetic data, as it could influence the overall magnetic response of the sample, potentially complicating the interpretation of the magnetic properties of $NaAgF_3$. The magnetic susceptibility data (Figure 44a) suggests that $NaAgF_3$ is paramagnetic down to around 20 K, temperature at which the susceptibility increases abruptly, suggesting a ferromagnetic transition. The transition temperature was determined from the maximum of $-\mathrm{d}\chi/\mathrm{d}T$ plot to be 18.8(1) K. The inverse of the magnetic susceptibility data (Figure 44b) was fitted with the Curie-Weiss law in the linear range from 100 to 300 K. The derived Curie constant of 0.48(2) emu · K/mol is in good agreement for the expected value for the $S = 1/2$ Ag^{2+} cations. However, large negative θ_{CW} of −161(5) K was determined, suggesting antiferromagnetic interactions are predominant. To get a deeper insight into the magnetism of the $NaAgF_3$, magnetisation was measured as a function of the magnetic field at the temperature of 2 K (Figure 44c), which is below the transition temperature. The hysteresis loop was observed, characterised with remnant magnetisation of 0.0019 μ_B/f.u. and coercive field of $H_c = 0.0866$ kOe. The magnetisation curve linearly increases with increasing magnetic field and does not attain saturation even at 50 kOe, reaching only about 0.08 μ_B/f.u, which is significantly below the expected saturation magnetisation of 1 μ_B/f.u for the $S = 1/2$ of the Ag^{2+} cation, which strongly suggests that the investigated compound exhibits antiferromagnetic behaviour. By comparing the measured remnant magnetisation to the full magnetic moment of 1 μ_B per Ag^{2+} cation, canting angle of approximately 0.1° was estimated. Additionally, since above the transition temperature

the effective magnetic moment decreases with decreasing temperature (Figure 44d), this further confirms antiferromagnetic nature of $NaAgF_3$.

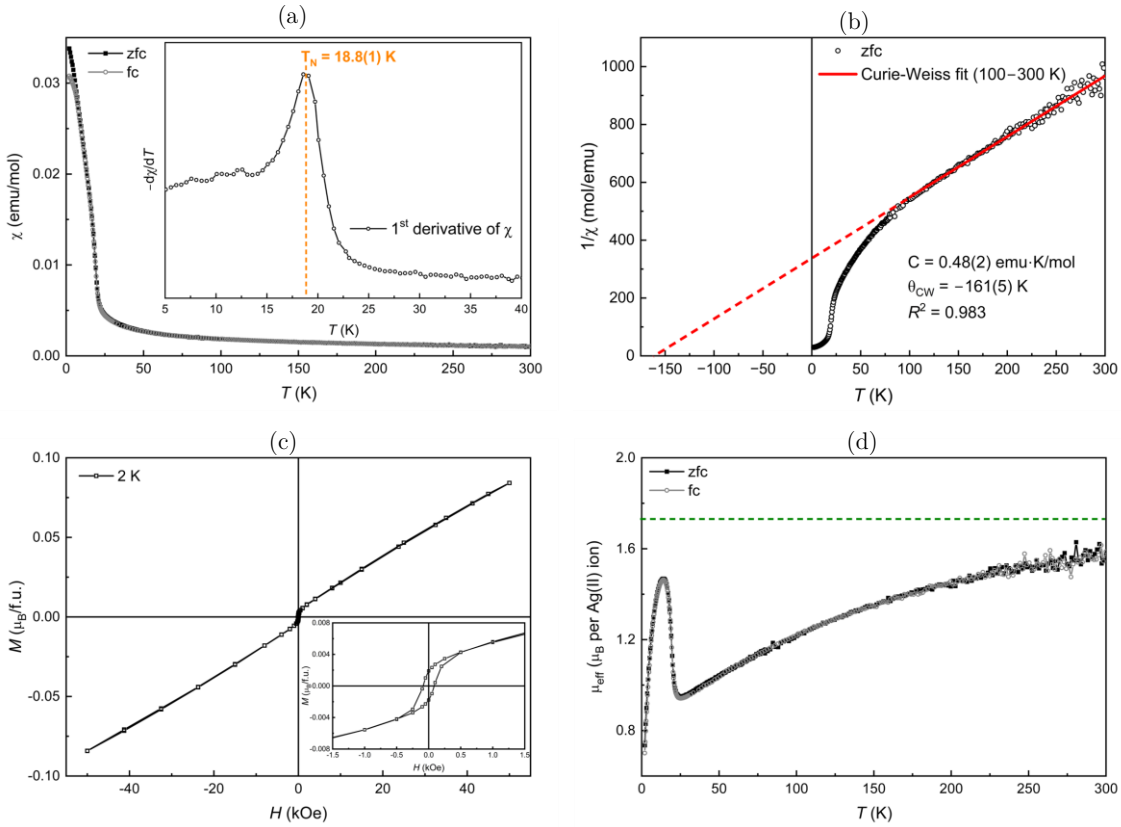


Figure 44: (a) Magnetic susceptibility curves (ZFC and FC) measured as a function of temperature in the field of 1 kOe. Inset shows the maximum of the first derivative of ZFC magnetic susceptibility, which corresponds to the transition temperature of $NaAgF_3$. (b) Curie-Weiss fit in the linear region between 100 and 300 K to the inverse of the ZFC magnetic susceptibility measured as a function of temperature in the field of 1 kOe. (c) Magnetisation of $NaAgF_3$ sample as a function of magnetic field measured at 2 K. A hysteresis shown in the inset indicates a ferromagnetic ground state. (d) Plot of the effective magnetic moment, μ_{eff}, as a function of temperature for FC and ZFC curves at 1 kOe.

Insights from the crystal structure of $NaAgF_3$ and the magnetic susceptibility data suggest that the investigated compound could be a 2D canted antiferromagnet. For the exact determination of the magnetic structure additional analysis, such as NPD measurements, should be considered.

In conclusion, $NaAgF_3$ was successfully synthesised by ball-milling of AgF_2 and NaF, followed by low-temperature or soft annealing. The resulting sample predominantly comprised the target phase, with Na_2AgF_4 and Na_3WF_8 identified as minor impurities. The crystal structure of $NaAgF_3$ was determined via 3D ED ($P\bar{1}$ space group), revealing a unique arrangement of $[AgF_6]$ octahedra that form layers in the *ac* plane. These layers are stacking along *b*-crystallographic direction and are separated by the layers of sodium cations. This structure is distinct from other members of the $MAgF_3$ series (M = K, Rb and Cs), which exhibit the layered perovskite structure. Consequently, the magnetic properties of $NaAgF_3$ are also unique compared to the rest of the series, as the magnetic measurements suggest that $NaAgF_3$ behaves as a 2D canted antiferromagnet.

3.2.2 M_2AgF_4 series (M = Na, K, Rb and Cs)

Since the cuprates — which become superconducting upon doping — display 2D antiferromagnetic properties, it is reasonable to search for analogous phases within the family of fluoridoargentates(II). Alkali metal fluoridoargentates(II) with the general formula M_2AgF_4 (M = alkali metal) exhibit a layered perovskite structure similar to that of La_2CuO_4, the parent compound of cuprate superconductors. Their structure stability can be assessed using the Goldschmidt tolerance factor. Cs_2AgF_4 and Rb_2AgF_4, which were first prepared in 1974 [22], both exhibit a layered perovskite structure, as the Goldschmidt tolerance factor is close to 1 (0.96 for Cs and 0.92 for Rb [3]). They crystallise in the *Bbcm* space group, with an antiferrodistortive arrangement of elongated $[AgF_6]^{4-}$ octahedra, which leads to weak ferromagnetic interlayer coupling. Cs_2AgF_4 exhibits 2D ferromagnetic properties with a T_C of 14.9 K [21] and an interlayer coupling constant J_{2D} of 3.8 meV. Similarly, Rb_2AgF_4 is a 2D ferromagnet with a T_C of 17.5 K and an interlayer J_{2D} coupling of 4.8 meV [36]. The size of the K^+ cation (1.51 Å for CN = 8) is smaller compared to Cs^+ (1.74 Å for CN = 8) and Rb^+ (1.61 Å for CN = 8), resulting in a tolerance factor < 0.9. Consequently, K_2AgF_4 exists in two polymorphs. The first, α-K_2AgF_4, was synthesised in 1971 by annealing a stoichiometric mixture of AgF_2 and KF at 480°C for 2 days [88]. This polymorph crystallises in the *Cmca* space group and exhibits a layered perovskite structure with a ferrodistortive arrangement of compressed $[AgF_6]^{4-}$ octahedra. It is characterised as a 2D ferromagnet with an ordering temperature of 13.4 K and a J_{2D} interlayer coupling of 3.4 meV [35]. In contrast, the β-K_2AgF_4 polymorph, which was prepared by solid-state reaction by annealing a stoichiometric mixture of AgF_2 and KF for 14 days at 300°C, adopts a post-perovskite structure and crystallises in the $P2_1/c$ space group [102]. It exhibits elongated, edge-sharing $[AgF_6]^{4-}$ octahedra that propagate along a crystallographic direction to form infinite double fluorine-bridged $[AgF_2]$ chains, giving the compound a 1D character. The precise magnetic characterisation of the β-K_2AgF_4 polymorph has been hampered by the presence of small amounts of ferromagnetic α-K_2AgF_4, but DFT calculations indicate that it exhibits extremely weak ferromagnetic coupling. The size of the Na^+ cation is even smaller, so it is expected to adopt a similar structure to β-K_2AgF_4. Indeed, Na_2AgF_4 crystallises in the $P2_1/c$ space group and exhibits a post-perovskite structure. A pure sample of Na_2AgF_4 was prepared in 2013 by a two-step synthesis method by thermal decomposition of $NaAgF_4$, a Ag(III)-based compound [101]. In contrast to β-K_2AgF_4 it is characterised as a 1D antiferromagnet with a J_{1D} of -0.6 meV, which is probably due to a strong through-space dipolar magnetic coupling resulting from an extremely short Ag^{2+}—Ag^{2+} separation.

The primary objective of this chapter was to synthesise M_2AgF_4 (M = Na, K, Rb and Cs) compounds in a phase-pure form, free from magnetic impurities, using ball-milling or a combination of ball-milling and soft annealing. Achieving this would allow a direct comparison of the quality of our samples with those reported in the literature, where the same compounds were typically prepared either through traditional solid-state methods or via a two-step synthesis involving the use of aHF. Additionally, another aim was to investigate the magnetic properties of the synthesised M_2AgF_4 compounds and compare the results with existing studies, providing a deeper understanding of how different preparation methods influence both the structural and magnetic characteristics of these materials.

3.2.2.1 Na_2AgF_4

In this study, two Na_2AgF_4 samples were prepared with synthesis conditions listed in the Table 22.

Table 22: Conditions for the synthesis of Na_2AgF_4 samples.

Synthesis method	Synthesis conditions
Ball-milling (BM)	NaF : AgF_2 = 2:1, t = 5 h, milling cycle = 15 min, ν = 30 Hz, BRR ≈ 13, d_{ball} = 10 mm
Ball-milling with annealing (BMA-300)	BM sample additionally annealed at T = 300 °C for t = 24 h

Laboratory PXRD data collected on BM and BMA-300 indicate that most of the starting materials, AgF_2 and NaF, were consumed during the reaction (Figure 45a). However, distinct differences between the diffraction patterns of the two samples can be observed. In the low 2θ region, the relative intensities of several peaks vary between the BM and BMA-300 samples. Additionally, the BM sample exhibits significantly broader diffraction peaks, a typical consequence of reduced crystallite size and the introduction of microstrain during ball-milling. In contrast, the diffraction peaks in the BMA-300 sample are sharper, which suggests crystallite growth and strain reduction during the annealing process.

The crystal structure of Na_2AgF_4 reported in reference [101] was used for the Rietveld refinement of the laboratory PXRD data. This compound crystallises in the monoclinic $P2_1/c$ space group with unit cell parameters a = 3.34160(5) Å, b = 10.4012(1) Å, and c = 6.07607(9) Å, and β = 65.971(1)°. In the structure, the Ag^{2+} cation is coordinated by six F^- atoms in a distinctive [2+2+2] coordination (Figure 45b). The nearly equivalent distances of the four shorter Ag–F bonds (2.081 Å and 2.061 Å) contrast with the two longer Ag–F bonds, which extend to 2.769 Å, leading to a noticeable axial elongation of the octahedral coordination environment. These edge-sharing octahedra are arranged along the a-crystallographic axis, forming double-fluorine-bridged [AgF_2] chains, imparting a pronounced 1D character to the compound's structure.

The Rietveld refinement of the BMA-300 sample, shown in Figure 45c, indicates that the majority of the sample consists of the targeted Na_2AgF_4 phase, with minor amounts of diamagnetic impurities, specifically unreacted NaF and AgF. Notably, when applying the same refinement model (three-phase fit: Na_2AgF_4, NaF, AgF) to the BM sample, the fit to the experimental data was poor, with R_{wp} values exceeding 10 %, which could not be reduced through typical refinement procedures. However, by introducing isovalent A-site mixing, where Ag^+ partially substitutes Na^+ cations due to their comparable ionic radii (Ag^+ = 1.15 Å and Na^+ = 1.02 Å, both for CN = 6), the fit improved. The refined composition $Na_{1.7}Ag^{I}_{0.3}Ag^{II}F_4$ resulted in an R_{wp} of around 6 %. However, even with this adjustment, the calculated pattern still showed large deviations from the experimental one.

Raman spectra of both samples reveal that, despite the structural differences observed in PXRD, the Raman-active modes of the two samples are quite similar (Figure 45d). Most of the Raman peaks are shifted by just 1–3 cm^{-1} between the BM and BMA-300 samples. The most pronounced shift was observed for the peaks, which were located at 369 cm^{-1} in the BMA-300 sample and at 375 cm^{-1} in the BM sample. The most intense peak at 447 cm^{-1} could be attributed to symmetric vibrations of $[AgF_4]^{2-}$ square subunits [102]. The

literature also reports five weaker Raman-active modes at 153, 222, 273, 330, and 370 cm^{-1}, though the origin of these vibrations was not determined [103]. The observed peak positions closely match those reported in the literature, indicating that the same phase was successfully synthesized.

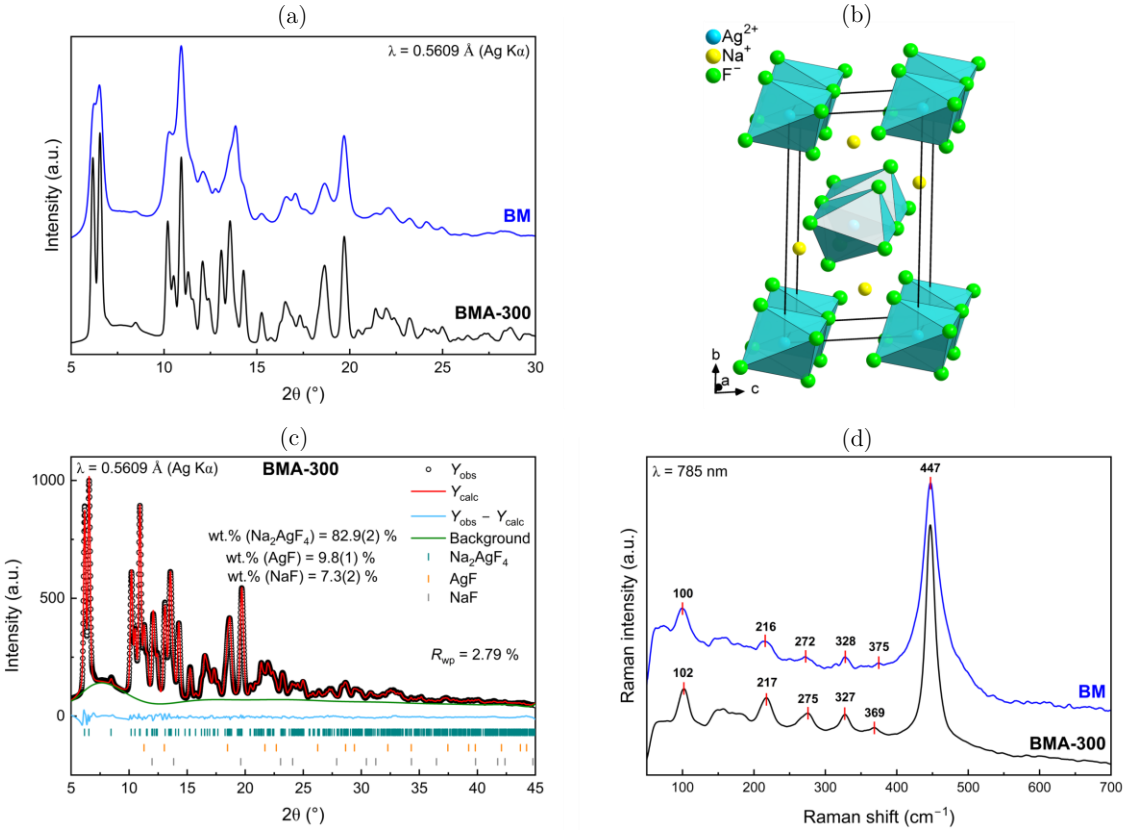


Figure 45: (a) Comparison of the laboratory PXRD data collected on BM and BMA-300 Na_2AgF_4 samples. (b) Unit cell of Na_2AgF_4. (c) Three-phase Rietveld refinement of the BMA-300 laboratory PXRD data. (d) Comparison of Raman spectra of BM and BMA-300 Na_2AgF_4 samples.

The PXRD analysis (Figure 45c) of the BMA-300 sample of Na_2AgF_4 indicates that it was successfully synthesised without any detectable magnetic secondary phases, confirming its phase-pure form. Structural analysis also suggested that the BM sample might exhibit a slightly different chemical composition. To further investigate these differences, magnetic characterisation was conducted on both samples to assess how their magnetic behaviour compares to the literature and to determine any variations in magnetic response.

Magnetic susceptibility measurements of the BM sample revealed paramagnetic behaviour down to 5 K (Figure 46a). However, a slight deviation from the Curie-Weiss law at lower temperatures hints at the onset of weak antiferromagnetic interactions. The Curie-Weiss fit produced a negative $\theta_{CW} = -5.0(5)$ K, which further confirmed antiferromagnetic coupling in the sample (Figure 46b). Since Na_2AgF_4 has already been characterised as a 1D antiferromagnet [101], the magnetic susceptibility data was fitted with a Bonner-Fisher fit for a uniform AFM spin 1/2 chain with an equation [16]:

$$\chi = \frac{\rho N_A \mu_B^2 g^2}{4 k_B T} + (1-\rho)\frac{N_A \mu_B^2 g^2}{k_B T}\frac{0.25 + 0.14995x + 0.30094x^2}{1 + 1.9862x + 0.68854x^2 + 6.0626x^3} + \chi_0 \quad (3.1)$$

where N_A is the Avogadro number, k_B is the Boltzmann constant, g is the g-factor, ρ is the molar ratio of $S = 1/2$ isolated magnetic moments and $x = |J|/(k_B T)$, where J is the superexchange constant. The resulting parameters obtained from the fit shown in the inset of the Figure 46a were reasonable but differed slightly from the literature, most notably the g-factor with the value of 1.844(2), lower than the reported value of 2.23. The large proportion of isolated magnetic moments (7.7(1) mol%) in the sample obscured the characteristic hill-like decrease in magnetic susceptibility, typical for 1D antiferromagnets. To address this, Bonner-Fisher function was plotted with previously obtained parameters, however without isolated moments ($\rho = 0$), with the main goal revealing how the magnetic susceptibility would behave in their absence. This model exhibited a maximum at 4.8(1) K, closely aligning with the literature-reported value of 4.6 K [101], further supporting the 1D antiferromagnetic nature of the BM Na_2AgF_4 sample.

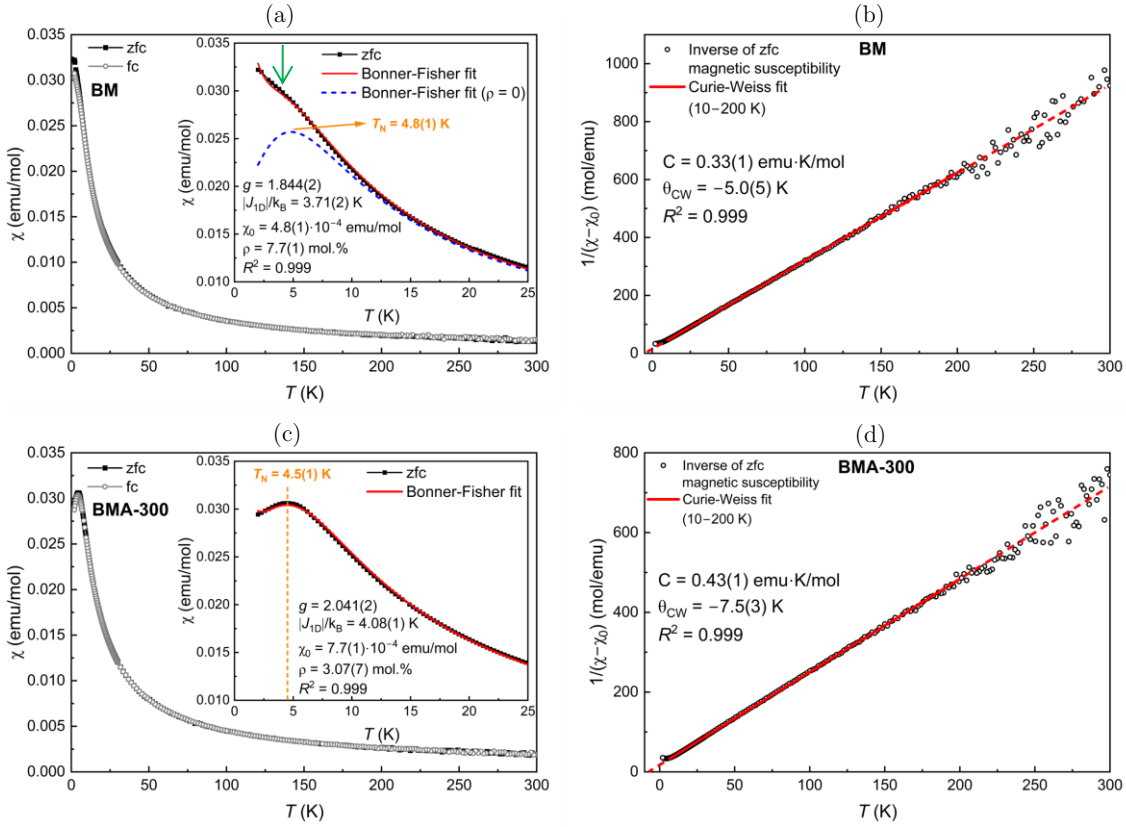


Figure 46: (a) Magnetic susceptibility measured as a function of temperature for BM Na_2AgF_4 sample. Inset shows two Bonner-Fisher fits in the 2-25 K region. (b) Curie-Weiss fit of the inverse of the ZFC magnetic susceptibility in the 10-200 K region of the BM Na_2AgF_4 sample. (c) Magnetic susceptibility measured as a function of temperature for BM-300 Na_2AgF_4 sample. Inset shows Bonner-Fisher fit in the 2–25 K region. (d) Curie-Weiss fit of the inverse of the ZFC magnetic susceptibility in the 10–200 K region of the BM Na_2AgF_4 sample.

The magnetic susceptibility data collected on the BMA-300 sample closely mirror data reported in the literature, with an antiferromagnetic transition observed with a maximum of magnetic susceptibility at the temperature of 4.5 K, closely matching the value of 4.6 K documented previously [101] (Figure 46c). The Curie-Weiss fit of this sample yielded a higher Curie constant compared to the BM sample, aligning more closely with the literature value of 0.48 emu · K/mol [101] (Figure 46d). However, a slightly more negative θ_{CW} of

−7.5(3) K was obtained, indicating slightly stronger antiferromagnetic interactions compared to the BM sample. The Bonner-Fisher fit, as displayed in the inset of Figure 46c, provided an excellent agreement with the experimental data. The obtained *g*-factor of 2.041(2), though lower than the literature value, further corroborates the sample's antiferromagnetic behaviour. In contrast to the BM sample, the BMA-300 exhibited fewer isolated magnetic moments (approximately 3 mol%), which had a minimal impact on the magnetic susceptibility. As a result, the antiferromagnetic transition was still clearly observed in the BMA-300 sample. The $|J|/k_B$ value was determined to be 4.08(1) K, corresponding to approximately −0.35 meV, suggesting that the 1D antiferromagnetic interactions within Na_2AgF_4 are relatively weak. This weak coupling is characteristic of low-dimensional antiferromagnetic systems, reinforcing structural and magnetic consistency with previously reported behaviour for Na_2AgF_4 [101].

The magnetic measurements of both the BM and BMA-300 samples reveal key distinctions in their behaviour. The BMA-300 sample exhibits a clear antiferromagnetic transition at 4.5 K, closely matching the expected value of 4.6 K from literature, indicating a possible 1D antiferromagnetic behaviour. On the other hand, the BM sample predominantly shows paramagnetic behaviour down to 5 K, with only a faint hint of a weak antiferromagnetic transition at lower temperatures (green arrow in Figure 46a). The BMA-300 sample also demonstrated stronger antiferromagnetic interactions, with a lower fraction of isolated spins, leading to a clearer magnetic response. In contrast, the BM sample's higher proportion of isolated moments obscured any clear magnetic ordering. These results suggest that the BMA-300 sample more closely reflects the expected magnetic properties of Na_2AgF_4, while the BM sample's deviation may be due to slight compositional differences impacting its magnetic structure.

In conclusion, Na_2AgF_4 was successfully synthesised through ball milling of AgF_2 and NaF, with subsequent annealing at 300 °C. PXRD analysis confirmed that the BMA-300 sample consisted predominantly of the target Na_2AgF_4 phase, with minor amounts of unreacted reagents (NaF and AgF). Rietveld refinement of the BMA-300 sample confirmed previously proposed monoclinic crystal structure in the $P2_1/c$ space group, where the silver(II) cation is coordinated by six fluorine atoms in octahedral arrangement, forming 1D chains along *a*-crystallographic direction. In contrast, the PXRD data of the BM sample indicated some lattice distortions and disorder, likely arising from partial substitution of Na^+ by Ag^+, suggesting that ball-milling alone was not sufficient for the synthesis of Na_2AgF_4. Raman spectroscopy of both samples revealed similar vibrational modes, indicating that both were composed of the same Na_2AgF_4 phase, despite differences in crystallinity and particle size. Magnetic measurements showed that the BMA-300 sample exhibits the expected 1D antiferromagnetic behaviour, with a transition temperature around 4.5 K, consistent with previous literature. In contrast, the BM sample exhibited primarily paramagnetic behaviour, with a weak hint of antiferromagnetic interactions at low temperatures.

3.2.2.2 β-K_2AgF_4

The compound K_2AgF_4 crystallises in two polymorphs, α and β, which can both be synthesised through annealing a stoichiometric mixture of KF and AgF_2 under different conditions. The α-K_2AgF_4 exhibits layered 2D structure of sheets of corner-sharing $[AgF_6]^{4-}$ octahedra in the *ac* plane (Figure 47a). In contrast, the β-K_2AgF_4 polymorph exhibits a quasi-1D structure of edge-sharing $[AgF_6]^{4-}$ octahedra, which form infinite double fluorine-bridged $[AgF_2]$ chains propagating along *a*-crystallographic direction, similar to Na_2AgF_4 (Figure 47b).

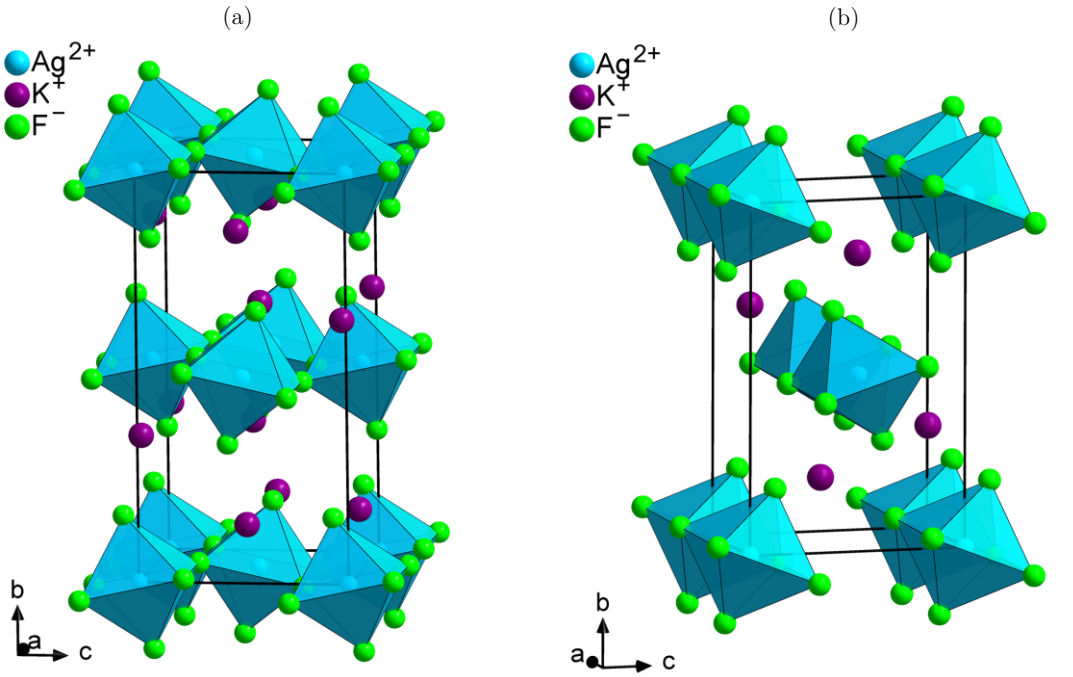


Figure 47: Crystal structure of (a) α-K_2AgF_4 and (b) β-K_2AgF_4.

Since the structural and magnetic properties of the alpha polymorph have already been thoroughly characterised, the primary focus was directed toward the beta phase. The key objective was to synthesise the beta polymorph in its pure form, free of magnetic impurities, to enable precise magnetic characterisation. Previous reports indicate that β-K_2AgF_4 was obtained with approximately 5 wt.% of the alpha phase, which interfered with magnetic measurements by introducing extraneous signal from the alpha form at low temperatures [102]. By optimising the synthesis method, it was aimed to eliminate this secondary phase and obtain a purer sample for accurate analysis of the intrinsic magnetic properties of the beta polymorph. Two samples β-K_2AgF_4 samples were prepared using the synthesis conditions listed in Table 23.

Table 23: Conditions used in this study for the synthesis of β-K_2AgF_4 samples.

Synthesis method	**Synthesis conditions**
Ball-milling (BM)	KF : AgF_2 = 2:1, t = 5 h, milling cycle = 15 min, ν = 30 Hz, BRR ≈ 13, d_{ball} = 10 mm
Ball-milling with annealing (BMA-300)	BM sample additionally annealed at T = 300 °C for t = 24 h

The phase analysis of the laboratory PXRD data collected on the BM sample revealed the presence of four phases: β-K_2AgF_4, α-K_2AgF_4, KF, and AgF. These phases were subsequently used for a quantitative analysis via Rietveld refinement of the laboratory PXRD data (Figure 48a). The analysis showed that approximately 75 wt.% of the sample

consisted of the targeted β-K_2AgF_4, with about 13 wt.% of α-K_2AgF_4 also present. Both of these phases contribute to the sample's magnetic properties. The rest of the sample (KF and AgF) was diamagnetic. In terms of magnetic purity, the sample quality was comparable to that reported in the literature [102].

To gain a deeper understanding of the synthesis of β-K_2AgF_4 via ball-milling, a time-dependent milling experiment was conducted (Figure 48b). The results suggest that the α-polymorph forms early in the process, indicating that it is the kinetic product of the reaction. As the milling continues, this phase gradually transforms into the more thermodynamically stable β-polymorph, closely mimicking the mechanisms observed in solid-state synthesis reported in the literature [102]. After approximately five hours of milling, the reaction reaches equilibrium since further milling does not affect sample's composition.

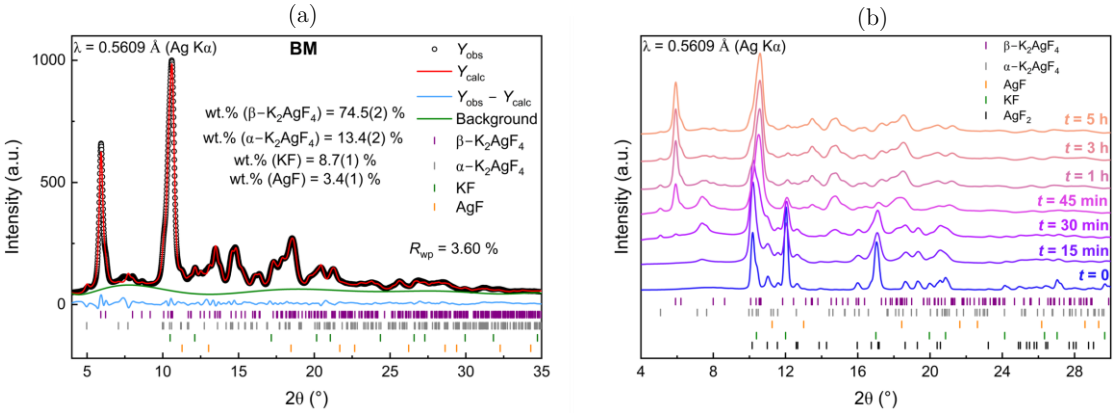


Figure 48: (a) Four-phase Rietveld refinement of the laboratory PXRD data collected on the BM K_2AgF_4 sample. (b) Laboratory PXRD data of time-dependent milling of K_2AgF_4.

The literature indicates that the β-K_2AgF_4 polymorph can be obtained by annealing the α-K_2AgF_4 phase at either 180 °C for 2 hours or 290 °C for 1 hour. Based on this, it was sought to transform the BM sample, containing the α-K_2AgF_4 polymorph, into the β-K_2AgF_4 polymorph through a more longer annealing process. The BM sample was annealed at 300 °C for 24 hours to ensure complete transformation. The results from laboratory PXRD data, as shown in Figure 49a, confirm the success of this transformation, as all peaks associated with the α-K_2AgF_4 polymorph disappeared after annealing.

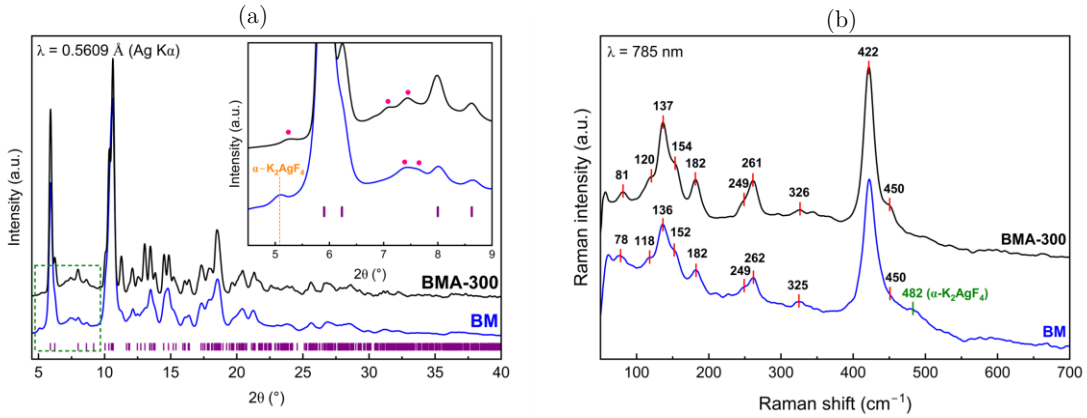


Figure 49: (a) Laboratory PXRD data for BM and BMA-300 β-K_2AgF_4 samples. Violet lines mark the Bragg reflections of β-K_2AgF_4, while pink full circles indicate an unidentified impurity. (b) Raman spectra of BM and BMA-300 β-K_2AgF_4 samples.

However, the annealing process also introduced additional peaks that could not be attributed to any known phases, suggesting the possible formation of a new phase or impurity. These findings are further supported by the comparison of Raman spectra for both BM and BMA-300 samples (Figure 49b). The peak at 482 cm^{-1}, which correspond to the α-K_2AgF_4 polymorph, was present in the BM sample but were completely absent in the BMA-300 sample after annealing. This corroborates the complete transformation from α to β polymorph. The Raman spectra obtained in this study closely resemble those reported in the literature for K_2AgF_4 polymorphs [36, 102]. However, the data collected here exhibits significantly higher resolution, allowing for a clearer distinction of the peaks and a more refined analysis of the phase transition during the reaction. The Rietveld refinement of the laboratory PXRD data collected for the BMA-300 sample included three phases: β-K_2AgF_4, AgF, and KF (Figure 50).

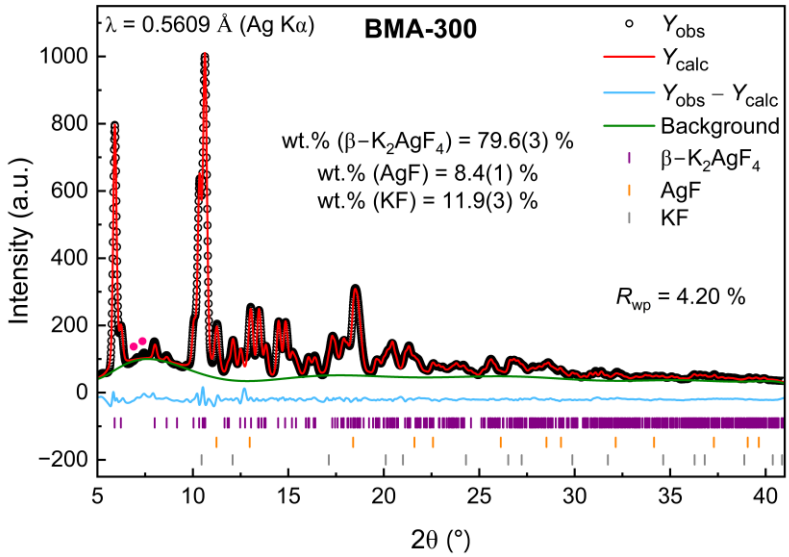


Figure 50: Three-phase Rietveld refinement of the laboratory PXRD data collected on the BMA-300 β-K_2AgF_4 sample. Pink full circles represent an unidentified impurity.

Approximately 80 wt.% of the sample consisted of the β-K_2AgF_4, while the remaining portion was made of diamagnetic AgF and KF, confirming the successful synthesis of the β polymorph and transformation of α polymorph. However, additional unidentified peaks, highlighted by pink dots, were observed. If these unidentified peaks correspond to a diamagnetic impurity, the sample remains suitable for further magnetic characterisation of β-K_2AgF_4 without interference from magnetic impurities.

Magnetic susceptibility measurements were carried out on both BM and BMA-300 samples, enabling a direct comparison of their magnetic properties and a comparison against values reported for solid-state-synthesised sample. The temperature dependent magnetic susceptibility is shown in Figure 51. For the BM sample, a clear ferromagnetic transition occurs at approximately 13.4 K, a value consistent with the literature for the α-K_2AgF_4 polymorph [36]. This observation supports the PXRD results, which confirmed the presence of the α-K_2AgF_4 in the BM sample. In contrast, the BMA-300 sample, which has

been annealed, shows no such transition. This confirms the complete transformation from α-K_2AgF_4 to the β-K_2AgF_4 polymorph, as evidenced by PXRD. Instead, a ferromagnetic transition is observed at around 6 K, suggesting that the unidentified phase detected in the PXRD pattern may be ferromagnetic. Further insight is provided by the Curie-Weiss fits. For the BM sample (Figure 51c), a Curie constant of 0.38 emu · K/mol and a θ_{CW} of 2 K were determined, both in excellent agreement with literature values [102], indicating a close resemblance to the sample synthesized via the solid-state method reported in the literature. On the other hand, the BMA-300 sample (Figure 51d) shows a slightly higher Curie constant of 0.51 emu · K/mol, which is comparable to the Curie constant reported for isostructural mixed-valence silver compound Ag_3F_4 (0.48 emu · K/mol [104]), highlighting their structural resemblance. Nevertheless, the θ_{CW} remains close to zero in BM and BMA-300 samples, indicative of extremely weak magnetic interactions. The plots of the effective magnetic moment versus temperature (Figure 51e and Figure 51f) highlight the contrasting levels of ferromagnetic impurities in the two samples. The BM sample shows a higher level of ferromagnetic contribution, consistent with the presence of a larger amount of β-K_2AgF_4. In the BMA-300 sample, however, the reduced amount of ferromagnetic impurity is consistent with the phase transformation to β-K_2AgF_4, although the contribution from the unidentified impurity remains evident. Interestingly, the magnetisation versus magnetic field data for both samples (Figure 51g and Figure 51h) exhibit a "butterfly" hysteresis pattern, indicative of a complex magnetic behaviour or even magnetoelectric behaviour of β-K_2AgF_4.

In summary, the sample synthesised by ball-milling closely resembles the one prepared via solid-state methods, with the advantage of a significantly reduced reaction time (5 hours versus 14 days). Moreover, the secondary α-K_2AgF_4 phase transforms into the more thermodynamically stable β-K_2AgF_4 upon annealing the BM sample. However, this process also introduces an unidentified ferromagnetic impurity, which orders ferromagnetically at approximately 6 K. Despite this complication, the Curie constant observed in the annealed sample aligns with that of isostructural compound Ag_3F_4, suggesting that it may provide a more accurate reflection of the intrinsic magnetism of β-K_2AgF_4. To gain further insights, future studies should explore the magnetic behaviour below 2 K to determine if β-K_2AgF_4 exhibits a similar low-temperature transition as the Ag_3F_4 phase.

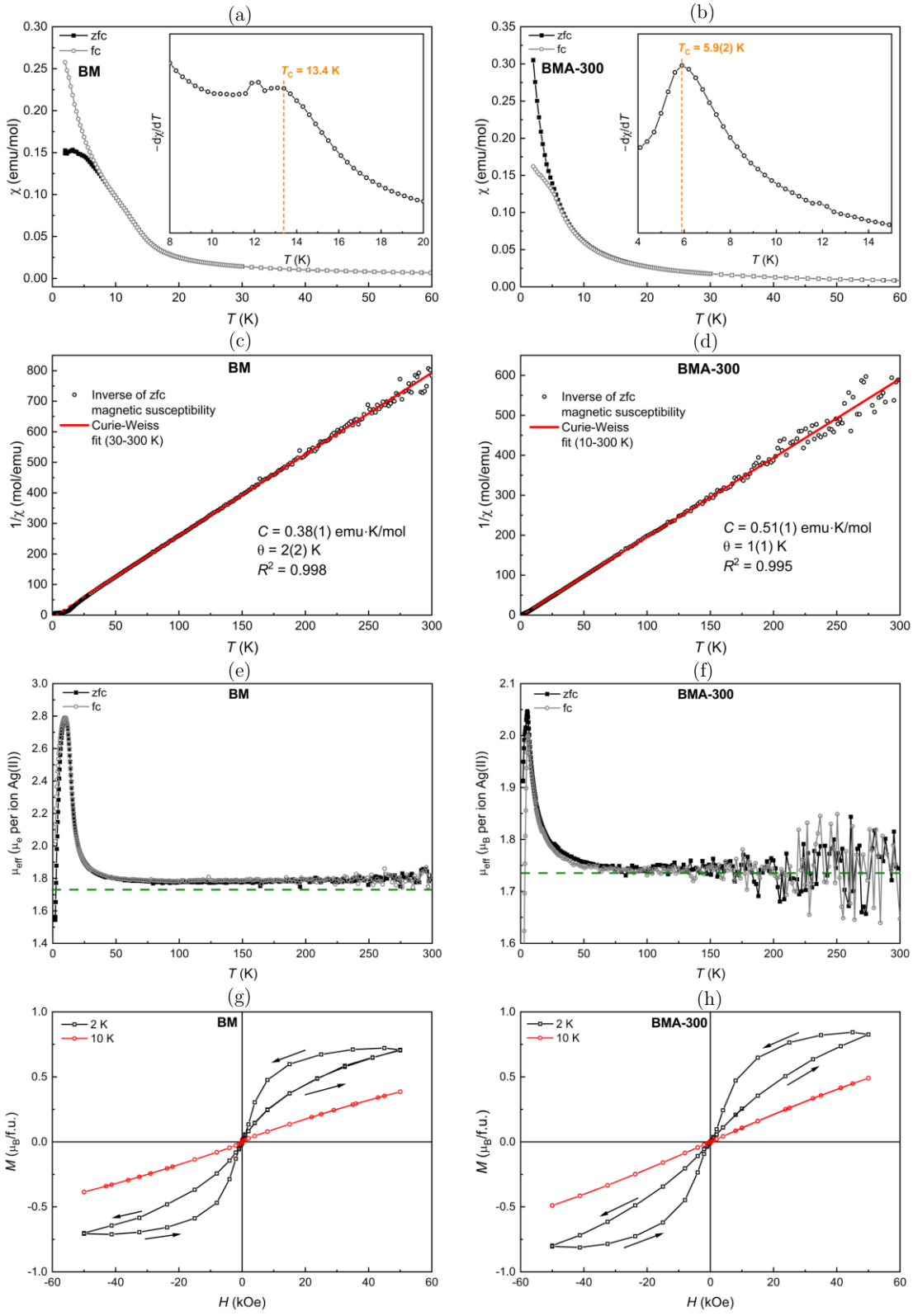


Figure 51: Magnetic susceptibility shown as a function of temperature for (a) BM and (b) BMA-300 samples. The insets in a and b show $-d\chi/dT$ vs. T plots. Curie-Weiss fits of an inverse of ZFC magnetic susceptibility for (c) BM and (d) BMA-300 samples. Effective magnetic moments plotted as a function of temperature for (e) BM and (f) BMA-300 samples. Magnetisation plotted as a function of magnetic field for (g) BM and (h) BMA-300 samples.

3.2.2.3 Rb_2AgF_4 and Cs_2AgF_4

The crystal structure of Cs_2AgF_4 has been previously studied in the literature; however two distinct space groups were proposed, each reflecting different structural features. The *I*4/*mmm* space group was first proposed by Odenthal in 1974, based on PXRD, where Cs_2AgF_4 was assumed to be isostructural with K_2NiF_4 [22] (Figure 52a). In this model, Ag^{2+} ions are coordinated by six fluoride ions, forming $[AgF_6]$ octahedra with a slight tetragonal distortion. The structure is characterised by compressed octahedra, with Ag–F bond lengths of 2.292 Å and 2.216 Å respectively, indicating shorter axial bonds due to the compression (Figure 52b). This symmetry and bond distribution closely resemble other compounds in the K_2NiF_4 family, and it was suggested that Rb_2AgF_4 could adopt a similar structure. However, a later study by McLain et al. [21], incorporating both PXRD and NPD, proposed that Cs_2AgF_4 instead adopts the *Bbcm* space group (Figure 52c). This introduces more significant distortion in the octahedral coordination of silver cation. In the structure, the $[AgF_6]$ octahedra are elongated, with Ag–F bond lengths of 2.208 Å, 2.010 Å, and 2.611 Å, indicative of a Jahn-Teller distortion common in Ag^{2+} compounds (Figure 52d). The connectivity of octahedra results in staggered orbital ordering of $z^2{-}x^2$ and $z^2{-}y^2$ orbitals, similar to K_2CuF_4 [105]. Here ligands are displaced from central positions, which leads to a lowering the crystal symmetry. Such arrangement of octahedra leads to strong ferromagnetic superexchange interactions through the unfilled in-plane $x^2{-}y^2$ orbitals. The bond valence sum (BVS) analysis further supported this assignment, as it provided a better match with the expected oxidation state and coordination environment of Ag^{2+}, favouring the *Bbcm* model over the *I*4/*mmm* structure. Thus, while the I4/mmm structure was initially favoured due to its similarity to known fluorides, the *Bbcm* space group has emerged as the more accurate description of the crystal structure of Cs_2AgF_4 and extended to Rb_2AgF_4.

Both Cs2AgF4 and Rb_2AgF_4 have been successfully synthesised in previous studies using a conventional high-temperature solid-state method. This approach involved annealing stoichiometric mixtures of CsF (or RbF) and AgF_2 at 500 °C for 24 hours. However, in this work, it was aimed to explore whether the ball-milling could be employed as a viable alternative to synthesise these phases. By using this energy-efficient and time-saving method, it was intended to compare the structural outcomes of the synthesised phases to those previously reported. The key objective was to examine the validity of the *Bbcm* space group, which has been proposed in recent studies. Additionally, it was sought to investigate how the ball-milling process would impact the magnetic properties of these compounds.

Violet polycrystalline samples were successfully prepared by ball-milling of commercially available reagents (RbF, CsF and AgF_2). The synthesis conditions are listed in Table 24.

The Rietveld refinement of the laboratory PXRD data, presented in Figure 53a and Figure 53b, suggests that both Rb_2AgF_4 and Cs_2AgF_4 were successfully synthesised via ball-milling. This method significantly improves upon high-temperature solid-state synthesis, reducing the reaction time from 24 hours to just 3 hours. However, in both cases, some contamination with AgF was observed. Moreover, in the Cs_2AgF_4 sample, additional unidentified peaks were present, indicating the existence of an impurity that could not be attributed to any known phase. Both Rietveld refinements shown in Figure 53 were performed using the *Bbcm* space group, which provided more accurate fits than the alternative *I*4/*mmm* space group. For Rb_2AgF_4 and Cs_2AgF_4, the R_{wp} factors increased to 3.21% and 5.60%, respectively, when using *I*4/*mmm*, confirming McLain *et al.* [21] that *Bbcm* better represents the crystallographic data.

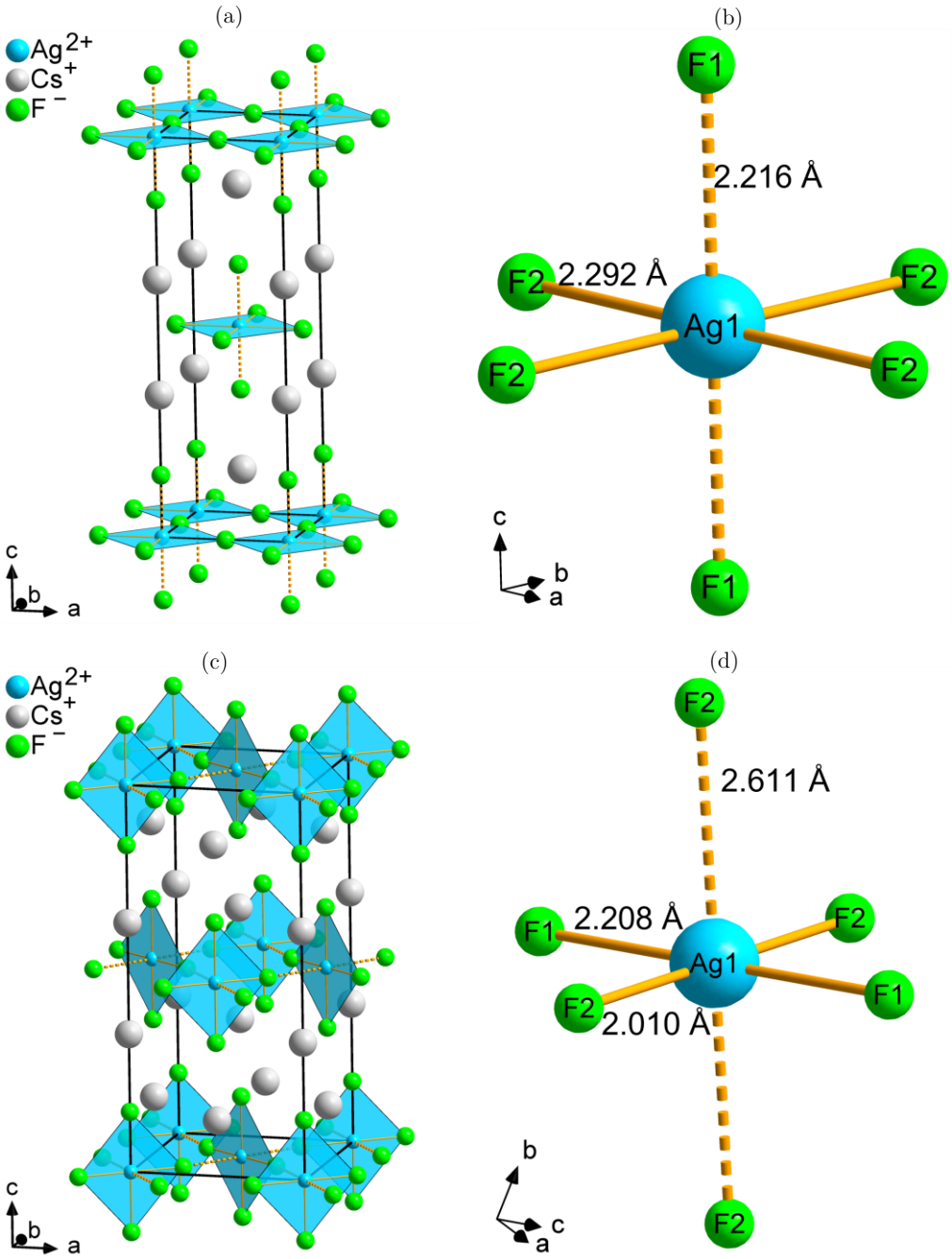


Figure 52: (a) Crystal structure of Cs_2AgF_4 crystallising in $I4/mmm$ space group and (b) coordination of Ag^{2+} cation forming an equatorially compressed $[AgF_6]$ octahedra. (c) Crystal structure of Cs_2AgF_4 crystallising in $Bbcm$ space group and (d) coordination of Ag^{2+} cation forming an axially elongated $[AgF_6]$ octahedra.

Table 24: Synthesis conditions for Rb_2AgF_4 and Cs_2AgF_4.

Synthesis method	**Synthesis conditions**
Ball-milling	CsF (or RbF) : AgF_2 = 2:1.1, t = 1 h, milling cycle = 15 min, ν = 30 Hz, BRR ≈ 50, d_{ball} = 15 mm

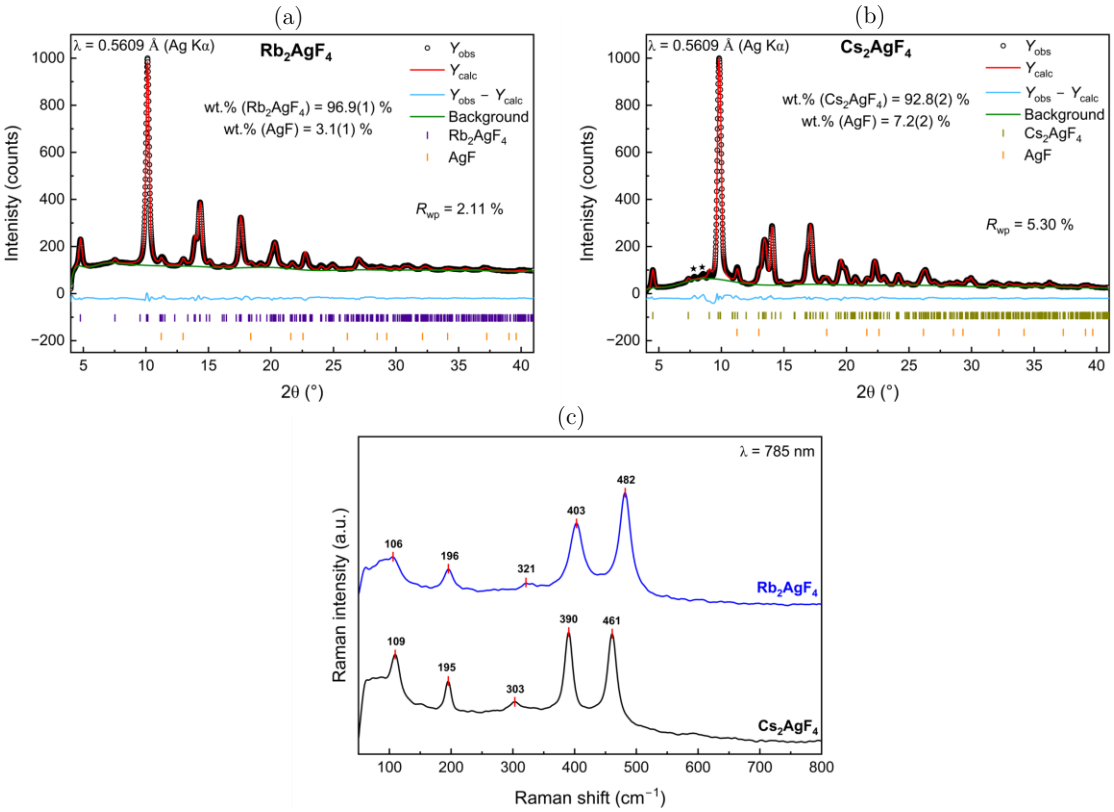


Figure 53: Rietveld refinement of the laboratory PXRD data obtained on the ball-milled (a) Rb_2AgF_4 and (b) Cs_2AgF_4. (c) Comparison of Raman spectra of Rb_2AgF_4 and Cs_2AgF_4 samples.

Raman spectroscopy, employed here as a complementary technique to PXRD, provided information about the vibrational modes and an additional dataset for comparison to the literature reports. The Raman spectra of both phases show high resemblance, which is expected due to their isostructural nature (Figure 53c). Both compounds displayed similar vibrational features with slight shifts towards higher wavenumbers were observed in comparison to the literature reports. In Rb_2AgF_4, the two most intense peaks were recorded at 482 cm^{-1} and 403 cm^{-1} respectively, whereas previous literature reports them at 470 cm^{-1} and 395 cm^{-1} [36]. Similarly, for Cs_2AgF_4, the most prominent peaks appeared at 461 cm^{-1} and 390 cm^{-1} respectively, compared to 455 cm^{-1} and 385 cm^{-1} as previously reported in the literature [36]. This uniform shift towards higher wavenumbers could arise from a systematic measurement error or a slight structural difference. Additionally, both spectra featured a weak signal around 300 cm^{-1}, which was also noted in earlier studies, although the peak's exact origin remains unidentified. The overall consistency of the Raman spectra with the literature not only supports the crystallographic findings but also underscores the reliability of ball-milling as an alternative synthesis method for these complex fluoride phases.

Since both PXRD and Raman analyses confirmed the successful formation of the targeted phases, magnetic characterisation was also performed on both ball-milled samples to assess whether their magnetic responses are consistent with those reported for the solid-state synthesised samples in the literature. The magnetic susceptibility data measured as a function of temperature, shown in Figure 54a and Figure 54b, indicates that both phases order ferromagnetically, which is in agreement to the literature reports [21, 22, 36].

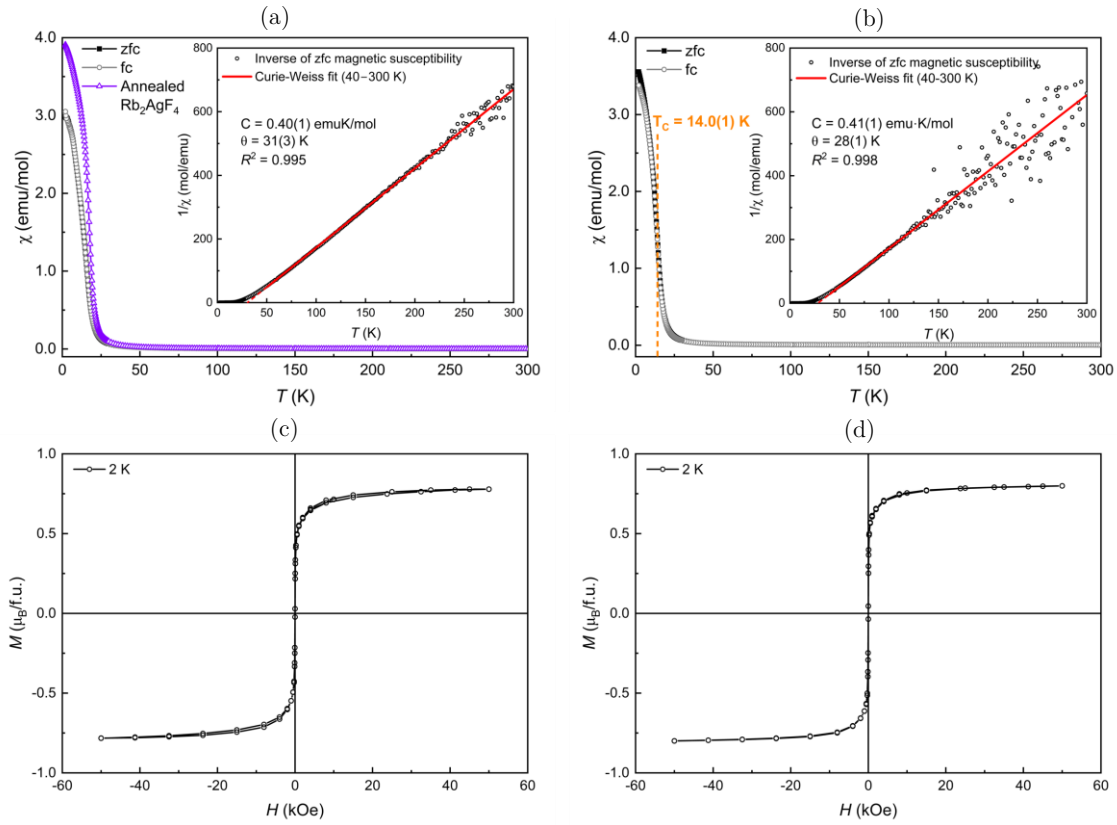


Figure 54: Magnetic susceptibility measured as a function of temperature with the Curie-Weiss fits presented in the insets for (a) Rb_2AgF_4 and (b) Cs_2AgF_4. Magnetization curves measured as a function of magnetic field at 2 K for (c) Rb_2AgF_4 and (d) Cs_2AgF_4.

However, slightly lower transition temperatures were found in this work. While the literature reports a transition temperature of 17.5 K for Rb_2AgF_4 [36] and 14.9 K for Cs_2AgF_4 [21], respectively, this work found 15.5(1) K for Rb_2AgF_4 and 14.0(1) K for Cs_2AgF_4 as determined from the maximum of the $-\mathrm{d}\chi/\mathrm{d}T$ vs. T plots. The transition temperature might be shifted slightly towards lower temperatures since the samples were prepared by ball-milling, which introduces many defects in the structure and induces microstrain, which might alter the bulk magnetic properties of the material. To test this hypothesis magnetic properties were measured also on ball-milled and additionally annealed sample of Rb_2AgF_4 (at 300 °C for 24 h), where transition temperature of 17.4(1) K was determined. This suggests that annealing resulted in the reduction of the microstrain and defects, which were induced during the ball-milling. Curie-Weiss fits for both investigated phases yielded similar Curie constant and θ_{CW}, which is not surprising given the fact that Rb_2AgF_4 and Cs_2AgF_4 are isostructural. The obtained Curie constant of 0.40(1) emu · K/mol for Rb_2AgF_4 and 0.41(1) emu · K/mol for Cs_2AgF_4 are in the expected range for $S = 1/2$ Ag^{2+} cation, while positive θ_{CW} of 31(3) K for Rb_2AgF_4 and 28(1) K for Cs_2AgF_4 indicate that ferromagnetic interactions are predominant in both phases. Ferromagnetism is also confirmed with the magnetisation curves shown in Figure 54c and Figure 54d, since below the transition temperature the magnetisation saturates already at about 10 kOe.

In this chapter, it was demonstrated that both Rb_2AgF_4 and Cs_2AgF_4 were successfully synthesized via ball-milling, with phase purity confirmed by PXRD and Raman spectroscopy. The *Bbcm* space group was identified as the correct structural model for both phases, further substantiated by Rietveld refinement, which showed a better fit compared

to the $I4/mmm$ space group, particularly with respect to the R_{wp} factors. Magnetic characterisation revealed that both compounds exhibit ferromagnetic ordering, consistent with previous reports, though slightly lower transition temperatures were observed—likely due to defects and microstrain introduced during ball-milling. Subsequent annealing of Rb_2AgF_4 reduced these defects, restoring the transition temperature closer to the value reported in the literature.

3.3 Synthesis, Structural and Magnetic Characterisation of the First Mixed-valent Binary Silver(I,II) Compounds

Mixed-valent compounds have attracted considerable attention due to their ability to exhibit novel electronic and magnetic phenomena resulting from the presence of multiple oxidation states of the same cation within a single structure. These materials can exhibit unique properties, such as increased conductivity, unusual magnetism and unconventional superconductivity, which are crucial for a better understanding of the fundamentals and technological applications. Silver, a transition metal with the remarkable ability to adopt a variety of oxidation states (0, +1, +2, +3), is a particularly interesting system to investigate. In combination with fluorine, which has the extraordinary ability to stabilise higher oxidation states, silver and fluorine offer a rich playground for the discovery of new mixed-valent phases. Within the binary silver-fluorine system, only six phases are currently known: Ag_2F [106, 107, 108, 109], AgF [110, 111], AgF_2 [29, 112, 113, 114], AgF_3 [115, 116], Ag_2F_5 [117, 118] and Ag_3F_8 [119]. In these compounds, silver exhibits a range of oxidation states, including +0.5, +1, +2 and +3. Remarkably, only two mixed-valent binary silver fluorides have been identified to date: Ag_2F_5 or $Ag^{II}F[Ag^{III}F_4]$ and Ag_3F_8 or $Ag^{II}[Ag^{III}F_4]_2$. In both cases, silver exhibits a mixed +2/+3 oxidation state, suggesting that binary silver(I,II) fluorides have yet to be discovered.

Despite the considerable interest in mixed-valent binary silver(I,II) fluorides, experimental attempts to synthesise these compounds have faced major challenges, even though theoretical calculations have predicted their stability under ambient conditions. Previous studies relying on density functional theory (DFT) have identified potentially stable compositions such as $Ag^{I}{}_2Ag^{II}F_4$ (Ag_3F_4) and $Ag^{I}Ag^{II}F_3$ (Ag_2F_3), which were thought to be thermodynamically stable at room temperature [120, 121, 122]. In particular, the first theoretical study [120] predicted that the $Ag^{I}{}_2Ag^{II}F_4$ phase would crystallise in one of three possible space groups: monoclinic $P2_1/c$, orthorhombic $Cmca$ or tetragonal $I4/mmm$. Of these, the monoclinic $P2_1/c$ structure, analogous to β-K_2AgF_4 [102] and Na_2CuF_4 [123], was considered to be the most energetically favourable. A subsequent theoretical investigation, however, suggested a single polymorph with space group $I\bar{4}2d$ (similar to $CdMn_2O_4$ [124]) as the ground state structure of $Ag^{I}{}_2Ag^{II}F_4$ up to 19 GPa [121]. Theoretical calculations also indicated another stable Ag(I,II) phase with the formula $Ag^{I}Ag^{II}F_3$, with several structural models considered in the first study, including $Pbnm$, $Pmcn$, $P\bar{1}$ and $C222_1$ [120]. It was suggested that these structures were energetically similar, but later theoretical work identified the $Cmcm$ space group as the ground state for $Ag^{I}Ag^{II}F_3$ [121]. However, the real-world synthesis of these predicted phases was hindered by practical challenges, including the low solubility of AgF_2 in aHF and its thermal instability at temperatures below 400°C [3, 37]. Despite the theoretical promise, these obstacles have so far prevented the successful experimental realisation of these mixed-valence silver(I,II) fluorides, highlighting the gap between theoretical predictions and experimental feasibility. This persistent difficulty highlights the complexity of stabilising Ag^{2+} species and suggests that further refinement of synthesis techniques or conditions may be necessary to obtain the predicted compounds.

3.3.1 $Ag^{I}{}_2Ag^{II}F_4$

The first experimental evidence of a phase which could be mixed-valence $Ag^{I}{}_2Ag^{II}F_4$ phase was documented in the PhD thesis of J. Gawraczinski [125], in which AgF_2 was studied with Raman spectroscopy. It was observed that when AgF_2 is illuminated with a green

laser of wavelength 532 nm, a new peak appears at about 420 cm^{-1} and becomes stronger with time. Due to its intensity and position in the Raman spectrum, this peak was attributed to the $[AgF_4]^{2-}$ moieties, which are also present in the Na_2AgF_4 and β-K_2AgF_4 compounds [101, 102]. The same experiment was repeated in this study and the same behaviour of AgF_2 was observed under the green laser where intense peak at about 417 cm^{-1} appeared (Figure 55). Since the ionic radius of Ag^+ (1.22 Å, assuming a coordination number of 7) falls between that of Na^+ (1.12 Å) and K^+ (1.46 Å), it is reasonable to expect that Ag^+ can behave similarly to an alkali metal cation and form compounds with comparable structures. Based on this, the author also proposed a formula for the unidentified phase, $Ag^{I}_2Ag^{II}F_4$, along with the chemical reaction leading to the decomposition product:

$$3AgF_2 \rightarrow Ag^{I}_2Ag^{II}F_4 + F_2 \tag{3.2}$$

The evolution of fluorine was confirmed by the loss of transparency in the capillaries containing AgF_2 after a few days of green laser illumination. This occurred even in regions not directly in contact with AgF_2, likely due to fluorine release and the resulting glass etching.

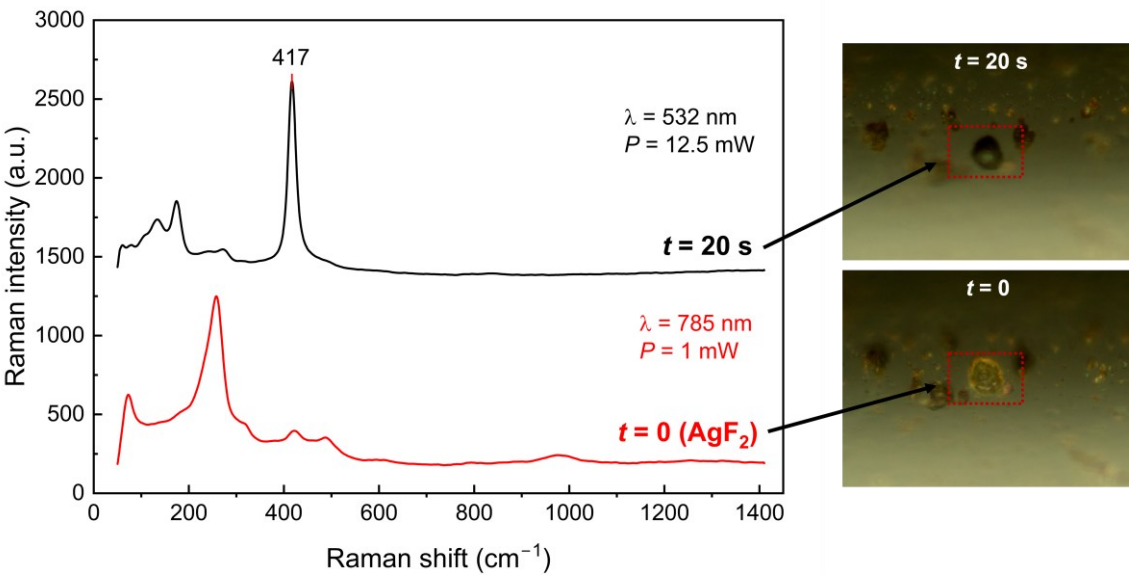


Figure 55: Room-temperature Raman spectrum of AgF_2 particle measured using 785 nm excitation laser with 1 mW power (red line) and Raman spectrum obtained after the same AgF_2 particle was illuminated with green laser with 532 nm wavelength and 12.5 mW power for 20 seconds (black line).

A compound containing Ag^+ and Ag^{2+} cations in a 2:1 ratio was prepared using the thermal solid-state method and by mechanochemistry (the synthesis conditions are listed in Table 25). The temperature chosen for the solid-state synthesis was 300 °C, as higher temperatures (> 350 °C) led to the sample decomposition. However, a lower reaction temperature led to a longer annealing time. In contrast, the ball-milling reaction indicated that the chemical reaction was complete after just 30 minutes of high-energy milling, depending on the milling parameters.

Table 25: Conditions for the synthesis of the 2:1 phase using the solid-state synthesis and ball-milling.

Synthesis method	**Synthesis conditions**
Solid-state synthesis	AgF_2:AgF=1:2, T = 300 °C, t = 72 h
Ball-milling	AgF_2:AgF=1:2, ν = 30 Hz, 15 minute milling cycle, 30 minutes total milling time, 15 mm diameter of tungsten carbide milling ball

The laboratory PXRD data (Figure 56a) indicate a potentially successful reaction, albeit with AgF, which could be attributed to the partial decomposition of AgF_2 during the reaction. Compared to the solid-state sample, the ball-milled sample exhibited significant peak broadening indicating nano-sized crystallites (about 10 nm), the presence of defects and microstrain induced during milling, as well as a higher background suggesting the presence of an amorphous phase. Since the crystal structure of β-K_2AgF_4 was one of the possible candidates for the crystal structure of the 2:1 phase, the Raman spectrum obtained on the new phase was compared with the Raman spectrum obtained on β-K_2AgF_4 synthesised by ball-milling (Figure 56b) [36, 102]. The intense band at 422 cm^{-1} observed in the Raman spectrum of the 2:1 phase could be attributed to the $[AgF_4]^{2-}$ units, which are characteristic of both β-K_2AgF_4 and Na_2AgF_4, indicating possible structural similarities between the new phase and these compounds. Assuming that the 2:1 phase is isostructural with β-K_2AgF_4, it probably crystallises in space group $P2_1/c$ and exhibits eighteen Raman active modes ($9A_g + 9B_g$). However, the Raman spectroscopy measurements on the 2:1 sample revealed only six peaks, which correspond to those of β-K_2AgF_4 as described in the literature [36, 102]. The similarity of the spectra indicates structural similarities between the two compounds.

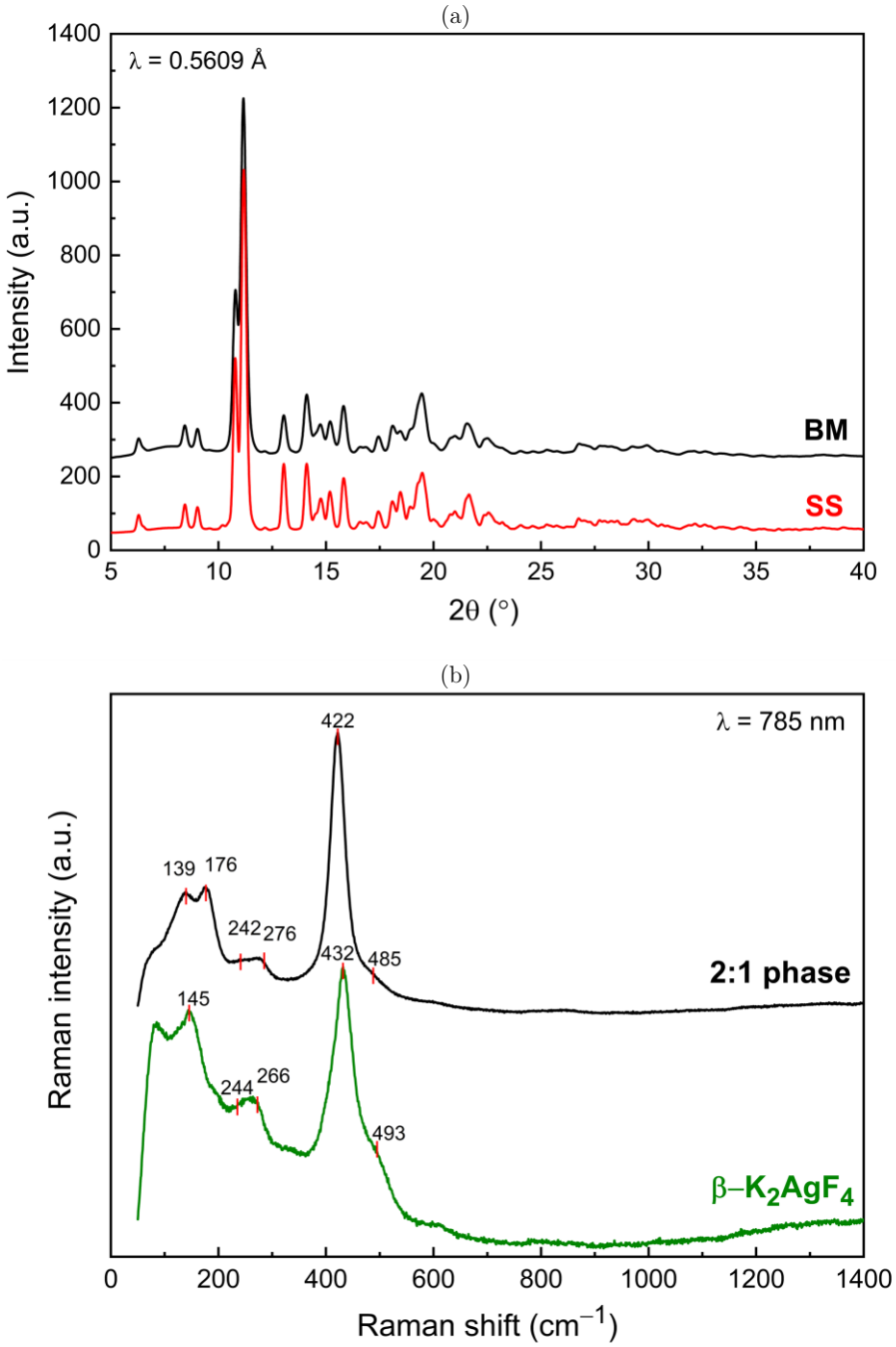


Figure 56: (a) Laboratory PXRD patterns of ball-milled (BM) and solid-state (SS) synthesised 2:1 phase samples (AgF_2:AgF molar ratio = 2:1). (b) Raman spectra of the 2:1 phase and β-K_2AgF_4, both synthesised by ball-milling.

For unit-cell indexing and structural refinement, high-resolution synchrotron PXRD data were collected on the light brown polycrystalline sample, which was prepared using the solid-state method (Figure 57a). The diffraction peaks that did not belong to either AgF_2 or AgF were indexed to a monoclinic unit cell with unit-cell parameters of a = 3.569(1), b = 9.887(1), c = 5.983(1), and β = 92.83° which were similar to those of β-K_2AgF_4. The structural model of β-K_2AgF_4 was then used for the Rietveld refinement of the synchrotron PXRD data (Figure 57b), which confirmed that the 2:1 phase crystallises in the $P2_1/c$ space group and that it is isostructural to β-K_2AgF_4. Based on the isostructural

nature of the 2:1 phase and β-K_2AgF_4, it can be concluded that the investigated phase has the formula $Ag^{I}_2Ag^{II}F_4$. In this structure, Ag^+ acts like an alkali metal cation at the A site, analogous to K^+ cation in β-K_2AgF_4. The crystallographic data of the Rietveld refinement are listed in Table 26.

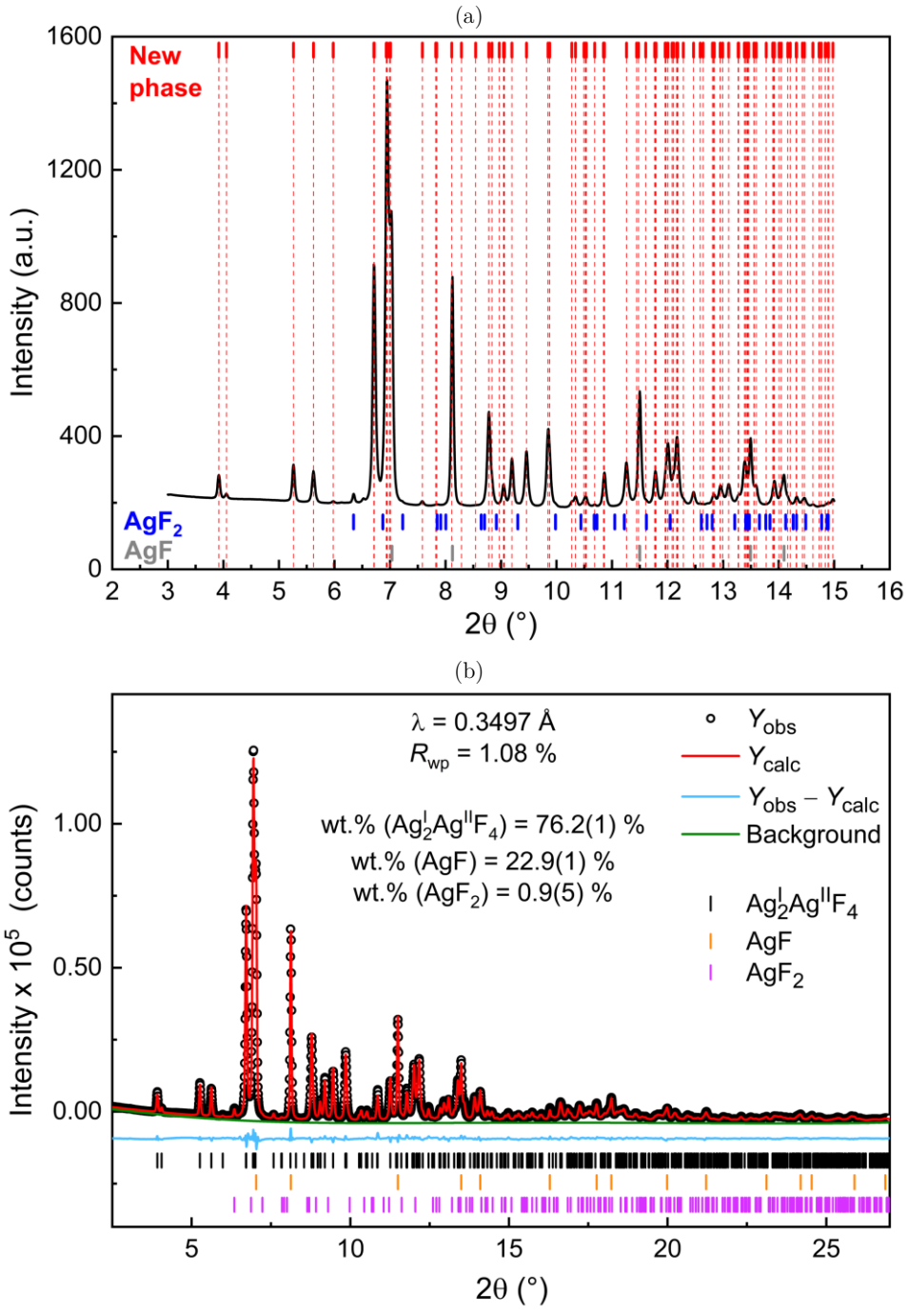


Figure 57: (a) Indexing ($P2_1/c$ space group) of the synchrotron PXRD data measured with $\lambda = 0.3497$ Å. (b) Three-phase Rietveld refinement of the synchrotron PXRD data collected on the $Ag^{I}_2Ag^{II}F_4$ sample prepared with by the solid-state method.

Table 26: Crystallographic parameters of $Ag^{I}_{2}Ag^{II}F_4$ phase obtained with the Rietveld refinement of synchrotron data.

$Ag^{I}_{2}Ag^{II}F_4$	
Space group	$P2_1/c$ (no. 14)
Chemical formula weight (g/mol)	399.6
Z	2
a, b, c (Å)	3.56910(8), 9.88659(15), 5.9829(2)
β (°)	92.8321(15)
V (Å^3)	210.857(4)
Ag1 (x, y, z)	0, 0, 0
U_{iso}	0.0110(4)
Oxidation state	+2
Ag2 (x, y, z)	0.5122(3), 0.17859(15), 0.43044(15)
U_{iso}	0.0162(3)
Oxidation state	+1
F1 (x, y, z)	0.5568(18), 0.4522(8), 0.2668(11)
U_{iso}	0.053(3)
F2 (x, y, z)	0.0155(18), 0.1971(8), 0.1391(10)
U_{iso}	0.0212(17)
GOF	1.61
R_{wp}	0.0108

It was originally assumed that the resulting weight ratio of unreacted reagents (AgF and AgF_2) would be approximately 1.74:1. Contrary to expectations, the refinement process unveiled approximately 23 wt.% AgF and only about 1 wt.% of AgF_2. This discrepancy led to the hypothesis that the increased AgF content could be due to decomposition of the sample in the capillary after sealing, a suspicion that was reinforced by the loss of capillary transparency. A PXRD measurement on a fresher sample prepared by the solid-state method confirmed this hypothesis and revealed an AgF content of 14.3(1) wt.%, emphasising the inherent reactivity of the sample (Figure 58a). In contrast to the sample synthesised by the solid-state method, the sample produced by ball-milling contained only 11.3(6) wt.% of AgF (Figure 58b). In addition to the reduced AgF content, the synthesis time was significantly shorter with ball-milling: just 30 minutes compared to 3 days for solid-state synthesis. This indicates that ball-milling is the preferred method for synthesising $Ag^{I}_{2}Ag^{II}F_4$.

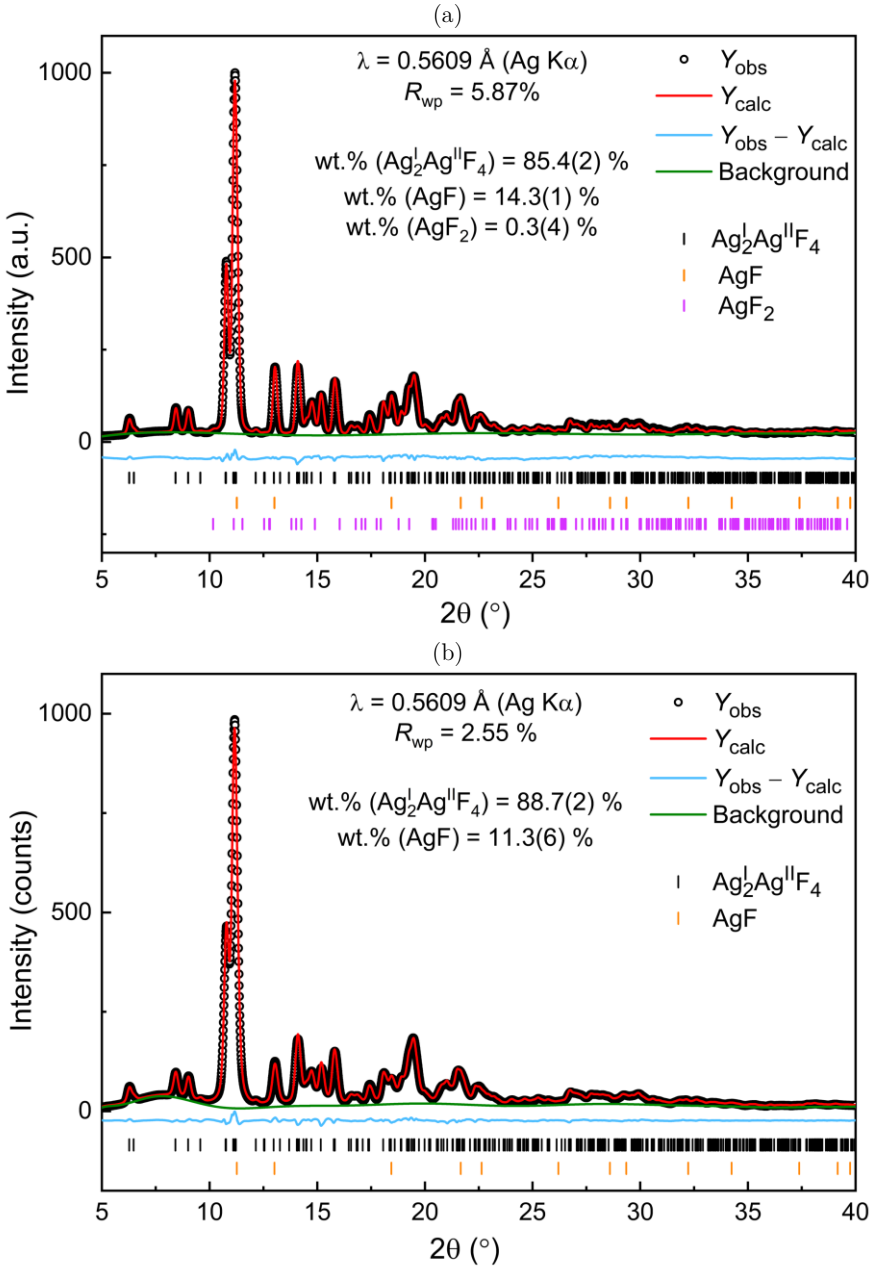


Figure 58: (a) Rietveld refinement of the laboratory PXRD data of solid-state sample of $Ag^{I}_2Ag^{II}F_4$. Wt.% ($Ag^{I}_2Ag^{II}F_4$) = 85.4(2) %; Wt.% (AgF) = 14.3(1) %, Wt.% (AgF_2) = 0.3(4) %. (b) Rietveld refinement of the laboratory PXRD data of mechanochemically synthesised sample of $Ag^{I}_2Ag^{II}F_4$; wt.% ($Ag^{I}_2Ag^{II}F_4$) = 88.7(2) %; wt.% (AgF) = 11.3(6) %.

The expanded unit-cell of $Ag^{I}_2Ag^{II}F_4$ is shown in Figure 59a. The Ag^{2+} cation is coordinated with six fluorine anions, with four almost equal (2.110(6) Å and 2.119(7) Å) and two longer Ag−F contacts (2.528(7) Å), forming an elongated $[AgF_6]^{4-}$ octahedron (Figure 59b). These double-fluorine bridged $[AgF_6]^{4-}$ octahedra are connected to form infinite chains, which propagate along the *a*-crystallographic direction (Figure 59c). On the other hand, the coordination environment of the Ag^{+} cation consists of seven fluorine anions forming a capped trigonal prism. The Ag−F bond lengths range from 2.391(7) Å to 2.884(8) Å. The BVS analysis for the two cations (Ag^{2+} (1.94) and Ag^{+} (1.00)) is in good agreement with the expected values of 2 for Ag^{2+} and 1 for Ag^{+} cation (Table 27).

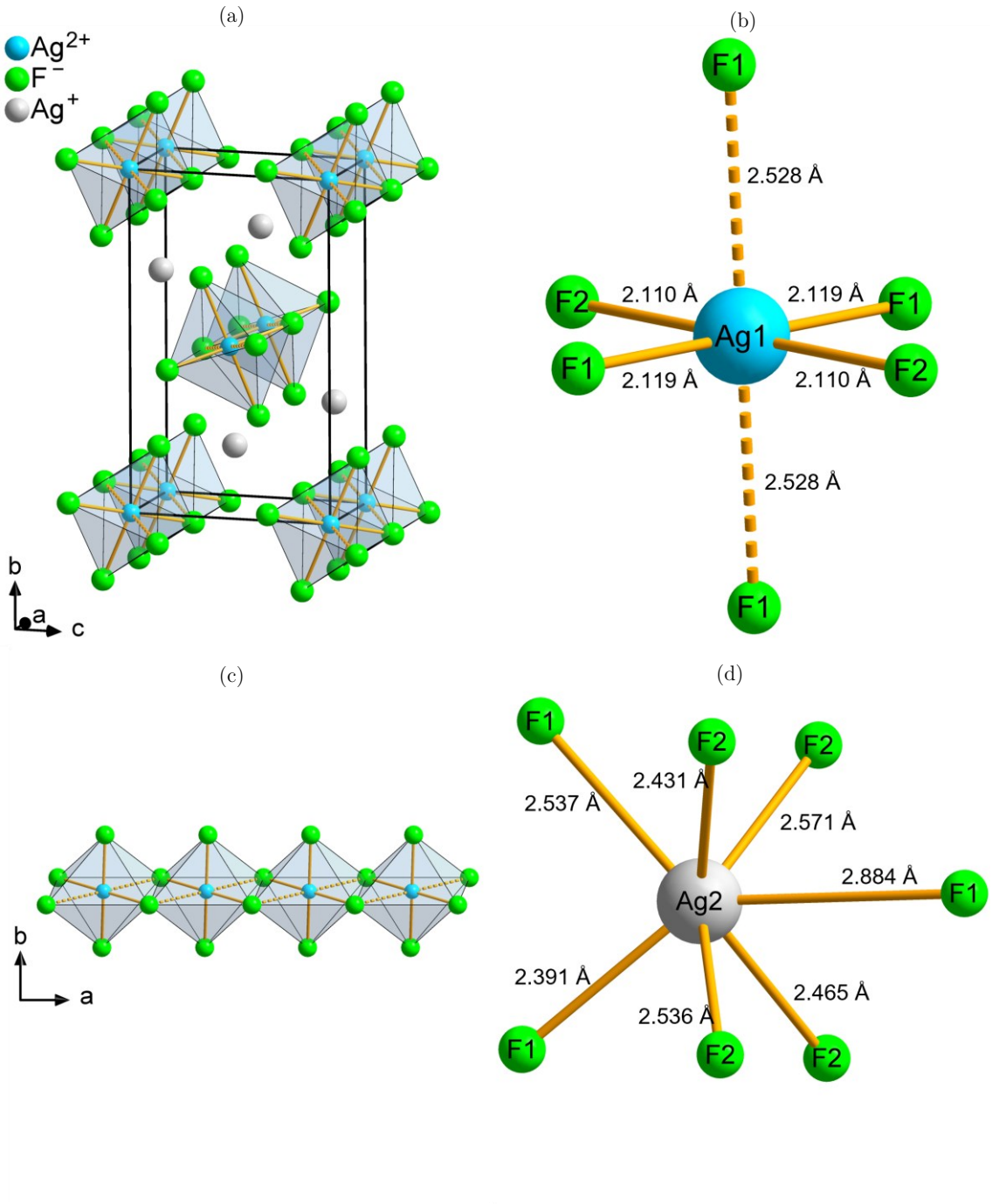


Figure 59: (a) The expended unit-cell of $Ag^{I}_{2}Ag^{II}F_{4}$. (b) Coordination surroundings with atom distances for silver(II) cation (Ag1). (c) The double-fluorine bridged chain, which propagates along the *a*-crystallographic direction. (d) Coordination surroundings with atom distances for silver(I) cation (Ag2).

Table 27: Interatomic distances and BVS analysis [99] for both silver atoms in $Ag^{I}_{2}Ag^{II}F_4$. The following bond valence parameters were employed: $b = 0.37$ Å; $R_0 = 1.80$ Å (Ag^{I}–F) and 1.79 Å (Ag^{II}–F) [126, 100].

Interatomic distances (Å)	
Ag1(II)–F1 × 2	2.110(6)
Ag1(II)–F1 × 2	2.119(7)
Ag1(II)–F2 × 2	2.528(7)
Ag2(I)–F1	2.391(7)
Ag2(I)–F1	2.431(7)
Ag2(I)–F1	2.464(7)
Ag2(I)–F2	2.536(7)
Ag2(I)–F2	2.537(8)
Ag2(I)–F2	2.571(7)
Ag2(I)–F2	2.884(8)
Bond valence sum	
Ag1(II)	1.94
Ag2(I)	1.00

The magnetic susceptibility data (Figure 60a) indicate that $Ag^{I}_{2}Ag^{II}F_4$ behaves like a paramagnet from room temperature down to 5 K, similar to β-K_2AgF_4 [102]. However, at about 3 K, a ferromagnetic transition is observed with a transition temperature of 2.8(1) K determined from the maximum of the $-\mathrm{d}\chi/\mathrm{d}T$. The inverse of the magnetic susceptibility data was corrected for a constant magnetic contribution of $2.8 \cdot 10^{-4}$ emu/mol and the data was fitted with a Curie-Weiss law in the range from 15 K to 300 K. The calculated Curie constant of 0.48(1) emu·K/mol agrees well with the expected value for the $S = 1/2$ Ag^{2+} ions. Interestingly, a negative Curie-Weiss temperature of $\theta_{CW} = -3.6(2)$ K was determined. To gain a deeper insight into the magnetic properties of $Ag^{I}_{2}Ag^{II}F_4$, the magnetization versus applied magnetic field, $M(H)$ curves, were investigated (Figure 60b). At 5 K, the magnetization exhibits a linear dependence on the applied magnetic field, with no observable remanent magnetization or coercivity. In contrast, at 2 K, a clear hysteresis loop appears below the transition temperature, characterized by a remanent magnetization of approximately 0.0165 μ_B/f.u. and a coercive field of $H_c = 0.076$ kOe. Even at the highest applied magnetic field of 50 kOe, the magnetisation remains relatively low at 0.07 μ_B/f.u. and increases linearly with the magnetic field strength. This value is well below the expected saturation magnetisation of S.g.- $\mu_B \approx 1$ μ_B /f.u. for the $S = 1/2$ spin of the Ag^{2+} ion, indicating the presence of canted antiferromagnetism. A preliminary estimate of the canting angle (∼0.9°) in the zero magnetic field was made by comparing the measured residual magnetisation with the full magnetic moment of 1 μ_B per Ag^{2+} ion.

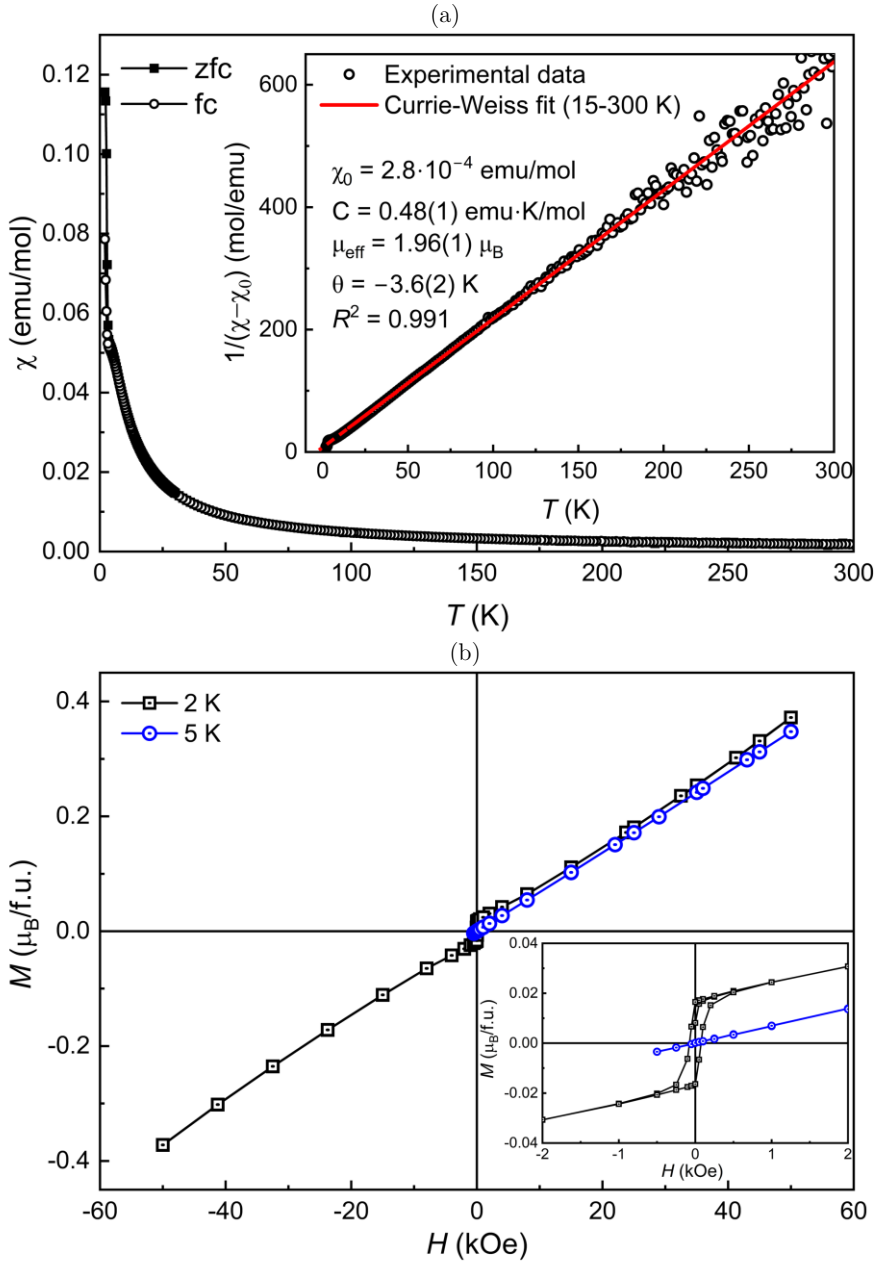


Figure 60: (a) Temperature-dependent magnetic susceptibility of mechanochemically synthesised $Ag^{I}_{2}Ag^{II}F_4$ sample measured in a magnetic field of 1 kOe. The inset shows the Curie-Weiss fit to the inverse of magnetic susceptibility in the 15–300 K range. (b) Magnetization of $Ag^{I}_{2}Ag^{II}F_4$ as a function of magnetic field measured at 2 K and 5 K, respectively. The inset shows a hysteresis indicating a ferromagnetic ground state.

To further investigate the magnetic structure of $Ag^{I}_{2}Ag^{II}F_4$ and confirm or refute this hypothesis, NPD data were collected from the mechanochemically synthesised sample. The measurements were performed above and below the transition temperature determined from the magnetic susceptibility measurements. The Rietveld refinement of the NPD data collected at 5 K, which is above the transition temperature, confirms the structure of $Ag^{I}_{2}Ag^{II}F_4$ (Figure 61a). On the other hand, the difference between the NPD data collected above and below the transition temperature in Figure 61b shows only a weak feature around 15° 2θ, which is insufficient for determining the magnetic structure of $Ag^{I}_{2}Ag^{II}F_4$.

Weak magnetic Bragg peaks, however, were expected due to the low magnetic dimensionality and small moment expected from the Ag^{2+} ions ($S = 1/2$).

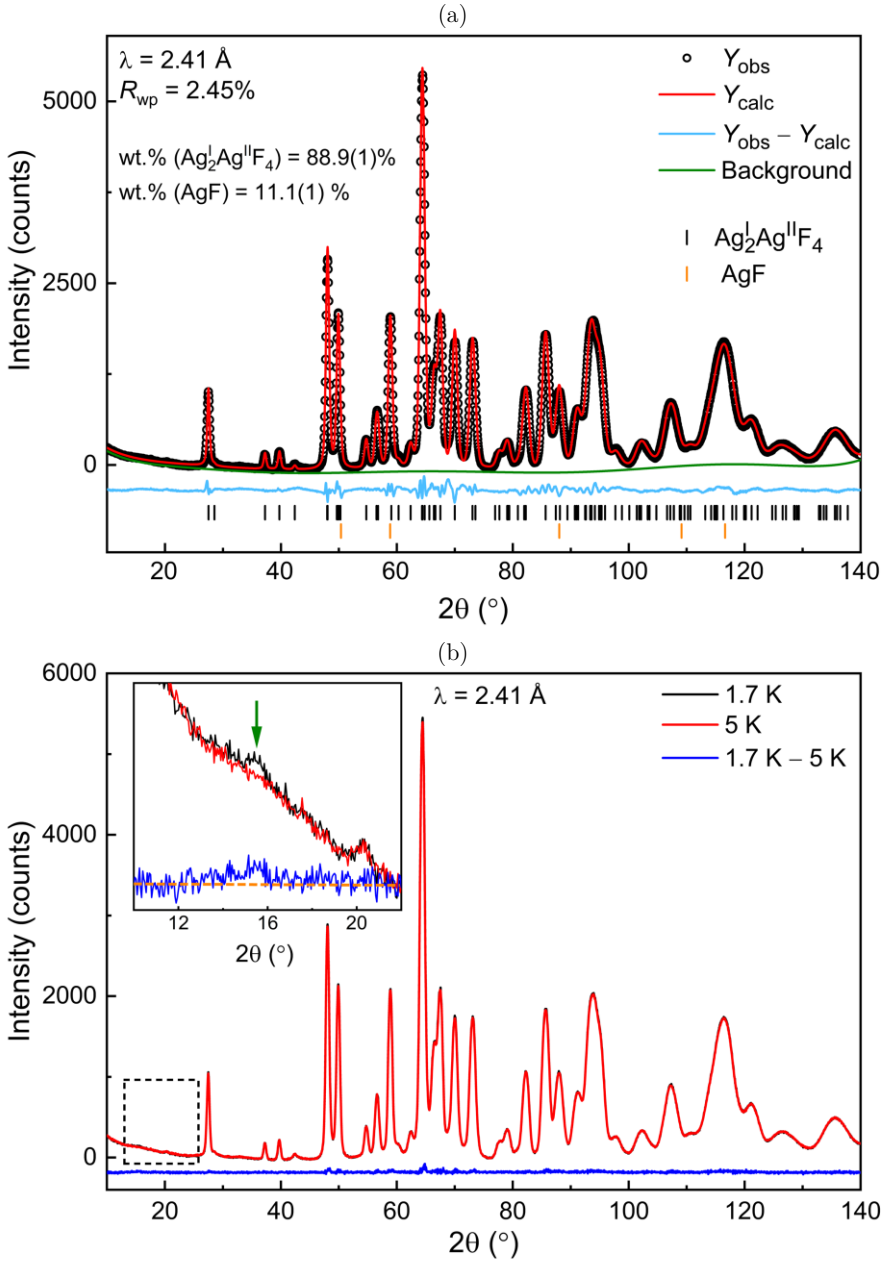


Figure 61: (a) Two-phase Rietveld refinement of the NPD data collected at 5 K. Wt.% ($Ag^{I}_2Ag^{II}F_4$) = 88.9(1)%; wt.% (AgF) = 11.1(1) %. (b) Comparison of the NPD data measured at 5 and 1.7 K shows a weak feature around 15° 2θ – green arrow in the inset.

Both the crystal structure and the magnetic data indicate that $Ag^{I}_2Ag^{II}F_4$ is a 1D canted antiferromagnet. A closer look to the low-temperature magnetic susceptibility in Figure 62 shows a broad peak before the ferromagnetic transition, with a maximum around 4 K, indicating 1D antiferromagnetic behaviour. The magnetic susceptibility data was also fitted with a Bonner-Fisher model for a $S = -1/2$ antiferromagnetic chain. An excellent fit was obtained in the range from 3.5 K to 300 K, supporting the presence of 1D spin correlations above the ordering temperature. The extracted g-factor of 2.292(2), slightly higher than

the free-electron value of 2.0023, and the $|J_{1D}|/k_B$ ratio of 2.818(8) K are consistent with expectations for a 1D AFM model. However, such a small value of the superexchange interaction constant indicates that the spins along the $[AgF_2]$ chains are extremely weakly coupled, which is supported by the fact that $Ag^{I}_2Ag^{II}F_4$ orders magnetically at low temperatures (below 3 K).

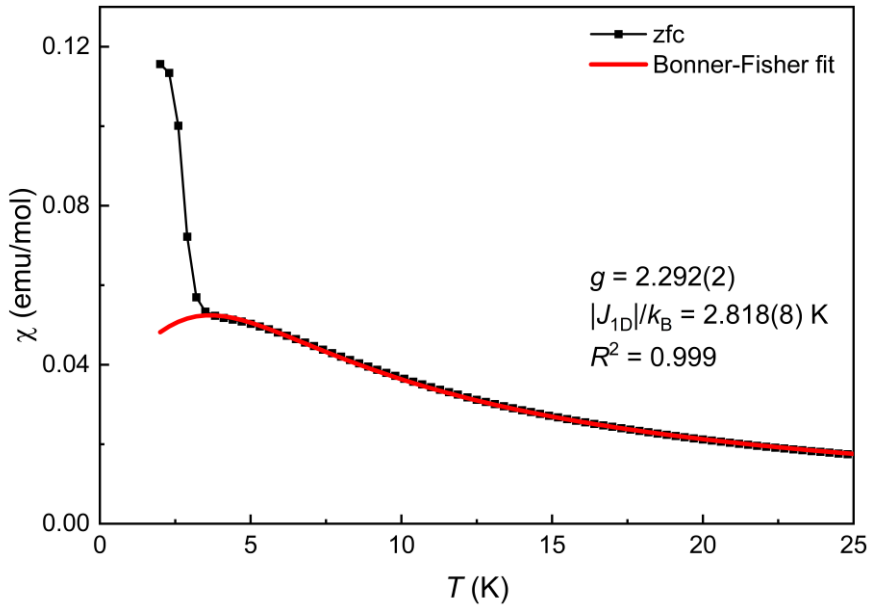


Figure 62: Bonner–Fisher fit to the ZFC magnetic susceptibility of the $Ag^{I}_2Ag^{II}F_4$ sample prepared by ball milling, measured in the 2–25 K temperature range.

The synthesis of $Ag^{I}_2Ag^{II}F_4$ through mechanochemistry represents a significant breakthrough in the accessible preparation of binary mixed-valent silver fluorides, successfully circumventing the thermal instability and high reactivity challenges inherent to Ag^{2+} species. Comprehensive structural characterisation via laboratory and synchrotron PXRD, coupled with Raman spectroscopic analysis, establishes that $Ag^{I}_2Ag^{II}F_4$ adopts a crystal structure analogous to the well-characterised phases Na_2CuF_4 and β-K_2AgF_4. Magnetic susceptibility measurements reveal a 1D canted antiferromagnetic ordering with a T_N of 2.8(1) K, demonstrating the profound influence of the mixed-valent silver framework on magnetic properties. This work underscores the efficacy of the mechanochemical approach in enabling access to previously elusive Ag^{2+}-containing phases at low temperatures, thereby expanding the accessible landscape of fluoridoargentate(II) materials and providing a foundation for future investigations into their electronic and magnetic characteristics.

3.3.2 $Ag^{I}Ag^{II}F_3$

The compound with a 1:1 ratio of Ag^{2+} to Ag^{+} cations was also a target in the reaction between AgF_2 and AgF. For the synthesis of the 1:1 phase, similar conditions were used as for the solid-state synthesis of $Ag^{I}_2Ag^{II}F_4$, with the exception that a small excess of 10 mol% AgF_2 was added here to minimise the formation of a 2:1 phase (Table 28).

Table 28: Synthesis conditions of the solid-state synthesis and ball-milling of 1:1 phase.

Synthesis method	**Synthesis conditions**
Solid-state synthesis	AgF_2:AgF=1.1:1, $T = 300$ °C, $t = 72$ h
Ball-milling	AgF_2:AgF=1.1:1, $\nu = 30$ Hz, 15 minute milling cycle (cooling with liquid nitrogen before milling), 1 hour total milling time, 15 mm diameter stainless steel milling ball and milling jar

On the other hand, immersing the milling jar into the liquid nitrogen between the milling cycles was a crucial step for the mechanochemical synthesis of the 1:1 phase, as only $Ag^{I}_2Ag^{II}F_4$ and unreacted AgF_2 were present in the samples that were not cooled between the milling cycles.

Preliminary analysis of the laboratory PXRD data collected on the 1:1 phase synthesised by the solid-state method indicated a successful reaction, as no peaks belonging to AgF were observed. To gain further insight, high-resolution synchrotron PXRD data was collected on the sample prepared with the solid-state method, which identified the presence of $Ag^{I}_2Ag^{II}F_4$ and AgF_2 among the phases. In addition, several peaks that did not correspond to these known phases were indexed to a triclinic $P\bar{1}$ space group (Figure 63), which has similar unit cell parameters to $AgCuF_3$ and $NaCuF_3$ [127].

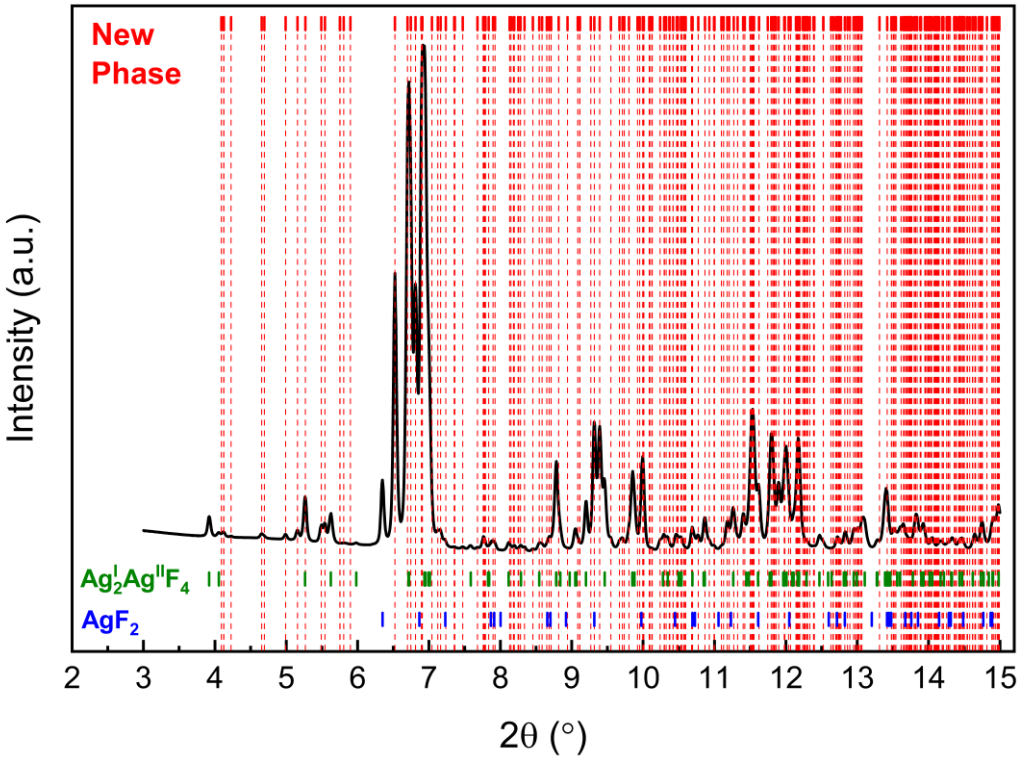


Figure 63: Indexing of the high-resolution synchrotron data of the 1:1 sample measured with $\lambda = 0.3497$ Å.

The structural model of $NaCuF_3$ was therefore used for a Rietveld refinement of the synchrotron PXRD data shown in Figure 64a, which confirmed that the 1:1 phase is isostructural to $NaCuF_3$ and revealed that the chemical formula of the investigated phase is $Ag^{I}Ag^{II}F_3$. The crystallographic data of the Rietveld refinement are listed in Table 29. Based on the Rietveld refinement of the synchrotron PXRD data of the 1:1 phase synthesised by the solid-state method, the sample consisted of only about 60 wt.% of the $Ag^{I}Ag^{II}F_3$ phase (Figure 64a). In contrast, the freshly prepared ball-milled sample, in which the milling jars were cooled to the temperature of liquid nitrogen (−196 °C) before the milling and between the milling cycles, had less than 5 wt.% of impurities (Figure 64b). Another experiment was carried out without the cooling of milling jars during the milling cycles. In this experiment, only AgF_2 and $Ag^{I}_2Ag^{II}F_4$ were observed in the laboratory PXRD data. This indicates that cooling was a crucial step as it prevented the decomposition of $Ag^{I}Ag^{II}F_3$ into AgF_2 and $Ag^{I}_2Ag^{II}F_4$ during the ball-milling process. This observation is in contrast to earlier suggestions reported in the literature that a high-temperature synthesis with temperatures reaching about 900 °C might be suitable for the synthesis of the 1:1 phase [120]. The results show that the low-temperature ball-milling method, in which the milling jars are cooled between the milling cycles, is a more successful approach for stabilising $Ag^{I}Ag^{II}F_3$.

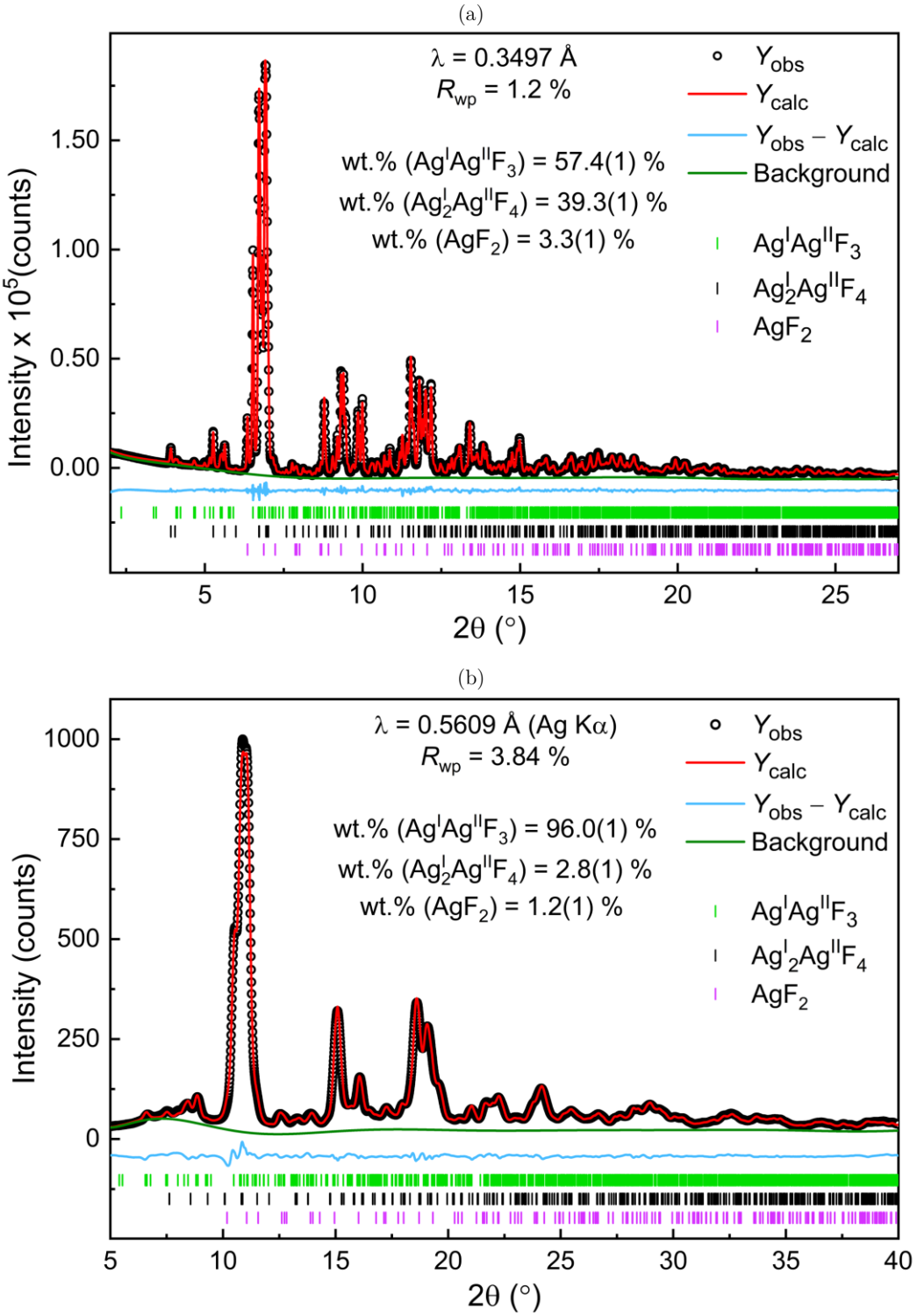


Figure 64: (a) Three-phase Rietveld refinement of a synchrotron data collected on the $Ag^{I}Ag^{II}F_3$ sample prepared by solid-state method. (b) Rietveld refinement of the laboratory PXRD data collected on a fresh mechanochemically synthesised $Ag^{I}Ag^{II}F_3$ sample measured at 100 K immediately after the synthesis.

Table 29: Crystallographic parameters of $Ag^{I}Ag^{II}F_3$ obtained with the Rietveld refinement of synchrotron data.

$Ag^{I}Ag^{II}F_3$	
Space group	*P−1* (no. 2)
Chemical formula weight (g/mol)	272.73
Z	4
***a*, *b*, *c* (Å)**	5.9577(1), 5.8217(1), 8.5467(2)
α, β, γ (°)	91.565(2), 90.644(2), 85.977(1)
***V* (Å³)**	295.582(6)
Ag1 (*x*, *y*, *z*)	0.0515(8), 0.9834(8), 0.2550(5)
U_{iso}	0.020(2)
Oxidation state	+1
Ag2 (*x*, *y*, *z*)	0.5501(8), 0.5066(8), 0.2444(5)
U_{iso}	0.025(2)
Oxidation state	+1
Ag3 (*x*, *y*, *z*)	0.5, 0, 0
U_{iso}	0.006(3)
Oxidation state	+2
Ag4 (*x*, *y*, *z*)	0, 0.5, 0
U_{iso}	0.005(3)
Oxidation state	+2
Ag5 (*x*, *y*, *z*)	0.5, 0, 0.5
U_{iso}	0.009(3)
Oxidation state	+2
Ag6 (*x*, *y*, *z*)	0, 0.5, 0.5
U_{iso}	0.009(3)
Oxidation state	+2
F7 (*x*, *y*, *z*)	0.064(3), 0.594(3), 0.733(1)
U_{iso}	0.021(6)
F8 (*x*, *y*, *z*)	0.212(3), 0.218(3), 0.559(3)
U_{iso}	0.042(7)
F9 (*x*, *y*, *z*)	0.204(2), 0.198(2), -0.078(2)
U_{iso}	0.008(6)
F10 (*x*, *y*, *z*)	0.310(3), 0.729(3), 0.430(2)
U_{iso}	0.014(6)
F11 (*x*, *y*, *z*)	0.291(2), 0.670(3), 0.046(3)
U_{iso}	0.016(7)
F12 (*x*, *y*, *z*)	0.562(3), 0.893(3), 0.771(1)
U_{iso}	0.014(6)
GOF	2.159
R_{wp}	0.0120

The $Ag^{I}Ag^{II}F_3$ compound is structurally related to the MAgF$_3$ series (M = K, Rb and Cs) [4], but due to the smaller size of the Ag^{+} cation compared to the K^{+}, Rb^{+} and Cs^{+} cations, larger distortions are present and consequently the symmetry is lower. This can be further explained by considering the discrepancy between the ionic radii of the A-site (Ag^{+}) and B-site (Ag^{2+}) cations, which leads to deviations from the ideal perovskite

structure. In the case of $Ag^{I}Ag^{II}F_3$, the smaller size of Ag^+ leads to a *t*-factor that deviates significantly from 1. This deviation typically leads to distortions in the octahedral framework and reduces crystal symmetry compared to analogue compounds with larger A-site cations such as K^+, Rb^+ and Cs^+, whose tolerance factors are closer to 1 and whose crystal structures are more symmetrical.

Table 30: Influence of the ionic radius of the M^+ cation on the crystal symmetry of MAgF$_3$ phases. Goldschmidt tolerance factors (t) were calculated with formula: $t = \frac{r_{M^+} + r_{F^-}}{(r_{Ag^{2+}} + r_{F^-}) \times \sqrt{2}}$, where r_{M^+} is the size of M^+ cation. For the calculations, the values for Ag^{2+} cation and F^- anion of $r_{Ag^{2+}} = 0.94$ Å (CN = 6) and $r_{F^-} = 1.33$ Å (CN = 6) were used.

***M*AgF$_3$ phase**	**Ionic radius of the M^+ cation [Å]**	**Goldschmidt tolerance factor**	**Space group**
$CsAgF_3$	1.88 (CN = 12)	1.00	*I*4/*mcm*
$RbAgF_3$	1.72 (CN = 12)	0.95	*I*4/*mcm*
$KAgF_3$	1.51 (CN = 8)	0.88	*Pnma*
$Ag^{I}Ag^{II}F_3$	1.22 (CN = 7)	0.79	*P*−1

Detailed comparison of the structural properties of the MAgF$_3$ series are provided in Table 30, including $CsAgF_3$, $RbAgF_3$, $KAgF_3$ and $Ag^{I}Ag^{II}F_3$, highlighting the effects of the ionic radius of the M^+ cation on the Goldschmidt tolerance factor and consequently on the crystallographic symmetry of these compounds. When the ionic radius of the M^+ cation decreases from Cs^+ (1.88 Å) to Ag^+ (1.22 Å), the Goldschmidt tolerance factor decreases accordingly from 1.00 to 0.79, reflecting a significant increase in lattice distortions. This trend is reflected in the symmetry of the crystal structures, where compounds with larger cations, such as $CsAgF_3$ and $RbAgF_3$, crystallise in the highly symmetric tetragonal space group *I*4/*mcm*, while the smaller K^+ cation leads to an orthorhombic structure with less symmetry (*Pnma*). The $Ag^{I}Ag^{II}F_3$ phase with the smallest cation and the most distorted lattice crystallises in the triclinic space group *P*−1, which has the lowest symmetry among these compounds.

Despite the differences in the crystal structure, similarities between the Raman spectra of $Ag^{I}Ag^{II}F_3$ and $KAgF_3$ were expected and the peaks were tentatively assigned using the literature reports of Raman spectra of $KAgF_3$ [94] (Figure 65).

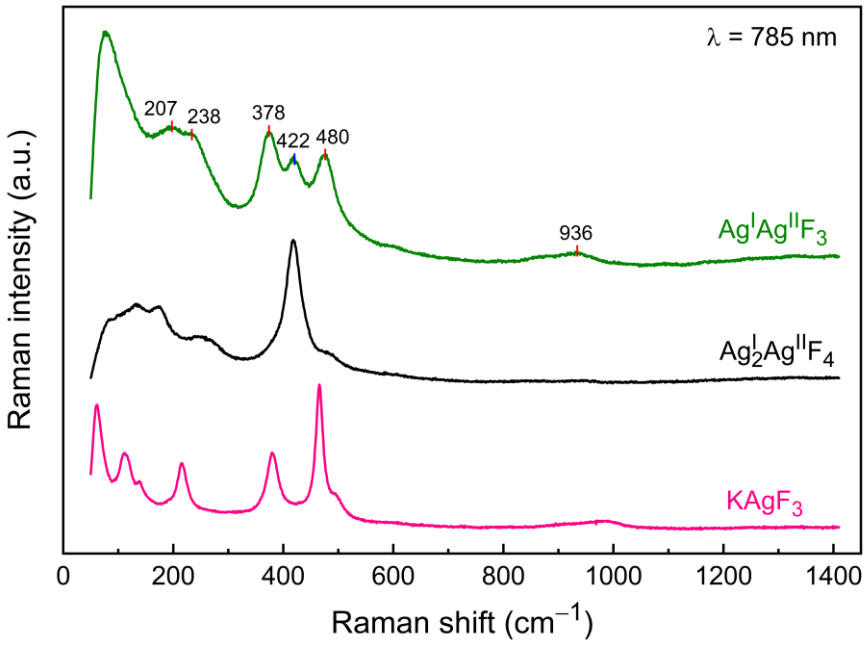


Figure 65: Raman spectra of freshly ball-milled $Ag^{I}Ag^{II}F_3$ and $Ag^{I}_2Ag^{II}F_4$ samples, measured with a 785 nm laser at 1 mW. For comparison, the spectrum of $KAgF_3$ prepared by the solid-state method is also shown.

The peak at 480 cm^{-1} was assigned to the stretching of the $[AgF_6]^{4-}$ octahedron (B_{2g}), but the peak is not completely symmetrical and may contain a left shoulder at about 455 cm^{-1}. The most intense peak at 378 cm^{-1} was attributed to the stretching of the $[AgF_2]$ plane (A_{1g}) and the peak at 207 cm^{-1} to the bending of the $[AgF_6]^{4-}$ octahedron (E_g). Similar to the Raman spectra of $KAgF_3$, there were two broader, less intense peaks between 850 and 950 cm^{-1} that could be attributed to impurity or a combination of two Raman-active modes. The peak at 238 cm^{-1} could not be assigned to any vibrational mode. Despite the very low content of the $Ag^{I}_2Ag^{II}F_4$ phase in the sample (about 3 wt.% according to the Rietveld refinement of the laboratory PXRD data), the most intense peak at 422 cm^{-1} was still observed.

Based on the structural analysis with PXRD and Raman spectroscopy, $Ag^{I}Ag^{II}F_3$ crystallises in $P\bar{1}$ space group and is isostructural with $NaCuF_3$. The crystal structure of $Ag^{I}Ag^{II}F_3$ is shown in Figure 66a while the packing along *c*- and *a*-crystallographic directions is shown in Figure 66b and Figure 66c, respectively.

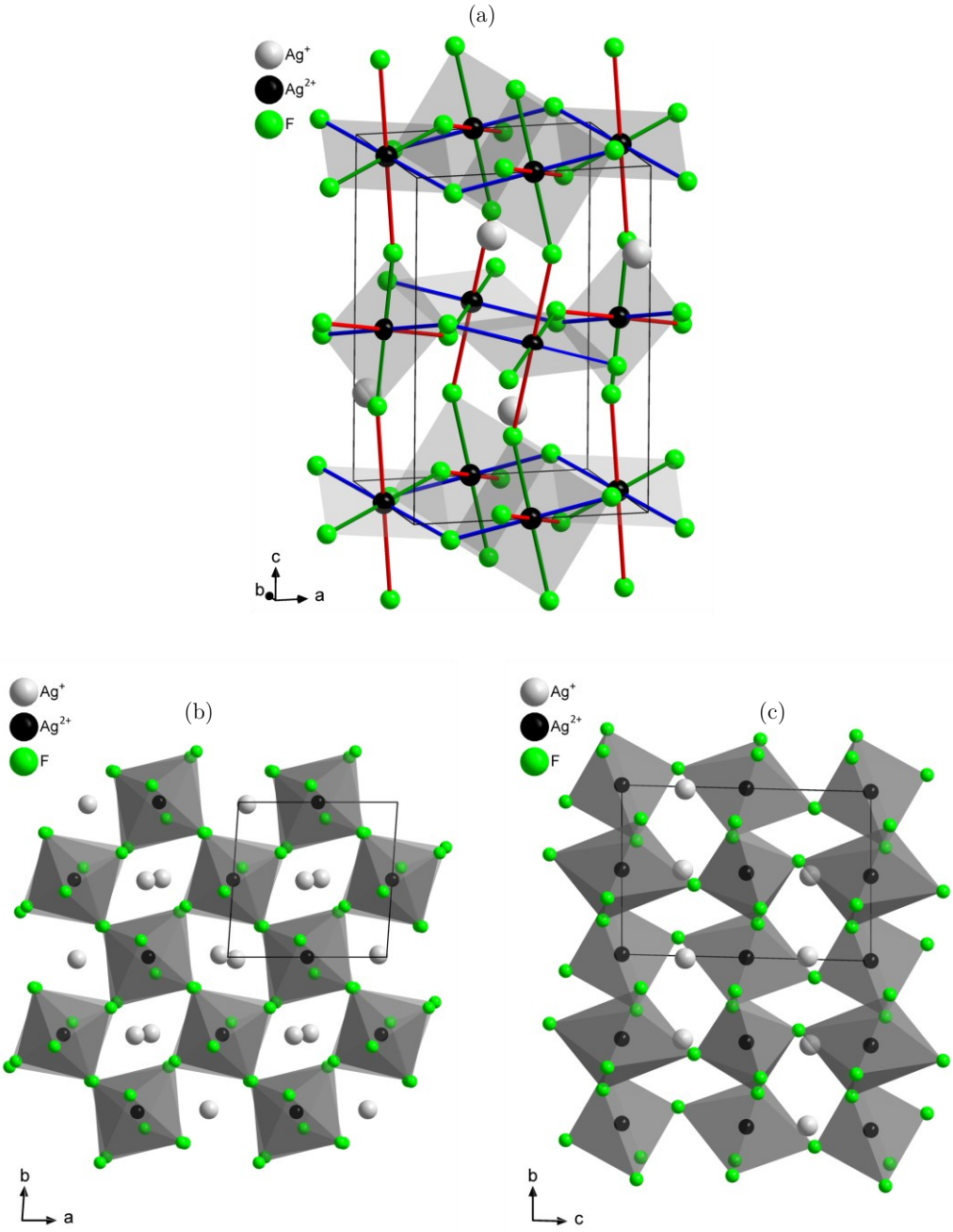


Figure 66: (a) Unit cell of $Ag^{I}Ag^{II}F_3$ with $[AgF_6]^{4-}$ octahedra color-coded by bond length: red = longest, blue = medium, green = shortest. (b) Packing of $[AgF_6]^{4-}$ octahedra along the *c* crystallographic axis. (c) Packing of $[AgF_6]^{4-}$ octahedra along the *a* crystallographic axis.

There are four non-equivalent Ag^{2+} sites and two non-equivalent Ag^{+} sites. Each of the Ag^{2+} cations is coordinated with six fluorine anions and forms an elongated $[AgF_6]^{4-}$ octahedron with two short, two medium and two long Ag—F contacts. The short and medium bond lengths range from 2.072(16) Å to 2.161(13) Å and the longer bond lengths from 2.403(11) Å to 2.441(16) Å. Due to the similar short and medium bond lengths, the octahedron shows axial elongation and is Jahn-Teller active. Similar to the compounds in the $M AgF_3$ series, the corner-sharing $[AgF_6]$ octahedra form a distorted perovskite structure. On the other hand, both non-equivalent Ag^{+} cations are coordinated with seven fluorine atoms with Ag—F contacts ranging from 2.341(16) Å to 3.072(20) Å. The values

obtained from the BVS analysis for Ag^{+} (Table 31) and Ag^{2+} (Table 32) cations agrees well with the expected oxidation states, which provides additional support for the correctness of the determined crystal structure.

Table 31: Interatomic distances and bond valence sum analysis [99] for two silver(I) atoms in $Ag^{I}Ag^{II}F_3$. The following bond valence parameters were employed: $b = 0.37$ Å and $R_0 = 1.80$ Å (Ag^{I}—F) [126, 100].

Interatomic distances (Å)	
Ag1(I)–F9	2.409(15)
Ag1(I)–F12	2.473(17)
Ag1(I)–F7	2.508(17)
Ag1(I)–F10	2.560(17)
Ag1(I)–F8	2.607(19)
Ag1(I)–F11	2.843(18)
Ag1(I)–F8	3.072(20)
Ag2(I)–F7	2.341(16)
Ag2(I)–F11	2.430(17)
Ag2(I)–F10	2.451(19)
Ag2(I)–F12	2.464(18)
Ag2(I)–F9	2.745(19)
Ag2(I)–F8	2.772(15)
Ag2(I)–F11	2.806(20)
Bond valence sum	
Ag1(I)	0.84
Ag2(I)	0.97

Table 32: Interatomic distances and bond valence sum analysis [99] for four silver(II) atoms in $Ag^{I}Ag^{II}F_3$. The following bond valence parameters were employed: $b = 0.37$ Å and $R_0 = 1.79$ Å (Ag^{II}—F) [126, 100].

Interatomic distances (Å)	
Ag3(II)–F12 × 2	2.066(11)
Ag3(II)–F9 × 2	2.147(13)
Ag3(II)–F11 × 2	2.407(16)
Ag4(II)–F11 × 2	2.081(15)
Ag4(II)–F9 × 2	2.161(13)
Ag4(II)–F7 × 2	2.403(11)
Ag5(II)–F10 × 2	2.078(16)
Ag5(II)–F8 × 2	2.115(16)
Ag5(II)–F12 × 2	2.435(11)
Ag6(II)–F7 × 2	2.072(16)
Ag6(II)–F8 × 2	2.087(11)
Ag6(II)–F10 × 2	2.441(16)
Bond valence sum	
Ag3(II)	2.09
Ag4(II)	2.03
Ag5(II)	2.10
Ag6(II)	2.18

In order to gain a deeper insight into the formation of $Ag^{I}Ag^{II}F_3$, a time-dependent milling experiment was carried out. The laboratory PXRD data were collected after every 15 minutes of ball milling and the qualitative and quantitative analysis were performed with Rietveld refinement of the laboratory PXRD data (Figure 67a). The results of this experiment suggest that the 1:1 phase is formed by the reaction of the intermediate $Ag^{I}{}_2Ag^{II}F_4$ with unreacted AgF_2:

$$\mathrm{Ag_2^{I}Ag^{II}F_4 + AgF_2 \rightarrow 2Ag^{I}Ag^{II}F_3} \tag{3.3}$$

The time-dependent milling experiment also revealed that the reaction is finalised after 60 minutes of ball-milling, which is a significant improvement compared to the solid-state synthesis, where the reaction takes approximately 3 days. However, it was observed that the ball-milled $Ag^{I}Ag^{II}F_3$ is metastable at room temperature and slowly decomposes into AgF_2 and $Ag^{I}{}_2Ag^{II}F_4$ (Figure 67b). The phenomenon that the $Ag^{I}Ag^{II}F_3$ phase produced by ball-milling is purer but less stable at room temperature than its counterpart synthesised with the solid-state method could be attributed to several interrelated factors. It is known that ball milling introduces a significant number of structural defects and produces a material with a much larger surface area [51]. These defects, including dislocations and grain boundaries, lower the thermodynamic stability and consequently increase the

reactivity of the material. In addition, the intense mechanical energy during ball-milling can lead to partial amorphization or increased structural disorder, which further impairs the stability of the phase. In contrast, solid-state synthesis typically results in a more ordered structure with fewer defects, resulting in a material that may contain more impurities but is more stable over time.

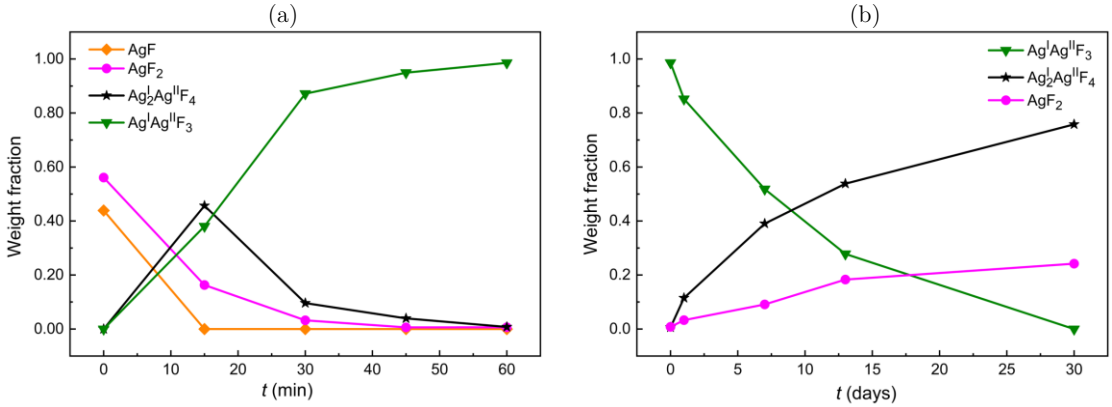


Figure 67: (a) Weight fractions of phases in the samples obtained by Rietveld refinement of laboratory PXRD data during the milling experiment. (b) Time-dependent phase composition of mechanochemically synthesized $Ag^{I}Ag^{II}F_3$ over 30 days, obtained by Rietveld refinement.

Due to the higher purity of the $Ag^{I}Ag^{II}F_3$ phase in the ball-milled sample with about 96 wt.% compared to only about 57 wt.% in the solid-state synthesised sample, the ball-milled sample was selected for magnetic measurements. However, as the ball-milled $Ag^{I}Ag^{II}F_3$ tends to decompose over time, the magnetic measurements were immediately performed on a freshly synthesised sample. The magnetic susceptibility data shown in Figure 68 indicates a ferromagnetic transition at 164 K, which can be attributed to AgF_2 quantified to less than 1 wt.% by Rietveld refinement of the laboratory data. This level of impurity is consistent with the observed magnetic susceptibility. In addition, a second ferromagnetic transition at around 3 K indicates the presence of $Ag^{I}{}_2Ag^{II}F_4$ impurities, which is confirmed by both laboratory PXRD laboratory PXRD data and Raman spectroscopy. In particular, a deviation from the Curie-Weiss law is observed at lower temperatures, indicating a weak antiferromagnetic transition with $T_N = 7.3(7)$ K, as determined from the maximum of the first derivative of the magnetic susceptibility. These results indicate that $Ag^{I}Ag^{II}F_3$ might exhibit a weak a 1D antiferromagnetic behaviour similar to the compounds in the MAgF$_3$ series.

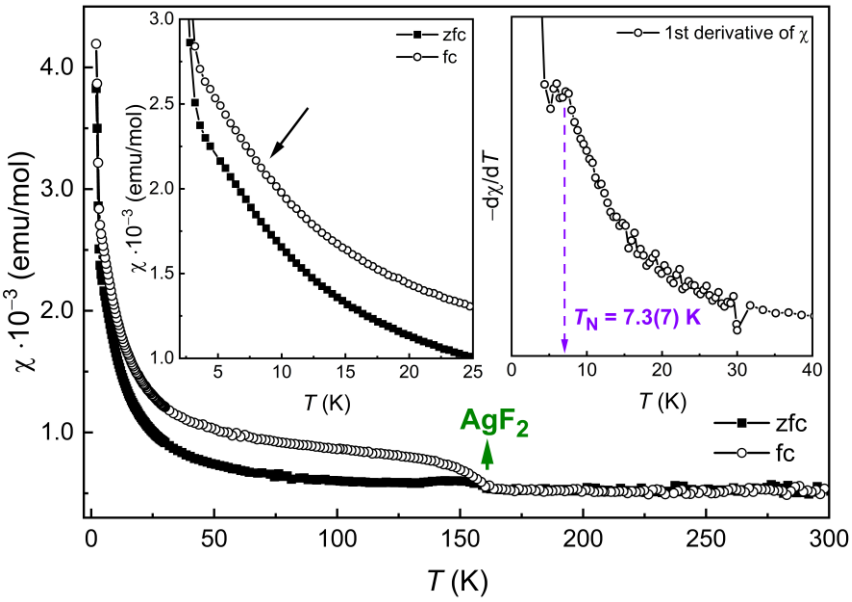


Figure 68: Temperature-dependent susceptibility, χ, of $Ag^{I}Ag^{II}F_3$, measured in a magnetic field of 1 kOe. The left inset shows magnified 2–25 K region and the right inset shows the first derivative of the magnetic susceptibility as a function of temperature, where the transition temperature of 7.3(7) K was determined.

The antiferromagnetic nature of $Ag^{I}Ag^{II}F_3$ is also supported by the values of the effective magnetic moment, μ_{eff}, at 300 K, which falls well below the theoretically expected value of 1.7 μ_B, reaching only 0.8 μ_B (Figure 69a). The effective magnetic moment further decreases with temperature and falls to about 0.2 μ_B, indicating dominant antiferromagnetic interactions throughout the investigated temperature range. Furthermore, magnetisation measurements as a function of magnetic field show that the magnetic moment des not saturate even at high magnetic fields, strongly suggesting persistent antiferromagnetic interactions (Figure 69b). The presence of weak hysteresis at low fields is probably due to traces of $Ag^{I}_2Ag^{II}F_4$ impurities.

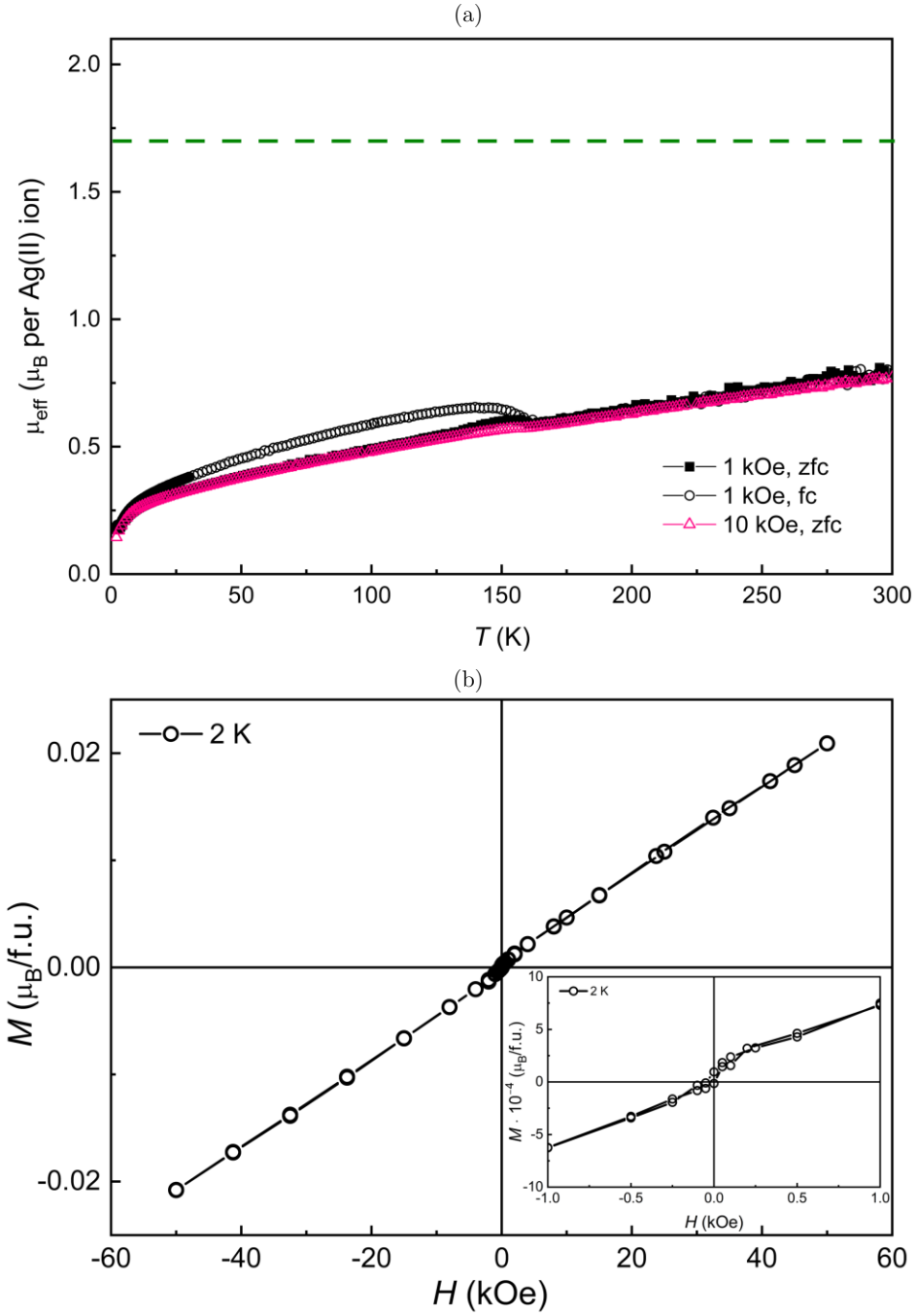


Figure 69: (a) Plot of the effective magnetic moment, μ_{eff}, as a function of temperature for field cooled and ZFC curves at 1 kOe and for the ZFC curve measured at 10 kOe. (b) Magnetization of $Ag^{I}Ag^{II}F_3$ as a function of magnetic field, measured at 2 K.

The mechanochemical synthesis of $Ag^{I}Ag^{II}F_3$ via ball-milling yields a metastable phase that, despite its thermodynamic instability, exhibits structural motifs consistent with the $AgCuF_3$ parent structure and displays 1D antiferromagnetic behaviour analogous to the $M AgF_3$ series (M = K, Rb, Cs). The synthesis of this kinetically stabilised phase, through a solvent-free, low-temperature synthetic route, exemplifies the unique advantages of mechanochemistry in accessing metastable compositions that would be inaccessible through conventional high-temperature methods. This discovery not only broadens the

compositional space of mixed-valent fluoridoargentates but also demonstrates the potential of mechanochemical strategies to bypass thermal decomposition pathways, thereby offering a promising methodology for the rational synthesis of new Ag^{2+}-based compounds with tailored magnetic and electronic properties.

3.4 Exploring the Ternary Systems Ag–Y–F and Ag–Bi–F: Synthesis of $Ag^{I}Ag^{II}_{2}YF_{8}$ and $Ag^{I}Ag^{II}_{2}BiF_{8}$

The field of fluoridoargentates(II) chemistry initially gained momentum through research on cuprate superconductors, where the layered structures of high-temperature superconductors inspired researchers to substitute Cu^{2+} with Ag^{2+} and O^{2-} with F^{-}, aiming to investigate analogous structural motifs. Of particular interest are ternary systems containing trivalent cations in combination with Ag^{2+} and F^{-}, inspired by La_2CuO_4, the parent compound of the cuprate superconductors. However, the literature lacks reports on such ternary systems containing trivalent cations like Y^{3+} or Bi^{3+} with Ag^{2+} and fluorine. This research therefore aims to explore the Ag-Y-F and Ag-Bi-F ternary systems, with the goal of identifying novel phases that could display unique structural, magnetic, or electronic properties, advancing the understanding of fluoridoargentate chemistry and its potential applications.

3.4.1 $Ag^{I}Ag^{II}_{2}YF_{8}$

Aside from $AgYF_4$ [128], where silver is stabilised in the +1 oxidation state, there are no prior reports on ternary Ag–Y–F phases in the literature or the ICSD database. To explore the ternary phase diagram of the Ag–Y–F system, a series of preliminary studies was initiated employing conventional solid-state synthesis. In these experiments, various AgF_2:YF_3 molar ratios (1:1, 3:2, 2:1 and 3:1) were systematically tested. Analysis of the resulting samples by both PXRD and Raman spectroscopy revealed a consistent trend: for the 1:1, 3:2, and 2:1 molar ratio, the AgF_2 precursor was entirely consumed, whereas some YF_3 remained detectable in the final products. Unexpectedly, no AgF peaks were observed, despite synthesis temperatures between 450 and 500 °C—well above the known decomposition temperature of AgF_2 to AgF (~360 °C).

The absence of AgF reflections strongly suggests the formation of a new mixed-valence Ag^{2+} phase rather than simple decomposition products. A near-complete conversion of reagents to product was achieved with a reagent molar ratio of AgF_2:YF_3 = 3:1, wherein 0.5 mmol of YF_3 and 1.5 mmol of AgF_2 were combined in a glove box, thoroughly homogenised for 15 minutes in an agate mortar, and subsequently annealed in a platinum crucible (synthesis conditions listed in Table 33). The reaction product exhibited two visually distinct regions: a green layer and a yellow layer. Both regions were manually separated for further analysis. It was also observed that the green part of the sample changed colour to black upon exposure to atmosphere. This feature is typical for Ag^{2+}–based compounds, since Ag^{2+} cation is reduced to Ag^{+} when it reacts with atmospheric moisture and in many cases, the reduction is accompanied by colour change from the starting colour into black. This observation provided an initial indication that the green region contains Ag^{2+} cations. In contrast, the yellow region retained its original colour when exposed to air, suggesting the absence of Ag^{2+} cations, although additional analyses were required to confirm this finding

Table 33: Conditions for the synthesis of $Ag^{I}Ag^{II}_{2}YF_{8}$ with three different methods.

Synthesis method	Synthesis conditions
Solid-state synthesis (SS)	Two cycles for 72 h at 490 °C, the sample was homogenised for 15 min between the cycles
Ball-milling (BM)	AgF_2:YF_3=3:1, ν = 30 Hz, 15 minute milling cycle, 4 hours total milling time, 15 mm diameter of tungsten carbide milling ball
Ball-milling with annealing step (BMA-350)	48 h at 350 °C

A phase with the formula $Ag^{I}Ag^{II}_{2}YF_{8}$ was identified in a green part of the SS sample and its crystal structure was determined via 3D electron diffraction. The investigated compound crystallises in the orthorhombic *Cccm* space group with the following unit cell parameters: $a = 7.8615$ Å, $b = 10.9849$ Å and $c = 7.7529$ Å. Its unit cell is shown in Figure 70a and the atomic parameters are listed in Table 34. There are two non-equivalent Ag^{2+} atoms in the crystal structure, Ag3 and Ag4. They are both coordinated with eight fluorine anions forming $[AgF_8]^{6-}$ units, however with slightly different distances between the central atom and their ligands. The first one, Ag3, exhibits four shorter (2.057(2) Å), two medium (2.569(3) Å) and two longer (3.101(3) Å) Ag–F contacts, which corresponds to [4+2+2] coordination (Figure 70b). On the other hand Ag4 atom exhibits two short (2.013(3) Å), two medium (2.149(3) Å) and four long (2.766(2) Å) Ag–F contacts (Figure 70c). Because the two shorter and two medium contacts are similar in length, the coordination of Ag4 cation could be viewed as [4+4] coordination. Interatomic distances and BVS analysis are listed in Table 35.

The crystal structure of Ag_3BiF_8 is defined by a layered arrangement that imparts a 2D character to the compound. Edge-sharing $[AgF_8]^{6-}$ units form layers in the *ac* plane (Figure 70d), which are separated with layers of Y^{3+} and Ag^{+} cations (Figure 70e). Both non-magnetic cations are eightfold coordinated by F^{-} anions, adopting a distorted square antiprismatic geometry with a [4+4] coordination. In this configuration, the Ag^{+} centers exhibit four shorter Ag–F contacts at 2.522(2) Å and four longer contacts at 2.677(2) Å, while the Y^{3+} cations display four shorter bonds at 2.204(2) Å and four longer bonds at 2.298(2) Å.

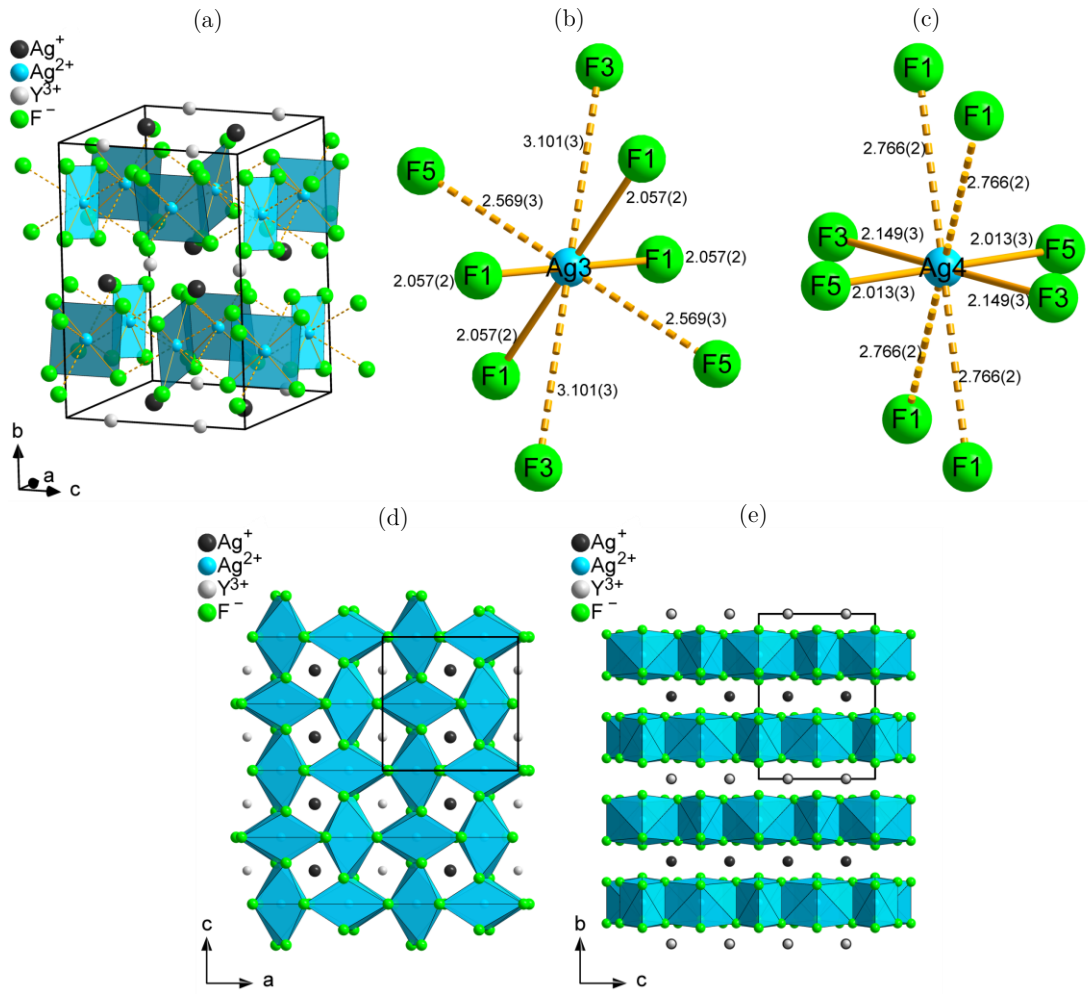


Figure 70: (a) Expanded unit cell of $Ag^{I}Ag^{II}_{2}YF_{8}$, where four short Ag–F contacts around Ag^{2+} cations are presented as square plaquettes; coordination surroundings with atom distances in Å for both non-equivalent divalent silver cations in the crystal structure – (b) Ag3 and (c) Ag4. (d) Single-layer of edge-sharing $[AgF_8]^{6-}$ units viewed along *b*-crystallographic direction. (e) Packing of $Ag^{I}Ag^{II}_{2}YF_{8}$ viewed along *a*-crystallographic direction.

Table 34: Atomic parameters for $Ag^{I}Ag^{II}_{2}YF_{8}$ determined via 3D ED.

Element	**Symbol**	***x***	***y***	***z***	U_{eqc}
Ag^{+}	Ag1	1	0.5	0.25	0.0135(2)
Ag^{2+}	Ag3	1.25	0.75	0.5	0.00638(17)
Ag^{2+}	Ag4	0.75	0.75	0.5	0.00744(17)
Y^{3+}	Y1	1.5	0.5	0.25	0.00373(16)
F^{-}	F1	1.2874(2)	0.6246(2)	0.3069(2)	0.0074(3)
F^{-}	F3	0.5808(3)	0.5963(3)	0.5	0.0057(4)
F^{-}	F5	0.9588(3)	0.6439(3)	0.5	0.0097(4)

Table 35: Interatomic distances and bond valence sum for all atoms in $Ag^{I}Ag^{II}_{2}YF_{8}$.

Interatomic distances (Å)	
Ag1(I)–F5 x 4	2.522(2)
Ag1(I)–F1 x 4	2.677(2)
Ag3(II)–F1 x 4	2.057(2)
Ag3(II)–F5 x 2	2.569(3)
Ag3(II)–F5 x 2	3.101(3)
Ag4(II)–F5 x 2	2.013(3)
Ag4(II)–F3 x 2	2.149(3)
Ag4(II)–F1 x 4	2.766(2)
Y1(III)–F1 x 4	2.204(2)
Y1(III)–F3 x 4	2.298(2)
Bond valence sum	
Ag1(I)	0.94
Ag3(II)	2.25
Ag4(II)	2.14
Y1(III)	3.16

To verify phase purity and confirm the correctness of the determined crystal structure, synchrotron PXRD was collected on the green SS $Ag^{I}Ag^{II}_{2}YF_{8}$ sample (Figure 71a). The structural model obtained with 3D ED provided an excellent fit to the room-temperature powder data with similar unit cell parameters: $a = 7.9329(1)$ Å, $b = 11.0809(3)$ Å and $c = 7.8182(2)$ Å. Beside the investigated compound, small amounts of unreacted reagents (AgF_2 and YF_3) were detected in the synchrotron PXRD data and quantified with Rietveld refinement analysis. In contrast to the PXRD data collected on the green SS sample where the vast majority of the sample constituted of the $Ag^{I}Ag^{II}_{2}YF_{8}$ phase, the laboratory PXRD data collected on the yellow SS sample revealed a highly complex pattern, suggesting that the sample consists of multiple phases (Figure 71b).

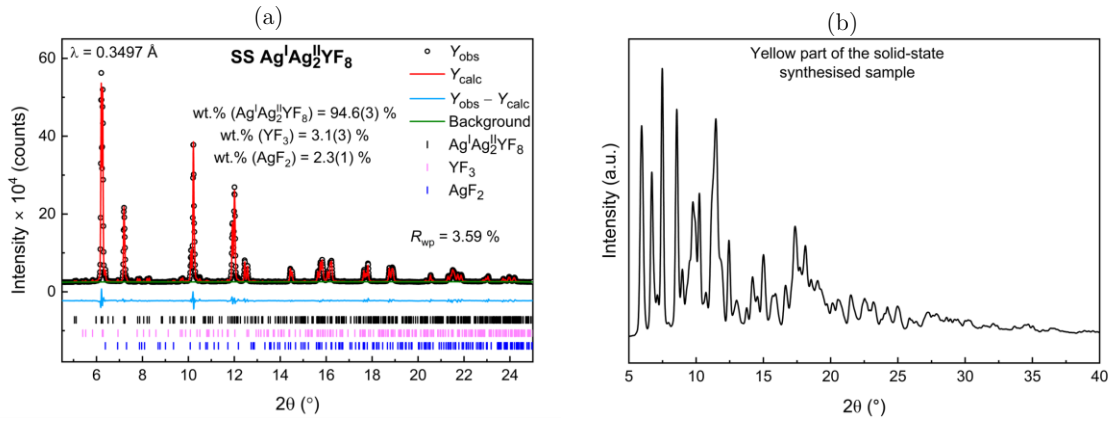


Figure 71: (a) Rietveld refinement of the synchrotron PXRD data collected on the green part of the solid-state synthesised $Ag^{I}Ag^{II}_{2}YF_8$ sample. (b) Laboratory PXRD data collected on the yellow part of the solid-state synthesised sample.

The formation of $Ag^{I}Ag^{II}_{2}YF_8$ can be rationalised by the proposed reaction mechanism:

$$3AgF_2 + YF_3 \rightarrow 2AgF_2 + AgF + \frac{1}{2}F_2 + YF_3 \rightarrow Ag^{I}Ag^{II}_{2}YF_8 + \frac{1}{2}F_2 \tag{3.4}$$

In the first step, AgF_2 starts to decompose when the reaction temperature reaches 360 °C and yields AgF. The decomposition, however, is only partial. In the second step, AgF reacts with YF_3 and the remaining AgF_2 to form the mixed-valence phase. However, a significant drawback of the thermal solid-state synthesis approach is its propensity to yield multiphase samples. In this case, the reaction product segregated into two visually distinct regions, which is undesirable for precise magnetic characterisation.

Another significant challenge arises from the properties of AgF, which has a melting point of approximately 435 °C. Since the reaction must be performed at temperatures above 450 °C to achieve a reasonable rate, AgF becomes volatile and condenses on the reactor walls, thereby altering the intended stoichiometry. Moreover, at these temperatures, AgF_2 gradually reacts with the platinum crucible. This phenomenon was observed upon completion of the reaction. To circumvent these issues, a mechanochemical approach was employed, followed by an annealing step, which proved effective in yielding phase-pure $Ag^{I}Ag^{II}_{2}YF_8$ (synthesis conditions listed in Table 33). Importantly, this method is both reproducible and scalable, a crucial advantage for subsequent NPD measurements.

The laboratory PXRD data and Raman spectra of the BMA-350 sample confirmed successful reaction with no detectable AgF_2 or YF_3 (Figure 72a and Figure 72b). In contrast to the BMA-350 sample, peaks associated with YF_3 were present in PXRD and Raman data of the BM sample. This indicates that ball-milling alone was insufficient for the complete conversion of reagents to the targeted $Ag^{I}Ag^{II}_{2}YF_8$ phase. Subsequent annealing of the ball-milled sample was therefore essential to complete the reaction. However, the annealing temperature and time required were significantly reduced compared to the conventional solid-state synthesis. An exceptional sample purity was achieved, as verified by Rietveld refinement of the laboratory PXRD data (Figure 72c).

The Raman spectrum of $Ag^{I}Ag^{II}_{2}YF_8$, shown in Figure 72d, reveals a series of peaks spanning from 74 to 509 cm^{-1}. A rigorous interpretation of Raman spectra goes beyond peak assignment based solely on comparative literature. Point group analysis should be carried out to identify Raman-active modes, and simulations of the spectra (e.g., using DFT calculations) are essential for reliable interpretation, as is standard practice in the field.

The laboratory PXRD analysis confirmed that the BMA-350 sample of $Ag^{I}Ag^{II}_{2}YF_{8}$ is single-phase, making it well suited for further magnetic characterisation. Magnetic susceptibility measurements were carried out over the temperature range from 300 K to 2 K. The data shows that the sample exhibits paramagnetic behaviour from 300 K down to approximately 12 K.

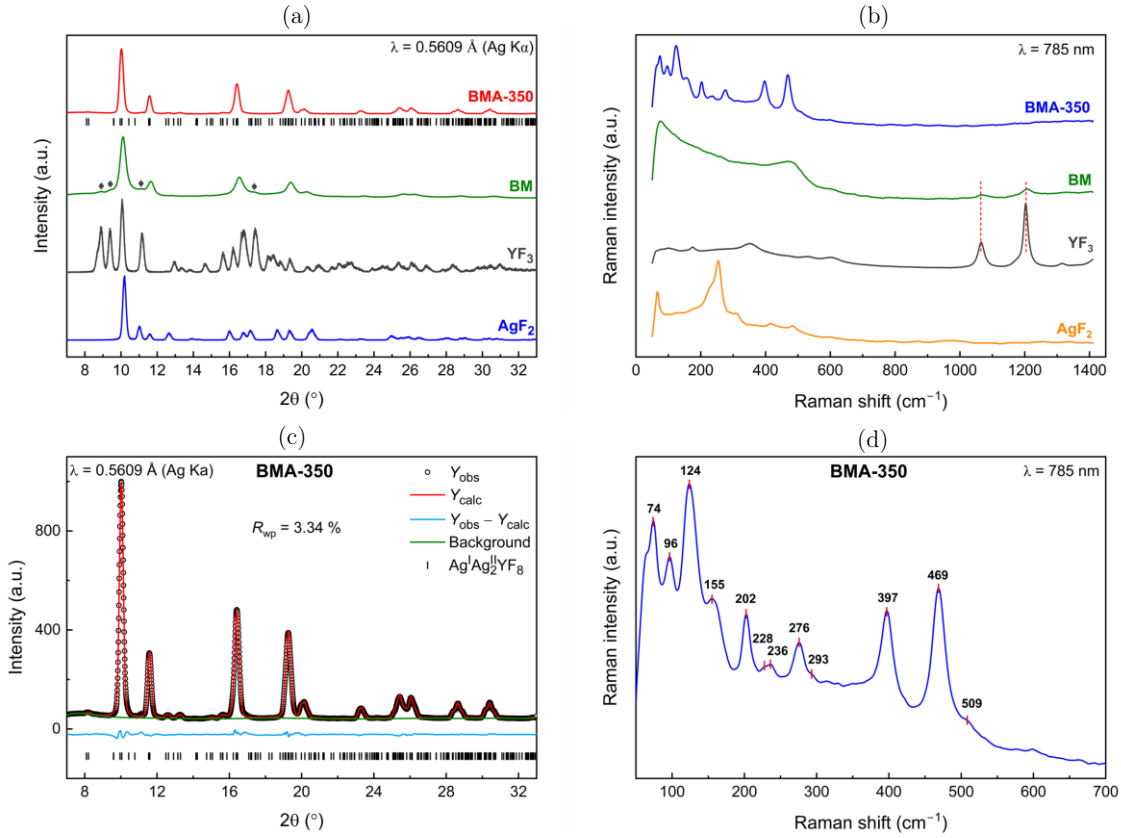


Figure 72: Comparison of (a) PXRD patterns and (b) Raman spectra of the starting materials (YF_3 and AgF_2), along with the BM and BMA-350 samples. Black squares in the PXRD pattern of the BM sample indicate reflections from YF_3. (c) Rietveld refinement of laboratory PXRD data collected for the BMA-350 sample. (d) Raman spectra of the BMA-350 sample with indicated peak positions.

Below 12 K, a pronounced drop in susceptibility is observed, indicative of the onset of antiferromagnetic ordering (Figure 73a). Fisher's heat capacity analysis allowed to precisely determine the T_N of 11.6(1) K [81] (inset in the Figure 73a).

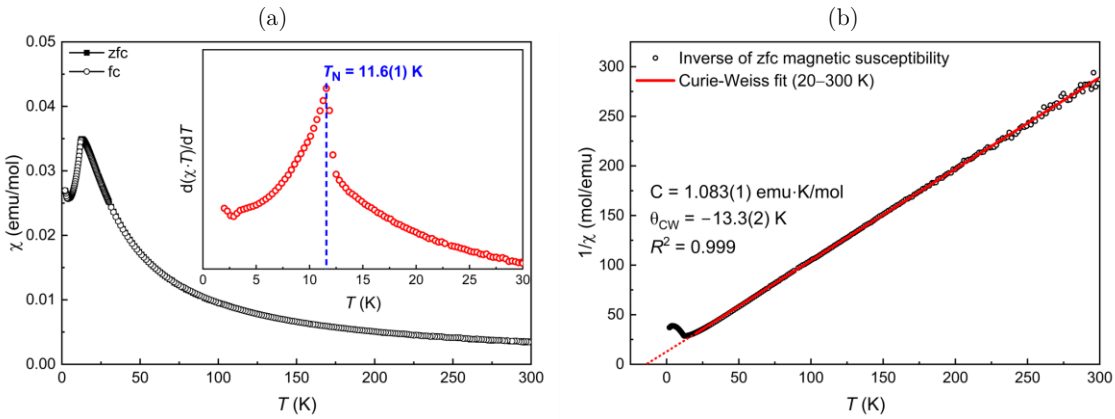


Figure 73: (a) Magnetic susceptibility of BMA-350 sample measured as a function of temperature in the field of 1 kOe. An inset shows Fisher's heat capacity, where the transition temperature of 11.6(1) K was determined. (b) Curie-Weiss fit to the inverse of ZFC magnetic susceptibility measured as a function of temperature.

With the main aim to determine the magnetic structure and additionally more accurately determine the position of fluorine atoms in the crystal structure, NPD data was collected on BMA-350 sample of $Ag^{I}Ag^{II}_{2}YF_8$. Rietveld refinement of the NPD data collected at 15 K yielded a slightly smaller unit cell than the one obtained from synchrotron X-ray diffraction data collected at room temperature, with refined lattice parameters of $a = 7.8755(4)$ Å, $b = 11.0216(6)$ Å, and $c = 7.7776(4)$ Å (Figure 74a). This discrepancy in unit cell size is consistent with the thermal contraction expected at lower temperatures. The Rietveld refinement of the NPD data provided a relatively good fit with an R_{wp} value of 4.08%, which agrees well with the crystal structure determined via 3D ED.

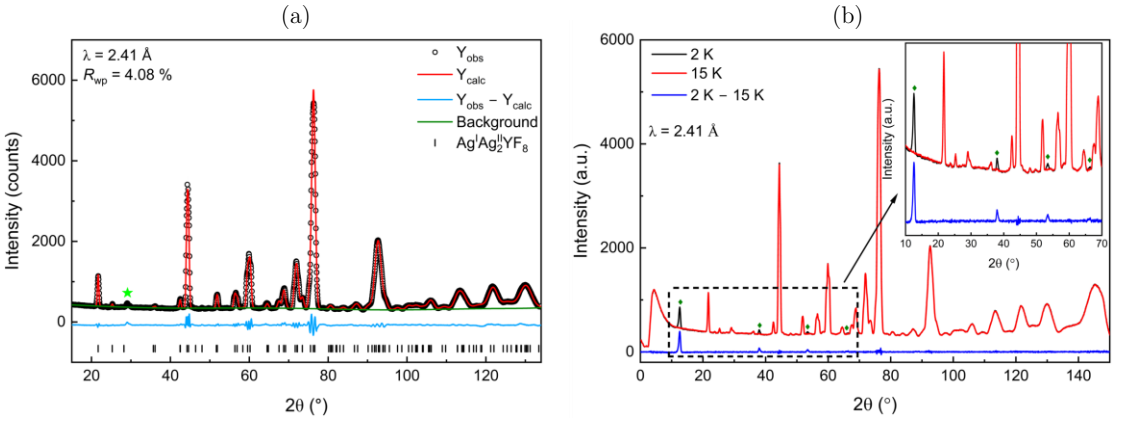


Figure 74: (a) Rietveld refinement of the NPD data collected on the BMA-350 sample at 15 K. Green star marks one unidentified peak. (b) The NPD data measured at 2 and 15 K and the difference plot. The inset shows region where magnetic peaks are observed (marked with dark green squares).

To further investigate the magnetic structure of $Ag^{I}Ag^{II}_{2}YF_8$, the NPD data collected below and above the magnetic transition temperature were compared. Four magnetic peaks emerged at low temperatures, providing key evidence for magnetic ordering in this compound. Using the FULLPROF suite, the magnetic propagation vector $k = [0, 1, 0]$ was determined, which was identified as the only commensurate solution suggested by the program. This propagation vector yielded three maximal magnetic space groups (P_Cccn, P_Amna and P_Cnnn), as calculated using the Bilbao Crystallographic Server [85, 86, 87].

However, attempts to fit the observed NPD data with any of these magnetic space groups were unsuccessful. This means that the magnetic structure may be incommensurate, which will require additional computational methods in order to elucidate the magnetic structure of the investigated phase.

In summary, $Ag^{I}Ag^{II}_{2}YF_{8}$ was synthesized using both high-temperature solid-state and mechanochemical methods. The mechanochemical approach, followed by a mild annealing step, was particularly effective, producing a phase-pure product suitable for detailed magnetic characterization. The crystal structure, determined via 3D ED, is orthorhombic with *Cccm* space group, featuring edge-sharing $[AgF_8]^{6-}$ units that form layers in the ac plane and give the compound a quasi-2D character. PXRD and NPD measurements confirmed the 3D ED structure. Magnetic susceptibility data show paramagnetic behavior from 300 K down to ~12 K, with a clear antiferromagnetic transition at 11.6(1) K, as determined from Fisher's heat capacity analysis.

3.4.2 $Ag^{I}Ag^{II}_{2}BiF_{8}$

Since the reaction between AgF_2 and YF_3 yielded $Ag^{I}Ag^{II}_{2}YF_{8}$, it was explored whether other trivalent cations could form stable phases with the general formula $Ag^{I}Ag^{II}_{2}MF_{8}$. The primary criterion guiding the selection of MF_3 precursors was the ionic radius of the M^{3+} cation for CN = 8. In our laboratory, LaF_3 and BiF_3 were readily available, with ionic radii 1.16 Å and 1.17 Å, respectively. These values differ by only approximately 14 % from the ionic radius of Y^{3+} for CN = 8, making LaF_3 and BiF_3 ideal candidates for investigating analogous $Ag^{I}Ag^{II}_{2}MF_{8}$ phases.

Using the synthetic approach previously established for the $Ag^{I}Ag^{II}_{2}YF_{8}$ phase (Table 33), analogous lanthanum-containing phase was targeted. However, Rietveld refinement of the laboratory PXRD data of the BM sample indicated the presence of only LaF_3 and AgF_2, suggesting that no new phase had formed through the milling process. After the ball-milled sample was annealed, additional peaks emerged in the laboratory PXRD data. Qualitative analysis attributed these new reflections to $Ag^{I}Ag^{II}F_3$ rather than a novel Ag–La–F phase. This observation was further supported by Rietveld refinement of the PXRD data from the annealed sample, which confirmed the composition as: $Ag^{I}Ag^{II}F_3$, LaF_3, and AgF_2. The weight fraction of LaF_3 remained nearly constant before and after annealing, indicating that LaF_3 was not incorporated into any reaction product, nor was it consumed during the milling or annealing stages. These findings suggest that under these reaction conditions, the targeted $Ag^{I}Ag^{II}_{2}LaF_{8}$ phase or any other novel Ag–La–F phase did not form.

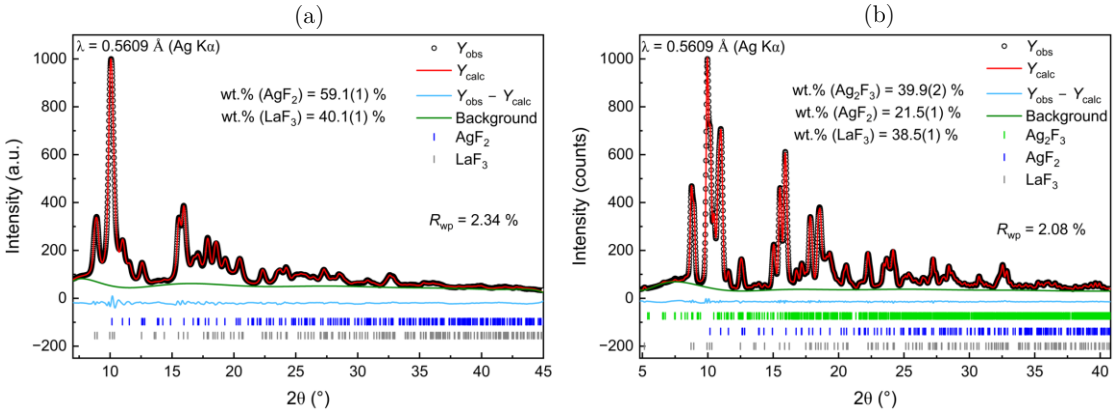


Figure 75: Rietveld refinement of the laboratory PXRD data collected on (a) BM sample and (b) BMA-350 sample.

On the other hand, the preliminary experiments with BiF_3 suggested that new phase or phases are formed. Initially, the solid-state method was employed, using a 3:1 molar ratio of AgF_2 to BiF_3, with the mixture annealed at temperatures between 450 °C and 490 °C. However, in most trials, the reaction led to the formation of a black melt at the base of the platinum crucible, indicating decomposition of the sample. In one partially successful experiment, a modified molar ratio of 1:2.2 was used, and the mixture was annealed at 450 °C for 48 hours. Qualitative analysis shown in Figure 76 (red PXRD pattern) revealed that the sample constitutes of both unreacted starting materials and additional unidentified peaks, suggesting the formation of a new compound in the Ag–Bi–F system. Further investigation involved a combination of ball-milling with subsequent annealing at 350 °C for 48 hours. The comparison of the laboratory PXRD data collected on SS and BMA samples suggested the formation of the same new Bi–Ag–F phase (Figure 76). However, in contrast to the solid-state synthesis, the BMA sample contained fewer unreacted reagents, evidenced by the weaker intensity of the most intense reflection of AgF_2 (located at ~10.2° 2θ) and the two BiF_3 peaks at ~9.3° 2θ.

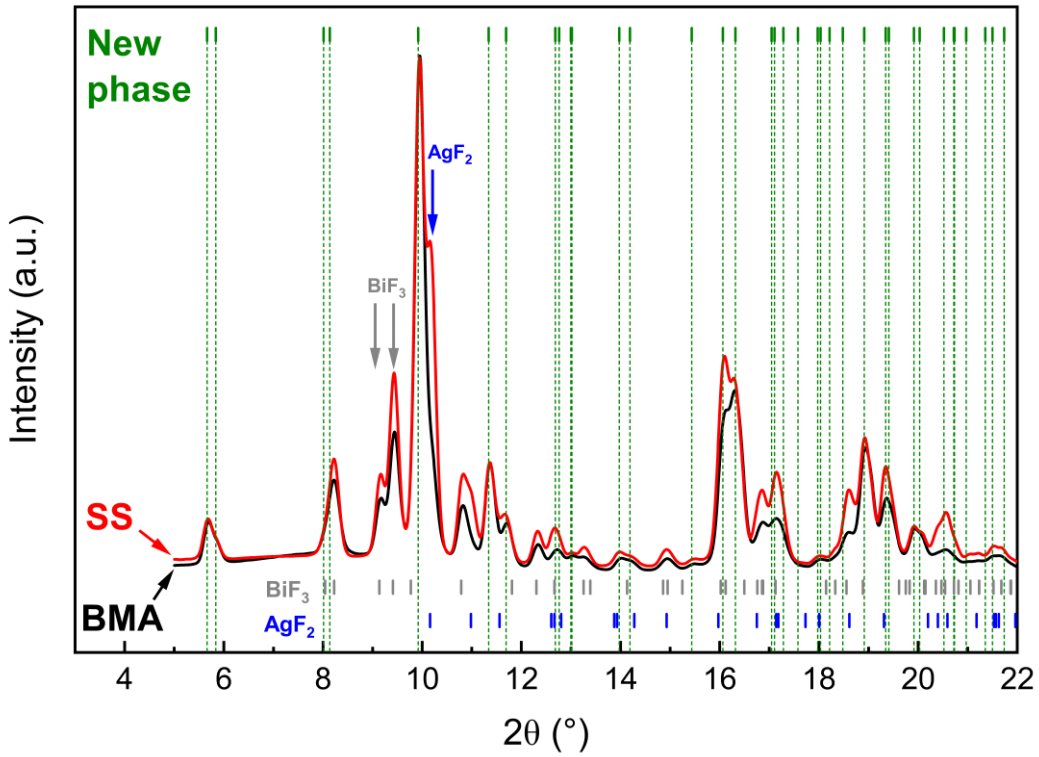


Figure 76: Comparison of the laboratory PXRD data collected on the SS (red pattern) and BMA (black pattern) samples using Ag Kα radiation (λ = 0.5609 Å). Green broken lines represent peaks of the new Ag–Bi–F phase.

The BMA sample was selected for further structural analysis using 3D ED, which enabled the successful determination of the crystal structure. The resulting phase was confirmed as $Ag^{I}Ag^{II}_2BiF_8$, with analogous formula to $Ag^{I}Ag^{II}_2YF_8$. Interestingly, $Ag^{I}Ag^{II}_2BiF_8$ crystallises in a different symmetry, adopting a tetragonal structure in the $P4/mcc$ space group with unit cell parameters $a = 5.740(2)$ Å and $c = 11.155(2)$ Å (Figure 77a). The divalent silver cation is coordinated with eight fluorine anions with four shorter (2.113(2) Å) and four longer (2.905 Å) Ag–F contacts, forming an $[AgF_8]^{6-}$ unit (Figure

77b). In contrast to $Ag^{I}Ag^{II}_{2}YF_{8}$, where the four fluorine anions closets to the Ag^{2+} cation lie in the same plane, here they form a tetrahedra around Ag^{2+} cation, which is quite rare coordination in the chemistry of divalent silver. The crystal packing in $Ag^{I}Ag^{II}_{2}BiF_{8}$ features a layered, 2D structure of edge-sharing $[AgF_{8}]^{6-}$ units extending within the *ab* plane, with Ag^{+} and Bi^{3+} cations occupying interlayer spaces (Figure 77c and Figure 77d). Both Ag^{+} and Bi^{3+} ions are coordinated with eight fluorine anions with equal bond lengths (2.578(3) Å for Ag^{+} and 2.392(2) Å for Bi^{3+}). Positions of atoms in the crystal structure and anisotropic displacement parameters are listed in Table 36. Additionally, the BVS analysis summarised in Table 37, supports the expected oxidation states of all cations, further corroborating the structural model.

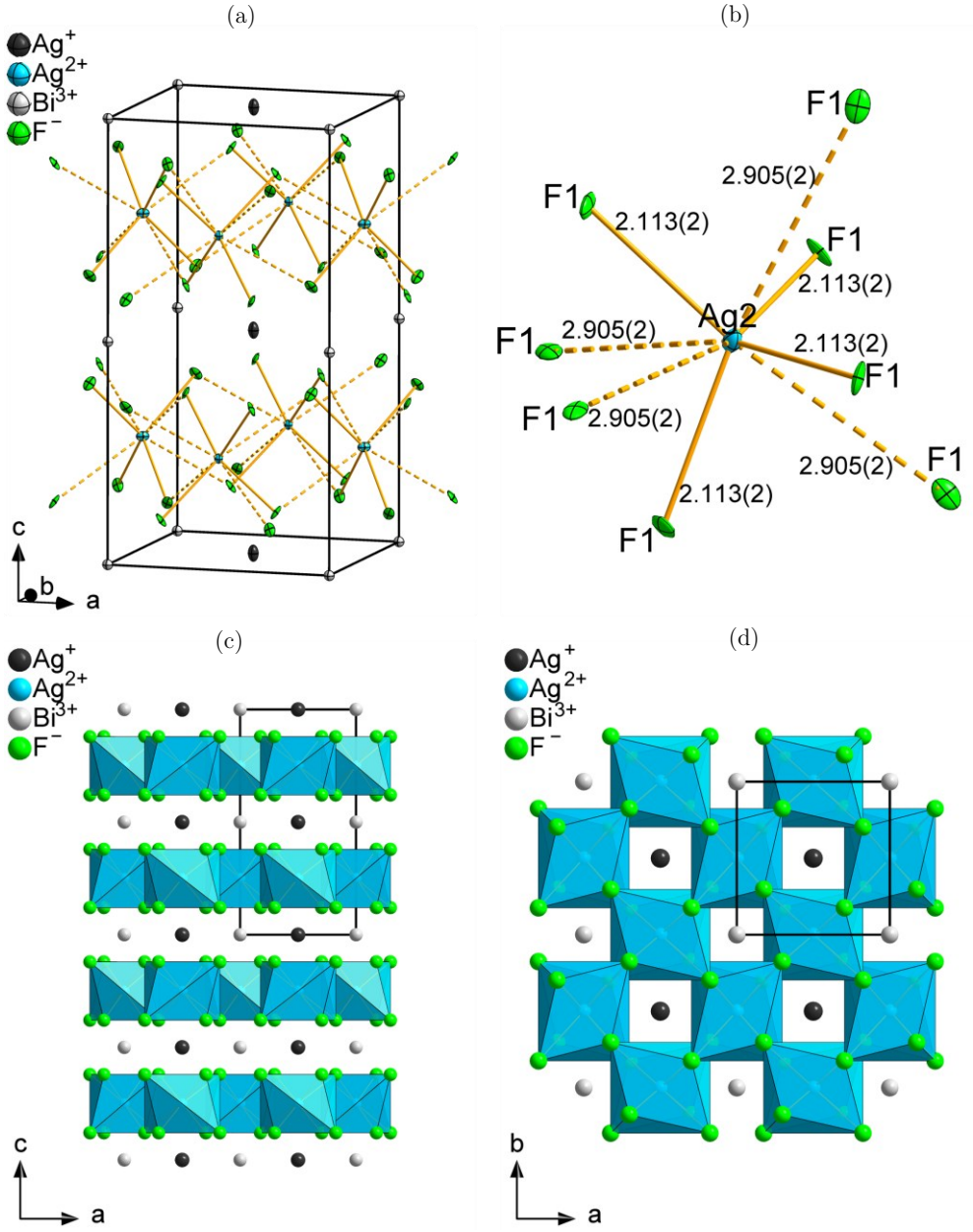


Figure 77: (a) Unit-cell of $Ag^{I}Ag^{II}_{2}BiF_{8}$. Shorter Ag–F contacts are represented with full orange bonds while longer Ag–F contacts are represented with broken orange bonds. Ellipsoids are drawn with 50 % probability. (b) Coordination surroundings of Ag2 (Ag^{2+}) cation with bond distances in Å. Crystal packing shown along (b) *b*-crystallographic direction and (c) *c*-crystallographic direction.

Table 36: Positions of atoms and atomic displacement parameters in the crystal structure of $Ag^{I}Ag^{II}_{2}BiF_{8}$ determined via 3D ED.

Element	Symbol	*x*	*y*	*z*	U_{eq}
Ag^{+}	Ag1	−0.5	−0.5	0	0.0099(4)
Ag^{2+}	Ag2	0	−0.5	0.25	0.0063(3)
Bi^{3+}	Bi1	0	0	0	0.0065(3)
F^{-}	F1	−0.1757(4)	−0.2964(4)	0.1207(2)	0.0076(6)

Table 37: Interatomic *M*–F (M = Ag^{+}, Ag^{2+}, Bi^{3+}) distances and BVS analyses for $Ag^{I}Ag^{II}_{2}BiF_{8}$.

Interatomic distances (Å)	
Ag1(I)–F1 x 8	2.578(3)
Ag2(II)–F1 x 4	2.113(2)
Ag2(II)–F1 x 4	2.905(3)
Bi1(III)–F1 x 8	2.392(2)
Bond valence sum	
Ag1(I)	0.98
Ag2(II)	1.87
Bi1(III)	2.7

Following the successful determination of the crystal structure using 3D ED, it was confirmed that bismuth indeed forms the compound with the formula $Ag^{I}Ag^{II}_{2}BiF_{8}$, analogous to $Ag^{I}Ag^{II}_{2}YF_{8}$. To synthesise the bismuth phase without or with minimal amounts of impurities, a similar approach to $Ag^{I}Ag^{II}_{2}YF_{8}$ was adopted, involving an initial ball-milling stage followed by an annealing step at 350 °C for 48 hours. Detailed synthesis conditions are outlined in Table 38.

Table 38: Synthesis conditions used for the $Ag^{I}Ag^{II}_{2}BiF_{8}$ phase.

Synthesis method	Synthesis conditions
Ball-milling (BM)	AgF_2:BiF=3:1, ν = 30 Hz, 15 minute milling cycle, 4 hours total milling time, 15 mm diameter of tungsten carbide milling ball
Ball-milling with an additional annealing step (BMA-350)	48 h at 350 °C

A comparative analysis of the laboratory PXRD patterns collected from the starting reagents, the BM sample, and the annealed BMA-350 sample indicates that after ball-milling, the reagents were fully consumed (Figure 78a). However, the resulting PXRD pattern from the BM stage did not correspond to the expected $Ag^{I}Ag^{II}_{2}BiF_{8}$ phase, as some reflections were not visible. Subsequent annealing of this intermediate at 350 °C yielded the targeted $Ag^{I}Ag^{II}_{2}BiF_{8}$ phase, with no detectable impurities in the PXRD pattern. This finding was further supported by a single-phase Rietveld refinement of the BMA-350 sample, yielding a low R_{wp} factor (Figure 78b), which reinforces the accuracy of the crystal structure initially determined via 3D ED.

Raman spectroscopy analysis of the BMA-350 sample revealed a complex vibrational profile, especially in the 50–250 cm^{-1} range where multiple peaks were observed (Figure 78c). While these spectral features indicate a rich vibrational landscape, further theoretical studies are necessary to assign specific peaks to their corresponding Raman-active modes, thus deepening an understanding of the structural dynamics within this novel phase.

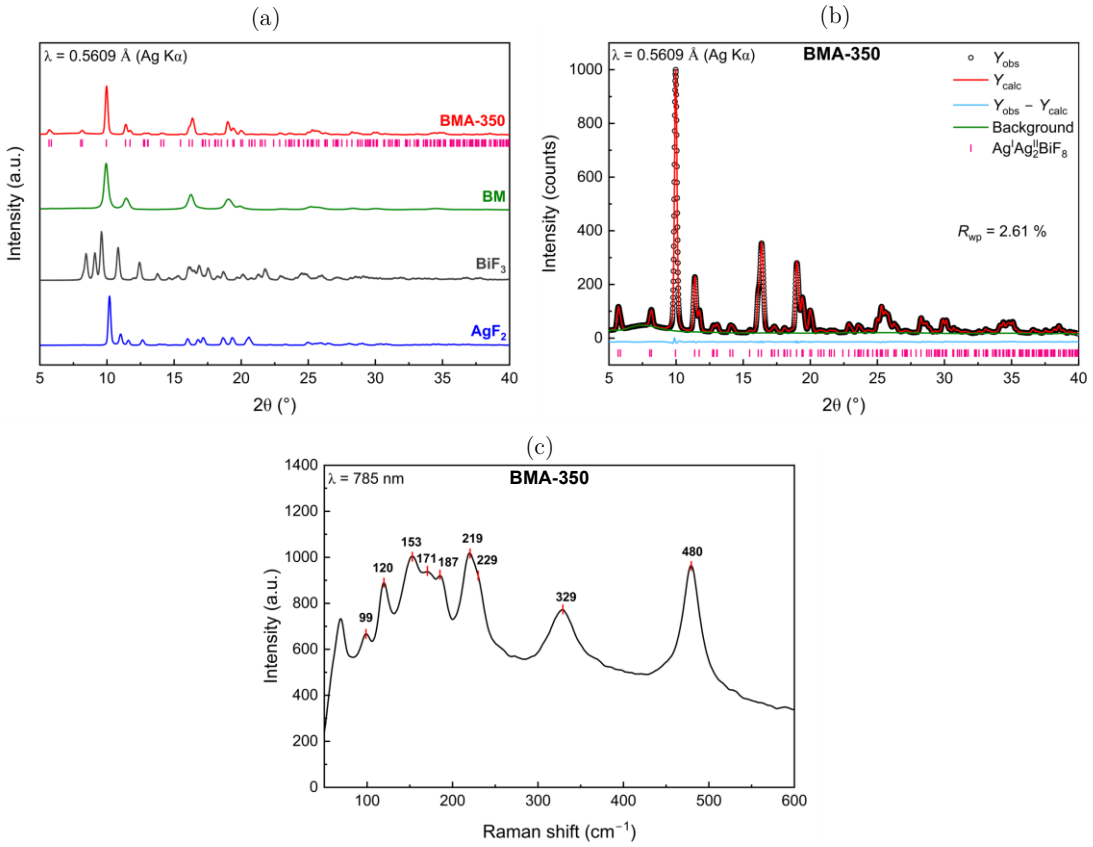


Figure 78: (a) Laboratory PXRD data of AgF_2, BiF_3, BM, and BMA-350 samples. Bragg reflections of $Ag^{I}Ag^{II}_2BiF_8$ are indicated with pink lines. (b) One-phase Rietveld refinement of the PXRD data for the BMA-350 sample. (c) Raman spectra of the BMA-350 sample with indicated peak positions.

Laboratory PXRD analysis of the BMA-350 sample revealed no detectable impurity phases; therefore, magnetic measurements were performed to characterize the intrinsic magnetic behavior of $Ag^{I}Ag^{II}_2BiF_8$. The temperature-dependent magnetic susceptibility (Figure 79a) exhibits a weak ferromagnetic transition near 164 K, consistent with the presence of trace AgF_2, which undergoes a ferromagnetic transition at a comparable temperature. The extremely low concentration of AgF_2 is corroborated by its absence in both Raman spectroscopy and PXRD data.

An additional ferromagnetic transition at approximately 80 K was observed in this sample, marked by a question mark in Figure 79a. However, this transition is not attributed as an intrinsic property of $Ag^{I}Ag^{II}_2BiF_8$, since the comparative analysis of the S2 sample, which was synthesised under slightly different conditions (shorter ball-milling time of 3 hours and a longer annealing step consisting of two 7-day cycles at 350 °C), reveals no such transition. The S2 sample, which contained about 95 wt.% of $Ag^{I}Ag^{II}_2BiF_8$ and 5 wt.% of $Ag^{I}_2Ag^{II}F_4$ as determined by Rietveld refinement of the PXRD data, shows no evidence of the 80 K transition (green data in Figure 79a). This suggests that the observed ferromagnetic transition at 80 K in the BMA-350 sample may indeed stem from an

unidentified secondary phase rather than the $Ag^{I}Ag^{II}_{2}BiF_{8}$ phase itself. At lower temperatures, a notable drop in magnetic susceptibility at around 15 K is observed, consistent with an antiferromagnetic transition, reminiscent of $Ag^{I}Ag^{II}_{2}YF_{8}$. The precise T_N of this transition was determined using Fisher's heat capacity [81], yielding a value of T_N=13.7(1) K (see inset in Figure 79a). This finding additionally corroborates the 2D antiferromagnetic character of $Ag^{I}Ag^{II}_{2}BiF_{8}$.

Curie-Weiss fits were also performed on both the BMA-350 and S2 samples (Figure 79b and Figure 79c). The Curie constants were found to be comparable. However, θ_{CW} was slightly more negative for the S2 sample than for the BMA-350 sample. This difference is likely attributable to the presence of a ferromagnetic impurity in the BMA-350 sample, which could cause a marginal increase in the θ_{CW}. Additionally, the minor $Ag^{I}_{2}Ag^{II}F_{4}$ impurity present in the S2 sample has also weak antiferromagnetic character, with a θ_{CW} of −3.6(2) K, which may have contributed to the observed θ_{CW} value in S2. From these results, it was concluded that the intrinsic θ_{CW} of the $Ag^{I}Ag^{II}_{2}BiF_{8}$ phase is likely between the values obtained for the two samples, suggesting a value between −30 and −36 K.

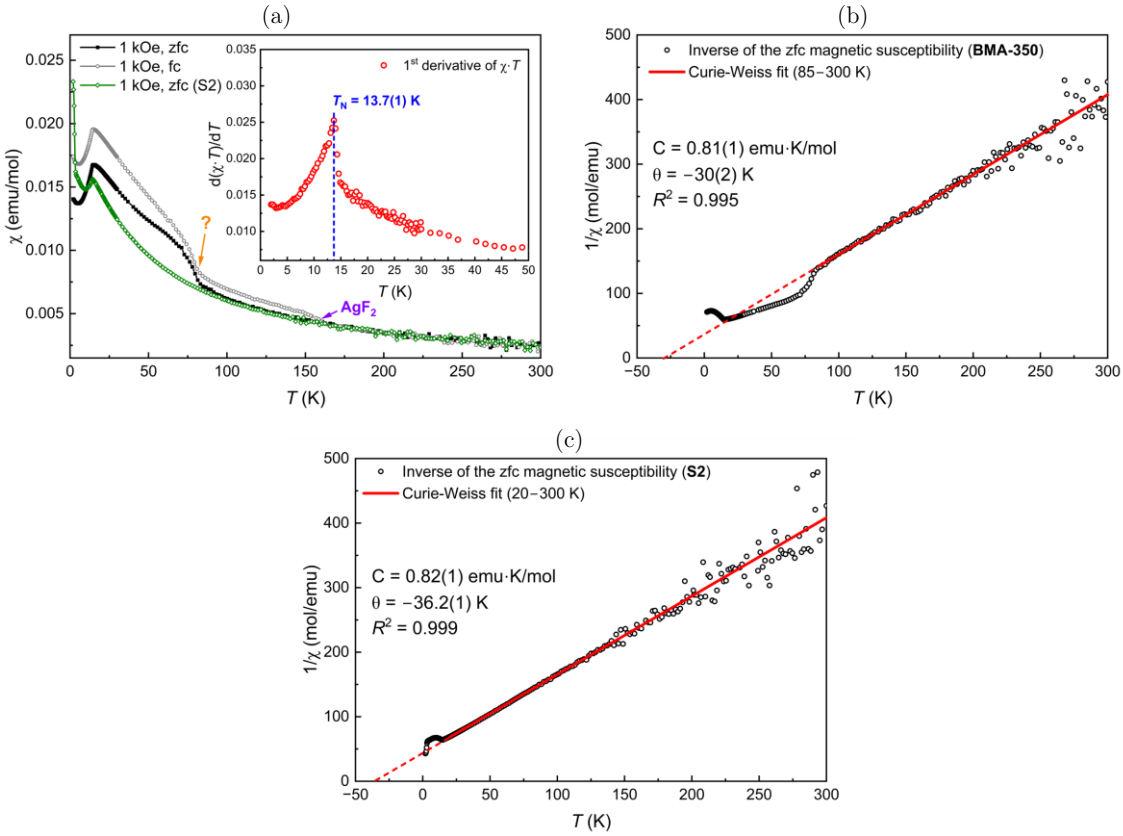


Figure 79: (a) Temperature-dependent susceptibility χ measured in a magnetic field of 1 kOe for BMA-350 and S2 samples. An inset shows Fisher's heat capacity as a function of temperature for the BMA-350 sample, where the transition temperature of 13.7(1) K is determined. The question mark points on an onset of ferromagnetic transition of unidentified impurity. (b) Curie-Weiss fit to the inverse of magnetic susceptibility for the BMA-350 sample and (c) S2 sample.

To determine the magnetic structure and accurately locate the fluorine atoms, NPD data were collected on the ball-milled and annealed $Ag^{I}Ag^{II}_{2}BiF_{8}$ sample. However, since the synthesis was optimized after the allocated beamtime, the sample used for the

measurements contained a larger fraction of unreacted starting materials (Figure 80). The synthesis conditions for this sample are summarized in Table 39.

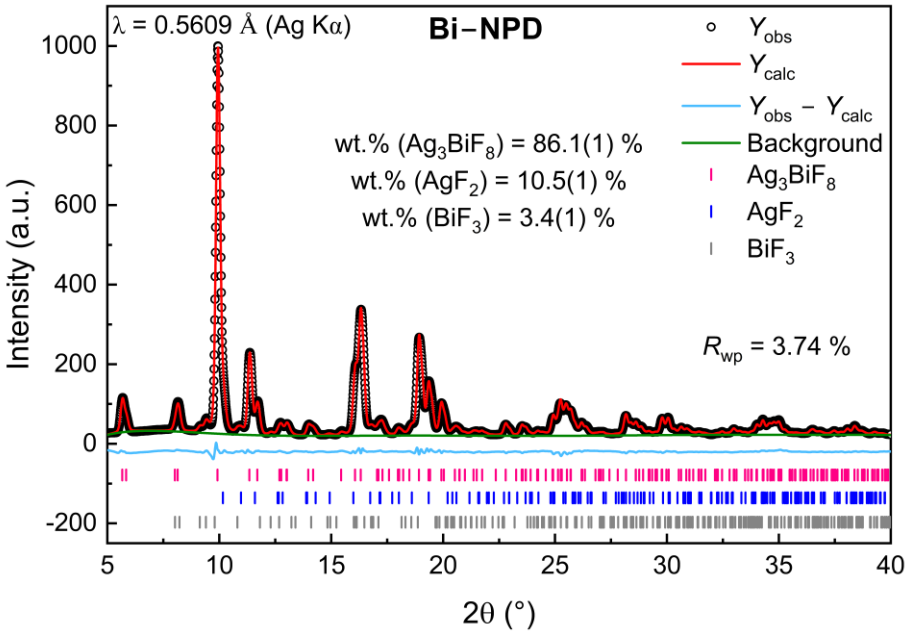


Figure 80: Rietveld refinement of the laboratory PXRD data collected on the Bi-NPD sample at the room temperature (synthesis conditions are reported in Table 39).

Table 39: The synthesis conditions for the preparation of the $Ag^{I}Ag^{II}_{2}BiF_{8}$ sample for the NPD data collection with the sample code Bi-NPD.

Synthesis method	Synthesis conditions
Ball-milling	AgF_2:BiF = 3:1, ν = 30 Hz, 15 minute milling cycle, 1.5 hours total milling time, 15 mm diameter WC milling ball.
Annealing	Annealed at 72 h at 350 °C, repeated for two cycles. The sample was homogenized between the cycles for 15 min

The Rietveld refinement of the NPD data collected above the transition temperature (Figure 81) corroborated the structural model previously determined via 3D ED, athough some discrepancies between the calculated model and experimental data were observed.

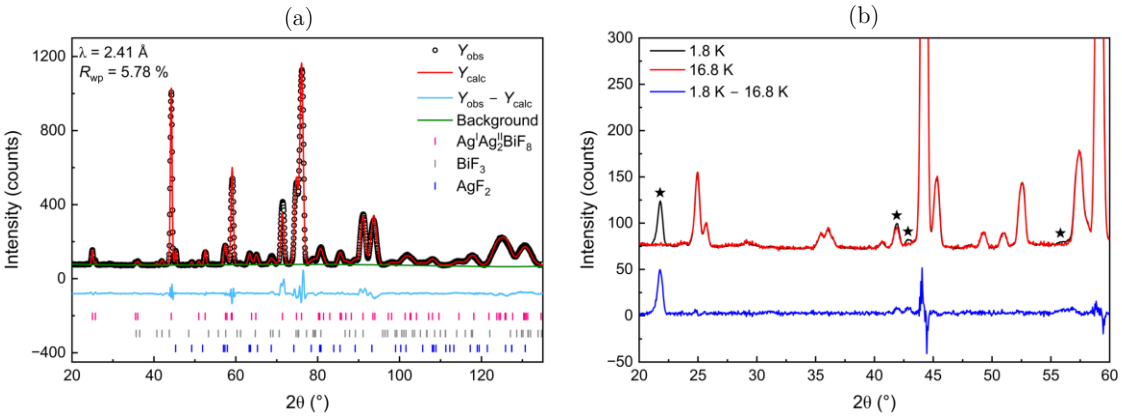


Figure 81: (a) Rietveld refinement of the 16.8 K NPD data collected on the Bi-NPD sample. (b) The NPD data measured at 1.8 (black) and 16.8 K (red) and the difference plot (blue). Magnetic peaks are marked with black star symbol.

Upon cooling the sample below the antiferromagnetic transition temperature, four additional peaks emerged in the diffraction pattern. These peaks, evident in the low-temperature data (Figure 82c) were used to identify the magnetic propagation vector k, with the most likely solution found to be $k = (1/8, 1/8, 1/4)$. Based on symmetry analysis conducted through the *Bilbao Crystallographic Server*, two maximal magnetic space groups were proposed, P_a2_1/c and P_a2/c. However, neither magnetic space group satisfactorily fit the observed magnetic peaks, implying that the magnetic structure may be incommensurate with the lattice, a scenario that is not uncommon in complex fluoride systems with competing interactions.

Temperature-dependent NPD measurements, conducted in 1 K increments from 16.8 K down to 1.8 K (Figure 82a), facilitated precise determination of the antiferromagnetic transition temperature. As evidenced by the emergence of the most intense magnetic peak around 21.8° 2θ, magnetic order appears around 13.7 K, a result that aligns closely with the derived T_N from the power-law fit (Figure 82b) and the transition temperature obtained from magnetic susceptibility analysis. Specifically, the peak in the first derivative of the $\chi \cdot T$ product at 13.7 K confirmed the onset of antiferromagnetic ordering, thereby substantiating the thermal evolution observed in the NPD data.

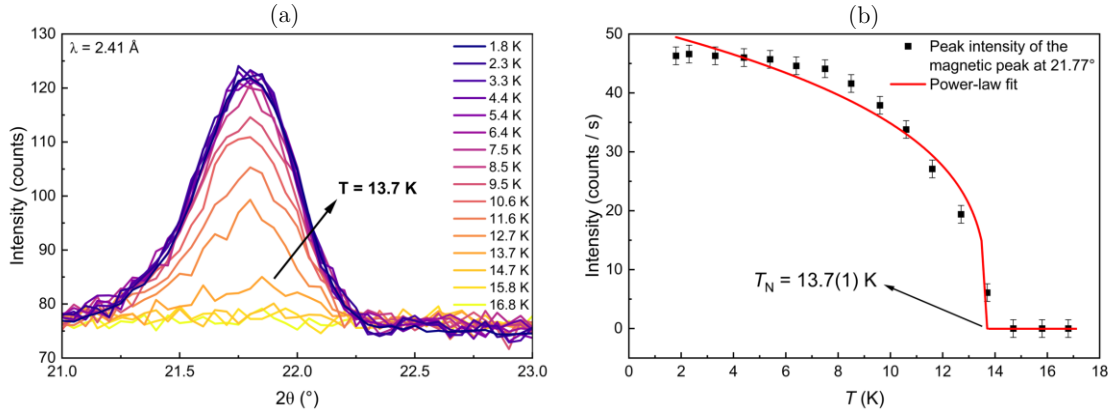


Figure 82: (a) Temperature dependent NPD data measured in the 1.8–16.8 K range with an approximate 1 K step magnified on the most intense magnetic peak at 21.8° 2θ. (b) Peak intensity of the lower-angle magnetic peak, 21.8°, versus temperature indicating T_N ~ 18 K. The solid line is a power-law fit with an equation: $I = I_0 \cdot (1 - \frac{x}{T_N})^{2\beta}$.

The research of ternary Ag^{2+}-based compounds has yielded contrasting outcomes between the lanthanum and bismuth analogues. While attempts to synthesise a La-containing phase ($Ag^{I}Ag^{II}_{2}LaF_{8}$) were unsuccessful, the use of BiF_3 resulted in the formation of a new, phase-pure compound, $Ag^{I}Ag^{II}_{2}BiF_{8}$, when ball milling was combined with a subsequent annealing step. The crystal structure of $Ag^{I}Ag^{II}_{2}BiF_{8}$ was unambiguously determined using 3D ED, revealing a tetragonal structure in the $P4/mcc$ space group with unit-cell parameters of $a = 5.740(2)$ Å and $c = 11.155(2)$ Å. This phase is defined by layers of edge-sharing $[AgF_8]^{6-}$ units in the ac plane that are separated by layers of Bi^{3+} and Ag^{+} cations, each coordinated by eight fluorine anions in a distorted square antiprismatic geometry. Magnetic susceptibility measurements indicate that the bismuth phase exhibits a clear antiferromagnetic transition at 13.7(1) K, as determined by Fisher's heat capacity analysis, with only minor ferromagnetic contributions arising from trace impurities. This result aligns with the NPD data, where the antiferromagnetic transition was observed at the same temperature. However, determination of the exact magnetic structure remains the subject of ongoing investigations.

Chapter 4

Conclusions

This thesis explores the potential of the Ag^{2+} cation ($S = 1/2$) in the field of magnetism, with particular emphasis on novel synthetic strategies, including mechanochemistry. Several key objectives have been achieved, advancing the understanding and development of fluoridoargentates(II). Mechanochemistry was benchmarked on the MAgF$_4$ series (M = Ba, Sr, Hg, Ca, Cd) by comparing results obtained from traditional high-temperature solid-state synthesis with those from ball-milling. Laboratory PXRD data confirmed the efficacy of mechanochemical synthesis, demonstrating it is a viable route for the preparation of fluoridoargentates(II).

Table 40: Overview of compounds synthesised and investigated in this thesis.

Phase	**Crystal system**	**Space group**	**Magnetic properties**
$BaAgF_4$	Tetragonal	$I4/mcm$	3D AFM
$SrAgF_4$	Tetragonal	$I4/mcm$	3D AFM
$HgAgF_4$	Tetragonal	$I4/mcm$	3D AFM
$CaAgF_4$	Tetragonal	$I4/mcm$	3D AFM
$CdAgF_4$	Tetragonal	$I4/mcm$	3D AFM
$NaAgF_3$	Triclinic	$P\bar{1}$	2D canted AFM
$KAgF_3$	Orthorhombic	$Pnma$	1D AFM
$RbAgF_3$	Tetragonal	$I4/mcm$	1D AFM
$CdAgF_3$	Tetragonal	$I4/mcm$	1D AFM
Na_2AgF_4	Monoclinic	$P2_1/c$	1D AFM
β-K_2AgF_4	Monoclinic	$P2_1/c$	Not determined
Rb_2AgF_4	Orthorombic	$Bbcm$ ($Cmca$)	2D FM
Cs_2AgF_4	Orthorombic	$Bbcm$ ($Cmca$)	2D FM
$Ag^{I}_2Ag^{II}F_4$	Monoclinic	$P2_1/c$	1D canted AFM
$Ag^{I}Ag^{II}F_3$	Triclinic	$P\bar{1}$	1D AFM
$Ag^{I}Ag^{II}_2YF_8$	Orthorhombic	$Cccm$	3D AFM
$Ag^{I}Ag^{II}_2BiF_8$	Orthorhombic	$P4/mcc$	3D AFM

The influence of milling parameters was systematically studied for $SrAgF_4$, minimizing AgF_2 decomposition and enabling the use of stoichiometric reagent ratios without excess AgF_2. Furthermore, single-crystal growth of $BaAgF_4$ was successfully achieved via high-temperature solid-state synthesis, allowing determination of its crystal structure using SCXRD, while the magnetic structure of $SrAgF_4$ was resolved through NPD. Furthermore, new compositional spaces were successfully accessed, yielding novel phases such as $NaAgF_3$, Ag_2F_3, Ag_3F_4, Ag_3YF_8, and Ag_3BiF_8, which were synthesised primarily via ball-milling, in some cases followed by soft annealing. Crystal structures of $NaAgF_3$, Ag_3YF_8, and Ag_3BiF_8 were determined using 3D electron diffraction, whereas synchrotron PXRD combined with theoretical predictions was employed to elucidate the structures of Ag_2F_3 and Ag_3F_4. Despite expectations in the literature, the realization of a 2D antiferromagnet with flat $[AgF_2]$ layers—an ideal silver analogue of La_2CuO_4—remains elusive. Nevertheless, this thesis demonstrates that mechanochemistry is a powerful alternative to classical high-temperature routes for fluoridoargentates(II). Mechanochemical synthesis reliably produces phase-pure $MAgF_4$ and related phases, significantly reducing AgF_2 decomposition and minimizing non-magnetic impurities compared to solid-state methods, although occasional WC contamination from the milling bodies may occur. Furthermore, mechanochemistry enables the stabilisation of otherwise inaccessible metastable compounds, exemplified by the first synthesis of Ag_3F_4, Ag_2F_3, $NaAgF_3$, Ag_3YF_8 and Ag_3BiF_8, often combined with a brief annealing step. Comparative magnetic studies indicate that while some materials ($KAgF_3$, $SrAgF_4$) display synthesis-dependent T_C, others (Ag_3F_4, Rb_2AgF_4, Cs_2AgF_4) show minimal variation, highlighting that the influence of the preparation method on magnetic ordering is highly system-specific.

This thesis demonstrates that mechanochemistry provides an efficient route to accelerate the discovery of fluoridoargentates(II) phases. It supports the ongoing investigation of potential superconductivity in this class of materials by enabling access to previously unattainable compounds.

Appendix A

Laboratory PXRD Data Collected on the Starting Material

Silver difluoride (AgF_2)

In this study, AgF_2 obtained from different suppliers (*Sigma Aldrich*, *Fluorochem*, and *Thermo Scientific*) was employed as a precursor in the synthesis of fluoridoargentates(II). It was observed that the synthesis outcome could be affected by the AgF_2 source.

Rietveld refinement of PXRD data collected on AgF_2 obtained from *Sigma Aldrich* is shown in Figure 83a. Similarly, a good fit was obtained for all AgF_2 sources in the same 2θ region. Above 9° 2θ, the PXRD patterns of AgF_2 from all three suppliers exhibit a high degree of similarity, indicating similar crystallinity and phase composition across all AgF_2 sources (Figure 83b). However, distinct differences emerge at lower angles (below 9° 2θ).

The AgF_2 from *Fluorochem* shows additional unidentified peaks that do not match any known phases in the database, suggesting potential impurities. This sample also exhibits a substantial amount of amorphous content, implying a lack of crystallinity or the presence of an unknown phase. In contrast, AgF_2 from *Sigma Aldrich* shows minimal amorphous content but displays minor peaks likely corresponding to trace amounts of Ag_3F_4. The AgF_2 from *Thermo Scientific* also has some amorphous phase but to a lesser degree than the *Fluorochem* sample.

These differences in the AgF_2 precursor led to variations in the PXRD patterns of some of the sample obtained in this thesis, as for example, $KAgF_3$ (Figure 83c). The $KAgF_3$ sample synthesised with AgF_2 from *Sigma Aldrich* exhibits the expected PXRD pattern. However, $KAgF_3$ synthesised with AgF_2 from *Fluorochem* has fewer peaks and displays higher symmetry, suggesting possible structural deviations. Additionally, solid-state synthesis using *Fluorochem's* AgF_2 consistently resulted in decomposition, with a white powder forming on the reactor walls, indicating the presence of an amorphous, volatile, impurity in AgF_2 provided by *Fluorochem*, that may promote decomposition at high temperatures. This underscores the critical role of the main precursor's purity in determining the synthesis outcome.

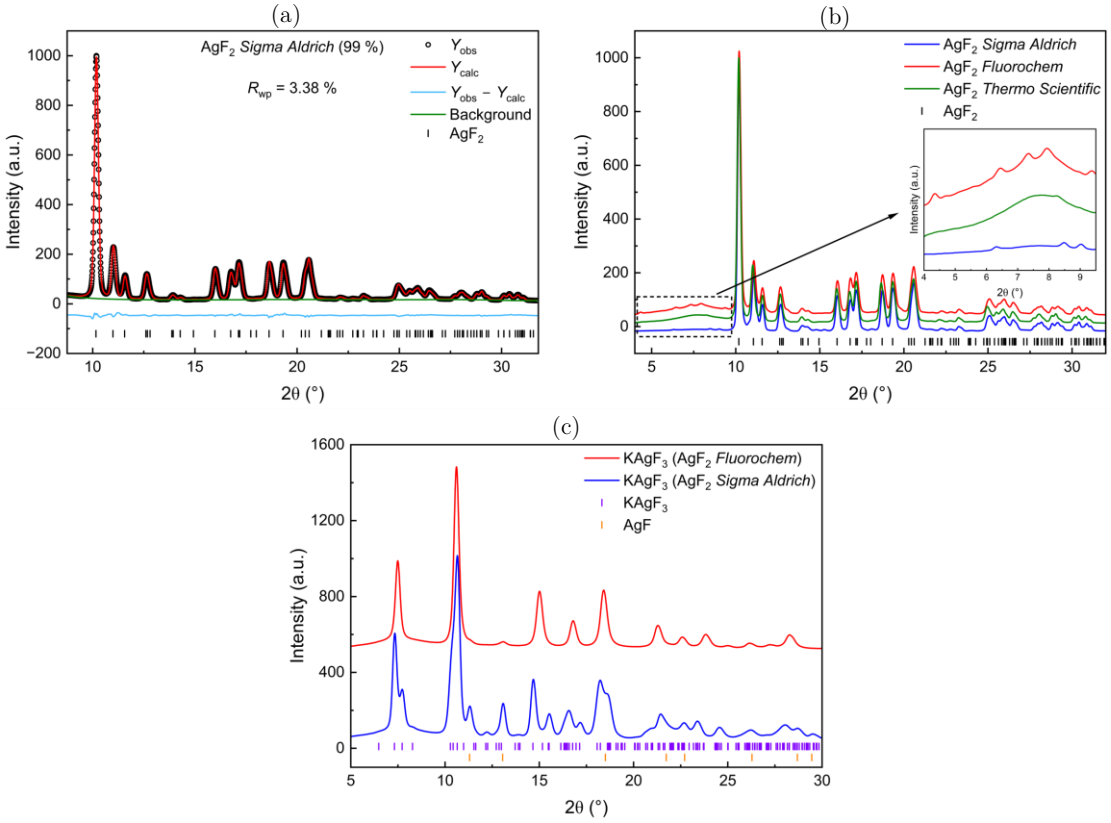


Figure 83: (a) Rietveld refinement of the room-temperature laboratory PXRD data (Ag Kα) collected on the AgF_2 provided by Sigma Aldrich. (b) Comparison of the PXRD patterns between AgF_2 purchased from Sigma Aldrich, Fluorochem and Thermo Scientific. (c) Laboratory PXRD data collected on the $KAgF_3$ samples, prepared by two different AgF_2 sources.

Other metal fluorides

The PXRD patterns of the metal fluorides used as starting materials in this study are presented below, providing a reference for their phase purity and crystallinity prior to their incorporation into the synthetic procedures.

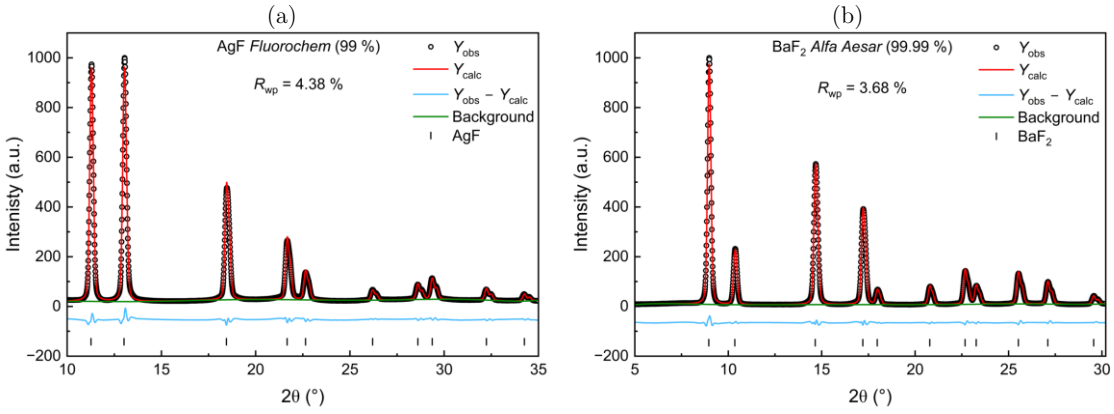


Figure 84: Rietveld refinement of the room-temperature laboratory PXRD data (Ag Kα) collected on (a) AgF and (b) BaF_2.

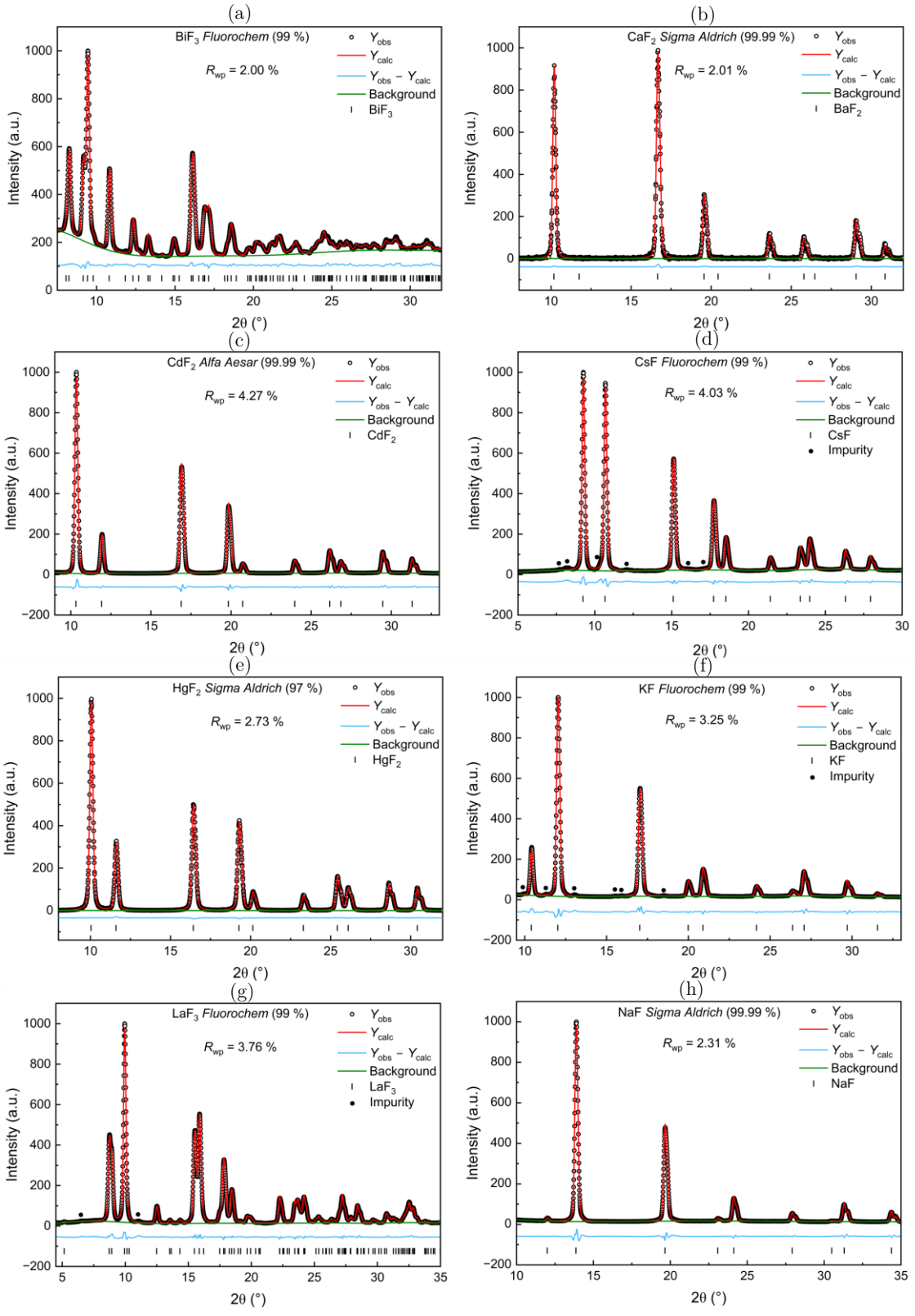


Figure 85: Rietveld refinement of the room-temperature laboratory PXRD data (Ag Kα) collected on (a) BiF_3, (b) CaF_2, (c) CdF_2, (d) CsF, (e) HgF_2, (f) KF, (g) LaF_3 and (h) NaF.

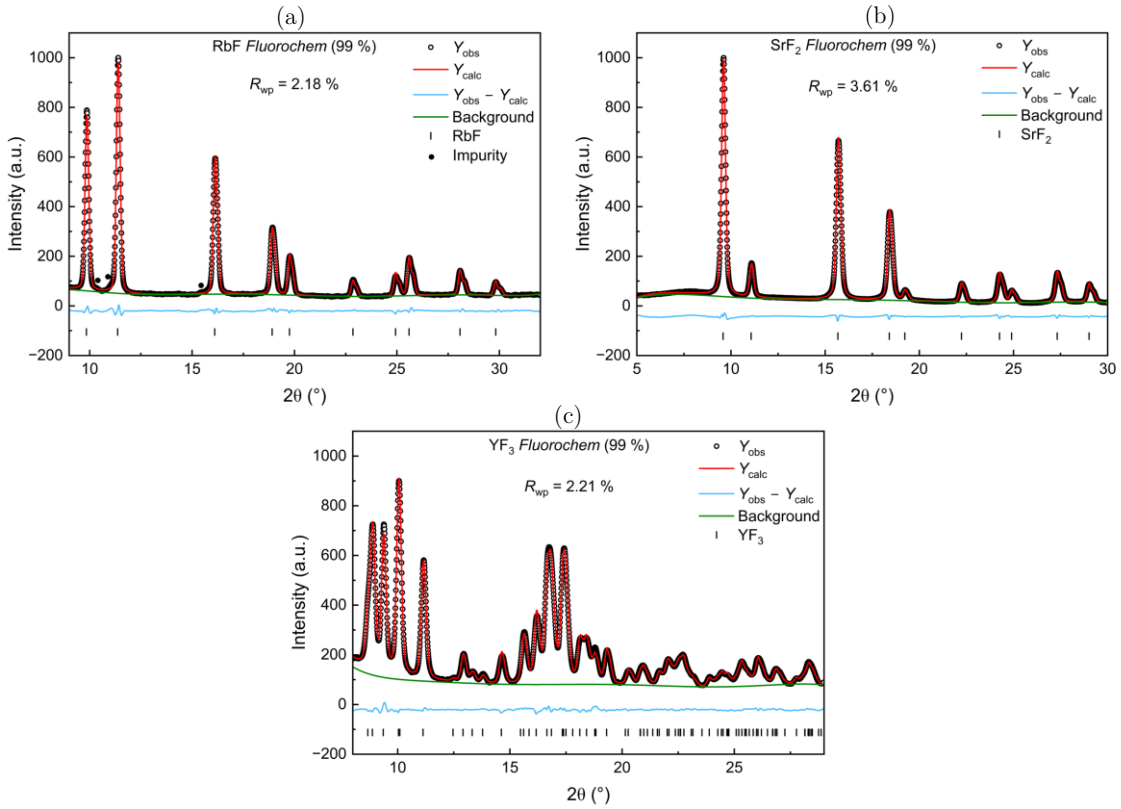


Figure 86: Rietveld refinement of the room-temperature laboratory PXRD data (Ag Kα) collected on RbF, SrF_2 and YF_3.

References

[1] W. Grochala and R. Hoffmann, "Real and Hypothetical Intermediate-Valence Ag^{II}/Ag^{III} and Ag^{II}/Ag^{I} Fluoride Systems as Potential Superconductors," *Angew. Chem. Int. Ed.,* vol. 40, pp. 2742–2781, 2001.

[2] W. Grochala and Z. Mazej, "Chemistry of silver(II): a cornucopia of peculiarities," *Phil. Trans. R. Soc. A,* vol. 373, p. 20140179, 2015.

[3] Z. Mazej, D. Kurzydłowski and W. Grochala, "Unique Silver(II) Fluorides: The Emerging Electronic and Magnetic Materials," in *Photonic and Electronic Properties of Fluoride Materials*, Elsevier, 2016, pp. 231–260.

[4] K. Koteras, J. Gawraczyński, G. Tavčar, Z. Mazej and W. Grochala, "Crystal structure, lattice dynamics and superexchange in $MAgF_3$ 1D antiferromagnets (M = K, Rb, Cs) and a $Rb_3Ag_2F_7$ Ruddlesden–Popper phase," *CrystEngComm,* vol. 24, pp. 1068–1077, 2022.

[5] F. a. W. M. Preishuber-Pflügl, "Mechanochemically synthesized fluorides: local structures and ion transport," *Dalton Trans.,* vol. 45, pp. 8675–8687, 2016.

[6] D. Ceriotti, P. Marziani, F. Maria Scesa, A. Collorà, L. C. Bianchi, L. Magagnin and M. Sansotera, "Mechanochemical synthesis of fluorinated perovskites $KCuF_3$ and $KNiF_3$," *RSC Mechanochem.,* vol. 1, pp. 520–530, 2024.

[7] P. Anitha Sukkurji, Y. Cui, S. Lee, K. Wang, R. Azmi, A. Sarkar, S. Indris, S. S. Bhattacharya, R. Kruk, H. Hahn and Q. Wang, "Mechanochemical synthesis of novel rutile-type high entropy fluorides for electrocatalysis," *J. Mater. Chem. A,* vol. 9, pp. 8998–9009, 2021.

[8] S. Blundell, Magnetism in Condensed Matter, Oxford: OUP Oxford, 2001.

[9] H. A. Kramers, "L´interaction Entre les Atomes Magnetogenes dans un Cristal Paramagnetique," *Physica,* vol. 1, pp. 182–192, 1934.

[10] P. W. Anderson, "Antiferromagnetism. Theory of superexchange interaction.," *Phys. Rev. B,* vol. 79, pp. 350–356, 1950.

[11] M. A. Kastner, R. J. S. G. Birgeneau and Y. Endoh, "Magnetic transport and optical properties of monolayer copper oxides," *Rev. Mod. Phys.,* vol. 70, pp. 897–928, 1998.

[12] N. M. Plakida, "Spin fluctuations and high-temperature superconductivity in cuprates," *Phys. C: Supercond. Appl.,* vol. 531, pp. 39–59, 2016.

[13] Q. Si and E. Abrahams, "Strong correlations and magnetic frustration in the high TC iron pnictides," *Phys. Rev. Lett.,* vol. 101, p. 076401, 2008.

[14] Z. Mazej, T. Gilewski, E. A. Goreshnik, Z. Jagličić, M. Derzsi and W. Gorchala, "Canted Antiferromagnetism in Two-Dimensional Silver(II) Bis[pentafluoridioxidotungstate(VI)]," *Inorg. Chem.,* vol. 56, pp. 224–233, 2017.

[15] C. R. Serrao, A. Sundaresan and C. N. R. Rao, "Multiferroic nature of charge-ordered rare earth manganites," *J. Phys.: Condens. Matter,* vol. 19, p. 496217, 2007.

[16] J. C. Bonner and M. E. Fisher, "Linear magnetic chains with anisotropic coupling," *Phys. Rev.,* vol. 135, p. A640, 1964.

[17] E. Ising, "Beitrag zur Theorie des Ferromagnetismus," *Z. Phys.,* vol. 31, pp. 253–258, 1925.

[18] A. N. Vasil'ev, M. M. Markina and E. A. Popova, "Spin gap in low-dimensional magnets," *Low Temp. Phys.,* vol. 31, pp. 203–223, 2005.

[19] C. Yasuda, S. Todo, K. Hukushima, F. Alet, M. Keller, M. Troyer and H. Takayama, "Néel Temperature of Quasi-Low-Dimensional Heisenberg Antiferromagnets," *Phys. Rev. Lett.,* vol. 94, p. 217201, 2005.

[20] D. Kurzydłowski and W. Grochala, "Prediction of Extremely Strong Antiferromagnetic Superexchange in Silver(II) Fluorides: Challenging the Oxocuprates(II)," *Angew. Chem.,* vol. 129, pp. 10248–10251, 2017.

[21] S. E. McLain, M. R. Dolgos, D. A. Tennant, J. F. C. Turner, T. Barnes, T. Proffen, B. C. Sales and R. I. Bewley, "Magnetic behaviour of layered Ag(II) fluorides," *Nat. Mater. ,* vol. 5, pp. 561–565, 2006.

[22] R. H. Odenthal, D. Paus and R. Hoppe, "Zur Magnetochemie des zweiwertigen Silbers Neue Fluoroargentate(II): Cs_2AgF_4, Rb_2AgF_4 und K_2AgF_4," *Z. Anorg. Allg. Chem.,* vol. 407, pp. 144–150, 1974.

[23] W. Grochala, "Greedy Ag(II) oxidizer: Can any inorganic ligand except fluoride endure its presence in ionic solids?," *J. Fluor. Chem.,* vol. 129, pp. 82–90, 2008.

[24] P. J. Malinowski, M. Derzsi, Z. Mazej, Z. Jagličić, B. Gaweł, W. Łasocha and W. Grochala, "$Ag^{II}SO_4$: A Genuine Sulfate of Divalent Silver with Anomalously Strong One-Dimensional Antiferromagnetic Interactions," *Angew. Chem. Int. Ed.,* vol. 49, pp. 1683–1686, 2010.

[25] D. Tudela, "SIlver(II) Oxide or Silver(I,III) Oxide?," *J. Chem. Educ.,* vol. 85, pp. 863–865, 2008.

[26] P. J. Malinowski, Z. Mazje and W. Gorchala, "Probing reactivity of the potent AgF_2 oxidizer. Part 2: inorganic compounds," *Z. Anorg. Allg. Chem.,* vol. 634, pp. 2608–2616, 2008.

[27] D. Grzybowska, P. J. Malinowski, Z. Mazej and W. Grochala, "Probing reactivity of the potent AgF_2 oxidizer. Part 1: organic compounds," *Coll. Czech. Chem. Commun.,* vol. 73, pp. 1729-1746, 2008.

[28] A. J. Bard, R. Parsons and J. Jordan, Standard potentials in aqueous solutions, New York: Marcel Dekker, 1985.

[29] H. Moissan, "Preparation du fluor pur," *Ann. Chem. Phys.,* vol. 24, pp. 224–282, 1891.

[30] P. Fischer, D. Schwazenbach and H. M. Rietveld, "Crystal and magnetic structure of silver difluoride: I. Determination of the AgF_2 structure," *J. Phys. Chem. Solids,* vol. 32, pp. 543–550, 1971.

[31] M. S. R. Cader and F. Aubke, "Hexafluoro antimonates(V) of divalent metals, synthesis and properties," *Can. J. Chem.,* vol. 67, pp. 1700–1707, 1989.

[32] W. J. Casteel, G. Lucier, R. Hagiwara, H. Borrmann and N. Bartlett, "Structural and magnetic properties of some AgF^+ Salts," *J. Solid State Chem.,* vol. 96, pp. 84–96, 1992.

[33] A. C. Walters, T. G. Perring, J. S. Caux, A. T. Savici, G. D. Gu, C. C. Lee, W. Ku and I. A. Zaliznyak, "Effect of covalent bonding on magnetism and the missing neutron intensity in copper oxide compounds," *Nat. Phys.,* vol. 5, pp. 867–872, 2009.

[34] Z. Hiroi, M. Takano, M. Azuma and Y. Takeda, "A new family of copper oxide superconductors $Sr_{n+1}Cu_nO_{2n+1+\delta}$ stabilized at high pressure," *Nature,* vol. 364, pp. 315–317, 1993.

[35] Z. Mazej, E. Goreshnik, Z. Jagličić, B. Gawel, W. Lasocha, D. Grzybowska, T. Jaron, D. Kurzydłowski, P. Malinowski, W. Kozminski, J. Szydłowska, P. Leszczynski and W. Grochala, "$KAgF_3$, K_2AgF_4 and $K_3Ag_2F_7$: important steps towards a layered antiferromagnetic fluoroargentate(II)," *CrystEngComm,* vol. 11, pp. 1702–1710, 2009.

[36] D. Kurzydłowski, T. Jaroń, A. Ozarowski, S. Hill, Z. Jagličić, Y. Filinchuk, Z. Mazej and W. Grochala, "Local and Cooperative Jahn−Teller Effect and Resultant Magnetic Properties of M_2AgF_4 (M = Na−Cs) Phases," *Inorg. Chem.,* vol. 55, pp. 11479–11489, 2016.

[37] W. Grochala, "The theory-driven quest for a novel family of superconductors: fluorides," *J. Mater. Chem.,* vol. 19, pp. 6949–6968, 2009.

[38] A. Grzelak, H. Su, X. Yang, D. Kurzydłowski, J. Lorenzana and W. Grochala, "Epitaxial engineering of flat silver fluoride cuprate analogs," *Phys. Rev. Mater.,* vol. 4, p. 084405, 2020.

[39] R. H. Odenthal and R. Hoppe, "Uber Fluoroargentate(II) $M^{II}[AgF_4]$ mit M^{II} = Ba, Sr, Ca, Hg, Cd, sowie Ba_2AgF_6," *Z. Anorg. Allg. Chem.,* vol. 385, pp. 92–101, 1971.

[40] A. W. Jache and G. H. Cady, "Solubility of Fluorides of Metals in Liquid Hydrogen Fluoride," *J. Phys. Chem.,* vol. 56, pp. 1106–1109, 1952.

[41] A. D. McNaught and A. Wilkinson, IUPAC Compendium of Chemical Technology, (the "Gold Book"), Oxford: Blackwell Scientific Publications, 1997.

[42] L. Takacs, "Quicksilver from cinnabar: The first documented mechanochemical reaction?," *J. Met.,* vol. 52, pp. 12–13, 2000.

[43] G. Agricola, "De Natura Fossilicum," 1546.

[44] G. Agricola, "De Re Metallica," 1556.

[45] V. Šepelák, A. Düvel, M. Wilkening, K. D. Becker and O. Heitjans, "Mechanochemical reactions and syntheses of oxides," *Chem. Soc. Rev.,* vol. 42, p. 7507−7520, 2013.

[46] A. Krusenbaum, S. Grätz, G. T. Tigineh, L. Borchardt and J. G. Kim, "The mechanochemical synthesis of polymers," *Chem. Soc. Rev.,* vol. 51, pp. 2873–2905, 2022.

[47] T. D., L. Loots and T. Friščić, "Towards medicinal mechanochemistry: evolution of milling from pharmaceutical solid form screening to the synthesis of active pharmaceutical ingredients (APIs)," *Chem. Commun.,* vol. 52, pp. 7760–7781, 2016.

[48] S. L. James, C. J. Adams, C. Bolm, D. Braga, P. Collier, T. Friščić, F. Greponi, K. D. M. Harris, G. Hyett, W. Jones, A. Krebs, J. Mack, L. Maini, A. G. Orpen, I. P. Parkin, W. C. Shearouse, J. W. Steed and D. C. Wadell, "Mechanochemistry: opportunities for new and cleaner synthesis," *Chem. Soc. Rev.,* vol. 41, pp. 413–447, 2012.

[49] J. L. Do and T. Friščić, "Mechanochemistry: A Force of Synthesis," *ACS Cent. Sci.,* vol. 3, pp. 13–19, 2017.

[50] T. Friščić, C. Mottillo and H. M. Titi, "Mechanochemistry for synthesis," *Angew. Chem.,* vol. 132, pp. 1030–1041, 2020.

[51] P. Balaž, M. Achimovičova, M. Balaž, P. Billik, Z. Cherkezova-Zheleva, J. M. Criado, F. Delogu, R. Dutkova, E. Gaffet, F. J. Gotor, R. Kumar, I. Mitov, T. Rojac, M. Senna, A. Streletskii and K. Wieczorek-Ciurowa, "Hallmarks of mechanochemistry: from nanoparticles to technology," *Chem. Soc. Rev.,* vol. 42, pp. 7571–7637, 2013.

[52] C. Suryanarayana, "Mechanical alloying and milling," *Prog. Mater. Sci.,* vol. 46, pp. 1–184, 2001.

[53] L. Takacs and J. S. McHenry, "Temperature of the milling balls in shaker and planetary mills," *J. Mater. Sci.,* vol. 41, pp. 5246–5249, 2006.

[54] N. K. Katiyar, K. Biswas and C. S. Tiwary, "Cryomilling as environmentally friendly synthesis route to prepare nanomaterials," *Int. Mater. Rev.,* vol. 66, pp. 493–532, 2021.

[55] V. Martinez, T. Stolar, B. Karadeniz, I. Brekalo and K. Užarević, "Advancing mechanochemical synthesis by combining milling with different energy sources," *Nat. Rev. Chem.,* vol. 7, pp. 51–65, 2023.

[56] G. Felix, N. Fabregue, C. Leroy, T. Metro, C. Chen and D. Laurencin, "Induction-heated ball-milling: a promising asset for mechanochemical reactions," *Phys. Chem. Chem. Phys.,* vol. 25, pp. 23435–23447, 2023.

[57] L. Opoczky, "Fine grinding and agglomeration of silicates," *Powder Technol.,* vol. 17, pp. 1–7, 1977.

[58] A. Z. Juhasz and L. Opoczky, Mechanical Activation of Minerals by Grinding: Pulverizing and Morphology of Particles, Chichester: Ellis Horwood, 1990.

[59] F. Preishuber-Pflügl, E. V., S. Nakhal, M. Lerch and M. Wilkening, "Defect-enhanced F− ion conductivity in layer-structured nanocrystalline $BaSnF_4$ prepared by high-energy ball milling combined with soft annealing," *Phys. Status Solidi C,* vol. 12, pp. 10–14, 2015.

[60] B. Ruprecht, M. Wilkening, S. Steuernagel and P. Heitjans, "Anion diffusivity in highly conductive nanocrystalline BaF_2:CaF_2 composites prepared by high-energy ball milling," *J. Mater. Chem.,* vol. 18, pp. 5412-5416, 2008.

[61] T. B. Massalski, "Phase Diagrams," in *Encyclopedia of Materials: Science and Technology*, Elsavier, 2001, pp. 6842–6851.

[62] R. OD., *CrysAlis PRO,* Wrocław, Poland: Rigaku Corporation, 2023.

[63] T. Degen, M. Sadki, E. Bron, U. König and G. Nénert, "The HighScore suite," *Powder Diffr.,* vol. 29, pp. S13–S18, 2014.

[64] B. H. Toby and R. B. Von Dreele, "GSAS-II: the genesis of a modern open-source all purpose crystallography software package," *J. Appl. Crystallogr. ,* vol. 46, pp. 544–549, 2013.

[65] A. A. Coelho, "TOPAS and TOPAS-Academic: an optimization program integrating computer algebra and crystallographic objects written in C++," *J. Appl. Cryst.,* vol. 51, pp. 210–218, 2018.

[66] M. Lozinšek, H. P. A. Mercier and G. J. Schrobilgen, "Mixed Noble-Gas Compounds of Krypton(II) and Xenon(VI); $[F_5Xe(FKrF)AsF_6]$ and $[F_5Xe(FKrF)_2AsF_6]$," *Angew. Chem. Int. Ed.,* vol. 60, pp. 8149–8156, 2020.

[67] G. M. Cheldrick, "Crystal structure refinement with SHELXL," *Struct. Chem.,* vol. 71, pp. 3-8, 2015.

[68] O. V. Dolomanov, L. J. Bourhis, R. J. Gildea, J. A. K. Howard and H. Puschmann, "OLEX2: a complete structure solution, refinement and analysis program," *J. Appl. Cryst. ,* vol. 42, pp. 339–341, 2009.

[69] H. Putz and K. Brandenburg, "Diamond - Crystal and Molecular Structure Visualization," Crystal Impact, Kreuzherrenstr. 102, 53227 Bonn, Germany, [Online]. Available: https://www.crystalimpact.de/diamond.

[70] L. Palatinus, P. Brázda, M. Jelínek, J. Hrdá, S. G. and M. Klementová, "Specifics of the data processing of precession electron diffraction tomography data and their implementation in the program PETS2.0," *Acta Cryst. B,* vol. 75, pp. 512–522, 2019.

[71] V. Petříček, M. Dušek and L. Palatinus, "Crystallographic Computing System JANA2006: General features," *Z. kristallogr. Cryst. Mater.,* vol. 229, pp. 345–352, 2014.

[72] L. Palatinus and G. Chapuis, "SUPERFLIP - a computer program for the solution of crystal structures by charge flipping in arbitrary dimensions," *J. Appl. Cryst. ,* vol. 40, pp. 786–790, 2007.

[73] O. Kahn, Molecular Magnetism, New York: VCH Publishers, 1993.

[74] S. Zhou, C. Dai, Q. Xu and J. Du, "The magnetic properties of multiferroic BaCoF4," *AIP Advances,* vol. 7, p. 055822, 2017.

[75] C. Ederer and N. A. Spaldin, "Electric-field-switchable magnets: The case of BaNiF4," *Phys. Rev. B,* vol. 74, p. 020401, 2006.

[76] E. G. Villora, K. Shimamura, F. Jing, A. Medvedev, S. Takekawa and K. Kitamura, "Ferroelectric and optical properties of single crystal BaZnF4," *Appl. Phys. Lett. 90,* vol. 90, p. 192909, 2007.

[77] S. Zhou, J. Wang, X. Chang, S. Wang, B. Qian, Z. Han, Q. Xu, J. Du, P. Wang and S. Dong, "Magnetoelectricity coupled exchange bias in $BaMnF_4$," *Sci. Rep.,* vol. 5, p. 18392, 2015.

[78] M. Eibschutz, L. Holmes, H. J. Guggenheim and D. E. Cox, "Magnetic behavior of the two-dimensional antiferromagnet $BaFeF_4$," *J. Phys. Colloques,* vol. 32, pp. 759–760, 1971.

[79] S. Siegel, "The Crystal Structure of $KBrF_4$," *Acta Cryst.,* vol. 9, pp. 493–495, 1956.

[80] R. H. Odenthal and R. Hoppe, "Zur Magnetochemie der Fluoroargentate(II): Messungen an $Ba[AgF_4]$, $Sr[AgF_4]$, Ba_2AgF_6 sowie $K[AgF_3]$ und $Cs[AgF_3]$," *Z. Anorg. Allg. Chem.,* vol. 407, pp. 151–156, 1974.

[81] M. E. Fisher, "Relation between the specific heat and susceptibility of an antiferromagnet," *Philos. Mag.-J. Theor. Exp. Appl. Phys.,* vol. 7, pp. 1731–1743, 1962.

[82] A. Kihal, B. Bouzabata, G. Fillion and D. Fruchart, "Magnetic and Structural Properties of Nanocrystalline Iron Oxides," *Phys. Procedia,* vol. 2, pp. 665–671, 2009.

[83] J. López-García, V. Sánchez-Alarcos, V. Recarte, J. A. Rodríguez-Velamazán, I. Unzueta, J. A. García, F. Plazaola, P. La Roca and J. I. Pérez-Landazábal, "Effect of high-energy ball-milling on the magnetostructural properties of a $Ni_{4.5}Co_5Mn_{3.5}Sn_{1.5}$ alloy," *J. Alloys Compd.,* vol. 858, p. 158350, 2021.

[84] J. Rodriguez-Carvajal, "Recent advances in magnetic structure determination by neutron powder diffraction," *Physica B.,* vol. 192, pp. 55–69, 1993.

[85] M. I. Aroyo, J. M. Perez-Mato, D. Orobengoa, E. Tasci, G. de la Flor and A. Kirov, "Crystallography online: Bilbao Crystallographic Server," *Bulg. Chem. Commun.,* vol. 42, pp. 183–197, 2011.

[86] M. I. Aroyo, J. M. Perez-Mato, C. Capillas, E. Kroumova, S. Ivantchev, G. Madariaga, A. Kirov and H. Wondratschek, "Bilbao Crystallographic Server I: Databases and crystallographic computing programs," *Z. Krist.,* vol. 221, pp. 15–27, 2006.

[87] M. I. Aroyo, A. Kirov, C. Capillas, J. M. Perez-Mato and H. Wondratschek, "Bilbao Crystallographic Server II: Representations of crystallographic point groups and space groups," *Acta Cryst.,* vol. A62, pp. 115–128, 2006.

[88] R. H. Odenthal and R. Hoppe, "Fluorargentate(II) der Alkalimetalle," *Monatsh. Chem.,* vol. 102, pp. 1340–1350, 1971.

[89] W. Grochala and P. P. Edwards, ""Unconventional covalent" $KAgF_3$ is metallic above 50 K," *Phys. Status Solidi B,* vol. 240, pp. 11–14, 2003.

[90] D. Kurzydłowski, Z. Mazej, Z. Jagličić, Y. Filinchuk and W. Grochala, "Structural transition and unusually strong antiferromagnetic superexchange coupling in perovskite $KAgF_3$," *Chem. Commun.,* vol. 49, pp. 6262–6264, 2013.

[91] J. M. Wilkinson, S. J. Blundell, S. Biesenkamp, M. Braden, K. Koteras, W. Grochala, P. Barone, J. Lorenzana, M. Z. and G. Tavčar, "Low-temperature magnetism of $KAgF_3$," *Phys. Rev. B,* vol. 107, p. 144422, 2023.

[92] D. Kurzydłowski and W. Grochala, "Large exchange anisotropy in quasi-one-dimensional spin -1/2 fluoride antiferromagnets with a $d(z^2)_1$ ground state," *Phys. Rev. B,* vol. 96, p. 155140, 2017.

[93] A. I. Popov and Y. M. Kiselev, "Fluoroargentates(II) of alkali-metals," *Zh. Neorg. Khim.,* vol. 32, pp. 2276–2280, 1987.

[94] K. Koteras, J. Gawraczyński, M. Derzsi, Z. Mazej and W. Grochala, "Lattice Dynamics of $KAgF_3$ Perovskite, Unique 1D Antiferromagnet," *Chemistry,* vol. 3, pp. 94–103, 2021.

[95] M. Šćepanović, M. Grujič-Brojčin, K. Vojisavljević, B. S. and T. Srećković, "Raman study of structural disorder in ZnO nanopowders," *J. Raman Spectrosc.,* vol. 210, pp. 914–921, 2010.

[96] X. Zhang, G. Zhang, T. Jia, Y. Guo, Z. Zeng and H. Q. Lin, "$KAgF_3$: Quasi-one-dimensional magnetism in three-dimensional magnetic ion sublattice," *Phys. Lett. A,* vol. 375, pp. 2456–2459, 2011.

[97] Z. Marinković Stanojević, Z. Branković, Z. Jagličić, M. Jagodič, L. Mančić, S. Bernik, R. A. and G. Branković, "Structural and magnetic properties of nanocrystalline bismuth manganite obtained by mechanochemical synthesis," *J. Nanopart. Res.,* vol. 13, pp. 3431–3439, 2011.

[98] M. Muroi, R. Street and P. G. McCormick, "Magnetic properties of ultrafine $MnFe_2O_4$ powders prepared by mechanochemical processing," *Phys. Rev. B,* vol. 63, p. 184414, 2001.

[99] I. D. Brown, The Chemical Bonding in Inorganic Chemistry: The Bond Valence Model, Oxford: Oxford University Press, 2002.

[100] N. E. Brese and M. O'Keeffe, "Bond-valence parameters for solids," *Acta Crystallogr.,* vol. B47, pp. 192–197, 1991.

[101] D. Kurzydłowski, Z. Mazej and W. Grochala, "Na_2AgF_4: 1D antiferromagnet with unusually short $Ag^{2+}\cdots Ag^{2+}$ separation," *Dalton Trans.,* vol. 42, pp. 2167–2173, 2013.

[102] D. Kurzydłowski, M. Derzsi, A. Budzianowski, Z. Jagličić, W. Koźmiński, Z. Mazej and W. Gorchala, "Polymorphism of Fluoroargentates(II): Facile Collapse of a Layered Network of α-K_2AgF_4 Due to the Insufficient Size of the Potassium Cation," *Eur. J. Inorg. Chem.,* vol. 2010, pp. 2919-2925, 2010.

[103] J. Gawraczyński, Ł. Wolański, A. Grzelak, Z. Mazej, V. Struzhkin and W. Grochala, "Phase Transitions and Amorphization of M_2AgF_4 (M = Na, K, Rb) Compounds at High Pressure," *Crystals,* vol. 12, p. 458, 2022.

[104] M. Belak Vivod, Z. Jagličić, G. King, H. C. T., M. Lozinšek and M. Dragomir, "Mechanochemical Synthesis and Magnetic Properties of the Mixed-Valent Binary Silver(I,II) Fluorides, $Ag^{I}_2Ag^{II}F_4$ and $Ag^{I}Ag^{II}F_3$," *J. Am. Chem. Soc.,* vol. 146, p. 30510−30517, 2024.

[105] D. I. Khomskii and K. I. Kugel, "Orbital and magnetic structure of two-dimensional ferromagnets with Jahn-Teller ions," *Solid State Commun.,* vol. 13, pp. 763–766, 1973.

[106] A. Hettich, "Über die Natur von Silbersubfluorid," *Z. Anorg. Allg. Chem.,* vol. 167, pp. 67–74, 1927.

[107] H. Terrey and H. Diamond, "The Crystal Structure of Silver Subfluoride," *J. Chem. Soc.,* vol. 64, pp. 2820-2824, 1928.

[108] M. B. Robin, K. Andres, T. H. Geballe, N. Kuebler and D. B. McWhan, "Metallic Conductivity and Superconductivity in Some Silver Clathrate Salts," *Phys. Rev. Lett.,* vol. 17, p. 917, 1966.

[109] K. Andres, N. A. Kuebler and M. B. Robin, "Superconductivity in Ag_2F," *J. Phys. Chem. Solids,* vol. 27, pp. 1747–1748, 1966.

[110] M. Lozinšek, M. Belak Vivod and M. Dragomir, "Crystal structure reinvestigation of silver(I) fluoride, AgF," *IUCrData,* vol. 8, p. x230018, 2023.

[111] H. Ott, "Die Strukturen von MnO, MnS, AgF, NiS, SnJ_4, $SrCl_2$, BaF_2; Präzisionsmessungen einiger Alkalihalogenide," *Z. Kristallogr.,* vol. 63, pp. 222–230, 1926.

[112] M. Ebert, E. Rodowskas and J. C. W. Frazer, "Higher valence states of silver," *J. Am. Chem. Soc.,* vol. 55, pp. 3056–3057, 1933.

[113] O. Ruff and M. Giese, "Die Fluorierung des Silbers und Kupfers," *Z. Anorg. Allg. Chem.,* vol. 219, pp. 143–148, 1934.

[114] A. Jesih, K. Lutar, B. Žemva, B. Bachmann, S. Becker, B. G. Müller and R. Hoppe, "Einkristalluntersuchungen an AgF_2," *Z. Anorg. Allg. Chem.,* vol. 588, pp. 77–83, 1990.

[115] R. Bougon, T. Bui Huy, M. Lance and H. Abazli, "Synthesis and Properties of Silver Trifluoride, AgF_3," *Inorg. Chem.,* vol. 23, pp. 3667–3668, 1984.

[116] B. Žemva, K. Lutar, A. Jesih, W. J. Casteel, A. P. Wilkinson, D. E. Cox, R. B. von Dreele, H. Borrmann and N. Bartlett, "Silver Trifluoride: Preparation, Crystal Structure, Some Properties, and Comparison with AuF_3," *J. Am. Chem. Soc.,* vol. 113, pp. 4192–4198, 1991.

[117] R. Fischer and B. G. Müller, "Synthese und Kristallstruktur von Silber(II)-Fluoriden $AgM^{IV}F_6$ (M^{IV} = Sn, Ti, Pb, Pd, Pt Rh)," *Z. Anorg. Allg. Chem.,* vol. 627, pp. 445–452, 2001.

[118] R. Fischer and B. G. Müller, "Die Kristallstruktur von $Ag^{II}F[Ag^{III}F_4]$," *Z. Anorg. Allg. Chem.,* vol. 628, pp. 2592–2596, 2002.

[119] O. Graudejus, A. P. Wilkinson and N. Bartlett, "Structural Features of $Ag[AuF_4]$ and $Ag[AuF_6]$ and the Structural Relationship of $Ag[AgF_4]_2$ and $Au[AuF_4]_2$ to $Ag[AuF_4]_2$," *Inorg. Chem.,* vol. 39, pp. 1545–1548, 2000.

[120] W. Grochala, "On possible existence of pseudobinary mixed valence fluorides of Ag(I) / Ag(II): a DFT study," *J. Mol. Model.,* vol. 17, pp. 2237–2248, 2001.

[121] D. Kurzydłowski, M. Derzsi, E. Zurek and W. Grochala, "Fluorides of silver under large compression," *Chem. Eur. J.,* vol. 27, pp. 5536–5545, 2021.

[122] N. Rybin, I. Chepkasov, D. Y. Novoselov, V. I. Anisimov and A. R. Oganov, "Prediction of Stable Silver Fluorides," *J. Phys. Chem. C,* vol. 126, pp. 15057–15063, 2022.

[123] D. Babel, "Untersuchungen an ternären Fluoriden. III. Die Struktur des Na_2CuF_4," *Z. Anorg. Allg. Chem.,* vol. 261, pp. 200–206, 1965.

[124] H. Müller-Buschbaum and W. Wollschläger, "Über ternäre Oxocuprate. VII. Zur Kristallstruktur von Nd_2CuO_4," *Z. Anorg. Allg. Chem.,* vol. 414, pp. 76–80, 1975.

[125] J. Gawraczyński, Optical Spectroscopy of Selected Divalent Silver Compounds, Warsaw: University of Warsaw, 2019.

[126] I. D. Brown and D. Altermatt, "Bond-valence parameters obtained from a systematic analysis of the inorganic crystal structure database," *Acta Crystallogr. B,* vol. 26, pp. 1320–1323, 1970.

[127] J. Tong, C. Lee, M. H. Whangbo, R. K. Kremer, A. Simon and J. Köhler, "Cooperative Jahn–Teller distortion leading to the spin-1/2 uniform antiferromagnetic chains in triclinic perovskites $AgCuF_3$ and $NaCuF_3$," *Solid State Sci.,* vol. 12, pp. 680–684, 2010.

[128] R. Lösch and C. Hebecker, "Notizen: Ternäre Fluoride vom Typ $AgLnF_4$ (Ln = Nd, Sm-Lu, Y)," *Z. Naturforsch. B,* vol. 32, pp. 1093–1094, 1977.

[129] H. K. Onnes, "The superconductivity of mercury," *Comm. Phys. Lab. Univ. Leiden,* vol. 122, pp. 122–124, 1911.

[130] E. Maxwell, "Isotope effect in the superconductivity of mercury," *Phys. Rev.,* vol. 78, p. 477, 1950.

[131] C. A. Reynolds, B. Serin, W. H. Wright and L. B. Nesbitt, "Superconductivity of isotopes of mercury," *Phys. Rev. ,* vol. 78, p. 487, 1950.

[132] J. Bardeen, L. N. Cooper and J. R. Schrieffer, "Theory of superconductivity," *Phys. Rev.,* vol. 108, pp. 1175–1204, 1957.

[133] L. N. Cooper, "Bound electron pairs in a degenerate fermi gas," *Phys. Rev.,* vol. 104, pp. 1189–1190, 1956.

[134] W. Buckel and R. Kleiner, Superconductivity: Fundamentals and Applications, Wiley-VCH, 2004.

[135] "The Nobel Prize in Physics 1972," [Online]. Available: https://www.nobelprize.org/prizes/physics/1972/summary/. [Accessed 10 06 2024].

[136] J. G. Bednorz and K. A. Müller, "Possible high T_c superconductivity in the Ba—La—Cu—O system," *Z. Phys. B: Condens. Matter,* vol. 64, pp. 189–193, 1986.

[137] M. K. Wu, J. R. Ashburn, C. J. Torng, P. H. Hor, R. L. Meng, L. Gao, Z. J. Huang, Y. Q. Wang and C. W. Chu, "Superconductivity at 93 K in a new mixed-phase Y-Ba-Cu-O compound system at ambient pressure," *Phys. Rev. Lett.,* vol. 58, p. 908, 1987.

[138] G. F. Sun, K. W. Wong, B. R. Xu, Y. Xin and D. F. Lu, "T_c enhancement of $HgBa_2Ca_2Cu_3O_{8+x}$ by Tl substitution," *Phys. Lett. A,* vol. 192, pp. 122–124, 1994.

[139] H. A. Jahn and E. Teller, "Stability of polyatomic molecules in degenerate electronic states - Orbital degeneracy," *Proc. R. Soc. Lond. A,* vol. 161, pp. 220–235, 1937.

[140] B. Keimer, S. A. Kivelson, M. R. Norman, S. Uchida and J. Zaanen, "From quantum matter to high-temperature superconductivity in copper oxides," *Nature,* vol. 518, pp. 179–186, 2015.

[141] V. I. Anisimov, D. Bukhvalov and T. M. Rice, "Electronic structure of possible nickelate analogs to the cuprates," *Phys. Rev. B,* vol. 59, pp. 7901–7906, 1999.

[142] K. W. Lee and W. E. Pickett, "Infinite-layer $LaNiO_2$: Ni^{1+} is not Cu^{2+}," *Phys. Rev. B,* vol. 70, p. 165109, 2004.

[143] D. Li, K. Lee, B. Y. Wang, M. Osada, S. Crossley, H. R. Lee, Y. Cui, Y. Hikita and H. Y. Hwang, "Superconductivity in an infinite-layer nickelate," *Nature,* vol. 572, pp. 624–627, 219.

[144] B. Žemva and N. Bartlett, "The room temperature preparation of metastable fluorides and potent oxidizers," *J. Fluor. Chem.,* vol. 127, pp. 1463–1466, 2006.

[145] K. Tokar, M. Derzsi and W. Grochala, "Comparative computational study of antiferromagnetic and mixed-valent diamagnetic phase of AgF_2: Crystal, electronic and phonon structure and p-T phase diagram," *Comput. Mater. Sci.,* vol. 188, p. 110250, 2021.

[146] C. Shen, B. Žemva, G. M. Lucier, O. Graudejus, J. A. Allman and N. Bartlett, "Disproportionation of Ag(II) to Ag(I) and Ag(III) in Fluoride Systems and Syntheses and Structures of $(AgF^+)_2AgF_4MF_6$ Salts (M = As, Sb, Pt, Au, Ru)," *Inorg. Chem.,* vol. 38, pp. 4570– 4577, 1999.

Bibliography